Deutsche Geodätische Kommission
bei der Bayerischen Akademie der Wissenschaften

Reihe C Dissertationen Heft Nr. 699

Lieselotte Zenner

Atmospheric and Oceanic Mass Variations and their role for gravity field determination

München 2013

Verlag der Bayerischen Akademie der Wissenschaften
in Kommission beim Verlag C. H. Beck

ISSN 0065-5325 ISBN 978-3-7696-5111-9

DGK Deutsche Geodätische Kommission
bei der Bayerischen Akademie der Wissenschaften

Reihe C Dissertationen Heft Nr. 699

Atmospheric and Oceanic Mass Variations and their role for gravity field determination

Vollständiger Abdruck
der von der Ingenieurfakultät Bau Geo Umwelt
der Technischen Universität München
zur Erlangung des akademischen Grades eines
Doktor-Ingenieurs (Dr.-Ing.)
genehmigten Dissertation

von

Dipl.-Ing. Lieselotte Zenner

München 2013

Verlag der Bayerischen Akademie der Wissenschaften
in Kommission beim Verlag C. H. Beck

ISSN 0065-5325 ISBN 978-3-7696-5111-9

Adresse der Deutschen Geodätischen Kommission:

Deutsche Geodätische Kommission
Alfons-Goppel-Straße 11 ● D – 80 539 München
Telefon +49 – 89 – 23 031 1113 ● Telefax +49 – 89 – 23 031 - 1283 / - 1100
e-mail hornik@dgfi.badw.de ● http://www.dgk.badw.de

Prüfungskommission
Vorsitzende: Univ.-Prof. Dr.-Ing. habil. Th. Wunderlich
Prüfer der Dissertation: 1. Prof. Dr.techn. R. Pail
2. Prof. Dr.rer.nat. M. Thomas, Freie Universität Berlin
3. Univ.-Prof. Dr.-Ing. Dr. h.c. mult. R. Rummel (i.R.)

Die Dissertation wurde am 22.11.2012 bei der Technischen Universität München eingereicht
und durch die Ingenieurfakultät Bau Geo Umwelt am 26.02.2013 angenommen.

Diese Dissertation ist auch auf mediaTUM – Dokumenten- und Publikationsserver der Technischen Universität München
<http://mediatum.ub.tum.de/node?id=1121142> elektronisch publiziert (Erscheinungsjahr 2013)

ISSN 0065-5325 ISBN 978-3-7696-5111-9

Abstract

High-frequency, time-varying mass redistributions in the ocean and atmosphere have an impact on GRACE gravity field solutions due to the space-time sampling characteristics of signal and orbit. Consequently, aliasing of these signals into the GRACE observations is present and needs to be taken into account during data analysis by applying atmospheric and oceanic model data (de-aliasing). As the accuracy predicted prior to launch could not yet be achieved in the analysis of real GRACE data, the de-aliasing process and related geophysical model uncertainties are regarded as a potential error source in GRACE gravity field determination. Therefore, this thesis is examining various aspects of the modelling of atmospheric and oceanic mass variations and the calculation of the de-aliasing product (AOD). The aim of the thesis is to identify potential starting points to further improve the de-aliasing process in order to obtain more accurate (GRACE) gravity field time series. As these time series provide estimates for the integrated mass transport in the Earth system, like the global water cycle and solid Earth geophysical processes, any increase in accuracy will lead to improvements in the geophysical interpretation of the results. So in conclusion, improving the de-aliasing is of relevance for a better understanding of geophysical processes in the Earth and on its surface.

In the first part of this thesis, the principle of GRACE gravity field processing as well as the basic equations for the calculation of the AOD product are reviewed. Furthermore, a newly developed and alternative procedure, which allows to propagate geophysical model uncertainties to the de-aliasing coefficients, is introduced.

The second part gives an overview of the geophysical models used within this work. The applied atmospheric, oceanic and hydrological model data as well as their uncertainties are presented and discussed. In addition, the BERNESE gravity field software used for the calculation of K-band range-rate residuals and monthly gravity field solutions is introduced.

The third and main part of this thesis is analyzing the impact of various changes in the AOD calculation on the de-aliasing coefficients itself as well as on GRACE data analysis, such as the impact of various de-aliasing approaches, like numerical integration instead of least-squares adjustment, surface pressure approach instead of vertical integration approach, or the use of a latitude-dependent gravity acceleration instead of a constant one. But also the impact of atmospheric and oceanic model uncertainties as well as the use of alternative (input) data is discussed and their impact on GRACE data analysis as well as on future gravity field missions is investigated.

Part four summarizes and discusses the various screws that can be turned during the modelling and calculation of the atmospheric and oceanic mass variations.

Although the impact of the analyzed de-aliasing scenarios is rather small concerning current (GRACE) gravity field time series, it could be shown within this thesis, that almost all investigated changes in the computation of the de-aliasing product are of great importance especially for future gravity field missions with improved observation accuracy and are therefore a key issue to be addressed in order to improve gravity field time series. In particular, the stochastic modelling of the geophysical input data and the herewith associated determination of reliable uncertainty estimates of the atmospheric and oceanic models plays a major role for de-aliasing and time-variable gravity field estimation.

Zusammenfassung

Hochfrequente Massenvariationen im Ozean und in der Atmosphäre haben einen direkten Effekt auf GRACE Schwerefeldlösungen. Aufgrund der hohen räumlichen und zeitlichen Auflösung dieser Massenvariationen sowie der Bahngeometrie können sie durch Satellitenbeobachtungen nicht genau genug abgetastet werden. In Folge dessen kommt es zu Aliasing-Effekten in den Satellitenmessungen. Um diese zu vermeiden beziehungsweise so gering wie möglich zu halten, werden die hochfrequenten zeitlichen Variationen der Atmosphöre sowie des Ozeans im sogenannten De-aliasing Prozess modelliert und während der Schwerefeldberechnung eliminiert. Da die angestrebte Genauigkeit von GRACE bisher noch nicht erreicht werden konnte, sieht man im De-aliasing Prozess und in den Unsicherheiten der darin eingehenden geophysikalischen Modelle eine mögliche Fehlerquelle. Die vorliegende Arbeit beschäftigt sich daher mit verschiedenen Aspekten in der Modellierung dieser atmosphärischen und ozeanischen Massenvariationen sowie in der Berechnung des De-aliasing Produktes (AOD). Ziel der Arbeit ist es, mögliche Ansatzpunkte für die Verbesserung des De-aliasing Prozesses aufzuzeigen, um so genauere (GRACE) Schwerefeldzeitreihen berechnen zu können. Diese werden als Abschätzung für Massentransporte im System Erde herangezogen, wie z.B. den globalen Wasserhaushalt und geophysikalische Prozesse im Inneren der Erde. Jede Verbesserung der Genauigkeit in den Schwerefeldzeitreihen führt zu einem besseren Verständnis dieser geophysikalischen Vorgänge. Das bedeutet also, dass die Optimierung des De-aliasing Prozesses von großer Bedeutung für ein besseres Verständnis von geophysikalischen Prozessen in und auf der Erde ist.

Der erste Teil dieser Arbeit fasst das Grundprinzip der GRACE Schwerefeldprozessierung sowie die wesentlichen Formeln zur Berechnung des De-aliasing Produktes zusammen. Des Weiteren wird ein neu entwickelter und alternativer Ansatz zur Berechnung des De-aliasing Produktes vorgestellt, mit welchem Unsicherheiten in den geophysikalischen Eingangsmodellen auf die De-aliasing Koeffizienten fortgepflanzt werden können.

Im zweiten Teil wird ein Überblick der in dieser Arbeit verwendeten geophysikalischen Modelldaten gegeben. Die verwendeten atmosphärischen, ozeanischen und hydrologischen Eingangsdaten sowie deren Unsicherheiten, werden vorgestellt und diskutiert. Des Weiteren wird die BERNESE Schwerefeldsoftware, welche zur Berechnung von K-band range-rate Residuen und monatlichen Schwerefeldlösungen verwendet wurde, vorgestellt.

Teil drei dieser Arbeit untersucht den Einfluss von verschiedensten Änderungen in der AOD Berechnung auf die De-aliasing Koeffizienten sowie die GRACE Datenprozessierung. Dazu gehören z.B. die Auswirkung verschiedener De-aliasing Ansätze, wie der numerischen Integration im Vergleich zur Kleinsten-Quadrate-Ausgleichung, der Verwendung des Bodendrucks statt des vertikal integrierten Drucks für die Atmosphäre, oder die Anwendung einer breitenabhängigen Schwerebeschleunigung statt einer konstanten. Aber auch der Einfluss von atmosphärischen und ozeanischen Modellfehlern und alternativen Daten wird diskutiert und deren Einfluss auf die GRACE Datenanalyse als auch auf zukünftige Schwerefeldmissionen untersucht.

Im vierten und letzten Teil dieser Arbeit werden die verschiedenen Stellschrauben, an denen während der Modellierung und Berechnung des De-aliasing Produktes gedreht werden kann, diskutiert und zusammengefasst.

Wenn auch der Einfluss der analysierten De-aliasing Szenarien auf gegenwärtige GRACE Schwerefeldzeitreihen relativ gering ist, konnte in dieser Arbeit gezeigt werden, dass nahezu alle untersuchten Änderungen in der Berechnung des De-aliasing Produktes von großer Bedeutung, insbesondere für zukünftige Schwerefeldmissionen mit höherer Beobachtungsgenauigkeit, sind. Die optimale Modellierung der atmosphärischen und ozeanischen Massenvariationen und der damit zusammenhängende De-aliasing Prozess sind somit ein Schlüsselthema auf dem Weg zu verbesserten Schwerefeldzeitreihen. Besonders die stochastische Modellierung der geophysikalischen Eingangsdaten und die damit verbundene Bestimmung von verlässlichen bzw. realistischen Fehlerabschätzungen der atmosphärischen und ozeanischen Modelle, spielt für das De-aliasing und die Bestimmung von zeitvariablen Schwerefeldern eine große Rolle.

Contents

1. Introduction

Mass redistributions inside, on, and above the Earth's surface are responsible for time variable gravity field forces, which directly influence a satellite's orbit. In case these variations have a frequency above the Nyquist frequency, which is defined by the repeat period of a satellite orbit, one has to take into account these mass variations in order to avoid aliasing due to undersampling. In case of a non-repeat cycle orbit (as for GRACE) one has to analyze the sampling characteristics of the actual orbit beforehand in order to identify the frequency, where aliasing will start to have impact on the resulting gravity field solutions. It is obvious that mass variations by tidal forces and in the coupled atmosphere/ocean system occur with much higher frequencies than the Nyquist frequency of a single satellite mission. As the GRACE observable is a distance (or distance change) between two satellites (separation approximately 220 km), in this context GRACE also has to be regarded as a single satellite mission, because no multiple observations are taken simultaneously at different locations. What concerns the signal strength, apart from ocean, atmosphere and Earth tides, which are taken into account in the gravity field determination process by models, also non-tidal atmospheric and oceanic mass variations have a strong impact on the GRACE microwave ranging system and cause aliasing, if not taken into account properly (*Han et al.* (2004), *Thompson et al.* (2004)). Therefore, in the standard GRACE data processing, the high-frequency atmospheric and oceanic signals are modelled and removed during the data analysis. This process is called high-frequency atmospheric and oceanic de-aliasing (AOD) and is described in *Flechtner* (2007a).

In addition it should be mentioned here that high-frequency in our context means that a multi-year mean is subtracted and that only deviations from this mean are taken into account and analyzed spectrally. As the quality of the GRACE gravity field solutions has still not reached the simulated pre-launch baseline accuracy, all contributing error sources have to be investigated and analyzed in detail. One potential error source could be the de-aliasing process and uncertainties of the geophysical models applied during this process. In this thesis we concentrate on the high-frequency de-aliasing due to atmospheric and oceanic mass variations and investigate in detail, if and how it could be improved.

The improvement of GRACE gravity field solutions is essential for many applications. Geophysicists, e.g., interpret the GRACE measurements in terms of various geophysical processes based on models and observations. It was shown in several studies that GRACE is of sufficient quality to observe effects of co-seismic and post-seismic deformations (e.g. Sumatra earthquake, *Chen et al.* (2007)). GRACE is also used to better model and calibrate geophysical fluid processes (*Werth et al.*, 2009). On the other hand, geophysical models are input to GRACE data analysis. Improved models will lead to more accurate GRACE measurements, and vice versa. GRACE, therefore, links geodetic and geophysical research aspects. Generating more accurate GRACE gravity field solutions will help us to better analyze and understand the mass redistributions on and in the Earth.

The thesis is structured into four major parts: the theory (I), the data used within this work (II), the analysis part with the performed investigations (III), and the summary with discussion (IV).

Part I deals with the theory of the whole de-aliasing process. After a short introduction on the principle of GRACE gravity field processing (Chapter 2), the basic equations of the standard de-aliasing process, as it is described in *Flechtner* (2007a), are summarized (Chapter 3). As the standard processing scheme assumes error-free atmospheric and oceanic parameters and as it is well known that in areas with sparse observations the atmospheric models are degraded in quality (*Salstein et al.*, 2008), there is some motivation to assume, that by taking into account uncertainties of the atmospheric and oceanic model parameters one could improve the de-aliasing product and consequently the gravity field solutions. This is why a mathematical model of error propagation of the atmospheric and oceanic model uncertainties into the gravity field de-aliasing coefficients was developed. The processing strategy and the formulas to be applied are shown in Chapter 4.

Part II gives an overview of the applied data within this thesis. The atmospheric and oceanic input parameters, provided by the European Centre for Medium-Range weather Forecasts (ECMWF) and the Ocean

Model for Circulation and Tides (OMCT), as well as the meteorological model errors, amongst others derived from model inter-comparisons between ECMWF and NCEP (National Centers for Environmental Prediction) or data from the Finite Element Sea Ice-Ocean Model (FESOM) were introduced in Chapter 5 and 6. The Bernese GPS Software, used to compute the K-band residuals and monthly gravity field solutions, as well as additional data, like the daily GRACE solutions, applied within this thesis, are presented in Chapter 7.

Part III summarizes the investigations performed within this thesis. First (Chapter 8), various de-aliasing approaches are compared to each other. The impact of every change made within the modelling and/or calculation of the de-aliasing coefficients is investigated on various processing levels: AOD coefficients, GRACE K-band residuals, and GRACE monthly gravity field solutions. The differences between numerical integration and least-squares adjustment, between the surface pressure and vertical integration approach as well as between using a constant or latitude-dependent gravity acceleration are shown in Chapter 8.1 and 8.2 and 8.3. While the role of the maximum degree and de-aliasing at all for gravity field determination is summarized in Chapter 8.4, Chapter 8.5 compares our TUM de-aliasing product to the official one provided by the GeoForschungsZentrum, Potsdam (GFZ).
Then, in Chapter 9, the impact of the atmospheric and oceanic error assumptions on the estimated de-aliasing coefficients, K-band residuals and monthly GRACE gravity field solutions is investigated. Differences between the error-free and error scenarios are computed and compared to the GRACE and future gravity field mission error predictions.
Chapter 10 deals with the impact of alternative and additional model data on the AOD coefficients and on GRACE. Alternative model data, in this context, means to investigate the effect of using ERA-Interim data instead of operational ECMWF data (Chapter 10.1), to analyze the impact of an enhanced spatial resolution of the ocean bottom pressure fields (Chapter 10.2) as well as analyzing the use of various mean fields, covering alternative time-spans than the currently applied ones, which are covering the period 2001 and 2002 (Chapter 10.3). Finally, the impact of an additional hydrological de-aliasing is investigated. Therefore, the daily ITG-GRACE solutions, provided by the Institute of Geodesy and Geoinformation, Bonn, are used and combined with the atmospheric and oceanic de-aliasing coefficients. Results are summarized in Chapter 10.4.

Part IV summarizes the investigated de-aliasing scenarios and discusses the achieved results.

Elements of this thesis, especially of Section 9 have already been published in international per-reviewed journals:

- Zenner et al. (2012): *Using atmospheric uncertainties for GRACE de-aliasing: first results*, in Geodesy for Planet Earth, IAG Symposia, Springer, 2012, 136, 147-152
- Zenner et al. (2012): *Non-tidal atmospheric and oceanic mass variations and their impact on GRACE data analysis Journal of Geodynamics*, 2012, 59-60, 9-15
- Zenner et al. (2010): *Propagation of atmospheric model errors to gravity potential harmonics - impact on GRACE de-aliasing*, Geophys. J. Int., 2010, 797-807

Part I.

THEORY AND BASIC FORMULAS

The following part reviews the de-aliasing process as well as its fundamental formulas, and introduces a newly developed de-aliasing procedure allowing to take geophysical model uncertainties into account.

First, in Sect. 2, an overview of the principle of GRACE Gravity Field Data Analysis, the processing scheme and the role of the de-aliasing process within the gravity field processing is given. Afterwards, the basic equations of the de-aliasing process are reviewed, and the two familiar approaches for the computation of the atmospheric potential are summarized (Sect. 3).

As the current de-aliasing approach does not allow to take model uncertainties into account, although it is well known, that in areas with sparse observations the atmospheric models are degraded in quality (*Salstein et al.*, 2008), an alternative de-aliasing process has been developed which allows to take model errors into account. The mathematical method of error propagation for the de-aliasing process as well as the determination of the de-aliasing coefficients, determined alternatively, are summarized in Sect. 4.

2. A short introduction to the principle of GRACE Gravity Field processing

The first chapter of this work intends to give an overview of the principle of GRACE Gravity Field Data Analysis. Like in *Flechtner and Gruber* (2007), the processing scheme will be simplified in order to point out the very basic principle and to give a better understanding of the de-aliasing process. Detailed information on this topic can be found in the GRACE Level-2 processing Standards (*Flechtner* (2007b)) and in the User Handbook (*Bettadpur* (2007)).

Figure 2.1 shows schematically the GRACE Data Analysis procedure. Starting point is the so-called equation of motion (EOM):

$$\ddot{\bar{r}} = -\frac{GM}{r^3}\bar{r} + \bar{F}_D \tag{2.1}$$

It describes the acceleration $\ddot{\bar{r}}$ acting on a satellite due to the existing conservative and non-conservative disturbance forces $\bar{F}_D$. Integrating Eq. (2.1) once or twice leads to the velocity and the position of the satellite. If there were no disturbance forces but only the central gravitational force $-\frac{GM}{r^3}\bar{r}$, the orbit $\bar{r}$ of the satellite would follow a Keplerian mean motion. In reality several forces are acting on a satellite, that means the orbit is no longer elliptical, and the determination of the satellite's orbit becomes more complex, as the disturbance forces $\bar{F}_D$ have to be modelled (and/or measured).

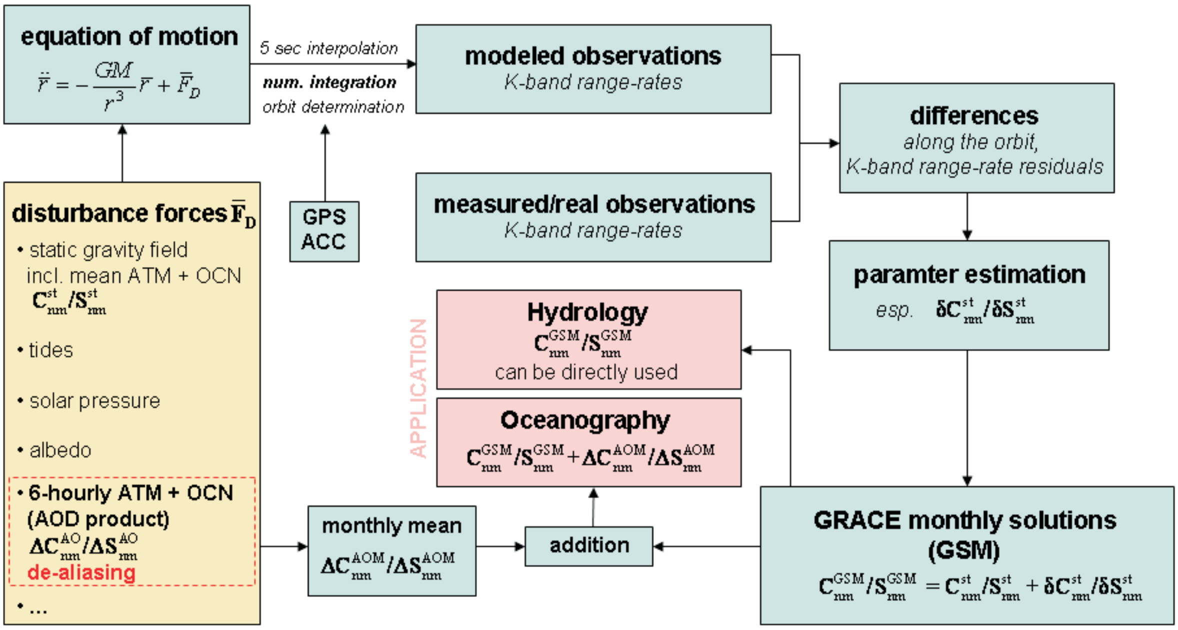

Fig. 2.1: Principle of the GRACE Data Analysis Processing

The **disturbance forces** $\overline{F}_D$ include *gravitational* and *non-gravitational* forces. In addition, in many gravity field processing software *empirical* parameters are introduced (see later for more details). Solar pressure, atmospheric drag and albedo are such *non-gravitational forces*, they act on the satellite's surface. They are causing additional accelerations, basically in flight-, radial- and cross-track direction of the satellite. For GRACE these accelerations are measured by the on-board accelerometer and are directly used for the correction of the measurements.
The *gravitational forces* are the sum of the geopotential perturbations and the direct planetary (esp. moon & sun) perturbations. For the geopotential perturbations a static a-priori Earth gravity field C_{nm}^{st}/S_{nm}^{st} including a mean atmosphere and ocean potential is introduced. Further potential fields generating perturbations on a satellite's orbit are tides. Therefore, also direct tides, solid Earth tides, ocean tides, and pole tides are included in the force model. In addition - and which is the most important part for this work - short-term atmospheric and oceanic mass variations cause potential variations and act as disturbance forces on a satellite's orbit. During GRACE gravity field analysis these variations are removed by the so-called atmosphere and ocean de-aliasing (AOD) product. This is done in order to avoid aliasing due to temporal undersampling, because GRACE is not able to adequately sample these short-term atmospheric and oceanic mass variations. Thus, these variations are modelled in 6-hourly intervals (see chapter 3) via geophysical models and are, after interpolation on the integration interval which is usually 5 seconds, 'removed' during gravity field determination. This process is called de-aliasing. Having modelled them correctly and realistically, the resulting GRACE gravity field solutions should not contain any atmospheric and oceanic signal with periods shorter than the sampling period of the gravity field solution (which is usually one month).
The mentioned *empirical forces* are introduced in the disturbance force models in order to treat the mismodelled or umodelled forces acting on a satellite. The intent of these empirical non-gravitational parameters, introduced during gravity field determination, is to absorb the poorly modelled parts of the force fields and to treat the measuring effects. In principle there are several types of empirical parameters like dynamic and kinematic ones. E.g., these empirical models are often used to absorb the biased accelerometer measurements. A more detailed description of the role of the empirical forces within orbit and gravity field determination is given, e.g., in *Kim* (2000), *Jäggi* (2006) and *Beutler et al.* (2010b). The main aspect concerning these empirical forces, and being relevant for this work is the fact, that each empirical parameter introduced in the orbit or gravity field determination might disturb the solution for the other non-empirical parameters, e.g. gravity field coefficients, as these empirical forces may absorb in addition geophysical signals, also model errors and unmodelled effects. This issue is revisited in chapter III.

After having modelled the disturbance forces, the orbit of the satellite is determined every 5 seconds by **numerical integration of the equation of motion** (Eq. (2.1)). In order to improve the model, GPS observations are introduced, which leads to an adaption of the orbit to the GPS observations. Like mentioned before the non-conservative forces can be directly measured by accelerometers, and enter to the EOM as correction terms to the accelerations (ACC) $\ddot{\vec{r}}$ on the left-hand side of Eq. (2.1). From the numerically integrated orbit (positions), **modelled/computed observations** are derived, which are then **compared to the measured ones**. For GRACE, basically inter-satellite K-band range-rates (KBRR) are computed and serve as modelled observations. If all force models (tides, static gravity field, AOD-model, . . .) as well as the real observations were error-free, the modelled/computed observations would be equal to the real measured observations. Since this is not the case, differences (residuals) between the modelled/computed and the real observations occur. This means that the residuals reflect, besides measuring errors, mainly deviations of the force models from reality, and unmodelled forces. The smaller these residuals are, the better the model fits to the reality. Later on, deeper analysis of these KBRR-residuals is performed (see part III), in order to investigate the effect of various de-aliasing products on GRACE gravity field processing.

In a next step, a **parameter estimation** (least-squares adjustment) is performed, in order to optimally transform these residuals into model improvements and calibration parameters of the measuring instruments, respectively. Because of the multiplicity and diversity of the parameters used in the force models, it is not possible to improve all parameters (or parameter groups) within this estimation process. Therefore, in the course of gravity field modelling, one concentrates on, besides the initial orbit and the calibration parameters of the accelerometer, the improvement of the static gravity field coefficients $\delta C_{nm}^{st}/\delta S_{nm}^{st}$. Depending on the time and space pattern of the observations (GPS and K-band), gravity field coefficients can be estimated. For GRACE this is usually done for a time interval of one month, which means that for every month improvements for a set of gravity field coefficients is estimated. Adding these improvements back to the a-priori static gravity field, the well known monthly gravity field solutions $C_{nm}^{GSM}/S_{nm}^{GSM}$ are obtained. The same procedure is applied for the daily (*Kurtenbach et al.*, 2009), weekly (*Flechtner et al.*, 2010), and 10-days (*Lemoine et al.*, 2007) GRACE solutions, processed by various research groups.

(Remark: Theoretically, every other parameter group could be improved by this process (e.g. force models). The improvements of one parameter group are gained at the cost of an error-free assumption of the other parameter group, as the other parameter group (e.g. static gravity field) has always to be assumed as error-free. During GRACE gravity field processing, as the name implies, the force models including the 6-hourly atmospheric and oceanic potential are regarded as error-free, while the model improvements are estimated for the static gravity field.)

With the processing sequence described above it should have become obvious, that the **GRACE monthly gravity field solutions** ($C_{nm}^{GSM}/S_{nm}^{GSM}$) do not contain any high-frequency atmospheric or oceanic mass variations. 'High-frequency' or 'short term' in this context means that periods shorter than 1 month, e.g. sub-daily, daily and weekly variations, are removed. The monthly solutions mainly contain hydrology and other unmodelled effects, like ice and post-glacial rebound as well as model, measuring and instrument errors. For oceanographers, it might be interesting to compare the GRACE solutions to their models. This is only possible if the beforehand removed atmospheric and oceanic potential is re-added. Otherwise no oceanic mass variations (or to be more precise only residual mass variations w.r.t. the a-priori ocean model) are visible in the monthly GRACE gravity field solutions, as - like described before - these variations are included in the disturbance forces and are eliminated within the de-aliasing process during gravity field determination. Before the de-aliasing coefficients can be re-added to the monthly gravity solutions, they have to refer to the same observation span, namely one month, as the gravity field solutions. Therefore, monthly means $\Delta C_{nm}^{AOM}/\Delta S_{nm}^{AOM}$ of the 6-hourly AOD coefficients are calculated. These monthly means of the (vertically integrated) atmospheric and oceanic mass variations are officially named GAC-products and are routinely provided by GFZ (*Flechtner*, 2007a). Only by the re-addition of this product ($\Delta C_{nm}^{AOM}/\Delta S_{nm}^{AOM}$ or GAC) to the corresponding monthly gravity field solutions, the full signal of the oceanic mass variations are visible in the gravity field solutions.

For the sake of completeness, also the meaning of the other officially determined and provided *GXX* products shall be explained (see *Flechtner* (2007a)). The following descriptions will probably become clearer when studying Sects. 3.1 & 3.2, as the notations in brackets are anticipated here.

- **GAA**: monthly mean of the vertically integrated atmospheric pressure (I_n, VI-approach). Difference to GAC is, that here no oceanic variations are included.
- **GAB**: monthly mean of the oceanic mass variations P_O. Difference to GAC is, that here no atmospheric variations are included.
- **GAC**: monthly mean of the vertically integrated atmospheric masses (I_n, VI-approach) plus oceanic mass variations. GAC is the sum of GAA and GAB.
- **GAD**: monthly mean of the atmospheric surface pressure (P_S, SP-approach) plus oceanic mass variations (P_O). In contrast to GAC the atmospheric masses are not vertically integrated, instead they are represented by the surface pressure itself.

For more details on the usage, especially of GAD and GAB, we refer to *Bettadpur et al.* (2006) in addition to *Flechtner* (2007a).

3. The de-aliasing process

As mentioned in Sect. 2 the de-aliasing process plays an important role in the course of gravity field data analysis with GRACE. The potential disturbances caused by short-term atmospheric and oceanic variations are acting on a satellite's orbit and are therefore modelled and enter the force model(s) used for the orbit integration. The following chapter summarizes the fundamental formulas for the determination of the atmospheric and oceanic de-aliasing coefficients.

At satellite altitude, i.e. for observations outside the attracting masses (here we are only interested in oceanic and atmospheric mass changes), the gravitational potential V can be regarded as a harmonic function and therefore expanded into a series of spherical harmonics (see. e.g. *Heiskanen and Moritz* (1967)):

$$V(P) = \frac{GM}{R} \sum_{n=0}^{\infty} \left(\frac{R}{r}\right)^{(n+1)} \sum_{m=0}^{n} \bar{P}_{nm}(\cos\theta) \left[\bar{C}_{nm}\cos m\lambda + \bar{S}_{nm}\sin m\lambda\right] \tag{3.1}$$

$$\left.\begin{array}{c}\bar{C}_{nm}\\ \bar{S}_{nm}\end{array}\right\} = \frac{1}{(2n+1)M} \iiint_{\Sigma} \left(\frac{r}{R}\right)^{n} \rho(r,\theta,\lambda)\cdot\bar{P}_{nm}(\cos\theta) \left\{\begin{array}{c}\cos m\lambda\\ \sin m\lambda\end{array}\right\} d\Sigma \tag{3.2}$$

with

r, θ, λ = spherical, geocentric coordinates
G = gravitational constant of the Earth
M = Earth mass
R = radius of the Earth's sphere
ρ = volume density
$d\Sigma$ = volume element
$\overline{P}_{nm}$ = associated fully normalized Legendre polynomials of degree n and order m
$\overline{C}_{nm}$,$\overline{S}_{nm}$ = fully normalized potential coefficients of degree n and order m

Remark: It has to be mentioned that equations (3.1) and (3.2) only hold for satellite observations, i.e. for masses "below" the measuring point P or observations taken outside the attracting atmospheric masses. This issue is further discussed in Sect. 11.

From Eq. (3.2) it can be seen that the potential coefficients are determined by the integration of the density ρ over all volume elements $d\Sigma$. Introducing $M = (4/3)\pi R^3\bar{\rho}$ with the mean density $\bar{\rho}$ of the Earth, and splitting the volume element ($d\Sigma = r^2 dr \sin\theta d\theta d\lambda$) into a surface ($d\sigma = \sin\theta d\theta d\lambda$) and a height dependent ($r^2 dr$) part, we get:

$$\left.\begin{array}{c}\bar{C}_{nm}\\ \bar{S}_{nm}\end{array}\right\} = \frac{1}{(2n+1)} \frac{3}{4\pi R\bar{\rho}} \iint_{\sigma} I_n(\theta,\lambda)\cdot\bar{P}_{nm}(\cos\theta) \left\{\begin{array}{c}\cos m\lambda\\ \sin m\lambda\end{array}\right\} d\sigma \tag{3.3}$$

$$I_n = \int_{R}^{\infty} \left(\frac{r}{R}\right)^{n+2} \rho(r,\theta,\lambda) dr \tag{3.4}$$

The degree-dependent, radial integration term I_n represents the variable load of the atmosphere and the ocean. I_n is also called surface load, as its physical unit $\frac{kg}{m^2}$ corresponds to a surface density. As integration limits usually the lower level (Earth surface R) and the top level of the atmosphere ($\sim$ 80 km) are chosen.

Equation (3.3) describes the direct effect of the gravitational attraction of the atmospheric and oceanic masses. Taking into account the elastic deformation of the solid Earth, induced by mass loading via the load Love numbers $k_n^{'}$ (*Munk and McDonald*, 1960), wet get the final formula for the determination of the atmospheric and oceanic potential coefficients:

$$\left.\begin{array}{c}\bar{C}_{nm}\\ \bar{S}_{nm}\end{array}\right\} = \frac{(1+k_n^{'})}{(2n+1)} \cdot \frac{3}{4\pi R\bar{\rho}} \int\int_{\sigma} I_n(\theta,\lambda) \cdot \bar{P}_{nm}(\cos\theta) \left\{\begin{array}{c}\cos m\lambda\\ \sin m\lambda\end{array}\right\} d\sigma. \tag{3.5}$$

In general the surface load (Eq. (3.4)) induced by the atmosphere is determined separately from the one induced by the oceanic masses. They are combined/added, before performing the numerical integration within Eq. (3.5).

The following chapters 3.1 and 3.2 will give an overview of two methods to determine the variable load I_n of the atmosphere and the ocean. At this point it shall be emphasized that the following formulas refer to a spherical Earth. This means the ellipsoidal shape of the Earth is neglected and approximated by a sphere. This is done as the computational effort for an ellipsoidal Earth is much higher. By the use of the spherical approximation, the more complicated ellipsoidal harmonics can be avoided.

3.1. SP approach - Using only the Surface Pressure

In the surface pressure (SP) approach one assumes that all atmospheric masses are condensed on a thin layer on the Earth's surface ($r = R$), and that they are sufficiently represented by the surface pressure P_S. The same assumption is made for the ocean. Here the ocean bottom pressure P_O represents the oceanic loading. This means that the radial integration within Eq. (3.4) has not to be performed, and the degree-dependency of I_n disappears as r becomes R on the Earth's surface. Applying the hydrostatic equation

$$dp = -\rho g dr \Leftrightarrow \rho dr = -\frac{1}{g} dp \tag{3.6}$$

to Eq. (3.4), leads to:

$$I_n = \frac{P_s}{g} \tag{3.7}$$

for the atmospheric loading and

$$I_n = \frac{P_O}{g} \tag{3.8}$$

for the oceanic loading. g hereby is a mean gravity acceleration of the Earth's sphere. Combining the oceanic with the atmospheric part and inserting Eqs. (3.7) and (3.8) into Eq. (3.5), the gravity coefficients are determined in the SP approach by:

$$\left.\begin{array}{c}\bar{C}_{nm}\\ \bar{S}_{nm}\end{array}\right\} = \frac{(1+k_n^{'})}{(2n+1)} \frac{3}{4\pi R\bar{\rho}g} \int\int_{\sigma} [P_S + P_O] \cdot \bar{P}_{nm}(\cos\theta) \left\{\begin{array}{c}\cos m\lambda\\ \sin m\lambda\end{array}\right\} d\sigma. \tag{3.9}$$

Before the atmosphere is combined with the ocean, a mean surface pressure field P_S^{ref} and a mean ocean pressure field P_O^{ref} are usually subtracted beforehand from the instantaneous atmospheric pressure P_S as well as from the ocean bottom pressure P_O in order to analyze gravitational variations. As the mean mass distribution of the atmosphere and ocean by definition belongs to the static part of the gravity field, only the deviations from the mean value have to be taken into account for the de-aliasing process in order to remove the short-term gravitational variations. Equation (3.9) turns then into the final formula:

$$\left.\begin{array}{c}\bar{C}_{nm}\\ \bar{S}_{nm}\end{array}\right\} = \frac{(1+k_n^{'})}{(2n+1)} \cdot \frac{3}{4\pi R\bar{\rho}g} \int\int_{\sigma} P_{AO} \cdot \bar{P}_{nm}(\cos\theta) \left\{\begin{array}{c}\cos m\lambda\\ \sin m\lambda\end{array}\right\} d\sigma. \tag{3.10}$$

with $P_{AO} = P_S - P_S^{ref} + P_O - P_O^{ref} = \Delta P_S + \Delta P_O$

After subtracting the mean fields, the numerical integration of P_{AO} is performed, and the atmospheric and oceanic potential coefficients are retrieved.

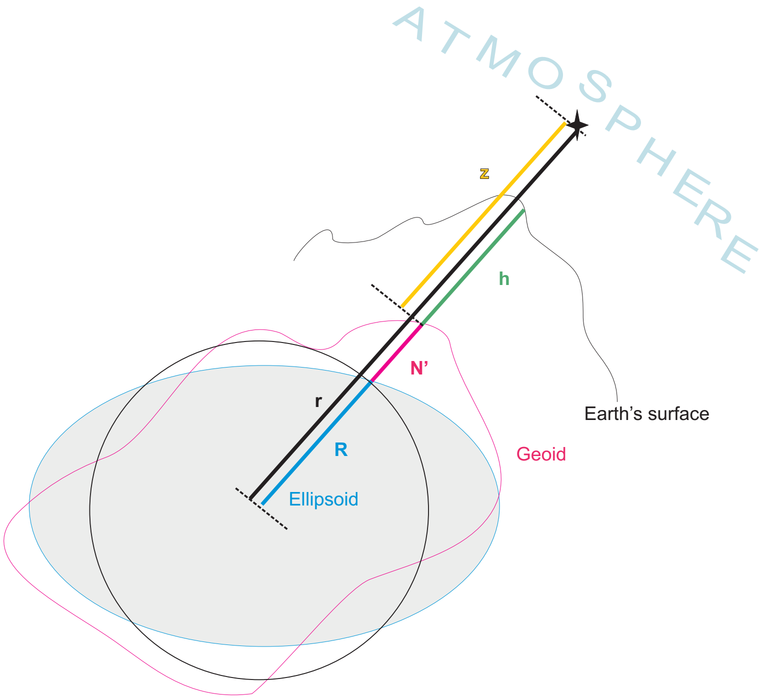

Fig. 3.1: *The variable component r used in the vertical integration approach (VI) of the atmosphere*

3.2. VI approach - Performing a vertical integration of the atmospheric masses

An alternative method to determine the atmospheric loading I_n is to take into account the vertical structure of the atmosphere. For the oceanic loading still the thin layer approach (see Sect. 3.1) holds, as the vertical depth of the ocean is much less (∼ maximum 11 km) than the depth of the atmosphere (∼ maximum 100 km).

Starting from Eq. (3.4) and inserting the hydrostatic equation with a height-dependent gravity acceleration g_r, leads to:

$$I_n = -\int_{P_S}^{0} \frac{1}{g_r} \left(\frac{r}{R}\right)^{n+2} dp \tag{3.11}$$

The height-dependent gravity acceleration g_r can be approximated from a mean gravity acceleration g at the Earth's surface by:

$$g_r = g \left(\frac{R}{r}\right)^2 \tag{3.12}$$

Then Eq. (3.11) turns into:

$$I_n = -\frac{1}{g} \int_{P_S}^{0} \left(\frac{r}{R}\right)^{n+4} dp \tag{3.13}$$

The variable of integration has now changed from the radial distance r to pressure p. This transformation has been performed, as atmospheric density fields are usually not available in atmospheric models like ECMWF or NCEP, whereas pressure data are available. The problem now is to find values for the radial distance r between the Earth's center of mass and the atmosphere/atmospheric layers.

Having a look at Fig. 3.1 one can see that the radial component (see, e.g., *Swenson and Wahr* (2002) and *Flechtner* (2007a)) is composed of:

$$r = R + N' + z \tag{3.14}$$

with R the radius of the Earth's sphere, N' a mean geoid height referring to the underlying Earth's sphere, and z the elevation (geometric height) above the mean geoid. The elevation z can be derived by the geopotential height H, which is defined by:

$$H = \frac{1}{g} \int\limits_0^z g_r dz \tag{3.15}$$

Inserting Eq. (3.12), we get:

$$H = \int\limits_0^z \left(\frac{R}{r}\right)^2 dz \tag{3.16}$$

Neglecting the difference between the sphere and the ellipsoid as well as the geoid height N', the geopotential height H is determined at a point above the Earth's surface $r = R + z$:

$$H = \int\limits_0^z \left(\frac{R}{R+z}\right)^2 dz \tag{3.17}$$

Although the introduced simplifications lead to higher errors in polar and equatorial regions (see. *Peters* (2007)), Eq. (3.17) is used in the current de-aliasing process to transform the geometric heights z into geopotential heights H. In a next step, the integration of Eq. (3.17) is performed:

$$\begin{aligned} H &= \int\limits_0^z \left(\frac{R}{R+z}\right)^2 dz = \left[R^2 \cdot \frac{-1}{R+z}\right]_0^z = R^2 \cdot \left(\frac{-1}{R+z} + \frac{1}{R}\right) \\ &= R - \frac{R^2}{R+z} = \frac{R\,(R+z) - R^2}{R+z} = \frac{R^2 + Rz - R^2}{R+z} \\ &= \frac{Rz}{R+z} \end{aligned} \tag{3.18}$$

After inversion of Eq. (3.18), we get a relation between the geopotential height H and the geometric height z:

$$z = \frac{H \cdot R}{R - H} = \frac{H}{1 - \frac{H}{R}} \tag{3.19}$$

Inserting z into Eq. (3.14) it follows:

$$r = R + N' + \frac{H}{1 - \frac{H}{R}} = \frac{R}{1 - \frac{H}{R}} + N' \tag{3.20}$$

With Eq. (3.20) we have found a solution for the radial distance r. Inserting Eq. (3.20) back into Eq. (3.13), leads to the well known formula for the vertical integration of the atmosphere (cf. *Flechtner* (2007a)):

$$\left.\begin{array}{c} \bar{C}_{nm} \\ \bar{S}_{nm} \end{array}\right\} = \frac{1 + k_n^{'}}{2n+1} \frac{3}{4\pi R \bar{\rho}} \int\limits_\sigma\int [I_n + P_O] \cdot \bar{P}_{nm}(\cos\theta) \left\{\begin{array}{c} \cos m\lambda \\ \sin m\lambda \end{array}\right\} d\sigma \tag{3.21}$$

with

$$I_n = -\frac{1}{g} \int\limits_{P_S}^0 \left(\frac{R}{R-H} + \frac{N'}{R}\right)^{n+4} dp. \tag{3.22}$$

The ellipsoidal shape of the Earth as well as the latitude and height-dependency of g are neglected within this approach.
As we are still only interested in the atmospheric and oceanic deviations from a mean-field, also here a mean vertically integrated pressure field I_n^{ref} and a mean ocean field are subtracted before the atmospheric part is combined with the oceanic part. The final formula for the combined atmospheric and oceanic potential follows:

$$\left.\begin{array}{c}\bar{C}_{nm}\\ \bar{S}_{nm}\end{array}\right\} = \frac{1+k_n'}{2n+1}\cdot\frac{3}{4\pi R\bar{\rho}g}\int\int_\sigma P_{AO}\cdot\bar{P}_{nm}(\cos\theta)\left\{\begin{array}{c}\cos m\lambda\\ \sin m\lambda\end{array}\right\}d\sigma. \tag{3.23}$$

with $P_{AO} = I_n - I_n^{ref} + P_O - P_O^{ref} = \Delta P_S + \Delta P_O$.

Equations (3.10) and (3.23) represent two alternative methods of taking the atmospheric mass variations into account.

In the following chapter 3.3 the exact processing sequence and the needed parameters for the determination of the atmospheric and oceanic de-aliasing coefficients by Eq. (3.23) are explained step by step.

3.3. Determination of the de-aliasing potential coefficients by numerical integration

As the geopotential height H for certain atmospheric layers in Eq. (3.22) is not directly available from meteorological analysis centers like ECMWF or NCEP, one has to calculate it first. This can be done as follows: Input parameters needed for the determination of the atmospheric potential are: point values of surface pressure P_s and geopotential height H_s grids (e.g. 1° × 1°) on the Earth's surface as well as point values of temperature T and specific humidity S at all 91 model levels of the atmospheric model at different time steps (00h, 06h, 12h, 18h). (For more details on the atmospheric model levels, see Sect. 5).

In a first step, the pressure $P_{k+1/2}$ at all model half-levels $k+1/2$ and the virtual temperature at all model full-levels k are computed according to Eqs. (3.24) and (3.25):

$$P_{k+1/2} = a_{k+1/2} + b_{k+1/2}P_s \tag{3.24}$$

$$T_{v_k} = (1 + 0.608S_k)T_k \tag{3.25}$$

$P_{k+1/2}$ can be derived using level dependent coefficients a, b provided with ECMWF meteorological data and surface pressure P_s. The virtual temperature T_{v_k} of each level k is a function of available temperature T and specific humidity S in the corresponding model levels. Pressure, virtual temperature, and the surface geopotential heights H_s are then used to calculate the geopotential heights $H_{k+1/2}$ for all levels according to Eq. (3.26)

$$H_{k+1/2} = H_s + \sum_{j=k+1}^{k_{max}} \frac{R_g T_{v_k}}{g}\cdot\ln\left(\frac{P_{j+1/2}}{P_{j-1/2}}\right) \tag{3.26}$$

Here $H_{k+1/2}$ and $P_{k+1/2}$ are the geopotential height and pressure at half level (layer interfaces), R_g is the gas constant for dry air. In addition, the mean geoid above the mean sphere N' in Eq. (3.22) is approximated by the geopotential height at the Earth's surface (orography), which is available from ECMWF, too.

Remark: The substitution of the mean geoid height N' with the geopotential height at the Earth's surface H_S ($N' = H_S/g$) has a non-negligible effect on the AOD coefficients. Comparing the AOD coefficients determined by using either N' or H_S in terms of geoid heights, has an effect of up to maximum 2 mm.

However, in the currently applied standard de-aliasing process routinely performed at GFZ (see Flechtner (2007a)) this substitution is performed and the surface geopotential height H_S *is used in current processing.*

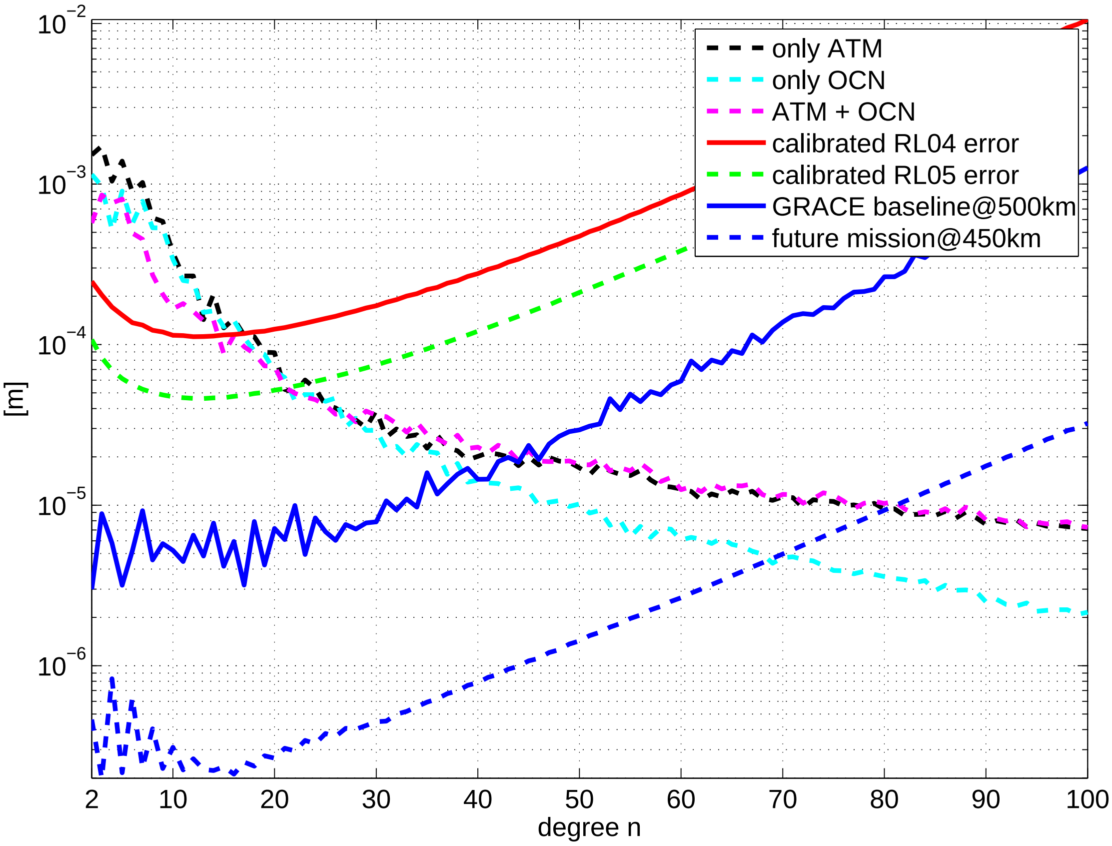

Fig. 3.2: Degree variances in terms of geoid heights for the atmospheric, oceanic and the combined atmospheric and oceanic potential, 01.08.2007, 00h. Unit: m.

Finally, the vertically integrated atmospheric pressure I_n can be calculated with Eq. (3.22). In a next step the atmospheric pressure I_n is combined with the ocean bottom pressure P_O to P_{AO} after subtracting the corresponding mean fields. In our investigations as well as in the current de-aliasing process these mean fields are covering the period 2001+2002. In the combination (in fact it is a simple addition) of the atmosphere and the ocean pressure the inverse barometer effect has been considered, as the ocean bottom pressure P_O only contains the pressure of the oceanic column. The inverse barometer effect describes the response of the ocean on the atmospheric pressure variations. E.g., low atmospheric pressure results in an increase of the mean sea level, and high atmospheric pressure will cause a stationary decrease of the ocean surface. Slightly exaggerated, this means, that over the ocean, atmospheric and oceanic mass variations compensate each other and no signal should be measurable at the ocean bottom pressure records. Of course this is only a model assumption and the ocean reacts with some delay on the atmosphere. But in principle one can state, that by adding the atmospheric and oceanic pressure, the combined signal w.r.t. the atmospheric pressure alone will be damped over the ocean due to the inverse barometer effect (cf., e.g. magenta line in Fig. 3.2).

After the combination of atmosphere and ocean the residual atmospheric and oceanic pressure P_{AO} is stored in a three dimensional array with longitude, latitude and degree as indices. Finally, the numerical integration is performed applying Eq. (3.23). The three-dimensional matrix, stored as an intermediate result, serves as input for the spherical harmonic analysis (SHA) by numerical integration. The SHA is also performed separately for each degree of the spherical harmonic series in order to take into account the degree-dependent exponent in Eq. (3.22). The result of the numerical integration are the combined atmospheric and oceanic potential coefficients $\bar{C}_{nm}$, $\bar{S}_{nm}$.

In general one could state, that the atmospheric variation is slightly higher than the one induced by the oceanic masses. This becomes obvious when having a look at the black and cyan dotted lines in Fig. 3.2. After the combination of the two components (cf. Fig. 3.2 magenta line) one can clearly see the inverse barometer effect in the low degrees, as the combined atmospheric and oceanic signal gets smaller compared to the atmosphere alone.

Furthermore, Fig. 3.2 illustrates the current RL04 (red line) and RL05 (green) GRACE error level, the pre-launch simulated accuracy (*Kim*, 2000), also called the GRACE Baseline (blue line) as well as a simulated accuracy of a possible future gravity field mission scenario (blue dotted line). The simulation performed to assess the performance of the shown future gravity field mission, is based on a collinear orbiting pair of satellites (similar to GRACE) separated by 220 km and flying at an altitude of 425 km (orbit inclination: 89°). Instead of the GRACE K-band microwave ranging instrument measuring the distance between the two satellites, the simulated mission is assumed to be equipped with a laser ranging system, based on the noise assumptions made in (*Sheard et al.*, 2012). This new instrument will improve the range-rate precision from $\sim 0.2\ \mu m/s$ to $\sim 0.6\ nm/s$ (*Loomis et al.* (2012), *Dehne et al.* (2009), *Pierce et al.* (2008)). Furthermore, the on-board accelerometers (ACC) are assumed to have about the same noise characteristics as those currently used for the Gravity field and steady-state Ocean Circulation Explorer mission (GOCE, *Floberghagen et al.* (2011)), which are about 100 times more sensitive than the GRACE accelerometers.

As the magenta line is partially above the RL04 (red), RL05 (green dotted), and future gravity field mission (blue dotted) lines, one can state here, that short-term atmospheric and oceanic mass variations do have a significant effect on current GRACE results and an even more significant impact on future gravity field missions.

4. Alternative de-aliasing process taking model errors into account

The formulas for the determination of the atmospheric and oceanic de-aliasing coefficients derived in chapter 3 do not allow to take model uncertainties into account. The input parameters of the VI approach such as temperature T, specific humidity S, surface pressure P_s, surface geopotential height H_s, and ocean bottom pressure P_O have so far been assumed to be error-free, although it is well-known that there are large uncertainties, in particular in the atmospheric surface pressure (*Ponte and Dorandeau*, 2003).

In order to quantify the effect of uncertainties in T, S, P_s, H_s and ocean bottom pressure P_O on the resulting de-aliasing coefficients $\bar{C}_{nm}$, $\bar{S}_{nm}$, we have developed a mathematical model to propagate the atmospheric field errors $(\sigma_T, \sigma_S, \sigma_{P_s}, \sigma_{H_s})$ into the pressure errors (σ_{I_n}) of the vertically integrated atmospheric column I_n.
The principle and the applied formulas are summarized in *Zenner et al.* (2010) and are described in more detail in the following chapters.

4.1. Error propagation for the de-aliasing process

Propagating model uncertainties into the pressure errors of the vertically integrated atmosphere I_n is based on the simplified law of error propagation (*Koch*, 1999):

$$f(x,y) \Rightarrow \sigma_f = \left(\left(\frac{\partial f}{\partial x} \right)^2 \cdot \sigma_x^2 + \left(\frac{\partial f}{\partial y} \right)^2 \cdot \sigma_y^2 \right)^{\frac{1}{2}} \tag{4.1}$$

Equation (4.1) states that the standard deviation σ_f of a function f depending on x and y can be determined from the uncertainties σ_x and σ_y of x and y and the partial derivatives of f with respect to x and y. Covariances between the input parameters σ_{xy} are neglected. Applying this simplified law of error propagation step by step to the above-mentioned sequence of formulas (Eqs. (3.24), (3.25), and (3.26) and (3.22)) we get

a) for the error of virtual temperature (due to clarity reasons the model level index k is neglected here for the parameters T and S)

$$\begin{aligned} T_v &= (1 + 0.608S)T \\ \Rightarrow \sigma_{T_v} &= \left(\left(\frac{\partial T_v}{\partial T} \right)^2 \cdot \sigma_T^2 + \left(\frac{\partial T_v}{\partial S} \right)^2 \cdot \sigma_S^2 \right)^{\frac{1}{2}} \end{aligned} \tag{4.2}$$

with the partial derivatives

$$\begin{aligned} \frac{\partial T_v}{\partial T} &= 1 + 0.608S \\ \frac{\partial T_v}{\partial S} &= 0.608T \end{aligned}$$

b) for the error of the "half-level" pressure:

$$\begin{aligned} P_{k+1/2} &= a_{k+1/2} + b_{k+1/2} \cdot P_s \\ \Rightarrow \sigma_{P_{k+1/2}} &= \left(\left(\frac{\partial P_{k+1/2}}{\partial P_s} \right)^2 \cdot \sigma_{P_s}^2 \right)^{\frac{1}{2}} \end{aligned} \tag{4.3}$$

with the partial derivative

$$\frac{\partial P_{k+1/2}}{\partial P_s} = \quad b_{k+1/2}$$

c) for the error of the geopotential height in "half-levels":

$$\begin{aligned}
H_{k+1/2} = &\quad H_s + \sum_{j=k+1}^{k_{max}} \frac{R_g T_v}{g} \cdot \ln\left(\frac{P_{j+1/2}}{P_{j-1/2}}\right) \\
\Rightarrow \sigma_{H_{k+1/2}} = &\quad \left(\left(\frac{\partial H_{k+1/2}}{\partial T_v}\right)^2 \cdot \sigma^2_{T_v} + \ldots\right. \\
+ &\quad \left(\frac{\partial H_{k+1/2}}{\partial P_{j+1/2}}\right)^2 \cdot \sigma^2_{P_{j+1/2}} + \ldots \\
+ &\quad \left.\left(\frac{\partial H_{k+1/2}}{\partial P_{j-1/2}}\right)^2 \cdot \sigma^2_{P_{j-1/2}} + \sigma^2_{H_s}\right)^{\frac{1}{2}}
\end{aligned} \tag{4.4}$$

with the partial derivatives

$$\begin{aligned}
\frac{\partial H_{k+1/2}}{\partial T_v} &= \quad \frac{1}{g}\sum_{j=k+1}^{k_{max}} R_g \cdot \ln\left(\frac{P_{j+1/2}}{P_{j-1/2}}\right) \\
\frac{\partial H_{k+1/2}}{\partial P_{j+1/2}} &= \quad \frac{1}{g}\sum_{j=k+1}^{k_{max}} R_g T_v \cdot \left(\frac{1}{P_{j+1/2}}\right) \\
\frac{\partial H_{k+1/2}}{\partial P_{j-1/2}} &= \quad -\frac{1}{g}\sum_{j=k+1}^{k_{max}} R_g T_v \cdot \left(\frac{1}{P_{j-1/2}}\right)
\end{aligned}$$

d) for the error of the vertically integrated atmospheric pressure:

$$\begin{aligned}
I_n &= \int_{P_s}^{0} \left(\frac{R}{R - H_{k+1/2}} + \frac{N'}{R}\right)^{n+4} dP \quad \Rightarrow \\
\sigma_{I_n} &= \left(\left(\frac{\partial I_n}{\partial H_{k+1/2}}\right)^2 \cdot \sigma^2_{H_{k+1/2}} + \left(\frac{\partial I_n}{\partial dP}\right)^2 \cdot \sigma^2_{dP}\right)^{\frac{1}{2}}
\end{aligned} \tag{4.5}$$

with the partial derivatives

$$\begin{aligned}
\frac{\partial I_n}{\partial H_{k+1/2}} &= \int_{P_s}^{0} (n+4)\left(\frac{R}{R - H_{k+1/2}} + \frac{N'}{R}\right)^{n+3} \cdot \left(-\frac{R}{\left(R - H_{k+1/2}\right)^2}\right) dP \\
\frac{\partial I_n}{\partial dP} &= \left(\frac{R}{R - H_{k+1/2}} + \frac{N'}{R}\right)^{n+4}
\end{aligned}$$

with $dP = P_{k+1/2} - P_{k-1/2} \Rightarrow \sigma_{dP} = \left(\sigma^2_{P_{k+1/2}} + \sigma^2_{P_{k-1/2}}\right)^{\frac{1}{2}}$

e) and finally for the error of the combined atmospheric and oceanic pressure:

$$P_{AO} = \Delta I_n + \Delta P_O \Rightarrow \sigma_{P_{AO}} = \left(\sigma^2_{\Delta I_n} + \sigma^2_{\Delta P_O}\right)^{\frac{1}{2}} \tag{4.6}$$

Equations (4.2) to (4.6) provide an opportunity to propagate uncertainties of the atmospheric input parameters to the vertically integrated atmospheric pressure I_n as well as to the combined atmospheric and oceanic pressure P_{AO}. The effect of errors in the various input parameters on the atmospheric pressure is discussed and illustrated in Sect. 9.2.

4.2. Determination of the de-aliasing potential coefficients by least-squares adjustment

In order to reach our goal of determining the effect of model uncertainties on the AOD product, the error of the combined atmospheric and oceanic pressure $\sigma_{P_{AO}}$ has to be further propagated to the potential coefficients. To do this, the present de-aliasing processing sequence is modified as it is shown in Fig. 4.1. As mentioned in Sect. 3, in the standard GRACE de-aliasing process the spherical harmonic analysis is performed by a numerical integration of P_{AO} for each degree separately (cf. Eq. (3.10)). Uncertainties in P_{AO} are not yet considered. In order to take the uncertainties in the combined residual atmospheric and oceanic pressure into account and to determine the effect of input parameter errors on the de-aliasing coefficients $\bar{C}_{nm}$, $\bar{S}_{nm}$, the present approach of numerical integration is replaced by a least-squares adjustment (Gauss-Markov model, see e.g. *Koch* (1999)). For this, Eq. (3.23) is rearranged into the observation equation:

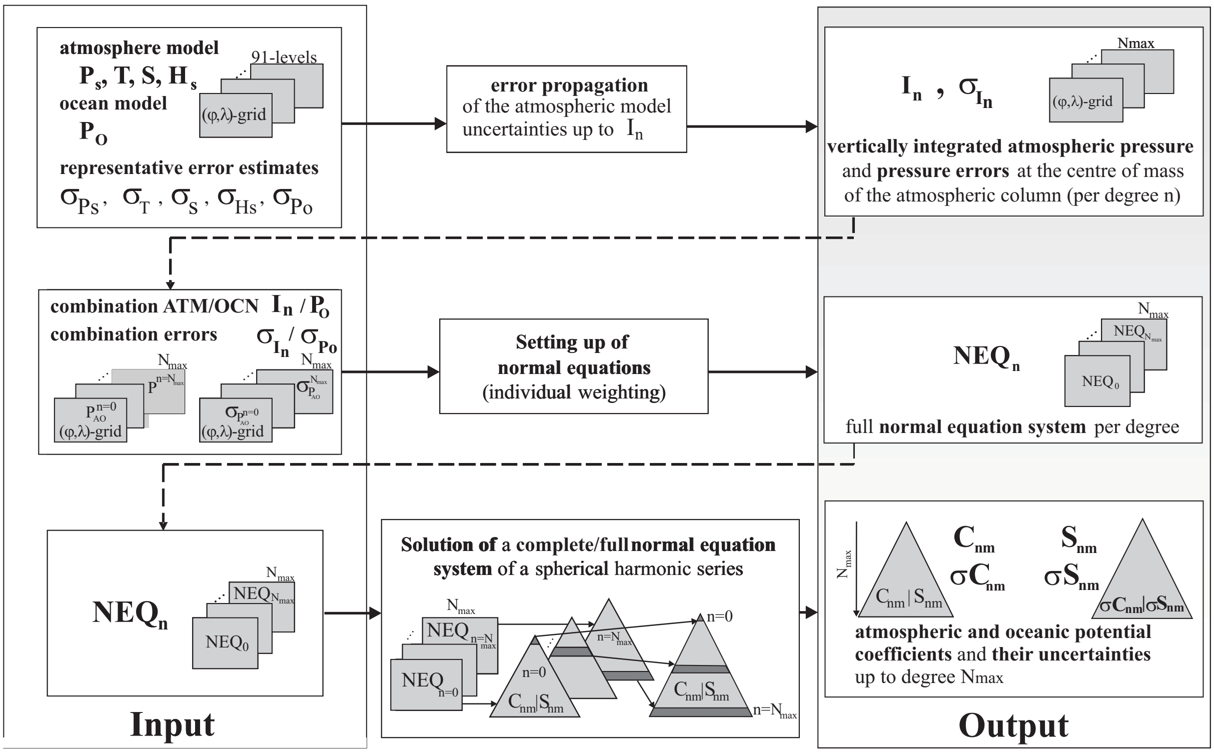

Fig. 4.1: Overview of the de-aliasing processing approach with error propagation

$$P_{AO} = -\frac{Mg}{R^2} \sum_n \frac{2n+1}{1+k'_n} \sum_m \bar{P}_{nm}(\cos\theta) \cdot \left[\bar{C}_{nm} \cos m\lambda + \bar{S}_{nm} \sin m\lambda\right], \tag{4.7}$$

and the basic formulas for least-squares adjustment:

(1) $Ax = l + v$ (2) $v^T P v \rightarrow min$ (3) $\hat{x} = (A^T P A)^{-1} A^T P l$ (4) $Q_{ll} = \sigma^2 P^{-1}$

are applied, where $\hat{x}$ are the adjusted unknowns x, l the observations, P the weighting matrix, and Q_{ll} the variance-covariance matrix of the observations. In our context the unknowns x are the atmospheric and oceanic potential coefficients $\bar{C}_{nm}$, $\bar{S}_{nm}$. The observations l are the combined residual atmospheric and oceanic pressure values P_{AO} on a global (φ,λ)-grid. To set up the the coefficient-matrix A, the partial derivatives of the observations l with respect to the unknown coefficients $\bar{C}_{nm}$ and $\bar{S}_{nm}$ are determined. Furthermore, the weighting matrix of the observations P is set up, where P is defined by the uncertainties $\sigma_{P_{AO}}$ of P_{AO}, which are determined by the error propagation model shown in Sect. 4.1. Like P, the variance-covariance matrix Q_{ll} is a diagonal matrix, as any co-variances are neglected here. This might be a drastic assumption, but will give a first impression of the impact of observation errors on the unknown potential coefficients. In the course of least-squares adjustment, the square sum of the residuals v are minimized under the metric P.(For further details on the principle least-squares adjustment see e.g. *Koch* (1999)).

To get the "new" AOD product, basically three steps are performed (cf. Fig. 4.1).
In a first step, the vertically integrated residual atmospheric pressure I_n and its error σ_{I_n} are calculated (via Eqs. (4.2) to (4.6)). Then the atmospheric pressure I_n and the ocean bottom pressure P_O as well as the corresponding errors are combined according to Eq. (4.6).
In a second step, the normal equation systems (NEQ, A^TPA, A^TPl) can be set up for each degree separately via the observations P_{AO} and the uncertainties of P_{AO} as individual weights (cf. second row in Fig. 4.1).
Afterwards and as a third step, every NEQ for each degree of the spherical harmonic series is solved separately. This can be done as the observations per degree n are assumed to be uncorrelated. Finally, the complete series of spherical harmonic coefficients $\bar{C}_{nm}$, $\bar{S}_{nm}$ including their error estimates $\sigma\bar{C}_{nm}$, $\sigma\bar{S}_{nm}$ are obtained (third row in Fig. 4.1).

Part II.

DATA: Atmospheric & oceanic data, uncertainties and GRACE data

In the following an overview of the data and analysis software used within this work is given.

The first part (Sect. 5) is dealing with the atmospheric model parameters and their uncertainties.

The second one (Sect. 6) introduces the oceanic input parameters as well as the applied error map.

In the third part (Sect. 7) an overview of the daily ITG-GRACE solutions and the BERNESE gravity field software used for the performed investigations, is given.

5. Atmospheric Data

This chapter will give an overview of the atmospheric input parameters used within this work. Due to the complexity of atmospheric models, no in-depth discussion of the latter and various individual parameters will be given here. Background and fundamentals on atmospheric physics and modelling can, e.g., be found in *Pichler* (1997), *Visconti* (2001), *Jacobson* (2005), *ECMWF* (2008a), *ECMWF* (2008b), and various other publications.

Within this study we used atmospheric data, provided by the European Centre for Medium-Range weather Forecasts (ECMWF). ECMWF is running a comprehensive earth-system model being the basis for all data assimilation and forecasting activities. This system is called *Integrated Forecasting System* (IFS). The IFS can be regarded as one integrated computer software system for all applications. Main components of the IFS are, e.g., data assimilation, ensemble prediction, atmospheric model, wave model and ocean model. Depending on the modifications made within the various software parts (e.g., increase of horizontal and/or vertical resolutions), different outputs – so-called *cycles* – are available at ECMWF. These various cycles lead to inconsistencies, e.g. jumps, in the operational data. Thus, one has to be careful with the analysis of model outputs covering time-intervals of several cycles. Note that this also applies to the de-aliasing product, covering already more than 10 years. In *Gruber et al.* (2008), e.g., it has been shown, that these model changes should not be underestimated and cause jumps in atmospheric mass estimations, possibly leading to miss-interpretations. Recently, *Duan et al.* (2012) have shown that glacier mass balance estimates could be contaminated by these jumps. In order to prevent these inconsistencies one could use the ECMWF re-analysis data (ERA-40 (*Uppala et al.*, 2001) or ERA-Interim (*Dee et al.*, 2001)). These products should ensure consistency as they are reprocessed with the same (software) settings. But, as the ERA-data are normally updated only once per month, they are currently not used for the (near-realtime) computation of the de-aliasing process. In Sect. 10.1 the impact of using ERA-Interim instead of the operational data is investigated.
For the determination of the de-aliasing coefficients, data from the operational atmospheric model[1] is used, as the operational data sets have a higher time and space resolution and contain all parameters. The data is available on the surface, on pressure and model levels. As described in Sect. 3.3, only surface and model level data are relevant for the computation of the de-aliasing product. The required parameters are routinely downloaded on an equidistant 1° × 1° latitude-longitude grid for every 6 hours of one day (00h, 06h, 12h, 18h) from the Meteorological Archival and Retrieval System (MARS) (*ECMWF*, 2009), the main repository of meteorological data at ECMWF.

5.1. Input parameters for the atmospheric de-aliasing process

The computation of the atmospheric potential requires two parameters on the model levels: **temperature** and **specific humidity**.

The model levels correspond to the vertical resolution of the parameters. Figure 5.1 illustrates the 91 vertical model levels (full-levels) of the atmospheric model. Level 91 thereby corresponds to the Earth's surface and level 1 to the top of the atmosphere ($\sim 80\ km$) (cf. Tab. 5.1). ECMWF updated the vertical resolution of the model on February 1st, 2006 from 60 to 91 levels. Comparing the blue (L60) and red (L91) model levels in Fig. 5.1, one can see, that the resolution is especially increased in the lower and mid atmospheric layers between approximately $3\ km$ ($\sim 700\ hPa$) and the tropical tropopause ($\sim 16\ km$, $\sim 100\ hPa$). 90% of the main atmospheric masses are represented by these lower atmospheric layers ($< 10\ km$, *Neumeyer et al.* (2004)). This means, that by the increase from 60 to 91 levels, an enhanced spatial representation of the atmospheric model data has been achieved. Together with the model level parameters, ECMWF is providing level dependent coefficients with which the pressure at half-levels can be calculated (cf. Eq. (3.24), Sect. 12).

---

[1] `http://www.ecmwf.int/products/data/archive/descriptions/od/oper/index.html`

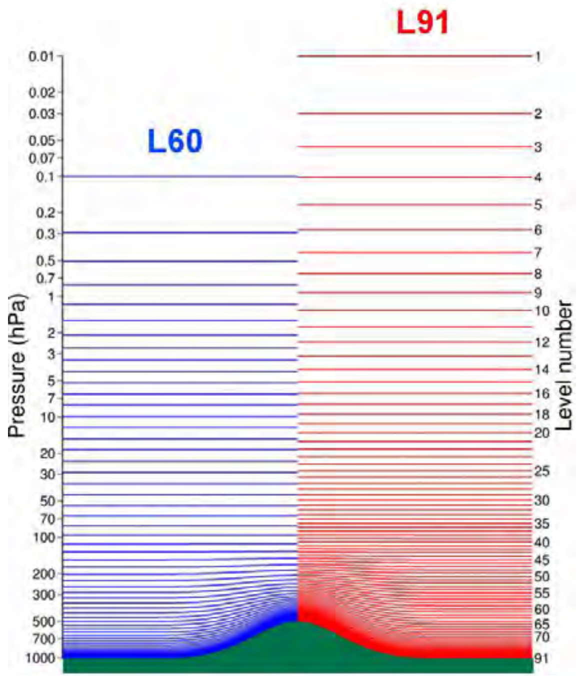

Fig. 5.1: *ECMWF model levels. ©ECMWF*

model level k	∼ height [km]
91	0
79	1
71	3
65	5
57	8
53	10
48	12
41	15
31	20
24	25
19	30
12	40
8	50
5	60
3	70
1	80

Tab. 5.1: *ECMWF model levels and the approximately corresponding heights above the Earth's surface referring to the U.S. standard atmosphere 1976 (U.S. Standard Atmosphere, 1976)*

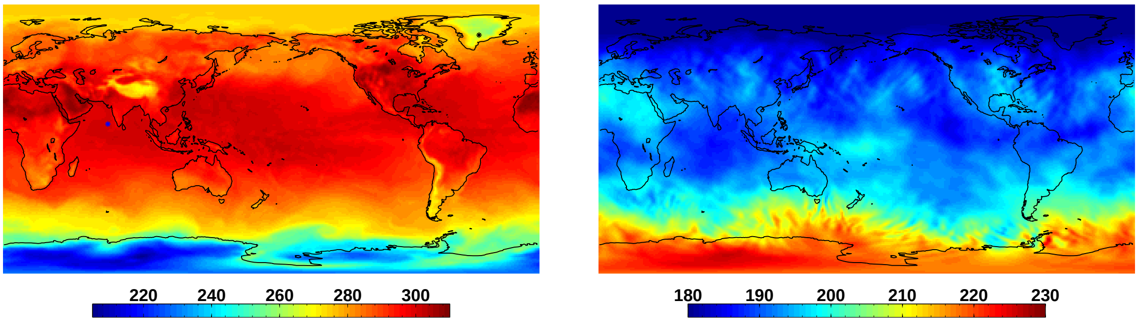

(a) temperature for $k = 91$

(b) temperature for $k = 1$

Fig. 5.2: *Temperature for (a) model level 91 (Earth's surface) and (b) model level k=1 (∼80 km height). 01.08.2007 00h. Unit: K.*

Figure 5.2 shows the temperature distribution on the Earth's surface and at the top level (∼ 80 km) of the atmosphere. The highest temperatures on the Earth's surface for the analyzed point in time reach up to maximum 312 K (39° Celsius) and have a minimum of 205 K (-68°). At an altitude of approximately 80 km, temperature ranges between minimum 175 K (-98°) and maximum 226 K (-47°). As one can see in Fig. 5.3, temperature is decreasing in the troposphere. The troposphere extends from the Earth's surface to 8 km (model level 57) at the poles and to 18 km (model level 37) at the equator. Above the troposphere follows the stratosphere with an extension to about 50 km (model level 8). Here, temperature is gradually increasing, due to the ultraviolet radiation absorbed by the ozone layer (*Pichler*, 1997). In about 50 km height temperature adopts values observed at the Earth's surface. In the mesosphere, which extends from the stratosphere to approximately 85 km, temperature is again decreasing with height.

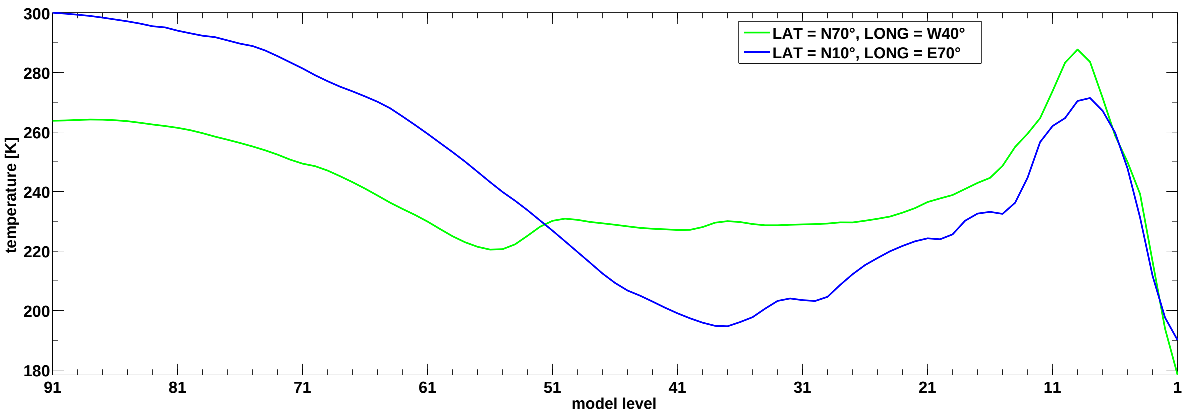

Fig. 5.3: Temperature profile of the 91 model levels for a near-equatorial oceanic point (blue) and a continental polar point (green). 01.08.2007 00h. Unit: K.

Figures 5.4 and 5.5 illustrate the specific humidity on the Earth's surface and at the top level of the atmosphere as well as the vertical profile, respectively. Specific humidity refers to the weight (amount) of water vapor contained in a unit weight (amount) of air (dry air plus water vapor). Specific humidity is usually expressed in grams of water vapor per kilogram air and is highly correlated with temperature (cf. Fig. 5.2), as warm air can hold more humidity (water vapor) than cold air. On the Earth's surface, specific humidity can adopt minimum, maximum and mean values of 3.7 mg/kg, 26.7 g/kg, and 10.2 g/kg with the highest values in the tropical and subtropical regions. For model level 1, specific humidity seems to be somehow generalized in three zonal regions. Values reach here only a few mg/kg (min: 1.3 ,max: 2.9, mean: 2.2, rms: 0.25).

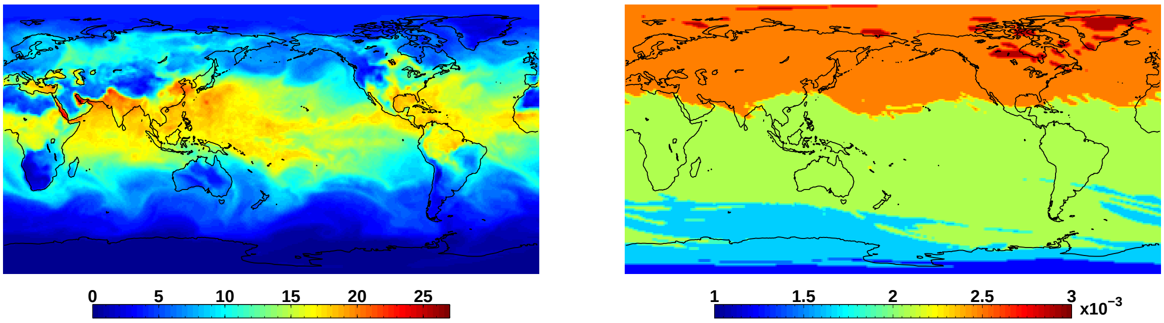

(a) spec. humidity for $k = 91$

(b) spec. humidity for $k = 1$

Fig. 5.4: Specific humidity for (a) model level 91 (Earth's surface) and (b) model level k=1 (~80 km height). 01.08.2007, 00h. Unit: g/kg.

Besides, temperature and specific humidity on model levels, **pressure** and **geopotential height** on the Earth's surface are required for the computation of the de-aliasing coefficients. Both parameters are illustrated in Fig. 5.6. While pressure at the Earth's surface for the analyzed point in time ranges between 488 hPa and 1038 hPa with a mean value of 986 hPa and a global rms of 66 hPa, surface geopotential height ranges between 0.01 m and 6 km with a mean value of 231 m and a rms of 627 m. In contrast to surface pressure, which varies with time, surface geopotential height is almost constant concerning the time interval of 2002 to now (GRACE observation time) relevant for the computation of the de-aliasing coefficients. Exceptions are two jumps between February 1st 2006, 00h and 06h, and January 26, 2010, when ECMWF has introduced new model versions. The model change at February 2006, e.g. affects the surface geopotential height with minimum, maximum, mean and rms values of -587 m, 774 m, -0.3 m, and 32.14 m (cf. Fig. 5.7). It should be noticed that these model changes are also reflected in the de-aliasing coefficients (cf. *Gruber et al.* (2008) and *Duan et al.* (2012)) and monthly GRACE gravity field solutions.

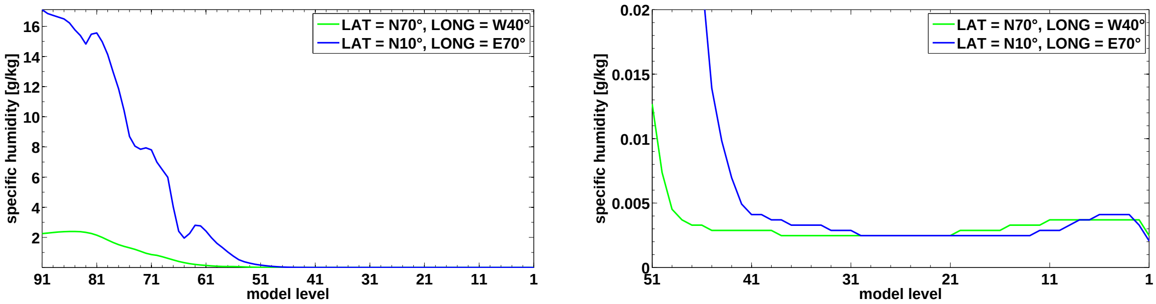

Fig. 5.5: Specific humidity profile of the 91 model levels for a near-equatorial oceanic point (blue) and a continental polar point (green). 01.08.2007, 00h. Unit: g/kg.

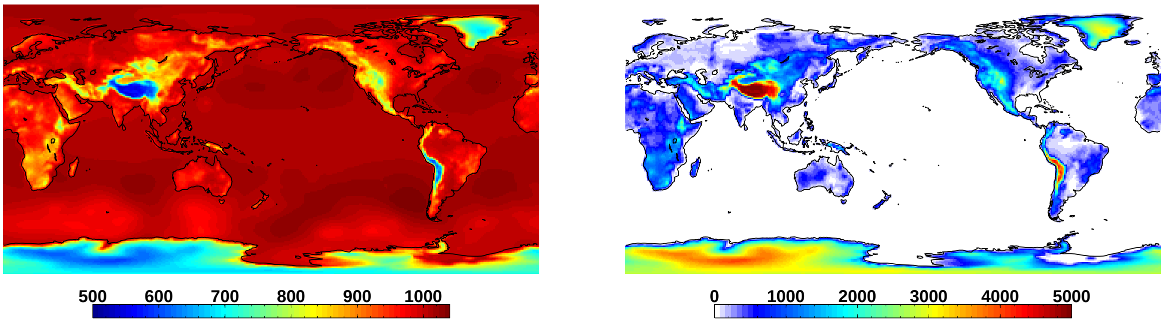

(a) surface pressure

(b) surface geopot. height

Fig. 5.6: (a) Surface pressure. Unit hPa. (b) surface geopotential height. Unit: m. 01.08.2007, 00h.

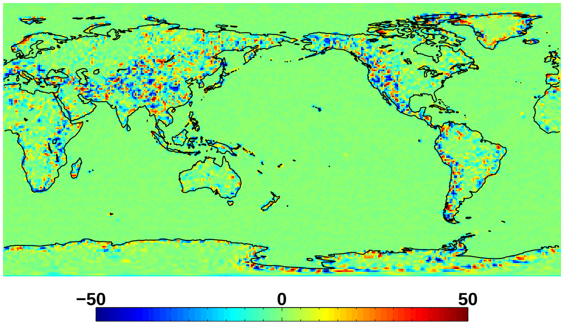

Fig. 5.7: Differences in surface geopotential height between 01.02.2006, 00h and 01.02.2006, 06h due to ECMWF model changes. Unit: m.

5.2. Uncertainties of the atmospheric input parameters

In addition to the input parameters described above, also their uncertainties are of interest for this work, as they are used for quantifying the effect of model uncertainties on the de-aliasing coefficients (see Sect. 9).

Temperature, specific humidity, surface pressure, and surface geopotential height errors - used within this work - are directly downloaded from ECMWF and reflect the errors in analysis from the operational atmospheric model. The errors in analysis result from the errors in the background fields, observation data and the model itself, in addition to the errors generated by the data assimilation techniques used (*Wei et al.*, 2010). It has to be pointed out that the error maps provided by ECMWF may be too optimistic as they result from the assimilation model and are pure outcome from a weighted combination of numerous measurements and advanced model predictions (*ECMWF* (2009)).

Figure 5.8 illustrates the **temperature error**. While the minimum, maximum, mean and rms values of temperature error on the Earth's surface adopt values of 0.63, 2.29, 1.04, and 0.13 K, the values at a height of $\sim$ 80 km are much higher and reach up to 4.07, 9.70, 5.99, and 0.92 K. As expected, especially in areas with sparse observations (e.g., polar regions), temperature uncertainties are higher.

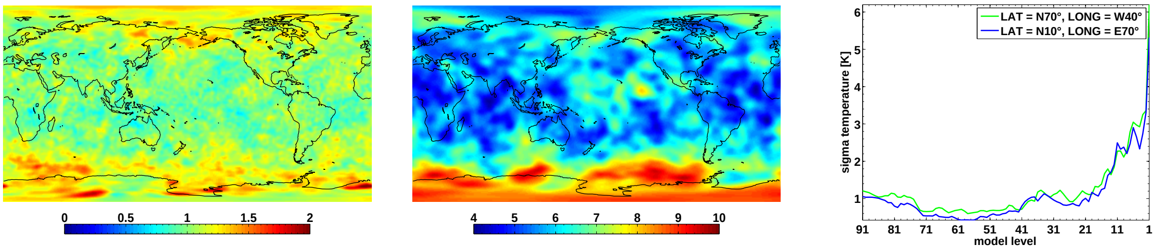

(a) σ_T for $k = 91$ (b) σ_T for $k = 1$ (c) profile σ_T

Fig. 5.8: ECMWF temperature error for (a) model level 91 (Earth's surface) and (b) model level k=1 (~80 km height), and (c) the vertical temperature profile. 31.07.2007, 21h. Unit: K.

The **specific humidity error**, illustrated in Fig. 5.9, is in general higher in regions with high humidity (tropical regions). On the Earth's surface, uncertainties in the specific humidity adopt values of minimum -1.6 mg/kg and maximum 2.2 g/kg (mean: 0.84 g/kg, rms: 0.46 g/kg). With increasing height, the specific humidity error is decreasing. At model level 41 and an altitude of approximately 15 km, the specific humidity error is almost zero with a maximum value of 0.9 mg/kg (cf. Fig. 5.9b).

The **uncertainties in the surface geopotential height** are illustrated in Fig. 5.10. With minimum, maximum, mean and rms values of 0.83 m, 10.32 m, 4.59 m and 1.01 m, the mean surface geopotential height error makes about 2% of the mean surface geopotential height. The largest errors appear in the Southern ocean areas as well as in near-continental regions, especially in the northern hemisphere.

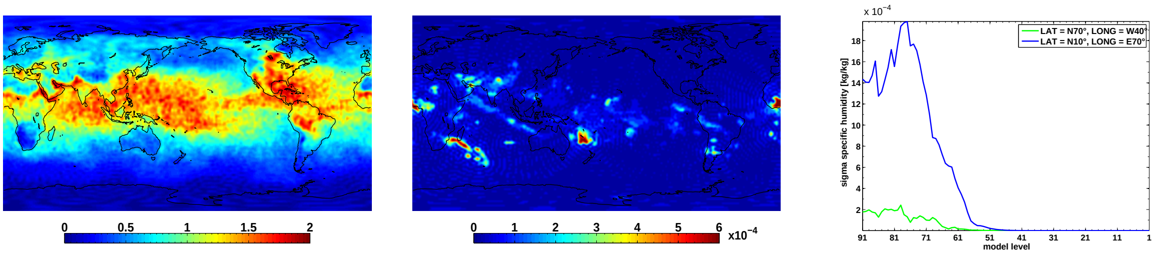

(a) σ_S for $k = 91$ (b) σ_S for $k = 41$ (c) profile σ_S

Fig. 5.9: ECMWF specific humidity error for (a) model level 91 (Earth's surface) and (b) model level k=41 (~ 15 km height), and (c) the vertical specific humidity profile. 31.07.2007 21h. Unit: g/kg.

The **surface pressure error provided by ECMWF** can be seen in Fig. 5.11. The geographical pattern is pretty similar to the one of the surface geopotential height error, as surface pressure strongly depends on the altitude. Larger uncertainties can be found in regions with high atmospheric variability (e.g., Southern ocean). The surface pressure error ranges between 0.11 hPa and 1.28 hPa with a mean value of 0.54 hPa and a global rms of 0.14 hPa. The ECMWF surface pressure error is applied in the case 2 error scenario (cf. Sect. 9.1).

In Sect. 9.2 it will be shown that surface pressure and surface pressure uncertainties are the dominant parameters for the determination of the de-aliasing coefficients and their uncertainties. As - like mentioned at the beginning of this paragraph - the uncertainties provided by ECMWF result from the assimilation model and are pure outcome from a weighted combination of numerous measurements and advanced model predictions, they may be regarded as too optimistic. Therefore, in addition, an alternative surface pressure error derived from model inter-comparisons, is used in Sect. 9.1 in order to further analyze the impact of surface pressure uncertainties on the de-aliasing coefficients.

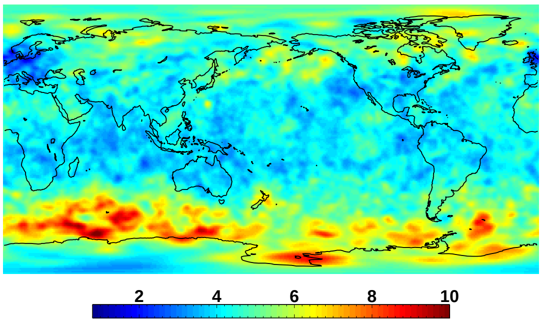

Fig. 5.10: ECMWF surface geopotential height error. Unit: m. 31.7.2007 21h.

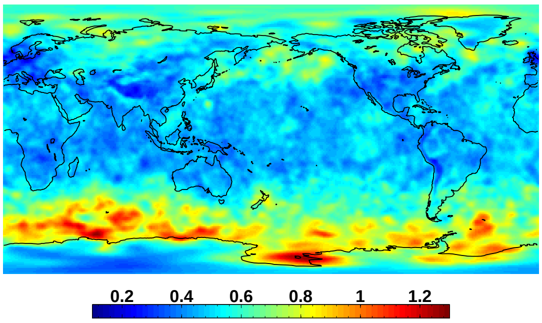

Fig. 5.11: ECMWF surface pressure error. Unit: hPa. 31.7.2007 21h.

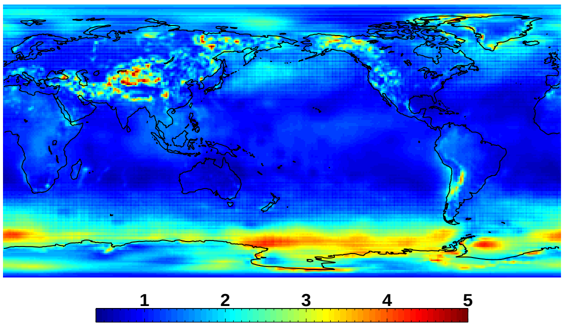

Fig. 5.12: Surface pressure error derived from NCEP/ECMWF model inter-comparisons. RMS of NCEP/ECMWF differences for 2007. Unit: hPa.

The **surface pressure error derived from model differences between NCEP/ECMWF** is shown in Fig. 5.12. Besides ECMWF, also the National Centers for Environmental Prediction (NCEP, *NCEP* (2010)) provides surface pressure values. From NCEP/ECMWF comparisons, surface pressure differences can be derived and used as an indicator of error. But one should mention that this is not a perfect method. The respective products differ in spatial and temporal resolution, in background models and in the topography used, whose differences often lead to a visible bias. It is therefore difficult to generate physically significant NCEP/ECMWF differences. As the surface pressure provided by NCEP is only given in a $2.5° \times 2.5°$ grid resolution, it is adapted to the ECMWF model ($1° \times 1°$ resolution) by interpolation before comparison, which is thus leading to an unbalanced analysis. Furthermore, one should keep in mind that the differences may not represent the true error distribution because common errors are cancelled out. Since a model result is a weighted sum of the real observation and a background model, the results are not fully independent. Therefore, even comparisons which coincide with in-situ observations are not always good validations of performance. In this work, the rms of the 6-hourly differences NCEP/ECMWF over one year is computed and this static error map is used in the error propagation (case 3 in Sect. cf. 9.1). The surface pressure error derived from these model inter-comparisons ranges between 0.36 hPa and 8.40 hPa with a mean value of 1.35 hPa and a global rms of 0.66 hPa.

One can recognize that in both surface pressure error maps (cf. Figs. 5.11 & 5.12) the main large-scale features are similar, but regional differences especially in areas with high atmospheric dynamics (Southern ocean) and in some continental areas (Himalayas, Andes) appear. Also the different scales should be noticed. Applying these two error maps as individual weightings in the error propagation procedure will result in two sets of AOD coefficients giving insight into the sensitivity of AOD and GRACE to various surface pressure error maps. Independently of the reliability of these two error maps, which can surely be critically questioned, these two error maps are used in Sect. 9 in order to gain insight into the effect of various geophysical model errors or patterns on AOD and GRACE.

6. Oceanic Data

For the determination of the oceanic part of the de-aliasing product, ocean bottom pressure fields from the Ocean Model for Circulation and Tides (OMCT, *Thomas* (2002)) are used.

As described in *Thomas* (2002), the OMCT has been developed by adjusting the originally climatological Hamburg Ocean Primitive Equation model (HOPE, *Wolff et al.* (1996), *Drijfhout et al.* (1996)) to the weather time-scale and coupling with an ephemeral tidal model. The model is based on nonlinear balance equations for momentum, the continuity equation, and conservation equations for heat and salt. The hydrostatic and the Boussinesq approximations are applied, which causes the model to rather conserve volume than mass. Artificially, the model is held constant by adding or removing a (small) homogeneous layer of mass at each time-step (*Greatbatch*, 1994) in order to make the simulated model data suitable for geodetic applications. However, the OMCT model can be configured to allow the total ocean mass to vary in accordance with freshwater fluxes due to precipitation, evaporation and continental runoff. Water elevations, three-dimensional horizontal velocities, potential temperature as well as salinity are calculated prognostically, vertical velocities are determined diagnostically from the incompressibility condition. Implemented in the OMCT is a prognostic thermodynamic sea-ice model (*Hibler*, 1979) that predicts ice-thickness, compactness and drift. Dynamic effects of loading and self-attraction of the water column are accounted for by means of a secondary potential proportional to the mass of the local water column (*Thomas et al.*, 2001). Atmospheric forcing includes wind stress, surface pressure as well as heat and freshwater fluxes. In order to ensure consistency with the atmosphere model used within the de-aliasing process, the input parameters are downloaded from ECMWF, too.

Like in the previous chapter 5, no in-depth discussion of the ocean model will be found here. Background, fundamentals and details on oceanic physics, modelling, and the OMCT ocean model itself can, e.g., be found in *Apel* (1987), *Wolff et al.* (1996), *Thomas* (2002) and *Dobslaw* (2007). A summarized overview of OMCT model input and output data can be found, e.g., in *Flechtner* (2007a).

This chapter will give an overview of the various ocean bottom pressure data sets and uncertainties used within this work.

6.1. Various ocean bottom pressure data

Between the computation of the official GFZ Release 04 (RL04) and Release 05 (RL05) AOD product a model change in the oceanic part has been performed. This has been done as some weaknesses in the RL04 series have been emerged during the years (see e.g. *Bonin and Chambers* (2011) and Sect. 10.4). In Sect. 10.2 the impact of the improved RL05 AOD product on AOD and GRACE is investigated.

In the following, the main changes between the RL04 (subsequently also called OMCT@1.875°) and RL05 (OMCT@1°) OMCT configurations are summarized. Details can be found in *Dobslaw et al.* (2012).

OMCT@1.875° vs. OMCT@1°. One of the main differences between the two releases is the spatial resolution which has been refined from 1.875° and 13 vertical levels for RL04 to 1° and 20 vertical levels for RL05. Furthermore, the applied time-step has been increased from 30 minutes for RL04 to 20 minutes for RL05. Both releases are forced with atmospheric surface pressure, surface wind stresses, 2m-temperature, and atmospheric freshwater fluxes provided every 6 hours by ECMWF. Also in both versions, the fluctuations in total ocean mass due to the incorporation of the Boussinesq approximation (volume conserving) in OMCT and imbalances in applied freshwater fluxes are adjusted at each time-step by means of a globally homogeneous shell of mass added to the top layer of the model. River runoff has neither been considered in the RL04 nor in the RL05 OMCT configurations. According to *Dobslaw et al.* (2012), horizontal eddy viscosity and vertical momentum transfer parameters were adjusted for OMCT RL05 in order to align the simulated bottom pressure and sea-level variability with available observations. This has been done by means of several sensitivity experiments. The OMCT@1° configuration is based on an initial spin-up run with climatological atmospheric boundary forcing, followed by real-time simulations with ERA Interim forcing (1989-2000) and subsequently operational ECMWF forcing since Jan 1st, 2001, both with a temporal resolution of 6 hours (*Dobslaw et al.*, 2012). Unlike for RL04, in the new RL05 OMCT release the semi-diurnal variability related to atmospheric tides is removed from the bottom pressure grids. Diurnal signals are retained in both releases.

Figure 6.1 illustrates the differences between RL04 and RL05 trends for three selective regions. Although clear correlations are visible, partially, the two ocean bottom pressure versions significantly differ from each other, not only in magnitude, but also in trend. In the Hudson Bay as well as in the Mediterranean Sea, e.g., even inverse trends are visible. The mean ocean bottom pressure variation (Fig. 6.2) shows deviations

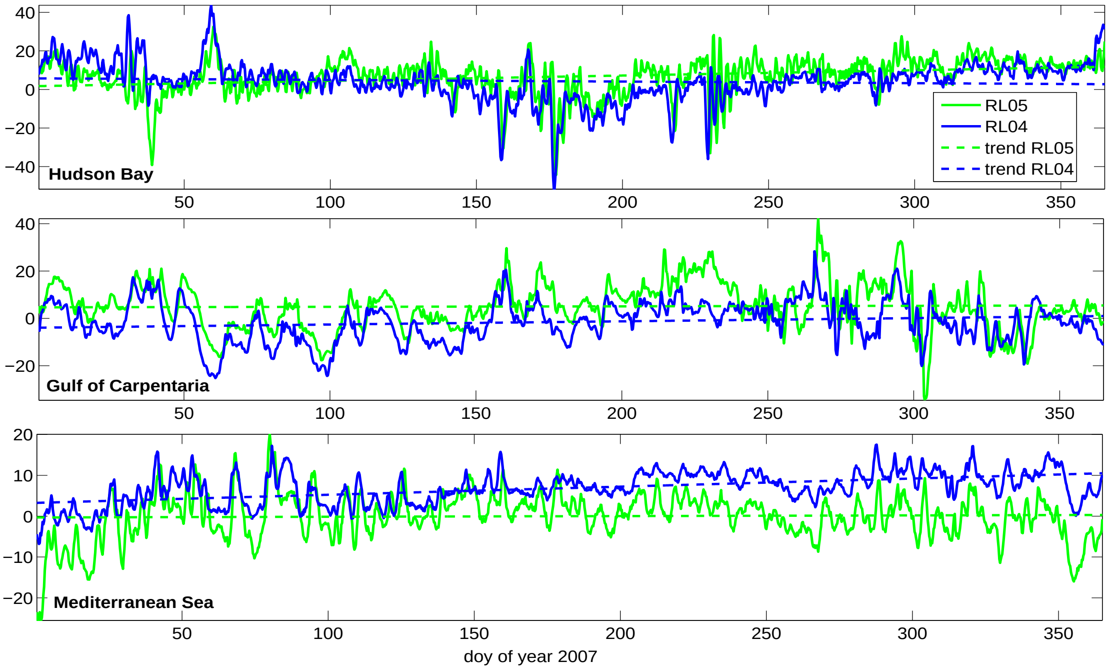

Fig. 6.1: Ocean bottom pressure variation for year 2007 in the Hudson Bay (top), in the Gulf of Carpentaria (middle), and the Mediterranean Sea (bottom) for RL04 OMCT@1.875° (blue) and RL05 OMCT@1° (green). Unit: hPa.

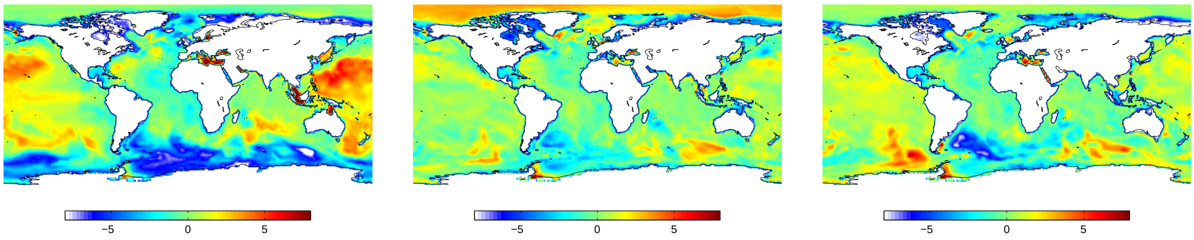

(a) (b) (c)

Fig. 6.2: Differences between the mean ocean bottom pressure variation of RL04 OMCT@1.875° and RL05 OMCT@1° for (a) January 2007, (b) April 2007 and (c) July 2007. Unit: hPa.

between OMCT RL04 and RL05 of maximum 77 hPa for January, 35 hPa for April, and 24 hPa for July 2007. The largest differences appear in the Antarctic Circumpolar Current (ACC). But also in the whole Pacific, especially for January 2007 (cf. Fig. 6.2a), large differences can be observed. Figure 6.3 illustrates the rms of ocean bottom pressure variation over one year for the two OMCT configurations. RL05 OMCT shows an higher variability in the North polar regions as well as in the ACC (cf. blue regions in Fig. 6.3c). Differences reach up to maximum 44 hPa. Further comparison between RL04 and RL05 ocean bottom pressure fields can be found in Sect. 10.2.

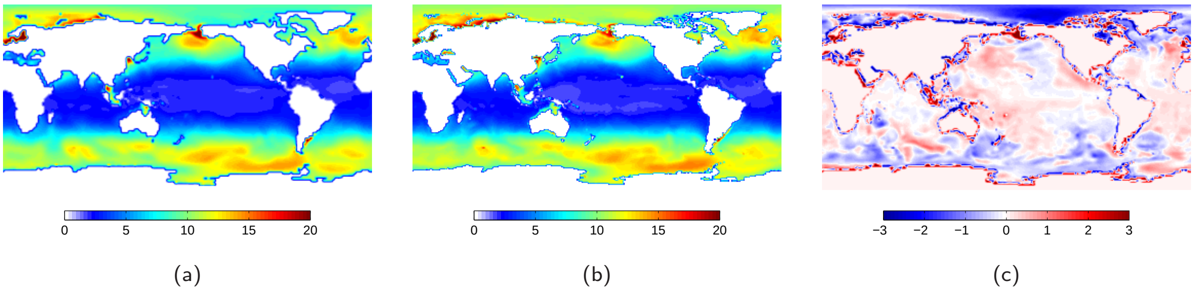

Fig. 6.3: Rms of ocean bottom pressure variation for (a) RL04 OMCT@1.875° and (b) RL05 OMCT@1° and (c) their differences. 2007. Unit: hPa.

6.2. Uncertainties of the ocean bottom pressure

Unlike for the atmosphere model, OMCT is not providing error maps for the ocean bottom pressure fields. Therefore, we used within this work ocean bottom pressure errors derived from the Finite Element Sea Ice-Ocean Model (FESOM). The uncertainties are available on a $1.5° \times 1.5°$ grid and have a temporal resolution of one day. The FESOM model is a pure forward model and strongly dependent on the atmospheric forcing. The Boussinesq approximation is applied, and in order to take the neglected conservation of mass into account, a correction is applied afterwards. Further details on the FESOM model can be found in *Timmermann et al.* (2009). For this study it is important to know that the ocean bottom pressure errors are derived by driving the model once by NCEP and once by ECMWF ERA-Interim data. As the meteorological models provide their data in different spatial and temporal resolutions, this will lead also here to some undesirable interpolation effects. The available ocean bottom pressure errors used in our investigations represent the daily rms between the two model runs. Before the ocean bottom pressure errors enter the error propagation (error cases 2 and 3 in Sect. 9.1) as individual weights, the data is interpolated to the required $1° \times 1°$ grid.

When comparing the ocean bottom pressure error in Fig. 6.4 to the surface pressure error derived from NCEP/ECMWF model differences (Fig. 5.12, Sect. 5.2) some clear similarities can be found. Although for the computation of the surface pressure error, operational ECWMF data is used (in contrast to reprocessed ERA-Interim data in the FESOM run), the NCEP/ECMWF model differences map clearly into the ocean bottom pressure error (e.g., Southern polar region).

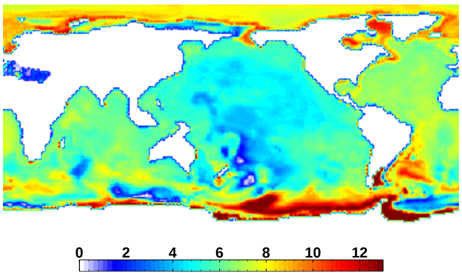

Fig. 6.4: Daily rms of ocean bottom pressure error derived from FESOM model simulations, 01.08.2007, Unit: hPa.

7. Additional Data & Software

7.1. Daily GRACE-solutions

In order to investigate the impact of an additional 'hydrological' de-aliasing (cf. Sect. 10.4), the daily ITG-Grace2010 (*Mayer-Gürr et al.*, 2010a) gravity field solutions of the year 2007, provided by the Institute of Geodesy and Geoinformation (IGG), University of Bonn, are used within this thesis.

Apart from instrument errors and unmodelled processes, like ice-melting and post-glacial rebound, the daily ITG-GRACE solutions should mainly contain hydrological signal - if one assumes that all background models (tides, AOD,...) are error-free and reflect the 'true world'.

IGG increased the temporal resolution of GRACE gravity field solutions from the standard (in the sense of originally and routinely provided by GFZ) monthly mean solutions to daily solutions. This has been done to minimize the aliasing of high-frequent mass variations. *Mayer-Gürr et al.* (2010b) showed that the usual parametrization of monthly gravity fields does not sufficiently represent the temporal variations of the Earth's gravity field. Therefore, *Kurtenbach et al.* (2009) developed a method to further increase the temporal resolution. In the following the applied method is summarized.

Increasing the temporal resolution of the gravity field solutions to one day requires the introduction of additional information about the temporal behavior of the gravity field. This is necessary as the increase in temporal resolution (from monthly to daily gravity fields) results in less observations per time span and therefore a reduced redundancy in the parameter estimation process, which is in turn leading to a decreased accuracy of the estimated gravity field coefficients.

In the approach developed by *Kurtenbach et al.* (2009), gravity field variations of the Earth are expressed as a dynamic process. The modelling of dynamic processes requires additional information about the auto-correlation function of the temporal variation of the Earth's gravity field. But this information is not available. Therefore, one tries to approximate this information from geophysical models. For the daily ITG-GRACE solutions temporal correlations, empirically deduced from the WaterGAP Global Hydrology Model (WGHM, *Döll et al.* (2003)), are used. In order to guarantee that the GRACE solutions are not biased towards the model values themselves but that only the stochastic behavior is exploited, the WGHM output of the years 1976 - 2000 (i.e. outside the GRACE time span) was applied. By utilizing the additional information from the WGHM model, the temporal resolution of the gravity field solutions could have been enhanced without losing spatial information.

Within a Kalman filter (*Kalman*, 1960) approach the dynamic processes are modelled and GRACE observations are fitted at the same time. According to *Kurtenbach et al.* (2009) the same background models (static gravity field, ocean tides, etc.) were introduced as for ITG-GRACE03s (*Mayer-Gürr*, 2007). Additionally the annual and semi-annual signals were estimated from the ITG-GRACE03s time series and were removed from the data. From these reduced observations the Kalman filter solution was calculated for each day. That means daily normal equation systems are set up and a weighted least-squares adjustment is performed, resulting in daily gravity field coefficients for degree $n = 2...40$ as differences to the static field ITG-GRACE2010s. The annual and semi-annual signal was restored afterwards. As during the Kalman filter process an implicit filtering has taken place, no filtering in a post-processing step of the output fields is necessary.

Detailed information on the exact procedure and modelling of daily gravity field solutions can be found in *Kurtenbach et al.* (2009) and *Kurtenbach* (2011).

Figure 7.1 illustrates the monthly mean of the daily ITG-GRACE solutions for August 2007 in terms of geoid heights. Clearly, the expected hydrological signal is visible (Amazon, Ganges, Zambezi). But also rather significant signal due to ice-melting (cf. Greenland) is reflected in the daily ITG solutions. This could have been expected, as 'ice' is not contained in the background models, which are 'reduced' from the GRACE solutions in the de-aliasing process.

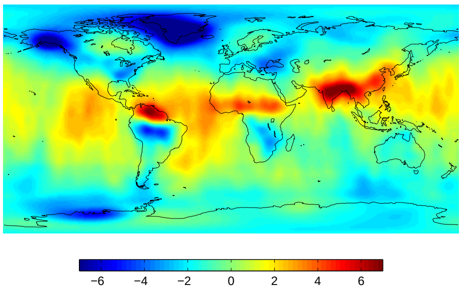

Fig. 7.1: Mean geoid height variation from daily ITG-GRACE solutions. August 2007, Unit: mm.

7.2. The BERNESE gravity field software

Within this thesis, the impact of the various de-aliasing scenarios is investigated on several processing levels. Amongst these are the K-band-range-rate residuals and monthly gravity field solutions (cf. Sect. III). These KBRR-residuals and monthly gravity solutions are computed by using the Bernese GPS Software (*Dach et al.*, 2007) and the Celestial Mechanics Approach (CMA). Details on the theoretical foundations of the CMA as well as on its application for GRACE data can e.g. be found in (*Beutler et al.*, 2010a) and (*Beutler et al.*, 2010b). The following chapter shall mainly give a brief overview of the Bernese Software and the settings used for the computation of the analyzed KBRR-residuals and monthly gravity field solutions.

According to *Beutler et al.* (2010b), the CMA is based on the orbit determination module of the Bernese GPS Software (*Dach et al.*, 2007), which is used by the CODE[1] Analysis Center of the International GNSS[2] Service to determine the orbits of the GNSS satellites. For gravity field determination based on the orbit of low Earth orbiters (LEOs), like GRACE, the GPS Software module has been generalized to allow for the introduction of pulses, piecewise constant, or piecewise linear accelerations for determining the orbit of LEOs (*Jäggi et al.*, 2006). The CMA was systematically upgraded for gravity field determination using single satellites equipped with spaceborne GPS receivers and constellations equipped with GPS and ultra-precise inter-satellite measurements (like the GRACE inter-satellite K-band measurements). *Jäggi et al.* (2010) tested for the first time the inter-satellite capabilities of the CMA to derive a gravity field based on GRACE low-low satellite-to-satellite tracking.

One of the key aspects of the CMA is its modularity which allows to study or improve individual contributions to a resulting orbit or gravity field. In this thesis, for example, the contribution of the non-tidal atmospheric and oceanic de-aliasing product has been investigated. By leaving all other settings unchanged, insight into the effect of using alternative AOD products is gained.

The orbit determination is based on kinematic positions and KBRR observations by using the gravity field model AIUB-GRACE02Sp (*Jäggi et al.*, 2009b), a precursor of AIUB-GRACE02S (*Jäggi et al.*, 2009a). The gravity field AIUB-GRACE02Sp was estimated at the Astronomical Institute of the University of Bern (AIUB), based on data from 2007 and using the CMA.

The solution AIUB-GRACE02Sp

- is based on the GRACE data (GPS, K-Band, and accelerometer) of the entire year 2007
- was generated using the GPS positions, the K-Band range-rates without taking the mathematical correlations into account, and the accelerometer measurements as empirically given (deterministic) functions
- was generated with a fixed scaling ratio of $\sigma^2_{kbd,rr}/\sigma^2_{ph} = 10^{-10} s^{-2}$ between the daily K-Band- and GPS-constituents of the NEQs

---

[1] Center for Orbit Determination in Europe

[2] Global Navigation Satellite System

- solved for all spherical harmonic coefficients between degrees 2 and 150 without imposing any constraints or regularization on them
- used the gravity field EGM96 (*Lemoine et al.* (1997)) as the a priori field and the solution was produced in one step
- solved for piecewise constant accelerations in the three directions (radial (R), along-track (S) and out-of-plane (W)) at 15-minute intervals constrained the mean values of the accelerations to $3 \cdot 10^{-9} m/s^2$ in the R-, S-, and in the W-directions
- constrained the differences between simultaneous accelerations of the same type between GRACE-A and GRACE-B to $3 \cdot 10^{-11} m/s^2$ for the R-, S-, and W-directions.

Except for one investigation, AIUB-GRACE02Sp has been used in all investigations as background gravity field model. Only in Sect. 10.4, where an additional hydrological de-aliasing is investigated, an alternative gravity field – AIUB-GRACE03S.010105 – is used. AIUB-GRACE03S.010105 is based on GRACE data covering a time-interval of seven years (2003-2009). Trends are simultaneously estimated with the static field up to d/o 30 with the reference epoch 1 January 2005. This has been done, as the daily ITG-GRACE solutions, used in Sect. 10.4 as hydrological signal, are given as differences to the static field ITG-GRACE2010s which is also referenced to 1 January 2005. Using another static model, which is not referring to this epoch, for the determination of the monthly gravity fields, would lead to visible trends in the monthly solutions. Therefore, to avoid these trends AIUB-GRACE03S.010105 has the same reference epoch as ITG-GRACE2010s.

In any case, it should be mentioned here, that the static gravity fields used in our investigations are not that important, as within this thesis the effect of changes in the AOD-product is always analyzed with respect to another one. In the scenarios compared to each other, the same static background models are used. The analyzed differences between the various scenarios compared to each other are independent of the introduced prior gravity field model.

Part III.

ANALYSIS: Various AOD products and their impact on GRACE data analysis

In the following part of this work, various changes in the calculation of the AOD product are made and the impact on GRACE data analysis is investigated. The changes made during the calculation of the AOD product are summarized in Fig. 7.2 and can be merged into three major groups:

Section 8 is dealing with various de-aliasing approaches. The impact of numerical integration instead of least-squares adjustment (Sect. 8.1) as well as the impact of the surface pressure approach instead of the vertical integration approach (Sect. 8.2) for the determination of the atmospheric masses is investigated. Furthermore, the effect of a constant vs. latitude-dependent gravity acceleration (Sect. 8.3), as well as the impact of the de-aliasing at all and the maximum truncation degree (Sect. 8.4) are analyzed. Also a comparison between the official GFZ RL04 solution and the TUM solution is performed (Sect. 8.5).

Section 9 is examining the impact of atmospheric and oceanic model uncertainties. First, various error scenarios are defined (Sect. 9.1). Then the effect of the atmospheric model errors on the vertically integrated atmospheric pressure (Sect. 9.2) are analyzed. Afterwards, the impact of the combined atmospheric and oceanic model errors on the AOD product and GRACE data analysis (Sect. 9.3) is investigated.

The third topic of using alternative and additional data for the computation of the de-aliasing coefficients is covered by Sect. 10. The first Sect. 10.1 analyzes the impact of using ECMWF ERA-Interim data instead of operational data. How an enhanced spatial resolution of the ocean model is affecting the AOD coefficients and further GRACE results is shown in Sect. 10.2. The impact of an alternative time-span used for the calculation of the atmospheric and oceanic fields is analyzed in Sect. 10.3. Last but not least, an additional 'hydrological' de-aliasing is performed, by using the daily ITG-GRACE solutions.

The effect of the various AOD scenarios is evaluated on various processing levels:

- **AOD coefficients**: the impact of the performed changes on the de-aliasing coefficients themselves are shown in terms of geoid heights on a global latitude/longitude grid as well as in terms of degree standard deviations for geoid heights. In order to get insight into the importance of the performed AOD changes, the impact is compared to the current RL04 and RL05 GRACE errors as well as to the predicted GRACE error level (GRACE Baseline) and a simulated future gravity field mission error level. Indeed, these plots of degree standard deviations are showing if the changes made in the AOD product are in the sensitivity range of GRACE and the future gravity field mission, but will not allow to draw a conclusion about the value (improvement or not) of the changes made.

- **Monthly gravity field solutions**: with the various AOD products, monthly gravity field solutions (MGFS) are calculated via the BERNESE gravity field software and are compared to each other. As nothing else than the AOD product has been changed during gravity field calculation, one will directly get insight into the effect of the AOD changes on a monthly gravity field solution. The parameter usually taken as a key parameter to assess the quality of a monthly gravity field solution is the so-called *global weighted rms (wrms)*. After subtraction of a best-known mean static gravity field, the assumption is made, that the *wrms* of a monthly gravity field solution becomes smaller and thus better, the more high-frequent mass variations are 'removed' during the de-aliasing process. Since the idea of the de-aliasing process is to model and 'remove' exactly these high-frequent mass variations, one assumes here, that the smaller the *wrms* becomes, the better the solution or in our context, the de-aliasing product is.

- **KBRR-residuals**: K-band-range-rate residuals are an intermediate result during gravity field modelling. One indication for an improved gravity field modelling are minimized or reduced KBRR-residuals. A decrease of KBRR-residuals implies that the modelled observations (here: atmospheric and oceanic mass variations) fit better to the 'real' observations made by GRACE and that the investigated AOD model is principally able to improve GRACE results. In the following chapters, the 5-second KBRR-residuals are analyzed against time, longitude, and latitude. The amplitude spectra and the square root of the power spectral density (*psd*) of the 5-second KBRR-residuals are shown. Furthermore, the daily rms of the 5-sec KBRR-residuals is analyzed over a certain time-span. In addition, the 5-second KBRR-residuals as well as the rms of the KBRR-residuals over the examined time-span are illustrated as a function of latitude and longitude. The differences between AOD case

A and AOD case B scenarios are illustrated on a global latitude-longitude grid and are in the following usually illustrated as red-blue colored plots. This is done in order to emphasize the positive or negative impact of the changes performed in the AOD product. The red color always indicates regions where the AOD product B performs better or leads to smaller KBRR-residuals than the AOD A product.

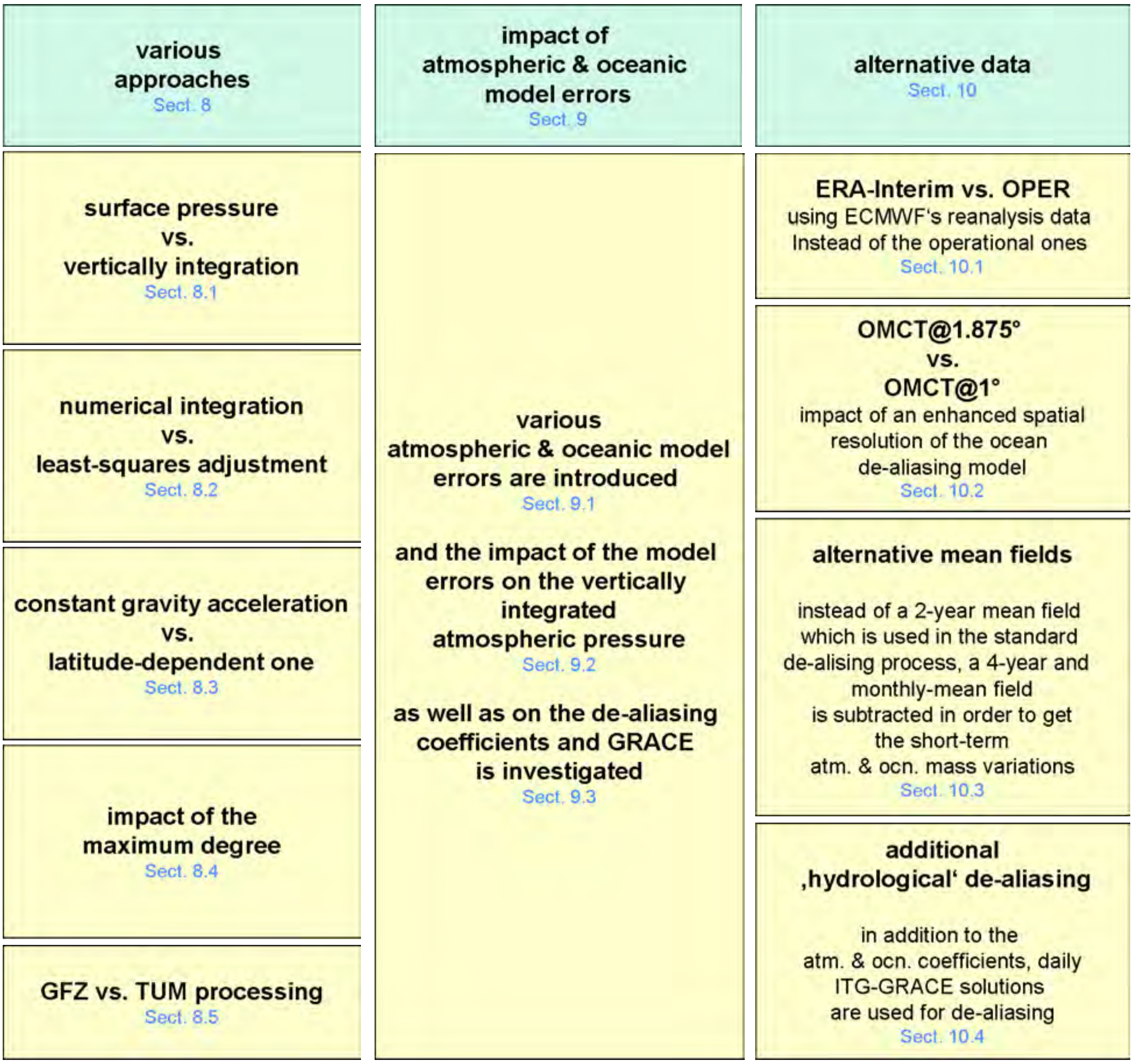

Fig. 7.2: Overview of the various studies on the AOD product. The Figure shows the structure of the following sections and their content.

8. Comparison of various de-aliasing approaches

8.1. Numerical integration vs. least-squares adjustment

The question arises how the potential coefficients determined by the least-squares adjustment (cf. Sect. 4.2) differ from those determined by the numerical integration (cf. Sect. 3.3). For the former equal weighting or error-free input parameters are assumed. The first thing catching someone's eye is the fact that by the least-squares approach not only the de-aliasing coefficients $\bar{C}_{nm}$, $\bar{S}_{nm}$ themselves but also atmospheric and oceanic error estimates $\sigma\bar{C}_{nm}$, $\sigma\bar{S}_{nm}$ are obtained. Originally, it was planned to use the atmospheric and oceanic error estimates directly during the gravity field determination process. But so far the current gravity field analysis software does not allow to take these errors into account. Amongst other reasons, this is because certain parameter groups including the de-aliasing coefficients have to be regarded as known/error-free during the parameter estimation (cf. Sect. 2). Thus, the use of the atmospheric and oceanic uncertainties in the course of gravity field processing is not yet implemented.

Impact of the NI and LSA approach on the AOD product

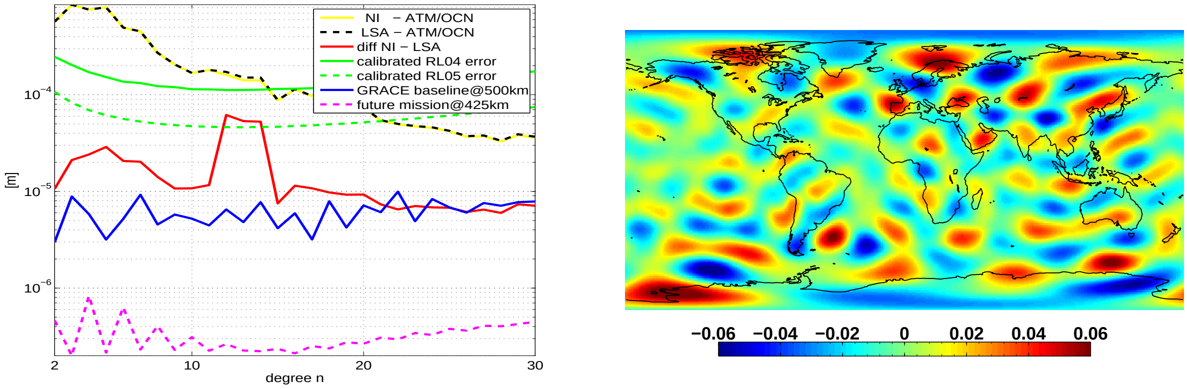

(a)

(b)

Fig. 8.1: Comparison of numerical integration and least-squares adjustment for the determination of the atmospheric and oceanic potential. (a) degree standard deviations in terms of geoid heights. Unit: m. (b) difference between numerical integration and least-squares adjustment in terms of geoid heights for 01.08.2007, 00h. Unit: mm.

In order to answer the question of the differences between the AOD coefficients determined by numerical integration and least-squares adjustment, we refer to Fig. 8.1. Here it can be seen, that under the assumption of error-free input parameters the numerical integration and the least-squares approach give approximately equivalent results (red line in Fig. 8.1a). Concerning the current error of GRACE (green dotted line) it will have hardly any effect whether the coefficients are determined by numerical integration (NI) or least-squares adjustment (LSA). However, with respect to the GRACE baseline (blue line) and the simulated future mission error level (magenta dotted line), one should be aware that the difference exceeds the sensitivity range of GRACE and future missions. Striking is the fact that especially for some degrees ($n = 12, 13, 14$) the differences between the two methods seem to be larger. The reason for this has not been further investigated within this work, as the differences are small, and as they have no effect on the intent of this work. Having a look at Fig. 8.1b one can observe an almost negligible effect on the AOD coefficients. The differences in the AOD coefficients of either using the numerical integration or the least-squares adjustment is clearly in the sub-mm-range (min: -0.07 mm, max: 0.07 mm, mean: 0.00 mm, rms: 0.02 mm).

Impact of the NI and LSA approach on a monthly gravity field solution

Analyzing Fig. 8.2, we observe that the alternative approaches lead to differences in a monthly gravity field solution of only up to maximum 0.05 mm (min: -0.04 mm, mean: 0.00 mm, rms: 0.01 mm). The global weighted rms of the monthly gravity fields only differs by 0.05 % between the two approaches.

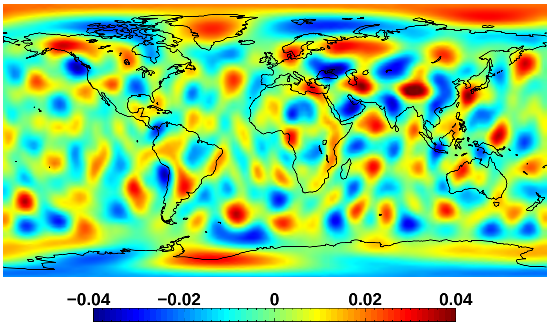

Fig. 8.2: Differences between the monthly gravity field solutions after subtracting the NI and LSA - AOD products. August 2007. Unit: mm.

	min	max	mean	wrms
NI	-10.071	8.060	0.010	1.518
LSA	-10.089	8.060	0.010	1.519
NI - LSA	-0.042	0.046	0.000	0.012

Tab. 8.1: Statistics on the differences between the monthly gravity field solutions after applying the NI and LSA AOD products. August 2007. Unit: mm.

Impact of the NI and LSA approach on the KBRR-residuals

The almost negligible effect on the KBRR-residuals is visible in Figs. 8.3 and 8.4. The rms differences between the NI and LSA-approach over 1 month of KBRR-residuals are clearly at the nm/s-level (min: -3.73 nm/s, max: 6.14 nm/s, mean: -0.05 nm/s, rms: 0.68 nm/s).

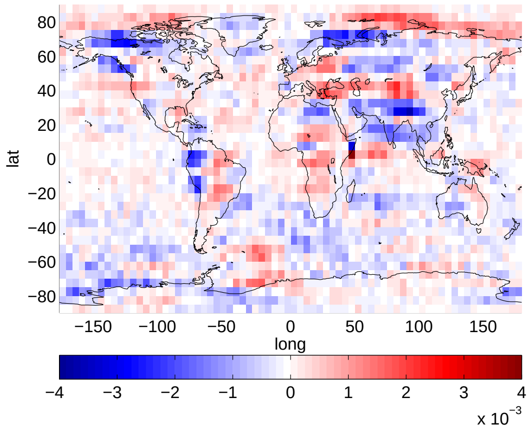

Fig. 8.3: Rms differences between NI and LSA-approach over 1 month of KBRR-residuals in bins of 5° × 5° in longitude and latitude. August 2007, Unit: $\mu m/s$.

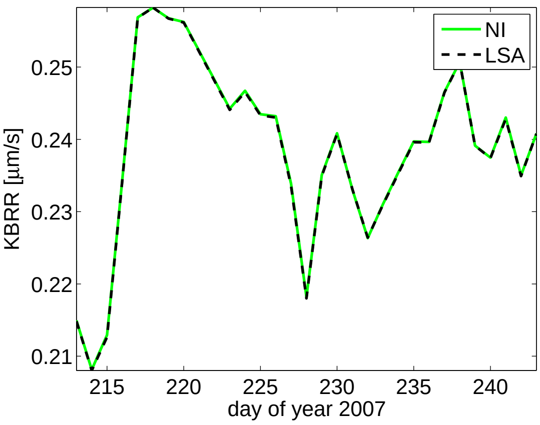

Fig. 8.4: Daily rms of KBRR-residuals after removing either the NI-AOD (green) or the LSA-AOD (black). August 2007, Unit: $\mu m/s$.

Regarding the computational requirements, one has to state, that the numerical effort for determining the AOD product by least-squares adjustment is much larger than by numerical integration. For d/o 100 a run-time of approx. 2 minutes for the NI-approach is faced a run-time of approx. 2 hours for the LSA-approach.

maximum degree	no. of unknowns	size of one NEQ	size of all NEQs
10	121	114 KB	1 MB
30	961	7 MB	218 MB
50	2601	52 MB	2.6 GB
70	5041	193 MB	14 GB
100	10201	794 MB	80 GB

Tab. 8.2: Computational requirements for the determination of the AOD product by least-squares adjustment. The numbers in the last two columns are rounded and reflect the size of one full normal equation system (NEQ) as well as the size of all ($nmax + 1$) normal equation systems.

As described in Sect. 4.2, the calculation of the AOD coefficients by LSA is divided into three steps. First, the atmospheric pressure is calculated. Then the most intensive part, the set up and solution of the normal equation systems (NEQs) per degree n, is performed. Table 8.2 shows the computational requirements of the least-squares adjustment. For the determination of the atmospheric and oceanic potential coefficients up to degree 30, 31 full normal equation systems have to be set up and solved. Each NEQ has the size of 7 MB, which results in approximately 218 MB for all ($nmax$+1) full equation systems. In principle these numbers are a solvable task for today's computer systems. In our case, the AOD product is calculated on the Linux cluster of the Leibniz Supercomputing Centre (LRZ). The computation time for one month (6 hourly) of AOD products up to d/o 30 reached from 2 hours to 1 week, strongly depending on the capacity and availability of the LRZ-cluster. Within this chapter, it was decided to limit the investigations to degree 30 in order to have a compromise between computation time and maximum degree. The fact, that a maximum degree of 30 is sufficient for the determination of the de-aliasing coefficients, is shown in Sect. 8.4.

The main motivation to switch from the much faster and currently applied NI-approach to the LSA-approach lies in the error propagation. In order to take uncertainties in the atmospheric and oceanic model parameters into account and to propagate them properly from the input parameters further on to the de-aliasing product, one has to choose the LSA-approach (cf. Sect. 4).

Summary - Numerical integration vs. least-squares adjustment

- differences in the AOD coefficients between the NI and LSA approach are in the sub-mm-range (min: -0.07 mm / max: 0.07 mm / mean: 0.00 mm / rms: 0.02 mm), which is safely below the sensitivity range of current GRACE gravity field solutions
- whether using the NI or LSA approach affects a monthly gravity field solution in the sub-mm-range (min: -0.04 mm, max: 0.05 mm, mean: 0.00 mm, rms: 0.01 mm)
- the global weighted rms of the monthly gravity field solutions increases by about 0.05 % when using the LSA approach instead of the NI approach
  (1.5177 mm for NI and 1.5185 mm for LSA)
- the daily rms of the KBRR-residuals over one month is almost identical for the LSA and NI approach (0.2379 μm/s vs. 0.2380 μm/s)
- the improvement by either using NI or LSA on the rms of KBRR-residuals is ambiguous. There are regions where the NI performs slightly better than the LSA and vice versa. However, the rms of KBRR-residuals is pretty small and lies in the nm/s-range
  (min: -3.73 nm/s, max: 6.14 nm/s, mean: -0.05 nm/s, rms: 0.68 nm/s)

In conclusion, we can retain, that for current gravity field determination it makes hardly any difference whether the AOD product is determined by the standard numerical integration (as it is performed in the current de-aliasing approach) or by the alternative least-squares adjustment. Concerning the actual or achieved (as opposed to the expected pre-launch) accuracy of gravity field determination with GRACE the differences between the LSA and NI approach are far below the current GRACE gravity field performance. Concerning the GRACE Baseline and the error predictions of future gravity field missions, using either the LSA or NI approach will have a significant effect. Although the computation time of the de-aliasing coefficients for the LSA approach is much higher, one has to change from the NI approach to the latter if model errors shall be taken into account (cf. Sect. 4).

8.2. Surface pressure approach vs. vertical integration approach

Two alternative methods of taking the atmospheric mass variations into account have been introduced in chapters 3.1 and 3.2. In the SP approach (Eq. 3.10) the surface pressure is used for the numerical integration of the atmospheric masses, thereby assuming that the atmospheric masses are condensed on a thin layer on the Earth's surface. In contrast, the VI approach (Eq. 3.2) takes the vertical structure of the atmosphere into account. Figure 8.5 shows the differences between the surface pressure and the vertically integrated pressure. They are in the range of 4.2 hPa and 6.3 hPa with a global rms of 0.28 hPa for degree $n = 0$. With increasing degree n also the differences are increasing. For degree $n = 30$ the differences are already by a factor of 9 larger than for $n = 0$.

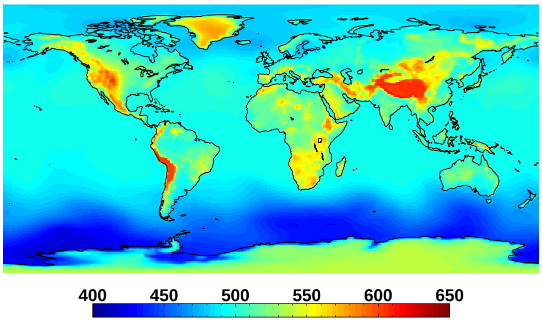

Fig. 8.5: Pressure differences between surface pressure P_S and vertically integrated pressure I_n (n=0) for 01.08.2007, 00h. Unit: Pascal.

For degree $n = 30$ the differences are already by a factor of 9 larger than for $n = 0$.

Impact of the SP and VI approach on the AOD product

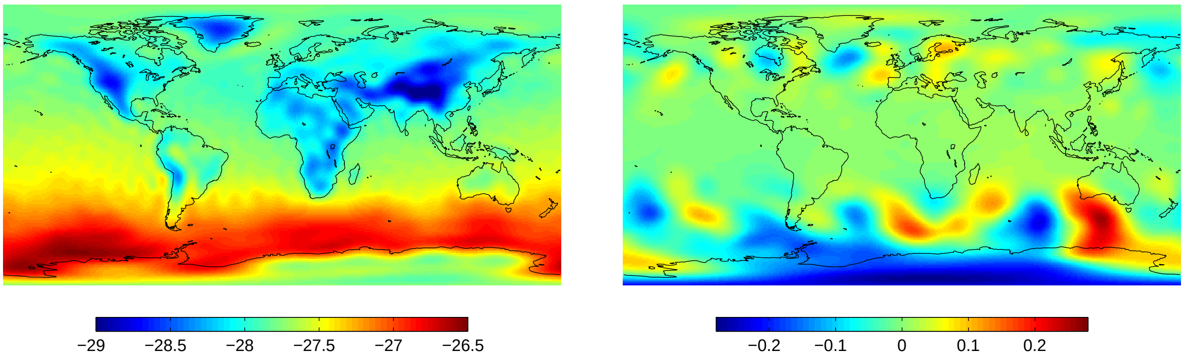

(a)

(b)

Fig. 8.6: Comparison SP and VI approach for atmospheric loading. Differences between the (a) full and (b) residual atmospheric potential in terms of geoid heights for 01.08.2007, 00h. Unit: mm.

When analyzing the full atmospheric potential on AOD level (cf. Fig. 8.6a), we observe differences between the two approaches at the centimeter level (min: -29.13 mm / max: -26.53 mm /mean: -27.67 mm /rms: 0.41 mm), which is less than 1% of the full atmospheric signal (which is in the range of about 5 m in terms of geoid heights). Regarding the effect of the two approaches on the residual (i.e. after subtraction of the mean atmosphere field) atmospheric potential, which is actually of interest for de-aliasing, the differences become almost negligible with a maximum, minimum, mean, and rms amplitude of 0.28 mm, -0.26 mm, 0.004 mm, and 0.05 mm, respectively (cf. Fig. 8.6b). From Fig. 8.7a, one can observe that the differences of the full atmospheric potential are clearly in the sensitivity range of the current GRACE performance. Regarding the differences of the residual potentials (magenta line in Fig. 8.7b) and comparing them to the current GRACE RL04 and RL05 error levels (black lines), the differences are much smaller, but still in the sensitivity range of current GRACE solutions and will be even more important when regarding the accuracy of future gravity field missions (cyan line in Fig. 8.7b).

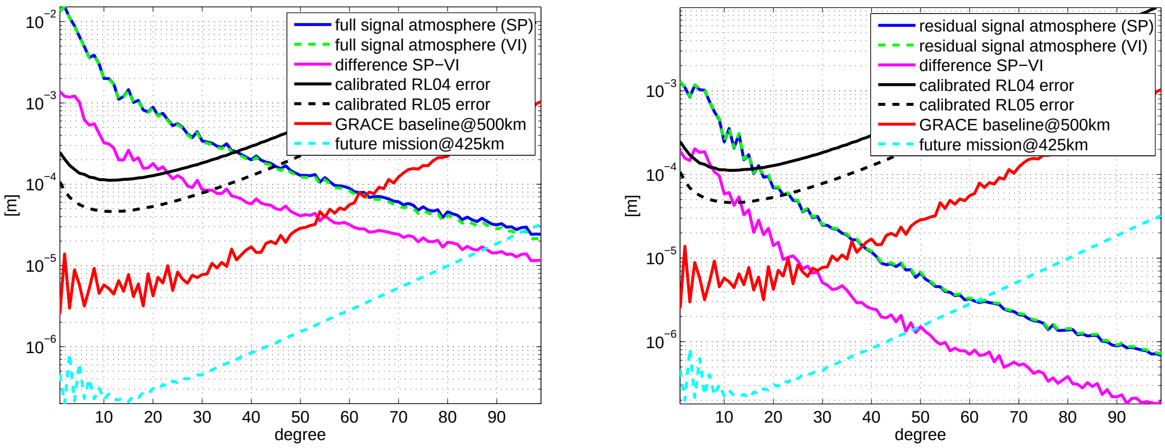

(a)

(b)

Fig. 8.7: Comparison SP and VI approach for atmospheric loading. Degree standard deviations of the (a) full atmospheric potential and the (b) residual atmospheric potential (after subtraction of a mean field) in terms of geoid heights for 01.08.2007, 00h. Unit: m.

Impact of the SP and VI approach on a monthly gravity field solution

Analyzing Fig. 8.8 and Tab. 8.3, we see that the alternative approaches lead to differences in a monthly gravity field solution up to maximum 0.97 *mm*. The global weighted rms of the monthly gravity fields only reduces/improves by about 0.5 % when using VI instead of SP.

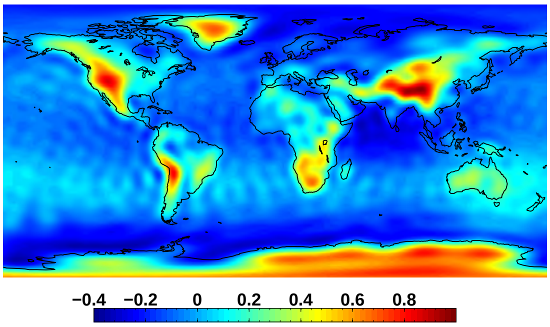

Fig. 8.8: Differences between the monthly gravity field solutions after subtracting either the SP or the VI AOD product. August 2007. Unit: mm.

	min	max	mean	wrms
SP - VI	-0.35	0.97	0.01	0.22

Tab. 8.3: Statistics on the differences between the monthly gravity field solutions after applying the SP and VI AOD products. August 2007. Unit: mm.

Impact of the SP and VI approach on the KBRR-residuals

Examining the rms over two months of KBRR-residuals as a function of latitude and longitude in an Earth-fixed system, one can state that the SP AOD compared to the VI AOD leads to slightly higher rms exactly in the same regions where the pressure differences are extreme. Comparing Fig. 8.5 and Fig. 8.9, high correlation patterns can be observed (Himalaya, Greenland, Antarctica, etc.), which proves that there is an almost one-to-one propagation of the pressure differences to the KBRR-residuals. Figure 8.11 illustrates that the KBRR-residuals could have been reduced globally by using the VI approach. Though, the improvement with respect to the SP approach is rather small with maximum 0.12 μm/s (min: -0.03 μm/s, mean: 0.01 μm/s, rms: 0.02 μm/s). The slight improvement of the KBRR-residuals by using VI is also visible in the daily rms (cf. Fig. 8.10). The mean value of the daily rms can be reduced by about 1 % from 2.14 μm/s to 2.12 μm/s.

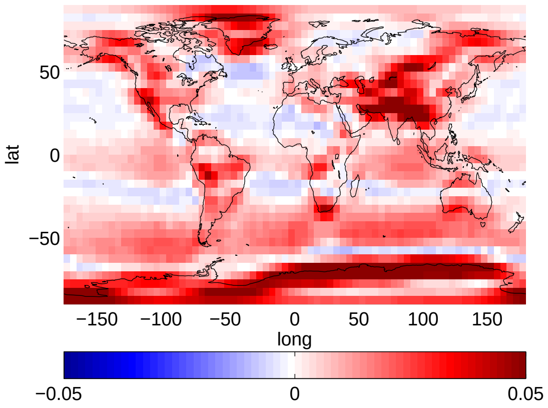

Fig. 8.9: Rms differences between SP and VI approach over two months (July & August 2007) in bins of 5° × 5° in longitude and latitude. Unit: μm/s.

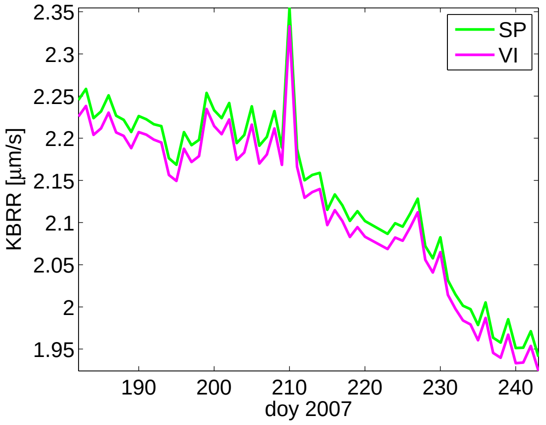

Fig. 8.10: Daily rms of KBRR-residuals for July and August 2007 after removing SP AOD (green) and VI AOD (magenta). Unit: μm/s.

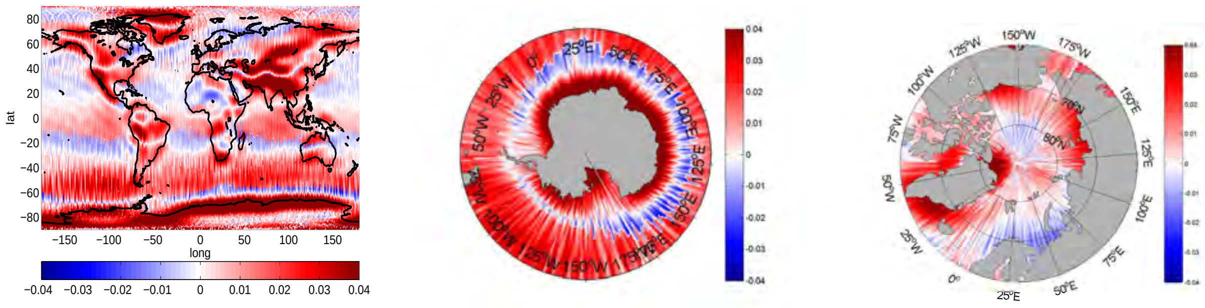

Fig. 8.11: KBRR-residual differences in bins of 1° × 1° in longitude and latitude between the SP and VI case for July & Aug 2007. Red indicates that the KBRR-residuals are reduced/improved by using the VI-AOD product w.r.t. the SP-AOD product. Blue indicates regions where the SP product reveals smaller (better) residuals. Unit: μm/s.

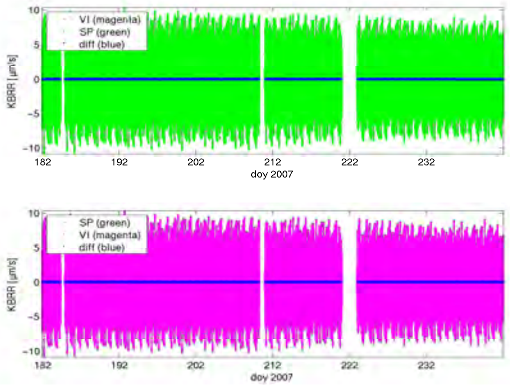

Fig. 8.12: KBRR-residuals in $\mu m/s$ for two months (July & August 2007) after removing the SP AOD (green) and the VI AOD (magenta) and their differences (blue).

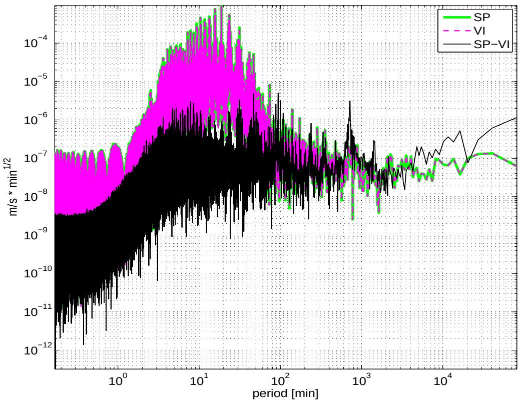

Fig. 8.13: PSD of 2 months (July & August 2007) KBRR-residuals after removing the SP AOD (green) and the VI AOD (magenta) and the PSD of the difference SP-VI (black)

As the improvements by using VI instead of SP are pretty small, no direct differences can be seen when plotting the KBRR-residuals against time (Fig. 8.12), longitude, and latitude (not shown). Also the differences between the psds (green and magenta) are pretty small. Therefore, in addition the psd of the differences between SP and VI is plotted. As it can be seen (black line in Fig. 8.13), the differences are small, but still significant at certain periods.

Summary - Surface pressure approach vs. vertical integration approach

- differences of the AOD coefficients between the SP and VI approach for the determination of the atmospheric potential are in the sub-mm-range and in the sensitivity range of current GRACE and future gravity field solutions
(min: -0.26 mm, max: 0.28 mm, mean: 0.004 mm, rms: 0.05 mm).
- whether using the SP or VI approach affects a monthly gravity field solution in the sub-mm-range (min: -0.35 mm, max: 0.97 mm, mean: 0.01 mm, rms: 0.22 mm)
- the global weighted rms of the monthly gravity field solutions improves/reduces by about 0.5 % when using the VI approach instead of the SP approach (only concerning the atmospheric part, no combination with the ocean)
- the daily rms over two months of the KBRR-residuals improves by about 1 % when using the VI instead of the SP approach
- the rms of the KBRR-residuals as well as the KBRR-residuals themselves are almost globally improved/reduced when using the VI approach. Rms of KBRR-residuals is affected at the level of nm/s (min: -10.89 nm/s, max: 93.50 nm/s, mean: 9.70 nm/s, rms: 13.13 nm/s)

In summary, we can retain, that both approaches do have their pros and cons. The VI approach demands more computational effort than the SP approach. E.g., the calculation of the de-aliasing coefficients up to d/o 100 via the VI approach takes about 1600 times longer than by the SP approach (160 seconds vs. 0.1 seconds). The foregoing investigations have shown that the VI approach leads to slightly better results on almost all levels (KBRR-residuals, monthly gravity field solution) of gravity field processing. Therefore, the VI approach is used in the standard GRACE data processing (*Flechtner*, 2007a). Although the improvements on GRACE results are pretty small, the vertical structure of the atmosphere has to be taken into account, especially for high precision applications and future gravity field missions, where the effect might be even more significant than in the current GRACE processing.

8.3. Latitude-dependent instead of constant gravity acceleration

In the following chapter, the impact of a latitude-dependent gravity acceleration instead of a constant one is analyzed. According to *Heiskanen and Moritz* (1967) the constant gravity acceleration g in Eq. 3.26 as well as in Eq. (3.22) can be substituted by

$$g(\theta) = \gamma_a(1 + f_2 \cos^2\theta + f_4 \cos^4\theta) \tag{8.1}$$

with

$$f_2 = -f + \frac{5}{2}m + \frac{1}{2}f^2 - \frac{26}{7}fm + \frac{15}{4}m^2 \quad \text{and} \quad f_4 = -\frac{1}{2}f^2 + \frac{5}{2}fm, \quad m = \frac{\omega^2 a^2 b}{GM}$$

The latitude-dependent gravity $g(\theta)$ can be determined by the defining parameters of a reference ellipsoid: the normal gravity γ_a at the equator, the flattening f, as well as the ratio m between the angular velocity ω, the semi-major and semi-minor ellipsoidal axis a and b, and the product of the Earth's mass M and the gravitational constant G (see *Heiskanen and Moritz* (1967)).

Impact of the latitude-dependent gravity acceleration on the vertically integrated atmospheric pressure & the AOD product

Figure 8.14a and Tab. 8.4 show the differences in the vertically integrated atmospheric pressure I_n when using either a constant or latitude-dependent gravity acceleration g. With maximum 0.16 hPa the differences are rather small. Having a look at Fig. 8.14b and Tab. 8.5 one can see, that the impact of the refined gravity acceleration on the AOD product is at the μm-level and barely in the sensitivity range of GRACE (cf. blue and red lines in Fig. 8.16), but will be more significant for future gravity field missions.

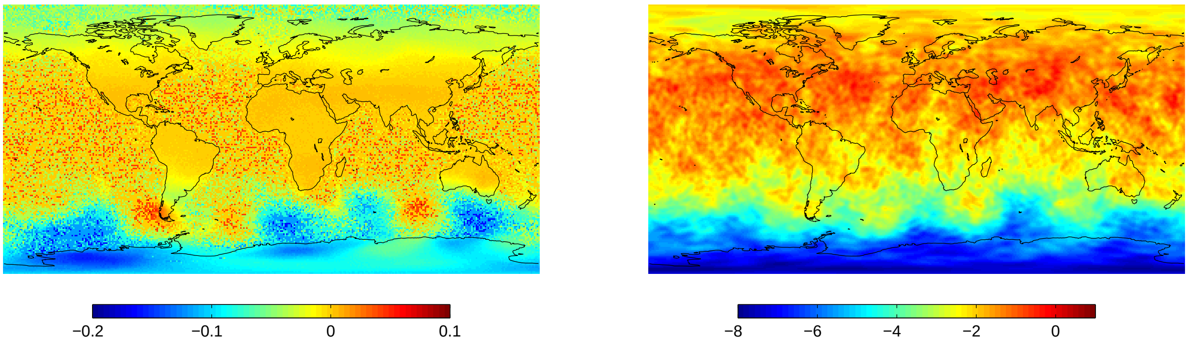

(a) n=10, 01.08.2007 00h, Unit: hPa (b) August 2007, Unit: μm

Fig. 8.14: Impact of using either a constant or latitude-dependent gravity acceleration on (a) the vertically integrated atmospheric pressure I_n and on (b) the AOD product in terms of geoid heights.

	min	max	mean	wrms
n=91	-0.16	0.08	-0.02	0.03
n=80	-0.16	0.08	-0.01	0.03
n=30	-0.08	0.04	-0.00	0.02

Tab. 8.4: Statistics on the differences between the vertically integrated atmospheric pressure I_n after applying a constant and latitude-dependent gravity acceleration. 01.08.2007 00h. Unit: hPa.

	min	max	mean	wrms
diff.	-8.07	0.06	-2.38	1.36

Tab. 8.5: Statistics on the differences between the AOD product after applying a constant and latitude-dependent gravity acceleration. August 2007. Unit: μm.

Impact of the latitude-dependent gravity acceleration on a monthly gravity field solution

Consequently, the impact of the latitude-dependent gravity acceleration on a monthly GRACE gravity field solution, shown in Fig. 8.15 and Tab. 8.6, is also rather small and in the μm-range. The global weighted rms only reduces/improves by about 0.05 ‰ when introducing a latitude-dependent g.

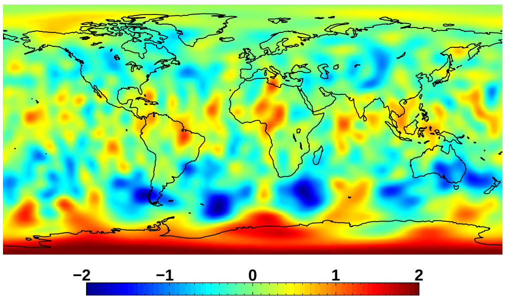

Fig. 8.15: Impact of using either a constant or latitude-dependent gravity acceleration on a monthly gravity field solution. August 2007, Unit: μm.

	min	max	mean	wrms
diff.	-1.99	2.08	-0.03	0.57

Tab. 8.6: Statistics on the differences between the monthly gravity field solutions after applying a constant and latitude-dependent gravity acceleration. August 2007. Unit: μm.

Impact of the latitude-dependent gravity acceleration on the KBRR-residuals

Analyzing the differences in the global rms over 1 month of KBRR-residuals (cf. Fig. 8.17), it can be stated, that the differences are very small and only in the sub-nm/s-range. Especially in the polar regions, the rms of the KBRR-residuals could have been reduced/improved by using a latitude-dependent gravity acceleration (red-colored regions in Fig. 8.17). How small the effect of a latitude-dependent gravity acceleration is, shows the fact, that the daily rms of the KBRR-residuals over one month (August 2007) is only improved/reduced by about 0.01 ‰.

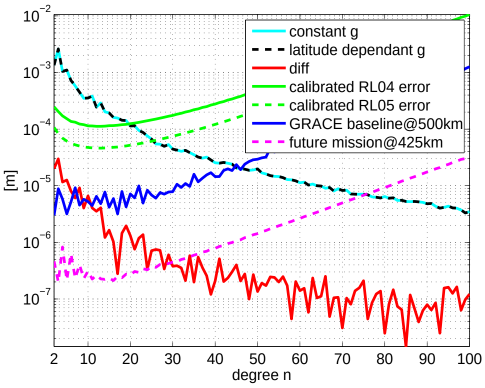

Fig. 8.16: Differences in terms of degree standard deviations for geoid heights between the AOD products after applying a constant and latitude-dependent gravity acceleration. August 2007. Unit: m.

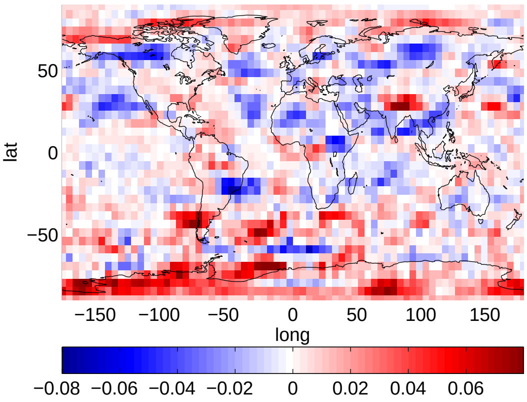

Fig. 8.17: Rms differences between using a constant and latitude-dependent gravity acceleration over 1 month of KBRR-residuals in bins of $5° \times 5°$ in longitude and latitude. August 2007, Unit: nm/s.

Summary - Latitude-dependent instead of constant gravity acceleration

- the latitude-dependent gravity acceleration has an impact of maximum 0.16 hPa on the vertically integrated atmospheric pressure I_n
  (min: -0.16 hPa, max: 0.08 hPa, mean: -0.02 hPa, rms: 0.03 hPa for level n=91)
- differences between the AOD products determined with a constant and latitude-dependent gravity acceleration are in the μm-range and thus barely in the sensitivity range of the GRACE mission, but up to d/o 30 very well in the sensitivity range of future gravity field missions
  (min: -8.07 μm, max: 0.06 μm, mean: -2.38 μm, rms: 1.36 μm)
- whether using a constant or latitude-dependent gravity acceleration affects a monthly gravity field solution in the μm-range
  (min: -1.99 μm, max: 2.08 μm, mean: -0.03 μm, rms: 0.57 μm)
- the global weighted rms of the monthly gravity field solutions is only reduced by 0.05 ‰when applying the latitude-dependent gravity acceleration
- the daily rms of the KBRR-residuals over August 2007 is slightly reduced ($\sim$ 0.01 ‰) when using a latitude-dependent gravity acceleration
- the improvements by using a latitude-dependent gravity acceleration on the rms of KBRR-residuals is ambiguous. Especially in the polar regions, the latitude-dependent g slightly performs better than a constant g. The rms of the KBRR-residuals is affected in the sub-nm/s-range.
  (min: -0.08 nm/s, max: 0.10 nm/s /mean: 0.00 nm/s, rms: 0.02 nm/s)

8.4. The impact of AOD depending on the maximum degree

The official Release 04 (RL04) de-aliasing product is provided up to d/o 100 and usually used completely up to this maximum degree during gravity field processing. In this chapter, the question whether any effect of applying AOD up to d/o 20, 40, 60 or 80 during gravity field processing is visible in the resulting KBRR-residuals or monthly gravity field solutions shall be answered.

In order to determine the sensitivity of monthly gravity fields and KBRR-residuals on the applied maximum d/o of the AOD product, five additional AOD cases to the standard AOD100 with maximum d/o=100, are defined:

- AOD80 = official AOD product only used up to d/o = 80 during gravity field processing
- AOD60 = official AOD product only used up to d/o = 60 during gravity field processing
- AOD40 = official AOD product only used up to d/o = 40 during gravity field processing
- AOD20 = official AOD product only used up to d/o = 20 during gravity field processing
- oAO = no AOD product at all is used during gravity field processing

Spectral content of the AOD coefficients

First the spectral content of the AOD coefficients shall be analyzed. For this purpose we introduce the quantity of degree rms (RMS_n).

$$RMS_n = \sqrt{\frac{1}{2n+1} \cdot c_n^2}. \tag{8.2}$$

It is in direct functional relation with the well known degree-variances c_n^2:

$$c_n^2 = \sum_{m=0}^{n} (\bar{C}_{nm}^2 + \bar{S}_{nm}^2). \tag{8.3}$$

The square-root of the quotient c_n^2 divided by the number of coefficients per degree n, results in RMS_n.

Figure 8.18 shows the 6-hourly degree rms of the AOD coefficients over one year (2007). It can be observed that most of main signal content of the de-aliasing coefficients lies in the potential coefficients smaller than approximately degree $n = 30$. The signal content of the coefficients larger than $n = 30$ has an already 2 to 3 times reduced order of magnitude. However, several intervals do have a much stronger signal content exceeding degree $n = 30$ (e.g. days 30, 78 or 334).

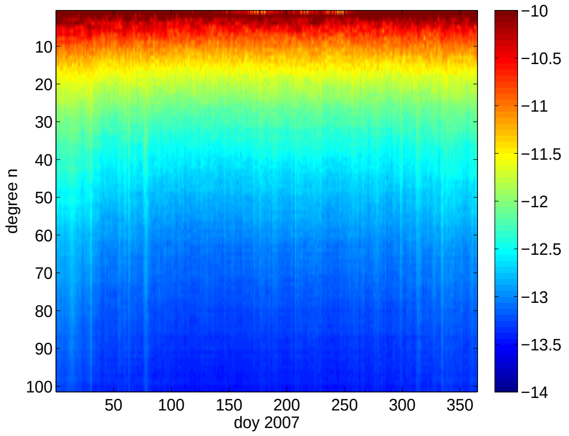

Fig. 8.18: Degree-RMS of the 6-hourly atmospheric and oceanic potential coefficients for year 2007. Unit: dimensionless, [log10].

Computing the amplitude spectrum of the 6-hourly AOD coefficients over one year of data, one can clearly observe (cf. Fig. 8.19) the dominating frequencies: Besides the daily (365 cpa, Fig. 8.19a) and semi-daily (730 cpa, Fig. 8.19c) frequencies, a distinctive amplitude for 705 cpa (cycles per year) can be found (cf. Fig. 8.19c). 705 cpa corresponds to 1.9315 cycles per day, which is 12.425 hours and can be ascribed to the lunar tide $M2$ (see e.g. *Wilhelm et al.* (1997)). Furthermore, relatively strong signals can be observed for longer periods. Not only the annual (1 cpa) and semi-annual (2 cpa) amplitudes are distinctive, but also periods of 60.8 days (6 cpa), 26.07 days (14 cpa), and 16.59 days (22 cpa) are visible in Fig. 8.19b.

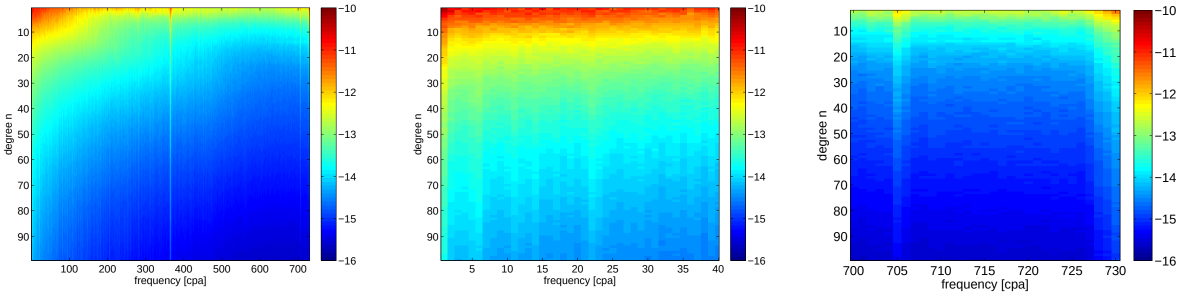

(a) (b) (c)

Fig. 8.19: Spectral amplitudes for one year (2007) of the AOD100 potential coefficients. Unit: dimensionless, [log10]. (b) and (c) are zoom-ins of the whole spectrum (a).

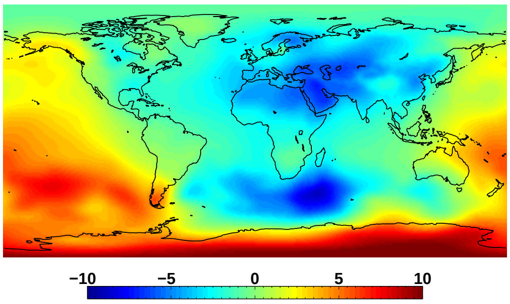

Fig. 8.20: AOD100 product in terms of geoid heights. 01.08.2007 00h. Unit: mm.

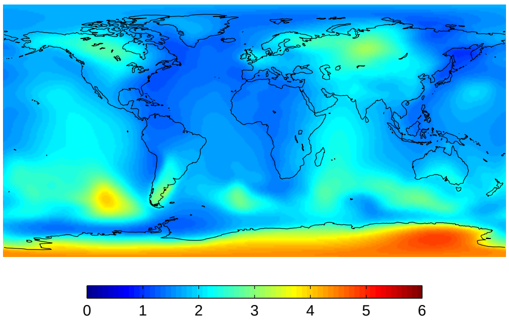

Fig. 8.21: RMS of AOD100 product over one month (August 2007), Unit: mm.

In a next step, the effect of the maximum degree n is investigated. As Fig. 8.19a shows, the atmospheric and oceanic potential coefficients contain the main signal in the spherical harmonic degrees n smaller than 30 to 40. Now, the question shall be answered, whether any effect of applying AOD up to d/o 20, 40, 60 or 80 during gravity field processing is visible in the resulting KBRR-residuals or monthly gravity field solutions. Therefore, the AOD potential coefficients are synthesized to geoid heights. Depending on the maximum d/o, or in other words depending on the cut-off frequency, different results are obtained. As the spatial distribution of the AOD products in terms of geoid heights are on the first sight almost identical for the various cut-off frequencies of the AOD cases, the differences with respect to the reference case (cf. Fig. 8.20) are shown in the following. Having a look at Fig. 8.22 and Tab. 8.7 reveals, that up to d/o 20 (Fig. 8.22a) almost 80% of the (total, maximum) atmospheric and oceanic signal (cf. Fig. 8.20) is covered, as the difference between the AOD100 and AOD20 reaches up to 2 mm. AOD40, AOD60 and AOD80 cover 88%, 95% and 98% of the signal, respectively.

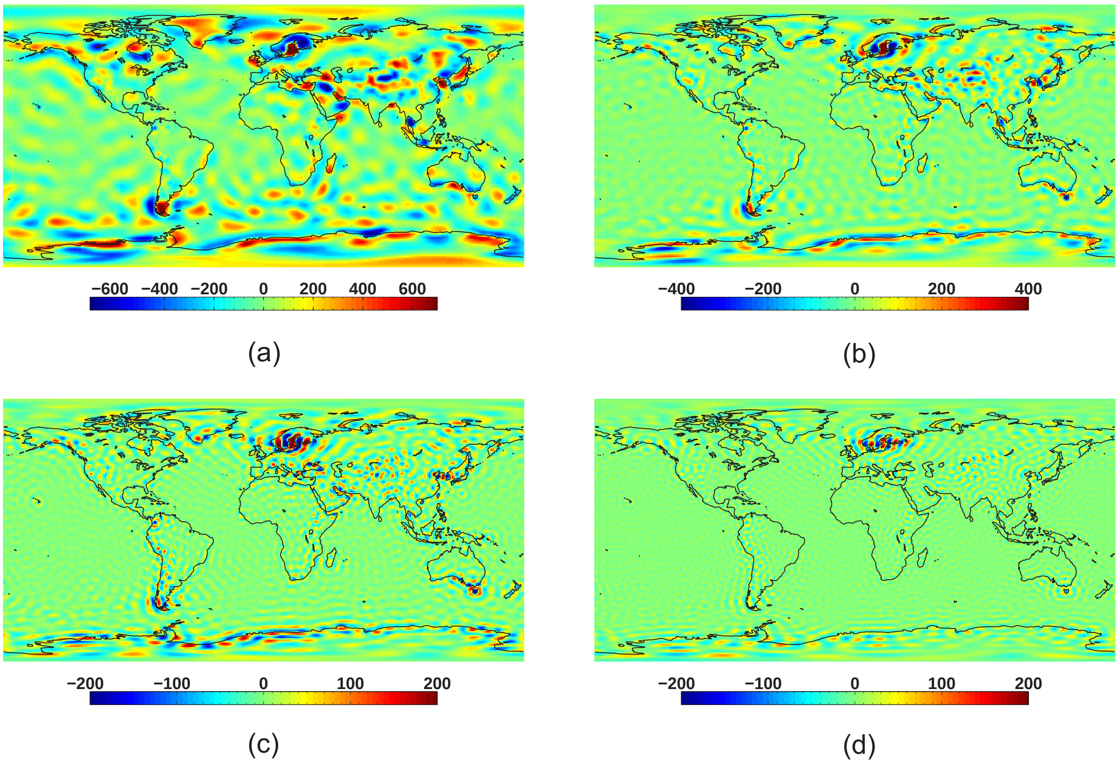

Fig. 8.22: Various maximum d/o for the AOD product and their differences in terms of geoid heights (a) AOD100 - AOD20, (b) AOD100 - AOD40, (c) AOD100 - AOD60, (d) AOD100 - AOD80. 1.08.2007 00h, Unit: μm.

	min	max	mean	rms
AOD100	−8.84	10.42	−0.03	3.30
AOD100 - AOD20	−0.95	2.17	0.00	0.15
AOD100 - AOD30	−0.89	1.69	0.00	0.09
AOD100 - AOD40	−1.00	1.17	0.00	0.06
AOD100 - AOD60	−0.64	0.55	0.00	0.03
AOD100 - AOD80	−0.23	0.26	0.00	0.02

Tab. 8.7: Statistics on the differences between various spectral resolutions of the official AOD product in terms of geoid heights. 01.08.2007. Unit: mm

Impact of different spectral AOD resolutions on a monthly gravity field solution

Only changing the maximum d/o of the AOD product, 5 monthly gravity field (MGF) solutions corresponding to the in Sect. 8.4 introduced AOD scenarios were determined by using the BERNESE gravity field software. Like before, as the computed gravity fields are on the first sight almost identical, the differences with respect to the standard gravity field solution, where the AOD product is used up to d/o 100, are shown in Fig. 8.23 and Tab. 8.8.

	min	max	mean	rms
MGF AOD100 [mm]	-10.09	8.13	0.01	1.51
MGF AOD100 - oAO [mm]	-3.38	2.86	0.00	1.11
MGF AOD100 - AOD20 [μm]	-604.24	554.93	0.59	150.59
MGF AOD100 - AOD40 [μm]	-536.21	420.73	0.58	117.36
MGF AOD100 - AOD60 [μm]	-539.28	423.98	0.58	117.56
MGF AOD100 - AOD80 [μm]	-540.79	424.34	0.58	117.58

Tab. 8.8: Statistics on the differences between various monthly gravity field solutions determined by only changing the maximum degree of the applied AOD product. August 2007.

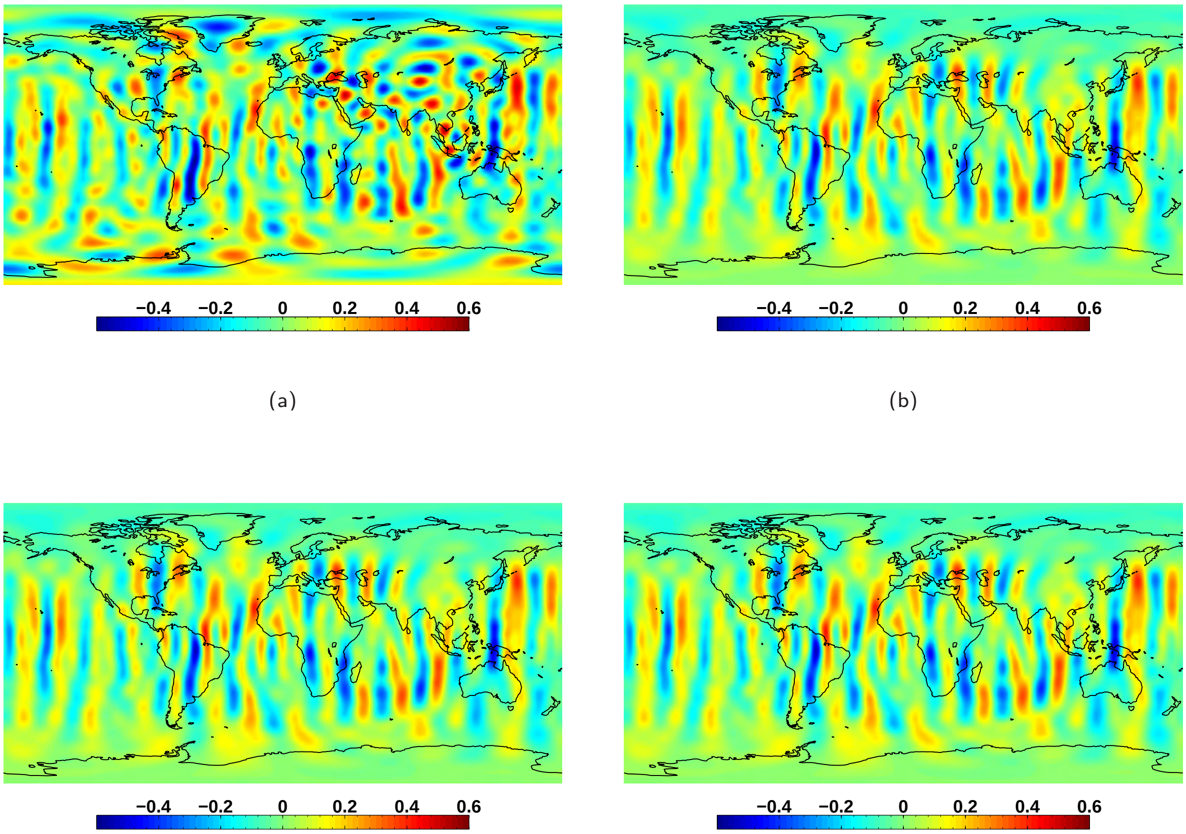

(a)

(b)

(c)

(d)

Fig. 8.23: Monthly gravity field solutions in terms of geoid heights using different maximum d/o for the AOD product.(a) AOD100 - AOD20, (b) AOD100 - AOD40, (c) AOD100 - AOD60, (d) AOD100 - AOD80. August 2007. Unit: μm.

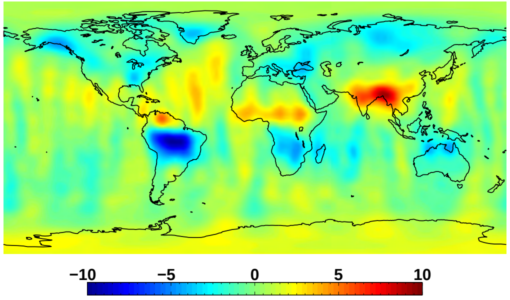

Fig. 8.24: Monthly gravity field solution after applying AOD100. August 2007. Unit: mm.

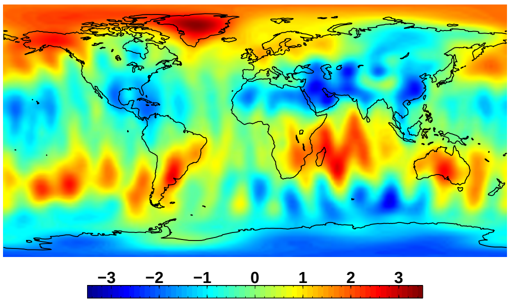

Fig. 8.25: Effect of applying or not applying (oAO) the standard AOD100 on a monthly gravity field solution. August 2007. Unit: mm.

Analyzing Fig. 8.25 and Tab. 8.8, the first issue that can be retained, is that applying or not applying AOD during gravity field determination has an effect of several *mm* on a resulting monthly gravity field solution. Secondly, when analyzing the differences of the monthly gravity field solutions after applying AOD100, AOD80, AOD60, AOD40, and AOD20, it can be observed, that whether the AOD product is applied up to d/o 20 (Fig. 8.23a), up to d/o 40 (Fig. 8.23b), up to d/o 60 (Fig. 8.23c) or up to d/o 80 (Fig. 8.23d), affects a monthly gravity field solution in the sub-*mm*-range. Using either AOD80, AOD60 or AOD40 instead of AOD100 has an effect of maximum 0.54 *mm* on a monthly gravity field solution. Applying AOD only up to d/o 20 instead up to d/o 100 will lead to slightly larger differences of maximum 0.60 *mm*.

Impact of different spectral AOD resolutions on the KBRR-residuals

Figure 8.26 shows the RMS over 1 month of KBRR-residuals in bins of 5° × 5° in longitude and latitude in an Earth-fixed system for the standard AOD100 case. One can see relatively high rms values in the northern Amazon, western Ganges and Zambezi area, which is caused by the unmodelled (or not sufficiently modelled) temporal variations of the gravity field and which can be mainly attributed to hydrology.
Figure 8.27 shows the RMS differences in the KBRR-residuals between applying no AOD product at all and applying the AOD100. Here, we see the total effect of atmospheric and oceanic de-aliasing on the level of KBRR-residual differences. The pattern in Fig. 8.27 should somehow reflect the model applied during gravity field determination if nothing else than the AOD product were changed during gravity field determination. Thus, Fig. 8.27 should reflect the standard AOD100 product being applied during gravity field modelling. To confirm this conclusion, one should have a look at the rms over the same month of the AOD100 coefficients (see Fig. 8.21). Comparing the rms of the AOD100 product in Fig. 8.21 with the effect of AOD on the level of KBRR-residuals in Fig. 8.27, we can see some correlations, e.g. in the Southern hemisphere (Antarctica, South America, oceanic region South-West of South America), but also correlations in the Northern hemisphere (e.g. North-West Asia and the Hudson Bay area). Of course the numerical values of Fig. 8.27 and Fig. 8.21 are not comparable as there is a whole adjustment process in between. However, one should also mention that the applied AOD model is not mapped totally into the KBRR-residuals. As mentioned before (Sect. 8.4), this is probably due to the empirical parameters co-estimated during gravity field determination and absorbing some signal.

The effect of using AOD up to various maximum d/o on the KBRR-residuals is illustrated in Fig. 8.28 and summarized in Tab. 8.9. Like before, the rms of the KBRR-residuals looks pretty similar for the various AOD cut-off frequencies. Therefore, the differences to the standard scenario (AOD100) are illustrated in Figs. 8.28a-d. The first eye-catching issue is the 'striping pattern', which is also reflected in the rms of the KBRR-residuals. The effect on the KBRR-residuals of either using AOD up to d/o 100, d/o 80 (Fig. 8.28d), d/o 60 (Fig. 8.28c) or d/o 40 (Fig. 8.28b) is maximum 0.148 μm/s. Even applying AOD20 instead of AOD100 affects the KBRR-residuals in the same range (cf. Tab. 8.9). However, Fig. 8.28a shows, that AOD20 seems to insufficiently de-alias high-frequent mass variations, as some (atmospheric and oceanic) signal patterns, e.g. in the Himalaya region and polar ocean regions, remain.

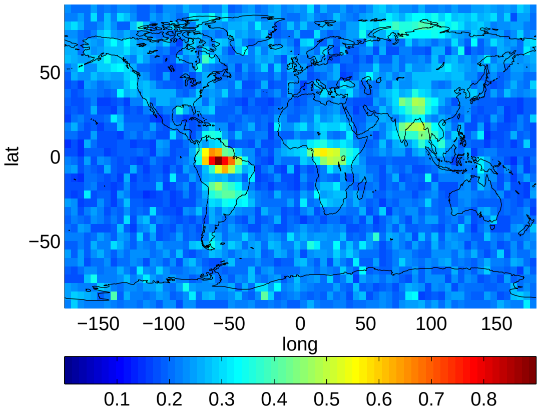

Fig. 8.26: Rms over 1 month (August 2007) of KBRR-residuals in bins of 5° × 5° in longitude and latitude. Standard AOD100 applied up to d/o 100. Unit: µm/s.

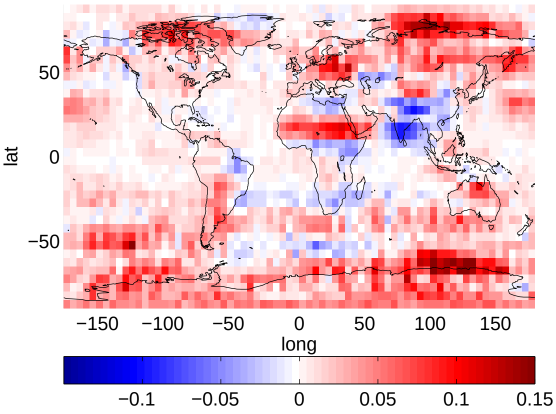

Fig. 8.27: Rms differences over 1 month (August 2007) of KBRR-residuals in bins of 5° × 5° in longitude and latitude. Rms shows the difference between applying (AOD100) and not applying AOD during gravity field processing. Unit: µm/s.

	min	max	mean	rms
KBRR AOD100	0.148	0.894	0.235	0.059
KBRR AOD100 - oAO	−0.198	0.101	−0.016	0.031
KBRR AOD100 - AOD20	−0.032	0.142	0.000	0.008
KBRR AOD100 - AOD40	−0.020	0.148	0.000	0.006
KBRR AOD100 - AOD60	−0.020	0.148	0.000	0.006
KBRR AOD100 - AOD80	−0.020	0.148	0.000	0.006

Tab. 8.9: Statistics on the rms differences of KBRR-residuals determined by changing the maximum degree of the applied AOD product. August 2007. Unit: µm/s.

Figures 8.29 and 8.30 show the amplitude spectra and the differences in the KBRR-residual spectra for the various cases. The amplitudes of the KBRR-residuals as a function of the period are illustrated in Figure 8.29. The magenta line shows the amplitudes after applying the standard AOD100, the black line shows the amplitudes when no AOD at all during gravity field determination has been applied. It can be observed, that in general the amplitudes of the spectral lines are reduced when applying AOD. Like before we can retain also here, that applying AOD is necessary as it has a significant impact on the gravity field solutions as well as on the KBRR-residuals. This is for example clearly illustrated in Fig. 8.31, where it is visible that the residuals are significantly reduced for almost all latitudes.

In Fig. 8.30 the differences between the amplitudes spectra w.r.t. the standard AOD100 casse are shown. The spectra differences are shown instead of the amplitude spectra themselves in order to emphasize the deviations more clearly. As shown in Fig. 8.29, using AOD instead of using no AOD at all (Fig. 8.30, blue) has a significant effect on the KBRR-residuals. One can also see that whether using AOD20 (black), AOD40 (green), AOD60 (magenta) or AOD80 (cyan) instead of AOD100 has hardly any effect on the KBRR-residuals, as the psd differences are of several magnitudes smaller.

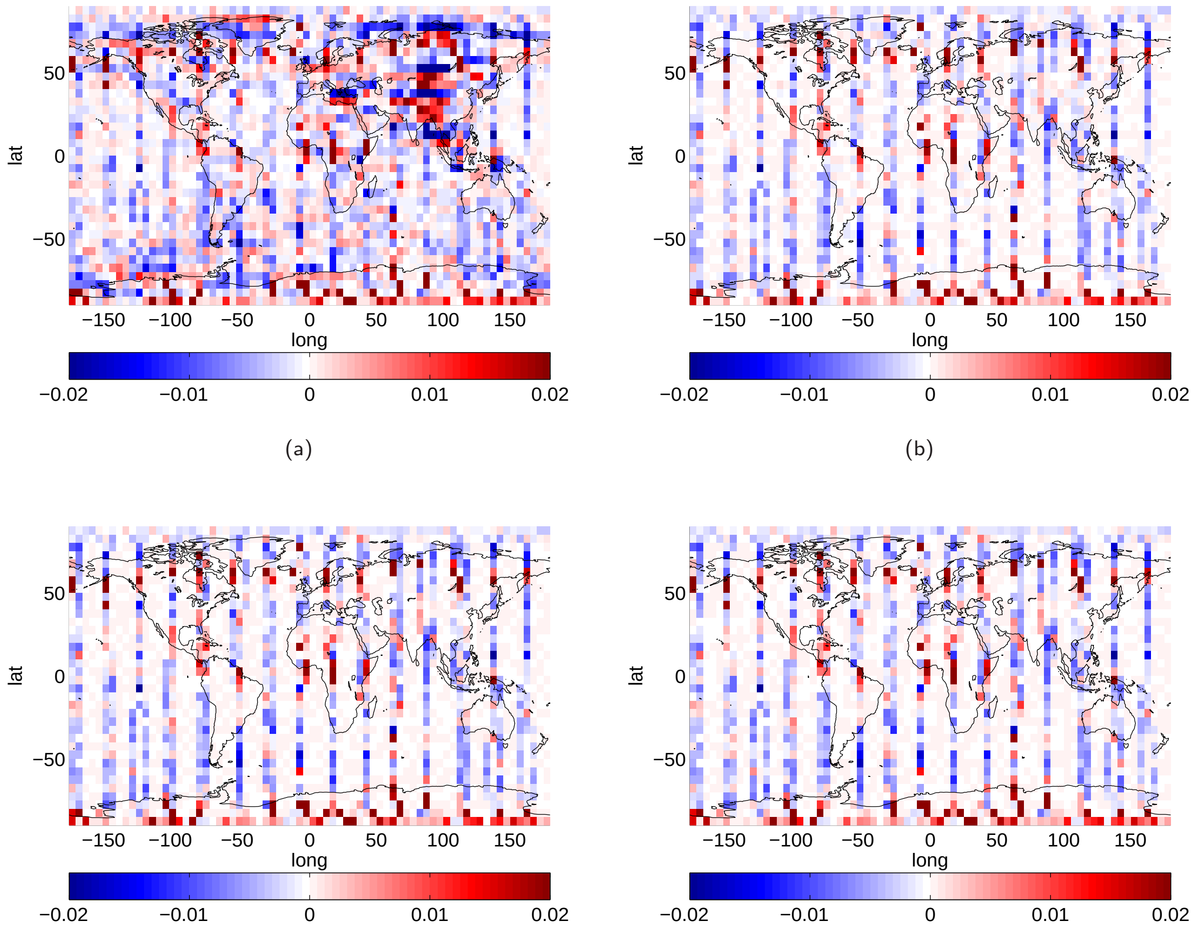

(a) (b)

(c) (d)

Fig. 8.28: RMS differences over 1 month (August 2007) of KBRR-residuals in bins of 5° × 5° in longitude and latitude. (a) AOD100 - AOD20, (b) AOD100 - AOD40, (c) AOD100 - AOD60, (d) AOD100 - AOD80. Unit: μm/s.

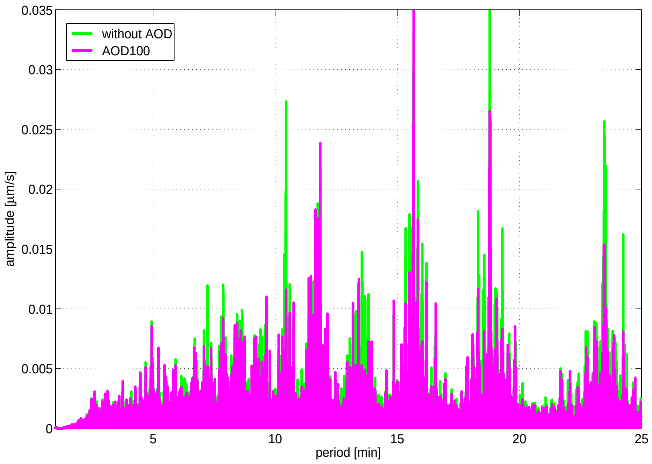

Fig. 8.29: Spectra of one month KBRR-residuals without AOD (green), and after removing the standard AOD product up to d/0 =100 (magenta). August 2007, Unit: μm/s.

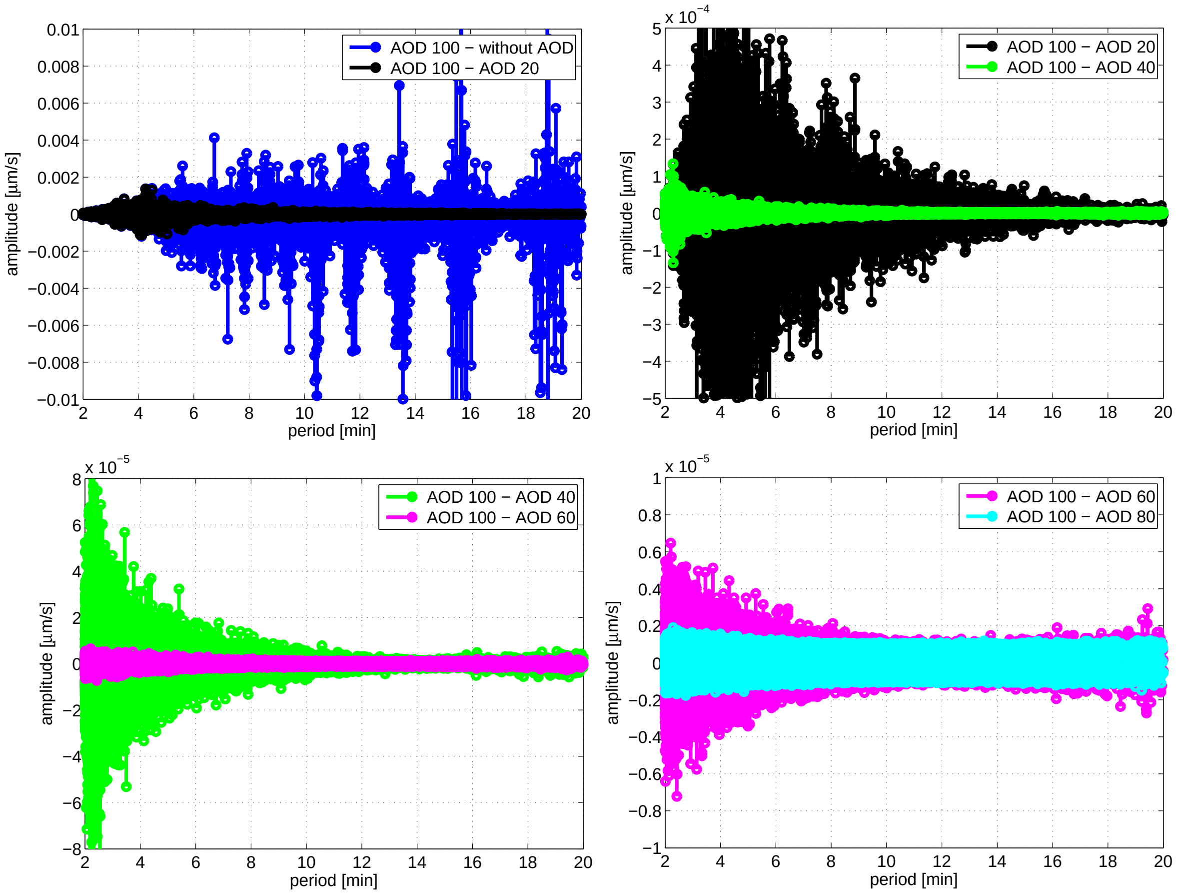

Fig. 8.30: Amplitude spectra differences of one month KBRR-residuals for various maximum AOD degrees. AOD100-without AOD (blue), AOD100-AOD20 (black), AOD100-AOD40 (green), AOD100-AOD60 (magenta), AOD100-AOD80 (cyan). August 2007, Unit: µm/s.

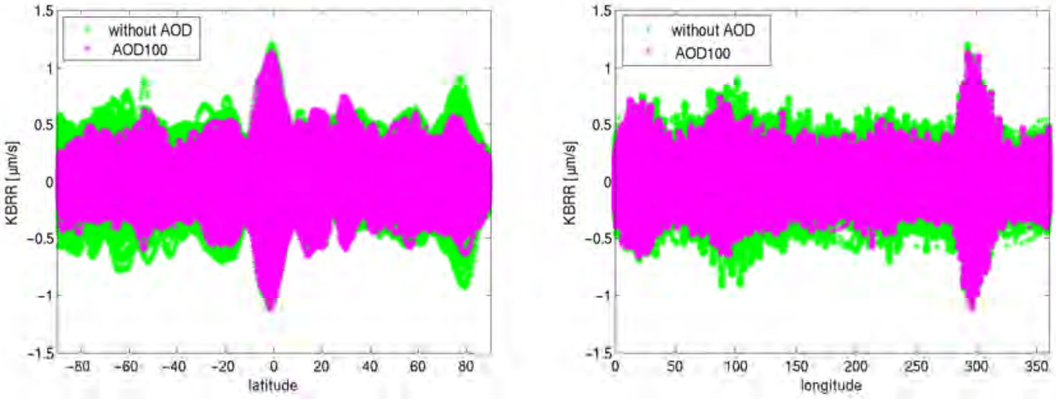

(a) (b)

Fig. 8.31: KBRR-residuals over 1 month (August 2007) plotted against (a) latitude and (b) longitude without AOD (green), and after removing the official AOD product up to d/o = 100 (magenta). Unit: µm/s.

Summary - The impact of AOD depending on the maximum degree

- the main atmospheric and oceanic signal content seems to be covered by the spectral coefficients up to d/o 30 (cf. Fig. 8.18)
- dominating amplitudes of the AOD coefficients: daily, half-daily, 12.425 hours (lunar M2 tide), annual, semi-annual
- effect on the AOD coefficients in terms of geoid heights
  - differences between AOD100 and AOD80, AOD60 are in the sub-mm-range
  - differences between AOD100 and AOD40/AOD20 can reach up to several mm (e.g. 2.2 mm for AOD20)
  - AOD20, AOD40, AOD60, AOD80 cover almost 80%, 88%, 95%, and 98% of the AOD100 signal
- effect on a monthly gravity field solution (MGFS)
  - applying AOD100 or applying no AOD affects a MGFS by several mm
  - AOD100 vs. AOD80/60/40/20 affects a MGFS in the sub-mm-range
- effect on the KBRR-residuals
  - applying AOD100 or applying no AOD affects the rms of KBRR-residuals in the sub-$\mu m/s$-range (min: -0.20 $\mu m/s$, max: 0.10, mean: -0.02 $\mu m/s$, rms: 0.03 $\mu m/s$ for August 2007)
  - AOD100 vs. AOD80/60/40/20 affects rms of the KBRR-residuals in the sub-$\mu m/s$-range (min: -0.03 $\mu m/s$, max: 0.14, mean: 0.00 $\mu m/s$, rms: 0.01 $\mu m/s$ for AOD20)

In summary, we can retain, that for gravity field determination it does not make much difference if the AOD product is applied up to d/o 100, 80, 60, 40 or 20. Concerning the actual or achieved (as opposed to the expected pre-launch) accuracy of gravity field determination with GRACE, it seems to be sufficient to apply the AOD product up to d/o 40 (or even only d/o 20). Nevertheless, AOD has to be applied during gravity field processing, as it has a significant impact on the monthly gravity field solutions as well as on the KBRR-residuals.

8.5. Comparison of the TUM de-aliasing with the official GFZ AOD product

In the following, we compare the official RL04 AOD product provided by GFZ[1] with the de-aliasing product determined by our TUM software, developed and modificated in the course of this thesis. Theoretically, both products should be identical, as the calculation is based on the same equations. Nevertheless, one recognizes some differences, especially in the atmospheric potential when comparing the two products.
While the oceanic potential in both solutions (GFZ vs. TUM) is almost the same (cf. Fig. 8.32b), the atmospheric potential for the TUM solution significantly deviates from the one of GFZ for degrees and orders higher than 25 (cf. Fig. 8.32a). The atmospheric potential determined by TUM seems to contain more signal than the GFZ solution. Having a look at the comparison between the official GFZ de-aliasing coefficients and ours in the spatial domain, one can see, that the differences in the atmospheric potential seem to be - at least partially - correlated with the topography (cf. Fig. 8.33g).

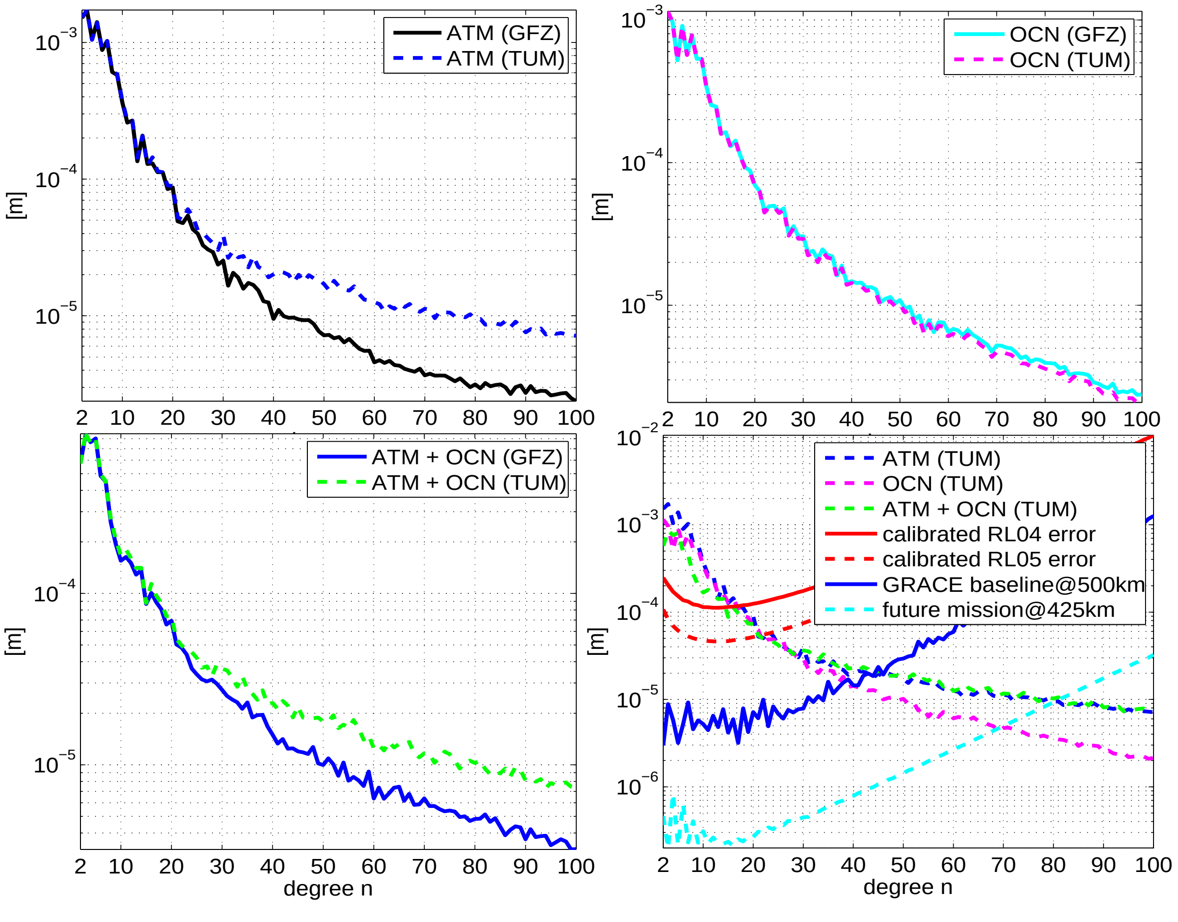

Fig. 8.32: Standard deviations in terms of geoid heights for the atmospheric, oceanic and the combined atmospheric and oceanic potential, 01.08.2007, 00h. Unit: m.

One explanation for the occurring differences could be the following: GFZ is downloading the input parameters needed for de-aliasing on a Gaussian grid (i.e., gridpoints along each latitude are equally spaced, gridpoints along each longitude are unequally spaced) in a resolution of 0.5°. Then the transformation of the Gaussian grids into equidistant 0.5° x 0.5° latitude-longitude grids is performed. Afterwards half-degree block-mean values are determined, and the vertical integration of the atmosphere is performed using Eqs. (3.22), (3.24), (3.25), and (3.26).

---

[1] e.g. available at *isdc.gfz-potsdam.de* under GRACE Products → Orbit And Gravity Field → Level 1B → GX-OG-1B-ATMOCN

	ATM				OCN				ATM+OCN			
	Min	Max	Mean	RMS	Min	Max	Mean	RMS	Min	Max	Mean	RMS
GFZ	-15.12	18.09	-0.01	5.07	-13.62	10.64	-0.07	3.16	-8.84	10.42	-0.03	3.30
TUM	-14.98	18.39	0.19	5.11	-13.61	10.61	-0.08	3.19	-8.74	10.66	-0.11	3.39
GFZ-TUM	-2.26	3.10	-0.20	0.23	-0.18	0.35	0.00	0.05	-2.16	3.19	-0.13	0.24

Tab. 8.10: Statistics on the differences between the official GFZ and the TUM AOD de-aliasing product in terms of geoid heights. 01.08.2007, 00h. Unit: mm.

TUM in contrast directly downloads from ECMWF the input parameters on an equidistant latitude-longitude grid with a resolution of only 1° x 1°. The procedures of building block-mean values and the applied formulas for the vertical integration should be the same as those GFZ is using. This lets us assume that the differences between the atmospheric de-aliasing coefficients are probably mainly due to the transformation from Gaussian grids to equidistant grids as well as due to the different spatial resolution of the input data. This assumption seems to be partly confirmed when comparing the geopotential heights, downloaded by GFZ on a Gaussian grid and transformed into an equidistant grid, with the geopotential heights downloaded directly on the equidistant latitude-longitude grid. In Fig. 8.34 differences of up to 3 km (mean: 0.9 m, rms: 141 m) in the geopotential height occur and are strongly correlated with the topography.

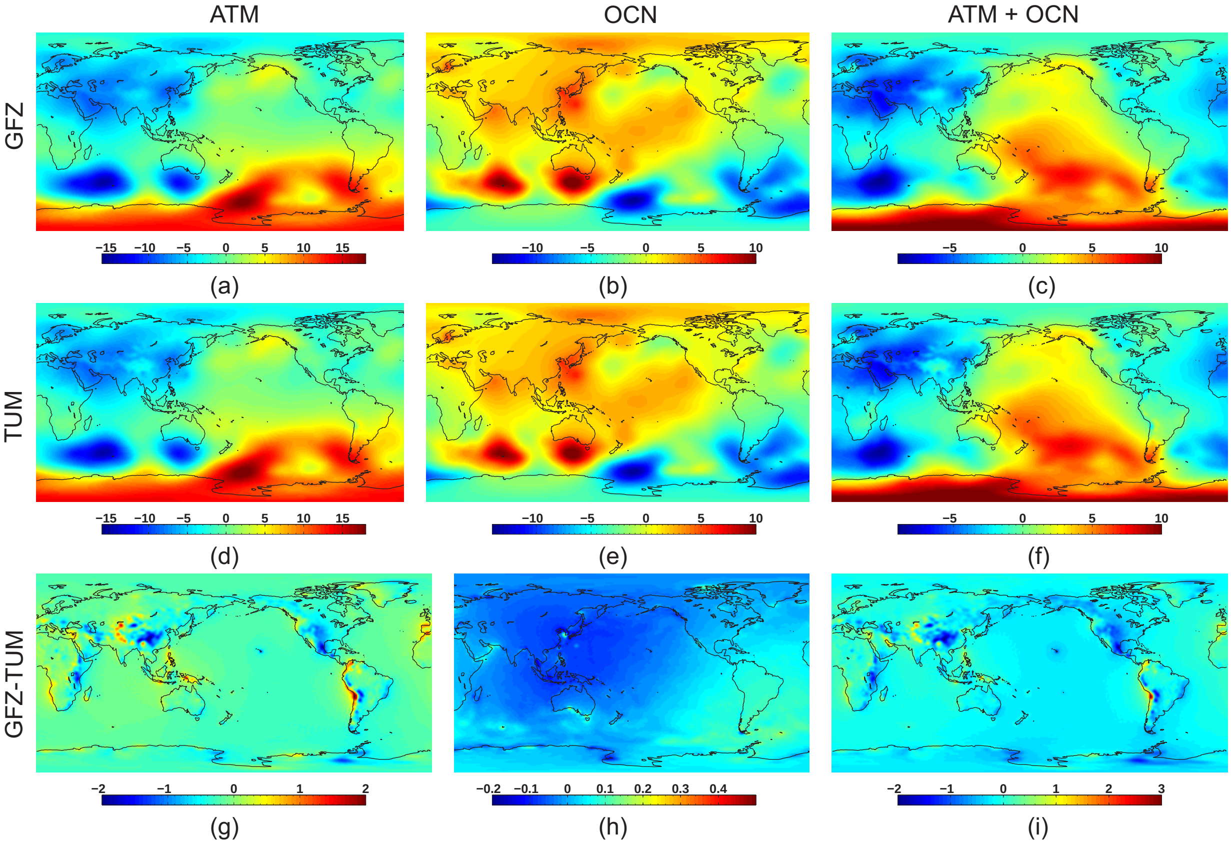

Fig. 8.33: Atmospheric ((a),(d)), oceanic ((b),(e)) and combined atmospheric & oceanic de-aliasing coefficients ((c),(f)) from GFZ and TUM and their differences ((g)-(i)) in terms of geoid heights, 01.08.2007, 00h. Unit: mm.

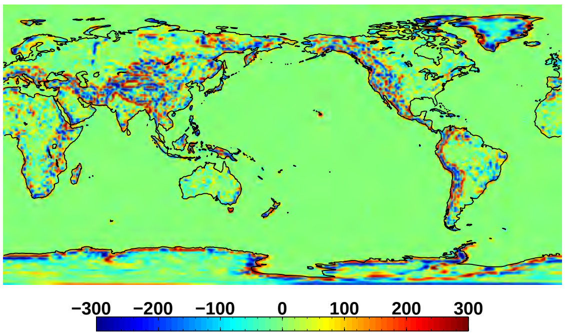

Fig. 8.34: Geopotential height differences between GFZ (after transforming the Gaussian grid into an equidistant latitude-longitude grid) and TUM (directly downloading the equidistant latitude-longitude grids), 01.08.2007, 00h. Unit: m.

Impact of GFZ and TUM de-aliasing product on a monthly gravity field solution

Either applying the GFZ or the TUM AOD coefficients up to d/o 100 affects a monthly gravity field solution with maximum 1.73 *mm* for August 2007 (cf. Tab. 8.11). Comparing Fig. 8.35c with Fig. 8.33i, some 'inverse correlation patterns' can be clearly recognized. Again, the correlations demonstrate that the differences in the AOD coefficients are propagated further to the monthly gravity field solutions. As there is a whole parametrization process in between the AOD product and the determination of monthly gravity field solutions, the maximum, minimum, and mean amplitudes of the differences are damped (cf. Tabs. 8.10 and 8.11). While the effect of GFZ vs. TUM on AOD level has a mean global effect of -0.13 *mm*, it has almost no impact on the monthly gravity field solution level (0.17 *mm*), although the maximum and minimum differences can reach up to several millimeters.

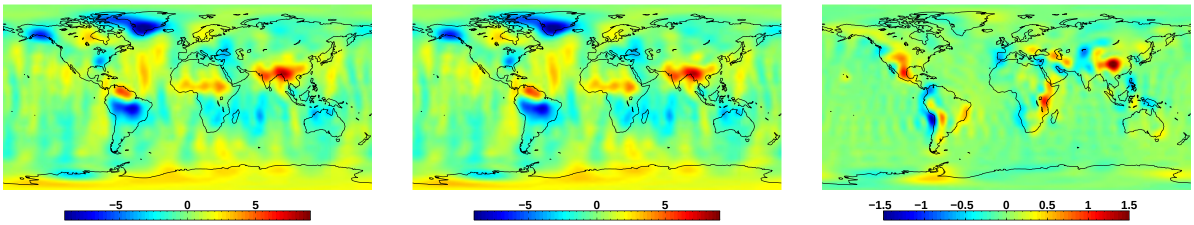

(a) GFZ (b) TUM (c) GFZ-TUM

Fig. 8.35: Monthly gravity field solutions after subtracting the (a) GFZ, (b) TUM AOD product and (c) their differences. August 2007. Unit: mm.

	min	max	mean	wrms
GFZ	-10.09	8.13	0.01	1.51
TUM	-10.00	8.09	0.01	1.52
GFZ - TUM	-1.46	1.73	0.00	0.17

Tab. 8.11: Statistics on the monthly gravity field solutions after subtracting the GFZ and TUM AOD product. August 2007. Unit: mm.

Impact of GFZ and TUM de-aliasing product on the KBRR-residuals

The impact of the two AOD versions on the KBRR-residuals is shown in Fig. 8.36. On the daily rms of the KBRR-residuals (Fig. 8.36a) hardly any impact of either using the GFZ (green) or TUM (black) solution can be observed. This is reflected in the mean daily rms, which is affected by only 0.6 nm/s (0.2372 μm/s for GFZ vs. 0.2378 μm/s for the TUM solution).

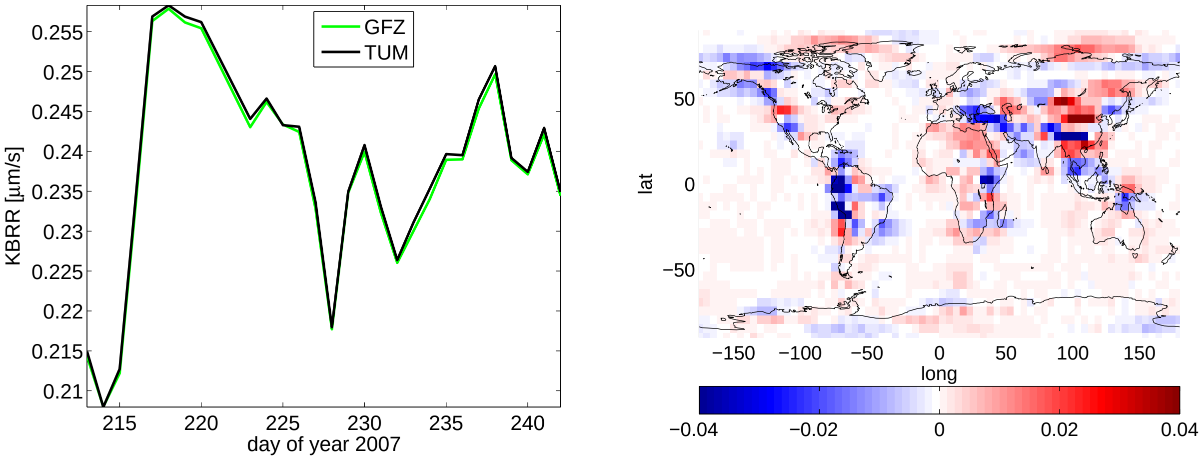

(a) (b)

Fig. 8.36: (a) Daily rms of KBRR-residuals after removing the GFZ-AOD (green) and TUM-AOD (black). (b) Rms differences between GFZ and TUM-approach over 1 month of KBRR-residuals in bins of $5° \times 5°$ in longitude and latitude. August 2007. Unit: μm/s.

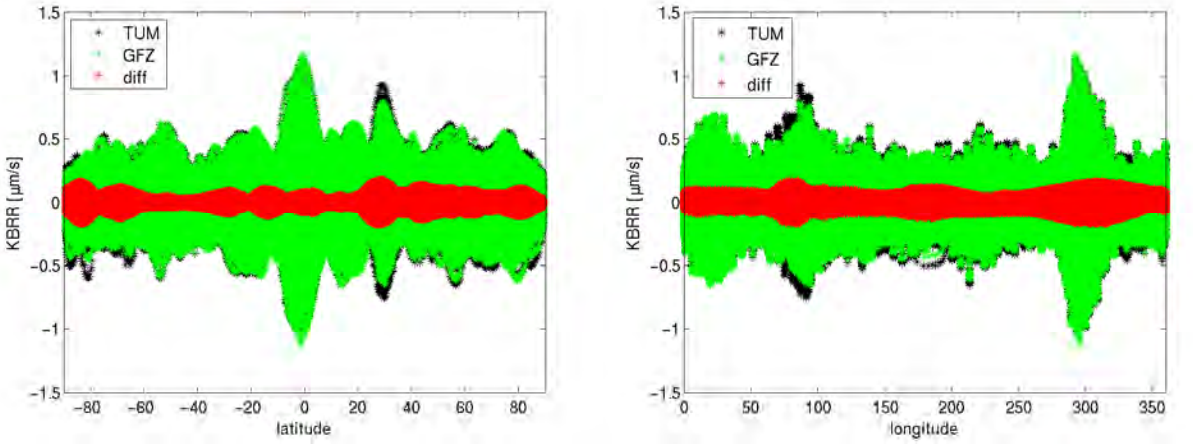

(a) (b)

Fig. 8.37: KBRR-residuals for August 2007 against (a) latitude and (b) longitude after removing GFZ AOD (green), TUM AOD (black) and their differences (red). Unit: μm/s.

Examining the rms over 1 month of KBRR-residuals as a function of latitude and longitude in an Earth-fixed system (Fig. 8.36b), one can state, that the TUM product compared to the GFZ solution leads to slightly higher (and in the course of gravity field determination worse) rms in the Norther Andes, in the central part of the Himalaya as well as in South Europe (cf. blue regions in Fig. 8.36b). Though, over the ocean, as well as in the Northern polar regions, TUM seems to lead to slightly better results or smaller rms (cf. red color in Fig. 8.36b). The small regional differences are also reflected in the KBRR-residuals plotted against latitude and longitude (Fig. 8.37). Nevertheless, the differences between the GFZ and TUM solutions on the level of KBRR-residuals are pretty small (min: -0.10 μm/s, max: 0.05 μm/s, mean: 3.34 nm/s, rms: 0.01 μm/s).

Summary - Comparison of the TUM de-aliasing with the official GFZ AOD product

- GFZ downloads the input parameters on a 0.5° x 0.5° Gaussian grid and transforms them to an equidistant latitude-longitude grid, while TUM directly downloads them on an equidistant 1° x 1° grid. A comparison between the geopotential height transformed from Gaussian grid into equidistant latitude-longitude grid with the geopotential heights downloaded on the equidistant latitude-longitude grid reveals significant differences of up to 3 km, which are strongly correlated with the topography
- the vertically integrated atmospheric part (ATM) of the de-aliasing coefficients for GFZ and TUM solution significantly deviate for degrees $n > 20$. Differences of up to 3.1 mm, especially in regions with rough topography, appear. This is supposed to be due to the transformation from Gaussian grid to equidistant grid and due to the different spatial resolution used (see first item)
- in contrast, the oceanic part (OCN) in both solutions fits much better. Here, only differences of up to 0.35 mm appear, probably due to the different spatial resolution
- the combined atmospheric and oceanic de-aliasing coefficients (ATM+OCN) deviate by several mm (min: -2.16 mm, max: 3.19 mm, mean: -0.13 mm, rms: 0.24 mm)
- whether using the GFZ or TUM solution affects a monthly gravity field solution in the mm-range (min: -1.46 mm / max: 1.73 mm / mean: 0.00 mm / rms: 0.17 mm)
- the effect on the daily rms of KBRR-residuals is hardly visible and is in the sub-nm/s-range (0.2378 μm/s for TUM vs. 0.2372 μm/s for GFZ solution)
- the effect on the rms of KBRR-residuals over 1 month in the sub-$\mu m/s$-range (max: 0.1 $\mu m/s$, mean: 0.3 nm/s, rms: 0.01 $\mu m/s$). Slightly better performance of the GFZ solution in the Andes, South Europe and Himalaya regions. Slightly better performance of the TUM solution over the oceans and Northern polar regions

This section has shown, that there is still room for improvement on both the GFZ and TUM side. Further investigations have to be made, in order to identify the strengths and weaknesses of both solutions and to work out further probably reasons for the differences between the two de-aliasing products.

9. The impact of atmospheric and oceanic model errors on AOD and GRACE

As the standard de-aliasing processing scheme assumes error-free atmospheric and oceanic parameters, and as it is well known that in areas with sparse observations the atmospheric models are degraded in quality (*Salstein et al.*, 2008), there is some motivation to assume, that by taking into account uncertainties of the atmospheric and oceanic model parameters one could improve the de-aliasing product and consequently the gravity field solutions.

This chapter is dealing with the impact of model uncertainties on the de-aliasing coefficients as well as on the gravity field determination from GRACE. Most of the results are summarized in *Zenner et al.* (2010), *Zenner et al.* (2012a) and *Zenner et al.* (2012b). The following chapters will give a more detailed analysis of this topic.

9.1. Defining various error scenarios

In order to answer the question whether uncertainties in the atmospheric pressure and ocean bottom pressure affect the atmospheric and oceanic de-aliasing coefficients (AOD) and subsequently GRACE gravity field results, we performed three error scenarios:

case 1: Without atmospheric and oceanic errors, corresponding to the standard GRACE product (AOD1B)

case 2: 6-hourly surface pressure errors from ECMWF, daily ocean bottom pressure errors derived from FESOM model

case 3: As case 2, but surface pressure errors from the difference ECMWF-NCEP (yearly rms 2007)

The case 1 is the error-free scenario. Error-free in this sense means that no stochastic model for the atmospheric and oceanic errors is introduced. According to the nomenclature, introduced in Sect. 4, case 1 assumes that all observations P_{AO} have the same weights, and the case 2 + 3 scenarios assume that the observations P_{AO} are weighted individually using $1/\sigma^2_{P_{AO}}$ on the diagonal of the weighting matrix. As described in Sect. 4, the observations P_{AO} are the combined atmospheric and oceanic pressure values and $\sigma_{P_{AO}}$ are the corresponding uncertainties. Besides the error of the ocean bottom pressure, only the surface pressure error is considered in the case 2 and case 3 error scenarios. This is done, as the surface pressure error is the dominating error source (see Sect. 9.2 and *Zenner et al.* (2010)).

9.2. Model uncertainties propagated to the vertically integrated atmospheric pressure

In this Section, the dominating error parameters of the atmospheric model are identified, and the reason for the choice of the three error scenarios is shown. Furthermore, the observations P_{AO} and uncertainties $\sigma^2_{P_{AO}}$ of the three error cases are discussed.

It is possible to determine the error σ_{I_n} of the vertically integrated atmospheric pressure resulting from uncertainties in the input parameters temperature T (temp), specific humidity S (shum), surface pressure P_s (sfcp), and surface geopotential height H_s (geoph) by using Eqs. (4.2) to (4.5). In order to identify the dominating error parameters of the atmospheric model, the uncertainties of the atmospheric parameters and their propagation are treated individually.

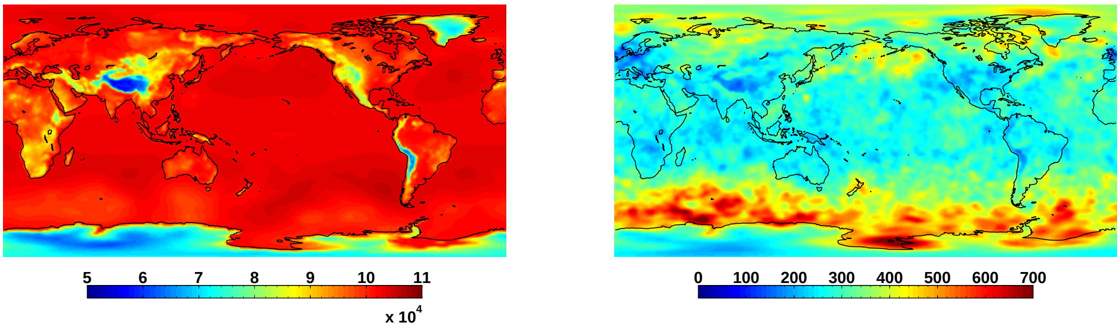

(a) total atmospheric pressure I_n

(b) σ_{I_n} due to surface pressure error

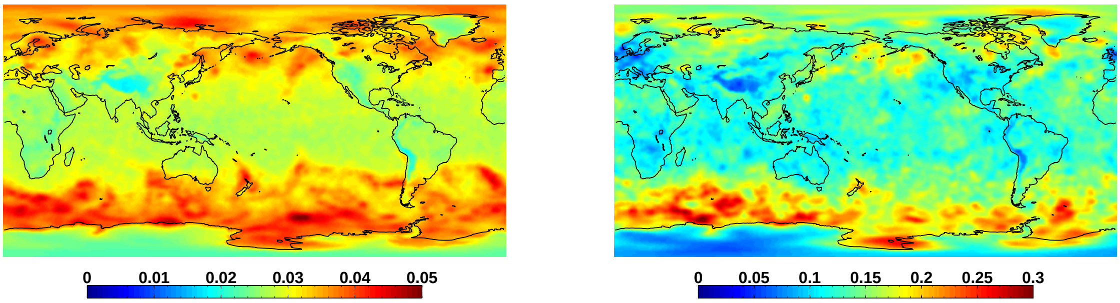

(c) σ_{I_n} due to temperature error

(d) σ_{I_n} due to geopotential height error

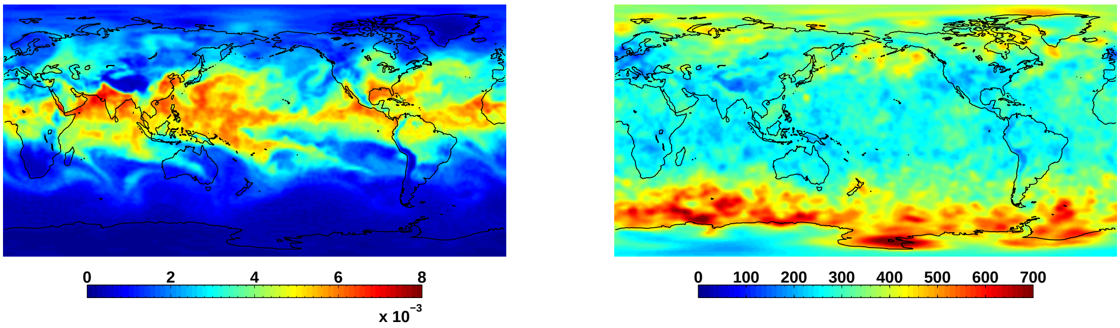

(e) σ_{I_n} due to specific humidity error

(f) σ_{I_n} due to all parameter errors

Fig. 9.1: Vertically integrated atmospheric pressure I_n (a) and the error σ_{I_n} of the vertical integral due to uncertainties in the four input parameters (b-f), Unit: Pascal, $n = 10$, 01.08.2007 00h.

First, we used the case 2 error maps for surface pressure as well as errors in the analysis, provided by ECMWF, for the remaining atmospheric input parameters. A discussion on the used error maps can be found in Sect. 5.2.

Figure 9.1 and Tab. 9.1 give insight into the impact of each atmospheric input parameter, or, to be more precise, the impact of uncertainties in each input parameter (Figs. 9.1b-f) on the vertically integrated atmospheric pressure I_n (Fig. 9.1a). The results are shown for degree $n = 10$. The general pattern and the conclusions which are drawn in the following are valid for each degree $n >= 2$. Basically, only the values in Fig. 9.1 are slightly increasing or decreasing for higher or lower degrees n because of the degree dependency of I_n and σ_{I_n} (cf. Eq. (4.5)). It can be recognized that uncertainties in the specific humidity (Fig. 9.1e), temperature (Fig. 9.1c) and geopotential height (Fig. 9.1d) have only very small effects on the vertical integral I_n with maxima of 0.008 Pa, 0.05 Pa, and 0.3 Pa respectively. Uncertainties in the surface pressure (Fig. 9.1b and Fig. 9.2b), on the other hand, have by far the largest effect of up to almost 750 Pa on the vertical integral I_n. It can be shown that whether the uncertainties are taken into account or not affects the pressure vertically integrated atmospheric pressure I_n in the range of 93 to 745 Pa or, equivalently, 9 to 76 mm water column, which is on average about 0.7 % of the total vertically integrated atmospheric pressure (Fig. 9.1a) or about 7 % of the residual vertical integrated atmospheric pressure (Fig. 9.2a). Comparison of Fig. 9.1b with Fig. 9.1f shows that the effect of uncertainties in only the surface pressure and the effect of uncertainties in all four input parameters is virtually and (almost statistically) the same. This in turn implies that the error of the vertically integrated atmospheric pressure I_n is dominated by the uncertainty of the surface pressure P_s, and the errors in temperature, specific humidity, and geopotential height are almost negligible. On the basis of these results, the pre-defined error scenarios were created. The main focus lies on the surface pressure uncertainty, as it is the dominating error-source. For this reason, various surface pressure uncertainties are investigated within this work (cf. Sect. 5.2). The errors of the other atmospheric input parameters are not decisive for the error of the vertically integrated atmosphere. Therefore, for these parameters no alternative error-maps are used as the ones provided by ECMWF.

Using the rather pessimistic (in comparison to the surface pressure error provided by ECMWF) surface pressure errors derived from the NCEP/ECMWF model differences has an effect on the vertical integral I_n of up to 39 hPa (Fig. 9.2c) or, equivalently, 40 cm water column, which on average is about 3 % of the total vertically integrated atmospheric pressure or about 30 % of the residual atmospheric pressure. As the NCEP/ECMWF surface pressure differences are larger than the surface pressure error provided by ECMWF, also the propagated error of the vertical integrated atmospheric pressure σ_{I_n} is larger in consequence. Furthermore, it can be clearly observed for both cases 2 and 3, that the error patterns of the introduced uncertainties are propagated almost one-to-one into the error of the vertically integrated atmospheric pressure. (cf. Fig. 9.2b & Fig. 5.11 and Fig. 9.2c & Fig. 5.12 in Sect. 5.2).

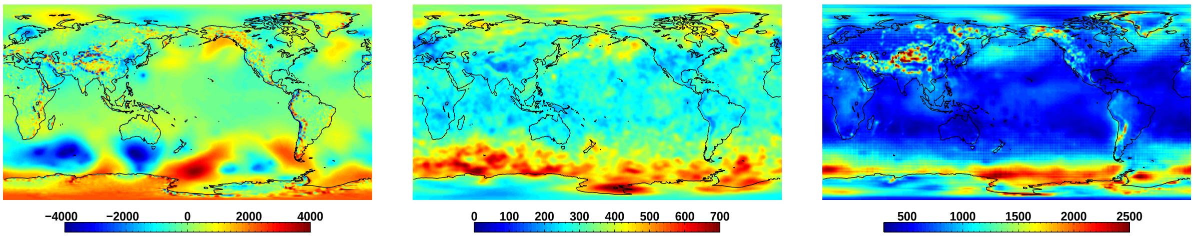

(a) residual atmospheric pressure I_n (b) σ_{I_n} for case 2 (c) σ_{I_n} for case 3

Fig. 9.2: Error σ_{I_n} of the vertical integrated atmospheric pressure I_n, 01.08.2007 00h, $n = 10$. Unit: Pascal.

	Min	Max	Mean	wRMS
total atm. pressure I_n	55406.93	105560.78	100301.14	6437.45
residual atm. pressure I_n	−8176.54	7153.80	−10.74	912.96
σ_{I_n} due to temp error	0.02	0.05	0.03	0.01
σ_{I_n} due to geoph error	0.04	0.30	0.14	0.03
σ_{I_n} due to shum error	0.00	0.01	0.00	0.00
σ_{I_n} due to all errors	93.40	745.17	314.79	82.01
σ_{I_n} due to sfcp error (case 2)	93.40	745.17	314.79	82.01
σ_{I_n} due to sfcp error (case 3)	296.09	3918.10	793.86	2359.07

Tab. 9.1: Statistics on the vertically integrated atmospheric pressure I_n and the error σ_{I_n} of the vertical integral due to uncertainties in the four input parameters, $n = 10$, 01.08.2007 00h, Unit: Pascal.

In a next step, by applying Eq. (4.6), the error of the vertically integrated atmosphere σ_{I_n} is combined with the ocean bottom pressure error σ_{P_O} (Fig. 9.3b, Sect. 6.2) to $\sigma^2_{P_{AO}}$ (Fig. 9.4b,c). The weighting matrix for the least-squares adjustment can now be set up by using $1/\sigma^2_{P_{AO}}$ on the main diagonal. Before the least-squares adjustment can be performed, also the residual atmospheric pressure I_n (Fig. 9.2a) and the residual ocean bottom pressure P_O (Fig. 9.3a) have to be combined according to Eq. (4.6) in order to get the observations P_{AO} (Fig. 9.4a).

The question that now arises is: Do the uncertainties in the combined atmospheric and oceanic pressure of up to 54 hPa for case 2 and 3 significantly affect AOD and GRACE results?

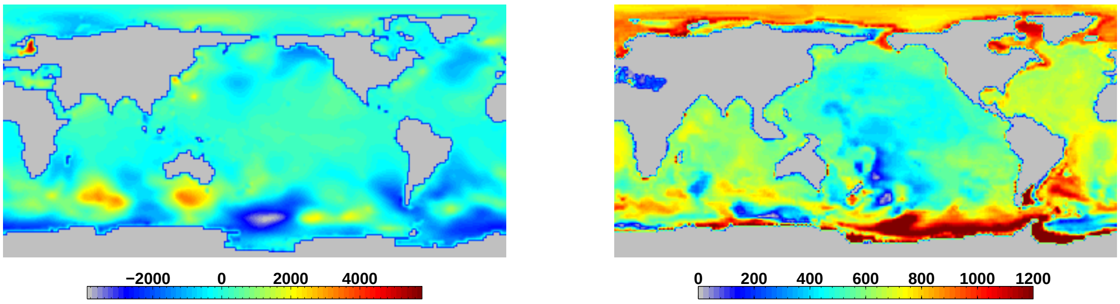

(a) residual ocbpr P_O (b) σ_{P_O}

Fig. 9.3: (a) Residual ocean bottom pressure (ocbpr) P_O and (b) the corresponding ocbpr error $\sigma_{P_{AO}}$, 01.08.2007 00h, Unit: Pascal.

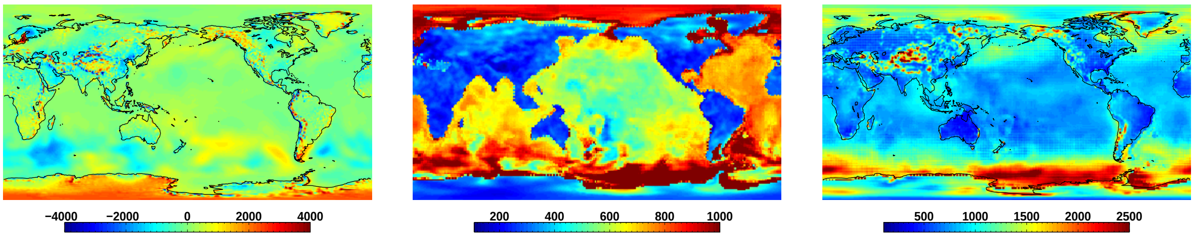

(a) P_{AO} combined pressure (b) $\sigma_{P_{AO}}$ for case 2 (c) $\sigma_{P_{AO}}$ for case 3

Fig. 9.4: Combined atmospheric and oceanic pressure P_{A0} and the corresponding error $\sigma_{P_{AO}}$ for (b) case 2 and (c) case 3, 01.08.2007 00h, n=10. Unit: Pascal.

	Min	Max	Mean	wRMS
combined pressure P_{AO}	−8214.68	5659.03	−10.59	646.68
$\sigma_{P_{AO}}$ case 2	108.94	5262.11	589.56	277.72
$\sigma_{P_{AO}}$ case 3	317.92	5364.29	967.28	377.37

Tab. 9.2: Statistics on the combined (residual) atmospheric and oceanic pressure P_{AO} and the corresponding error $\sigma_{P_{AO}}$ for case 2 and case 3, 01.08.2007 00h, $n = 10$, Unit: Pascal.

9.3. Impact of model uncertainties on the AOD coefficients and GRACE data analysis

In order to answer this question the least-squares adjustment for these scenarios is performed, and three sets of AOD products are obtained. Figure 9.5 shows the differences between the case 1, case 2 and case 3 AOD products in terms of geoid heights. Having a look at Tab. 9.3 one can see, that the effect in terms of geoid heights of 6-hourly ECMWF surface pressure uncertainties and daily ocean bottom pressure errors (case 2) is in the range of -0.95 to 1.18 *mm* with an rms of 0.15 *mm* (cf. Fig. 9.5a). Comparing Fig. 9.5a and Fig. 5.11 in Sect. 5.2, one can retain that mainly the error is reflected in the differences, as the weighting is the only deviation between the two error cases. Larger differences appear in regions where the weights for the observations are extreme (e.g., Himalaya region or region South-West of Africa). Using the rather pessimistic surface pressure errors from NCEP/ECMWF differences (case 3) leads to about 2-3 times larger values of min -3.05, max +0.61 and rms 0.7 *mm*. Again the distribution of the differences reflect the used NCEP/ECMWF differences (cf. Fig. 9.5b and Fig. 5.12 in Sect. 5.2).

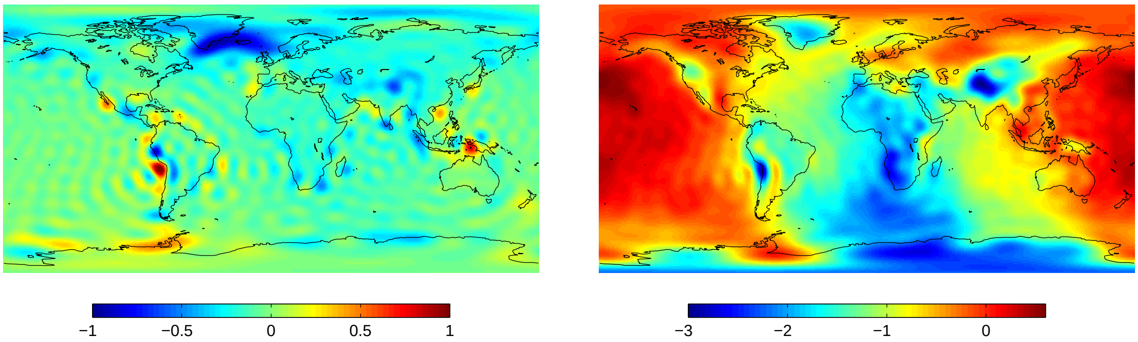

(a) case 1 - case 2

(b) case 1 - case 3

Fig. 9.5: Differences between the case 1, case 2 and case 3 AOD products in terms of (a) + (b) geoid heights. Unit: mm. August 2007.

	min	max	mean	wrms
case 1	−6.03	5.90	0.37	2.61
case 2	−5.84	5.94	0.47	2.58
case 3	−4.66	5.91	1.12	2.09
case 1 - case 2	−0.95	1.18	−0.09	0.15
case 1 - case 3	−3.05	0.61	−0.75	0.75

Tab. 9.3: Statistics on the case 1/2/3 AOD coefficients and their differences in terms of geoid heights. August 2007. Unit: mm.

Inspecting the degree standard deviations of the AOD differences (Fig. 9.6) between the three error scenarios, one can state that with respect to the GRACE baseline (blue dotted line) the effect of atmospheric and oceanic model uncertainties (black and magenta lines) is clearly in the sensitivity range of GRACE and GRACE Follow-on (black-dotted line). Regarding the current (calibrated GFZ RL04) GRACE error (green line) only case 3 (magenta), that is the rather pessimistic surface pressure error map from NCEP/ECMWF differences, will affect GRACE results. As the magenta line is 'above' the current GRACE error budget - at least for the very long wavelengths - one can expect an effect in the gravity field solution as well.

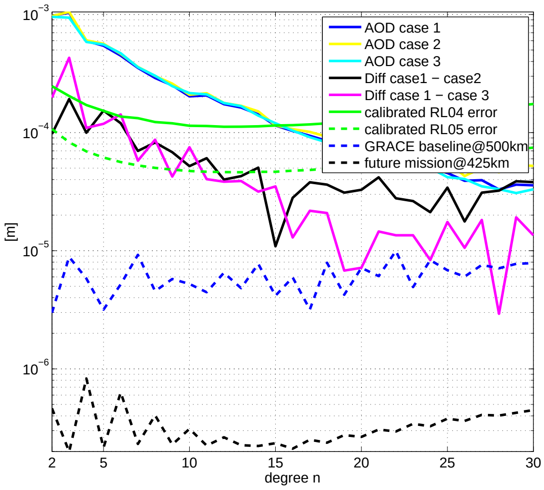

Fig. 9.6: Differences between the case 1, case 2 and case 3 AOD products in terms of degree standard deviations for geoid heights. Unit: m, August 2007.

Impact of model uncertainties on a monthly gravity field solution

Figure 9.7 shows the difference between case 1, case 2 and case 3 in the resulting gravity field solution. Comparing Figs. 9.7a and 9.5a, as well as, Figs. 9.7b and 9.5b, we can note that ΔAOD propagates almost one-to-one into (regional) geoid changes. For case 1, the minimum, maximum and rms values for the output signal are -1.35, 0.95 and 0.17 *mm* (cf. Fig. 9.7a). Using the rather pessimistic surface pressure errors from the NCEP/ECMWF model difference leads - like the AOD differences - to about 2-3 times larger values of -1.29, 2.32 and 0.4 *mm* in the resulting geoid height differences (cf. Fig. 9.7b).

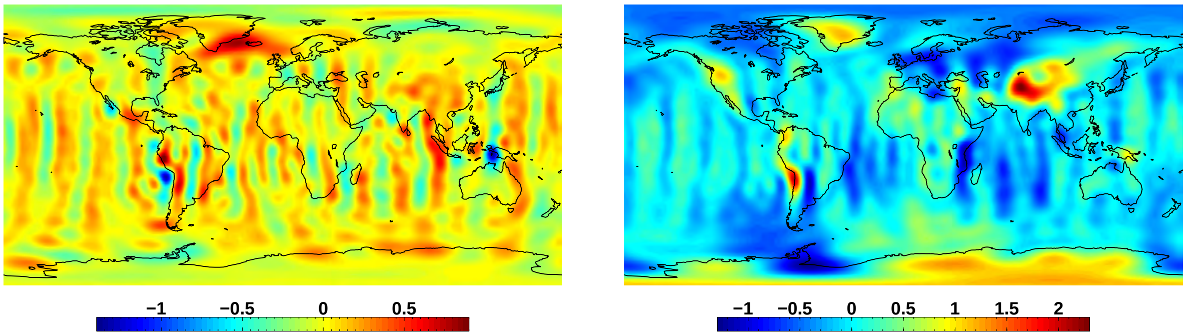

(a) case 1 - case 2 (b) case 1 - case 3

Fig. 9.7: Differences between the case 1, case 2 and case 3 monthly gravity field solutions. August 2007. Unit: mm.

	min	max	mean	wrms
case 1	-9.58	9.10	0.01	1.50
case 2	-9.48	8.93	0.01	1.51
case 3	-9.61	9.10	0.01	1.49
case 1 - case 2	-1.35	0.95	$2.37e-4$	0.17
case 1 - case 3	-1.29	2.32	$1.36e-3$	0.40

Tab. 9.4: Statistics on the case 1/2/3 monthly gravity field solutions and their differences in terms of geoid heights. 01.08.2007. Unit: mm.

Impact of the model errors on the KBRR-residuals

In a next step, we analyze the KBRR-residuals as an intermediate result during gravity field modelling. Reduced KBRR-residuals are one indication for an improved gravity field modelling. Analyzing the differences in the global rms over 1 month of KBRR-residuals (cf. Fig. 9.8b,c), we can state, that again the introduced error maps are reflected in the rms differences, although the differences are very small and only in the sub-μm range (cf. Tab. 9.5). Figure 9.8a illustrates the rms of KBRR-residuals after removing the standard error-free AOD. Relatively high rms values can be observed in the Amazon, Ganges, and Zambezi area, which is caused by the unmodelled temporal variations of the gravity field, and which can mainly be attributed to hydrology (but also to post-glacial rebound and ice melting).

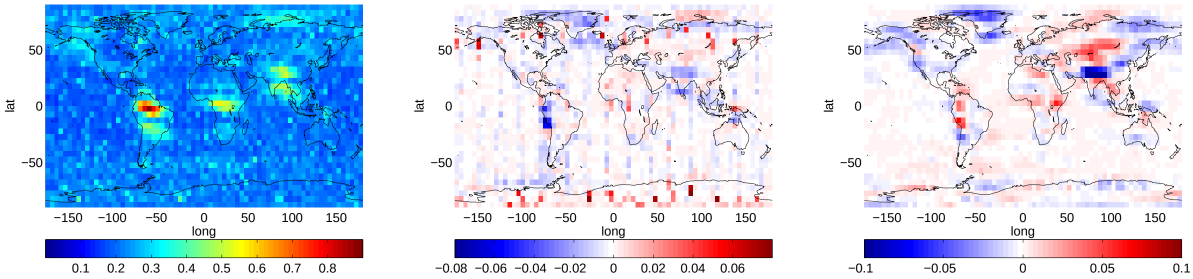

(a) case 1 (b) case 1 - case 2 (c) case 1 - case 3

*Fig. 9.8: Rms over 1 month (Aug 2007) of KBRR-residuals in bins of 5° × 5° in longitude and latitude.
(a) case 1, (b) rms differences between case 1 and case 2, (c) rms differences between case 1 and case 3. Unit: μm/s.*

Regarding the KBRR-residual differences in longitude/latitude bins of 5° × 5° (Fig. 9.9), again one can see that the effect of case 2 and case 3 w.r.t. case 1 is in the sub-μm-range. It seems to be, that regions where case 2 and 3 can improve the KBRR-residuals (red) are pretty balanced with regions where case 1 delivers better (smaller) residuals. Especially for case 3, one can observe several improvements/reductions in the KBRR-residuals (cf. red color in Figs. 9.9d,e,f), for instance in some Asian regions and areas North-East of Scandinavia as well as in some near polar oceanic regions. However, also areas where the case 2 and case 3 AOD products lead to larger residuals exist, like some near-coastal regions of the Antarctica, as well as South and North of Greenland.

	min	max	mean	wrms
case 1	0.148	0.887	0.236	0.060
case 2	0.151	0.894	0.238	0.061
case 3	0.148	0.890	0.238	0.062
case 1 - case 2	−0.077	0.149	−0.002	0.008
case 1 - case 3	−0.135	0.068	−0.002	0.014

Tab. 9.5: Statistics on the rms over 1 month (Aug 2007) of KBRR-residuals and KBRR-residual differences for case 1/2/3. Unit: μm/s.

Figure 9.10 illustrates the KBRR-residuals for the three cases for a time period of 1 hour of August 4, 2007. As it was expected, since the impact of case 2 is not in the sensitivity range of current GRACE solutions, the case 2 AOD product (black dotted line) does not have a significant effect on KBRR-residuals and is pretty similar to the error-free case 1 scenario (green line). However, the case 3 AOD seems to significantly reduce the KBRR-residuals (magenta line) at least in this short period of data. Analyzing the daily RMS of the KBRR-residuals for the three cases (Fig. 9.11), it can be seen that the curves are very similar, but

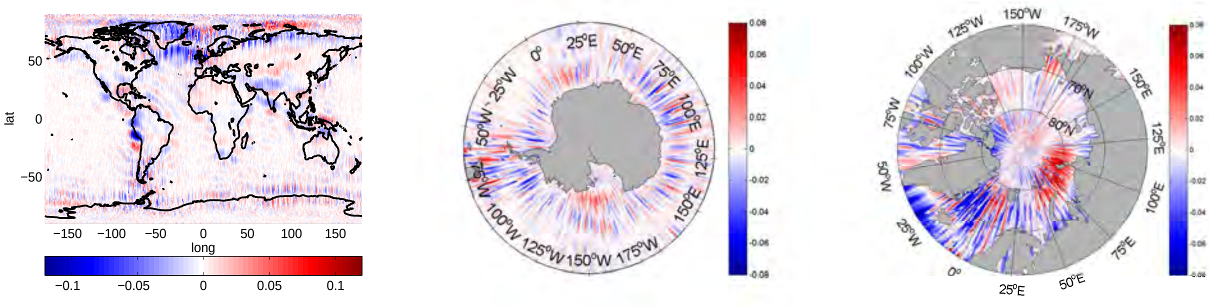

(a) case 1 - case 2 (b) case 1 - case 2 (c) case 1 - case 2

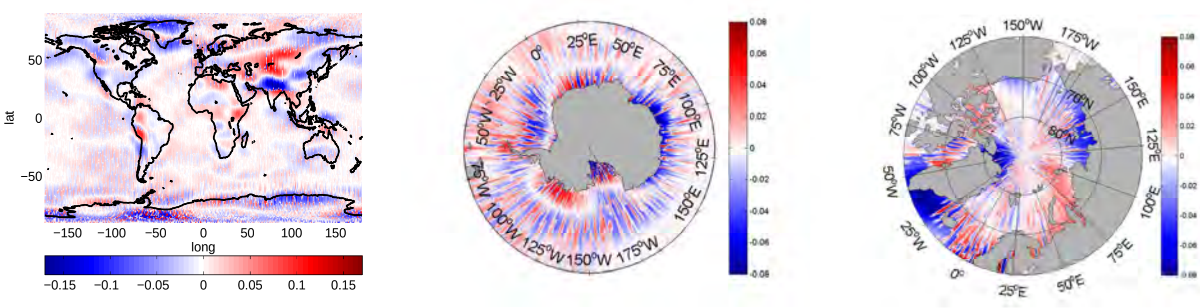

(d) case 1 - case 3 (e) case 1 - case 3 (f) case 1 - case 3

Fig. 9.9: KBRR-residual differences in bins of $1^\circ \times 1^\circ$ *in longitude and latitude between the case 1/2/3 AOD. Red indicates that the KBRR-residuals are reduced/improved by using the case 2 or case 3 AOD w.r.t. the case 1 AOD. Blue indicates regions where the error-free case 1 product shows smaller (better) residuals. Unit: µm/s.*

generally case 2 and case 3 show slightly larger residuals. We can thus retain here that no positive effect in the daily rms values of the KBRR-residuals by propagating the model errors is visible. But having a closer look at the KBRR-residuals reveals that there is a clear decrease visible consistently in the 5-seconds sampled residuals at least for some specific periods.

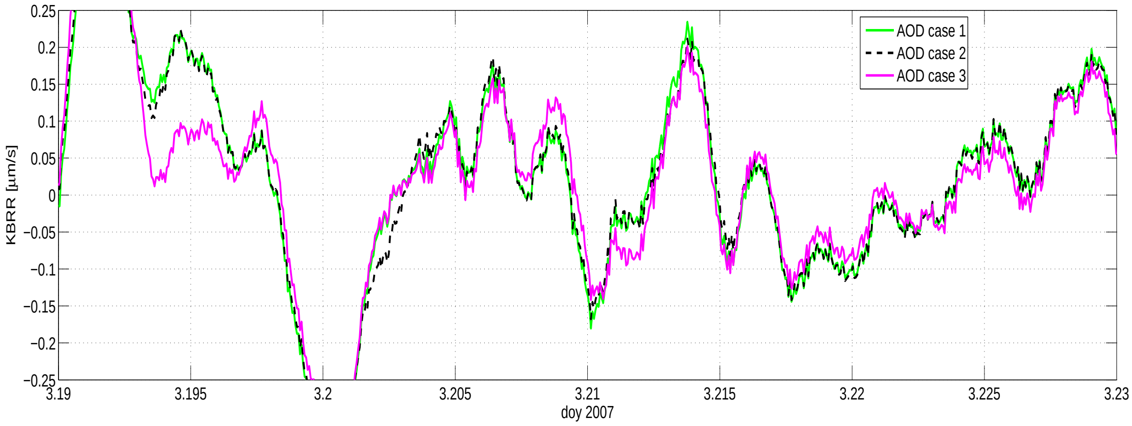

Fig. 9.10: KBRR-residuals for one hour of 04.08.2007 . Unit: µm/s.

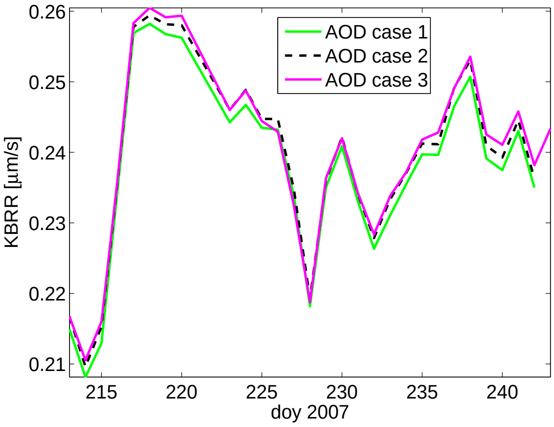

Fig. 9.11: Daily rms of KBRR-residuals for August 2007 after removing the case 1 (green), case 2 (black), and case 3 (magenta) AOD. Unit: $\mu m/s$.

The three experiments can also be analyzed in the spectral domain by computing the power spectral density. The results are shown in Fig. 9.12. Also here, no significant improvement can be observed by using case 2 or case 3 AOD instead of case 1 AOD. Analyzing the KBRR-residuals for the three scenarios against longitude (Fig. 9.13) and latitude (Fig. 9.14), the same conclusions can be drawn. Case 1 and case 2 hardly show any differences. Comparing case 1 (green) and case 3 (magenta) slightly smaller KBRR-residuals for almost all longitudes can be observed for case 1. Regarding the KBRR-residuals against latitude it seems, that case 3 leads to slightly better results between -20° and +20° (cf. Fig. 9.14b).

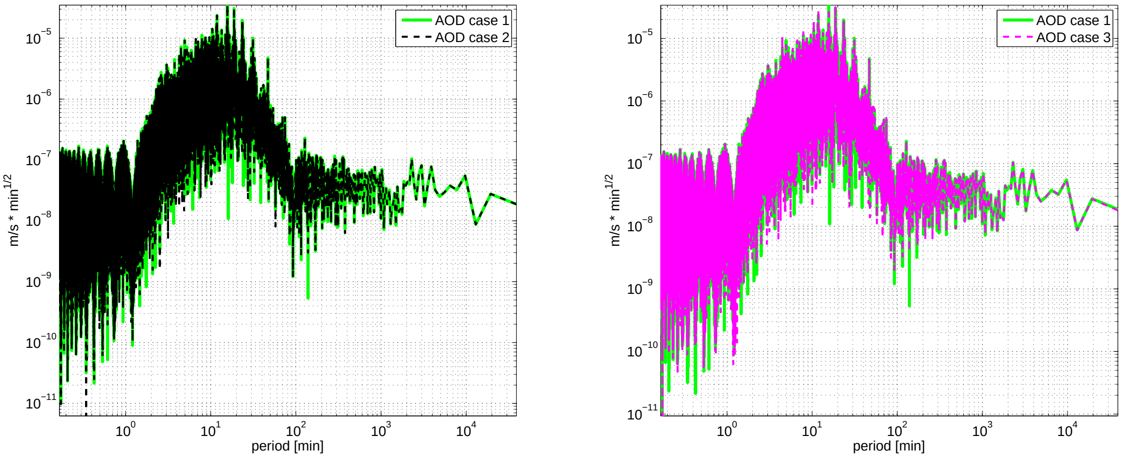

Fig. 9.12: PSD of 1 month (August 2007) KBRR-residuals after removing the case 1 AOD (green), the case 2 AOD (black) and the case 3 AOD (magenta).

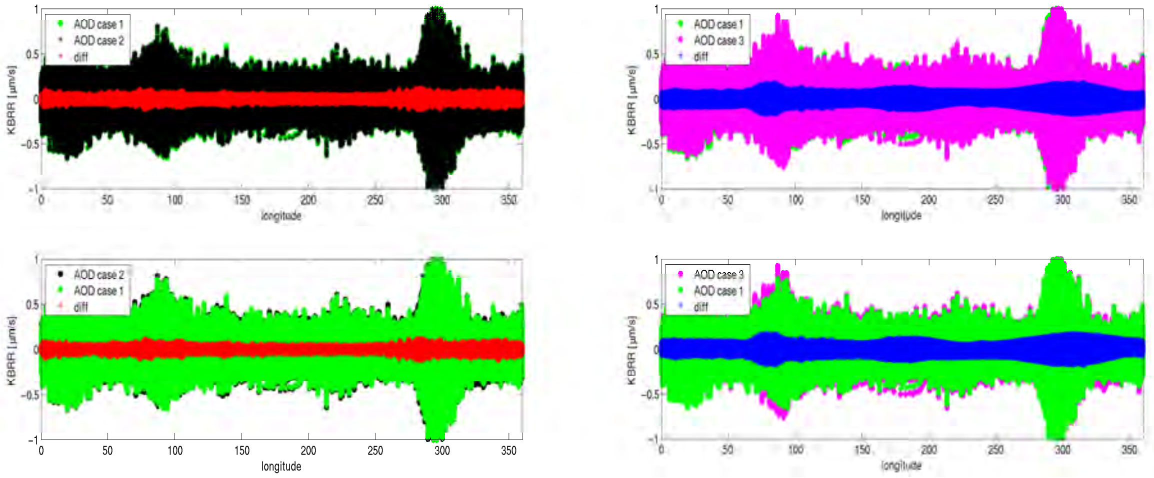

(a) case 1 - case 2

(b) case 1 - case 3

Fig. 9.13: *KBRR-residuals for August 2007 against longitude after removing the case 1 AOD (green), case 2 AOD (black), case 3 AOD (magenta) product and their differences (red, blue). Unit: μm/s.*

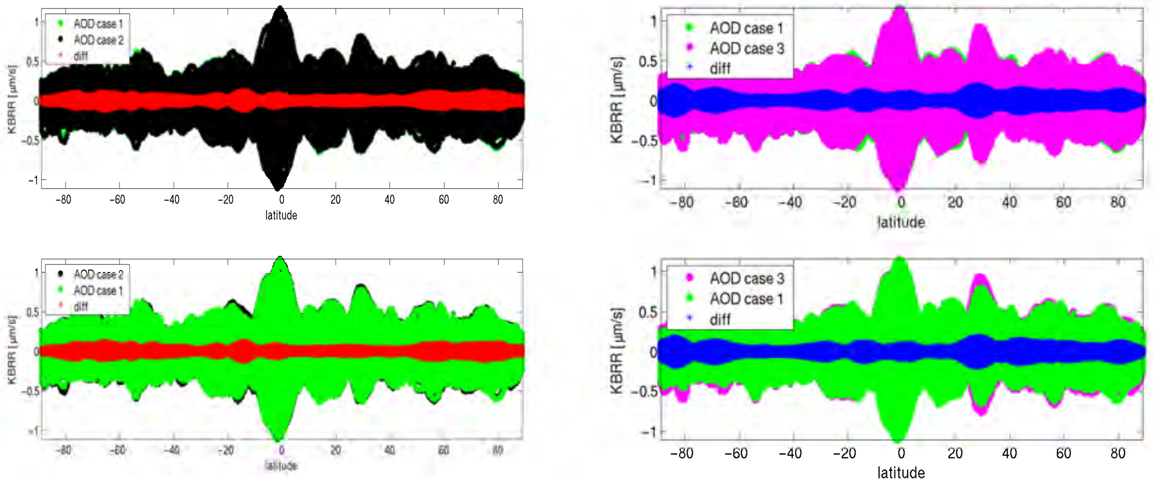

(a) case 1 - case 2

(b) case 1 - case 3

Fig. 9.14: *KBRR-residuals for August 2007 against latitude after removing the case 1 AOD (green), case 2 AOD (black), case 3 AOD (magenta) product and their differences (red, blue). Unit: μm/s.*

Summary - The impact of atmospheric and oceanic model errors on AOD and GRACE

- uncertainties in the atmospheric model parameters, such as specific humidity, geopotential and temperature, are almost negligible, whereas uncertainties in the surface pressure have the most significant impact on the vertically integrated atmospheric pressure I_n
- thus, the impact of two different surface pressure error maps are investigated within this thesis: surface pressure error provided by ECMWF and surface pressure error, derived from model intercomparisons between NCEP and ECMWF; for the ocean part, daily ocean bottom errors derived from various FESOM model runs are used
- differences in the AOD coefficients between the case 1, case 2 and case 3 approach can reach up to several mm and are - at least for case 3 - in the sensitivity range of current GRACE and future gravity field solutions
  (case 1 - case 2: min: -0.95 mm, max: 1.18 mm, mean: -0.09 mm, rms: 0.15 mm)
  (case 1 - case 3: min: -3.05 mm, max: 0.61 mm, mean: -0.75 mm, rms: 0.75 mm)
- whether using the case 1, case 2 or case 3 AOD product affects a monthly gravity field solution in the mm-range
  (case 1 - case 2: min: -1.35 mm, max: 0.95 mm, mean: 0.00 mm, rms: 0.17 mm)
  (case 1 - case 3: min: -1.29 mm, max: 2.32 mm, mean: 0.00 mm, rms: 0.40 mm)
- whether applying case 2 or case 3 AOD instead of case 1 increases the mean daily rms of the KBRR-residuals by 0.6 % and 0.8 %, respectively
  (0.2380 μm/s for case 1 vs. 0.2395 μm/s for case 2 vs. 0.2400 μm/s for case 3)
- effect on the rms of KBRR-residuals over 1 month is in the sub-$\mu m/s$-range
  (case 1 - case2: min: -0.08 $\mu m/s$, max: 0.15 $\mu m/s$, mean: - 1.9 nm/s, rms: 0.01 $\mu m/s$)
  (case 1 - case3: min: -0.14 $\mu m/s$, max: 0.07 $\mu m/s$, mean: - 2.4 nm/s, rms: 0.01 $\mu m/s$)
  Slightly better performance of the case 3 solution in the some regions: Asia, near-polar oceans, and North-East of Scandinavia

In summary, we can retain that surface pressure errors have a significant effect on GRACE temporal gravity field solutions. Although, the effect of uncertainties in the surface pressure concerning the GRACE baseline, are pretty small, we have shown, when analyzing the KBRR-residuals on a global latitude and longitude grid, that the KBRR-residuals could have been partly improved (reduced) when applying the case 3 AOD. However, no improvement is visible in the daily rms of the KBRR-residuals. On the other hand, taking the global rms of a monthly gravity field solution as a validation parameter for the quality of a solution, we can retain, that applying case 3 AOD instead of the standard case 1 AOD leads to 1.2 % better results. Anyway, our results have shown, that a deeper analysis of this issue is required. Longer time-series of KBRR-residuals have to be analyzed. Furthermore, the determination of reasonable error values for surface pressure and ocean bottom pressure as well as the use of 6-hourly uncertainties for atmosphere and ocean should also be subject to further investigations.

10. The impact of alternative and additional model data on AOD and GRACE

10.1. Operational ECMWF data vs. ERA-Interim

Like mentioned before, e.g., in Sect. 5, for the determination of the de-aliasing product, data from the operational (OPER) atmospheric model is used. However, these operational data sets are not consistent, as they are subject to model changes from time to time. For example, in Fig. 10.1 one can clearly observe two significant jumps in the OPER surface pressure data due to an increase of the vertical and horizontal resolution of the model. In order to prevent these inconsistencies one could use e.g. ECMWF's re-analysis data ERA-Interim. The ERA-Interim data products should ensure consistency as they are reprocessed with the same (software) settings. Though, one should be aware that there are significant differences in the OPER and ERA-Interim data (cf. Figs. 10.2 & 10.3). Surface pressure differences of up to locally 140 hPa can appear (mean: 0.18 hPa, rms: 8.46 hPa) and are mainly correlated with the topography. One reason for this is probably the various vertical and horizontal resolutions of the data. The ECMWF OPER model provides the input parameters for the de-aliasing product for 91 levels, ERA-Interim for 60 levels. With the resolution change from 60 to 91 model levels also the orography used in the atmospheric model was increased or decreased accordingly. As surface pressure, the most important parameter in the computation of the AOD product, changes with height, also surface pressure values changed, which in consequence is leading to differences especially in regions with rough topography. The impact of the OPER and ERA-Interim data on GRACE data analysis will be subject of this Section.

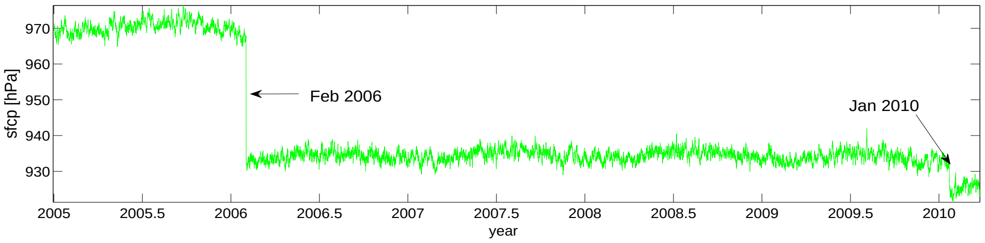

Fig. 10.1: ECMWF operational surface pressure (OPER) for January 2005 to March 2010 for one example point in the Andes (lat: 112°, lon: 291°). Unit: hPa.

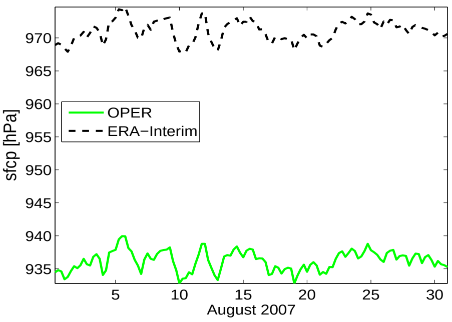

Fig. 10.2: OPER (green) and ERA-Interim (black) ECMWF surface pressure time series for August 2007 for one example point in the Andes (lat: 112°, lon: 291°). Unit: hPa.

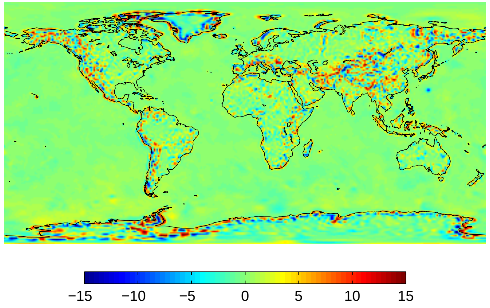

Fig. 10.3: OPER and ERA-Interim surface pressure differences. 01.08.2007 00h, Unit: hPa.

Impact of ERA-Interim on the AOD product

Figure 10.4 as well as Tab. 10.1 are showing the differences in the monthly mean AOD product of August 2007 when using either the operational (OPER) or ERA-Interim data. The differences reach up to several *mm* and are also here highly correlated with the topography, which is - as explained above - probably due to the increased horizontal and vertical resolution of the orography used in the two models.

Regarding the degree standard deviations in Fig. 10.5, one can state, that using either ERA-Interim data or operational data from ECMWF, is in the sensitivity range of current GRACE RL05 solutions, even though only for the very long wavelengths ($n \leq 10$). Having a view on the GRACE baseline and the future gravity field mission accuracy, using ERA-Interim instead of the operational data will play also for the shorter wavelengths of up to d/o 30 and 60, respectively, a more significant role.

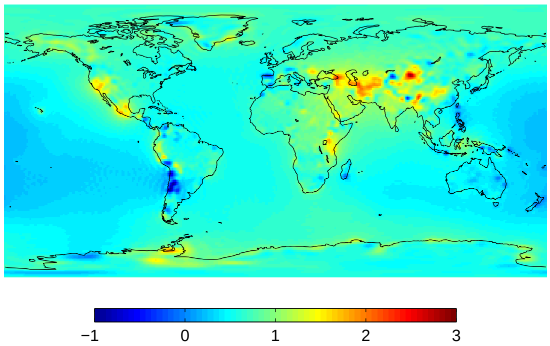

Fig. 10.4: Impact of using either ECMWF OPER or ERA-Interim data on the AOD product. August 2007, Unit: mm.

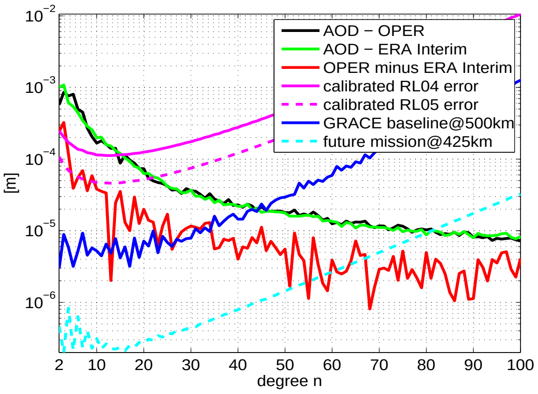

Fig. 10.5: Differences (red) in terms of degree standard deviations for geoid heights between the AOD products after applying ECMWF OPER (black) and ERA-Interim (green) data. August 2007. Unit: m.

	min	max	mean	wrms
OPER	-6.43	5.88	0.37	2.61
ERA-Interim	-7.66	5.58	-0.22	2.78
diff.	-1.16	2.94	-0.59	0.26

Tab. 10.1: Statistics on the differences between the AOD product after applying ECMWF OPER and ERA-interim data. August 2007. Unit: mm.

Impact of ERA-Interim on a monthly gravity field solution

The impact of the ERA-Interim data on a monthly gravity field solution is shown in Fig. 10.6 and Tab. 10.2. Differences are in the *mm*-range and show the same (inverse) pattern as the AOD differences (cf. Fig. 10.6 & Fig. 10.4). Regarding the global weighted rms of the monthly gravity field solution, one can state, that here almost no effect is visible. When using the ERA-Interim data, the rms slightly increases by about 0.3 % from 1.517 $\mu m/s$ to 1.522 $\mu m/s$. Also, when having a look at Fig. 10.6, a striping pattern is visible. This might be probably due to spatial aliasing. Like mentioned at the beginning of this Section, the ERA-Interim data is provided by ECMWF on 60 vertical model levels, whereas the operational data has a resolution of 91 model levels. The minor resolution of the ERA-Interim data might not sufficiently represent the atmospheric masses which is reflected in a monthly gravity solution by these stripes.

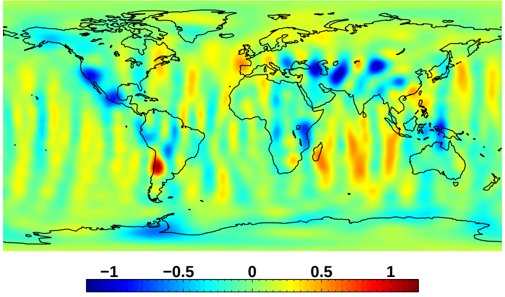

Fig. 10.6: Impact of using either ECMWF OPER or ERA-Interim data on a monthly gravity field solution. August 2007, Unit: mm.

	min	max	mean	wrms
OPER	-10.00	8.09	0.01	1.52
ERA-Interim	-9.76	8.51	0.01	1.52
diff.	-1.16	1.16	0.00	0.20

Tab. 10.2: Statistics on the differences between the monthly gravity field solutions after applying ECMWF OPER and ERA-interim data. August 2007. Unit: mm.

Impact of ERA-Interim on the KBRR-residuals

Having a look at the KBRR-residuals as a function of time (Fig. 10.7), no significant differences are visible. Also in the daily rms of the KBRR-residuals in Fig. 10.8 no significant effect can be observed. The daily rms is only reduced/improved by about 0.04 % when using the ERA-Interim data instead of the operational ones. The impact of ERA-interim on the global rms over 1 month of KBRR-residuals is illustrated in Fig. 10.9.

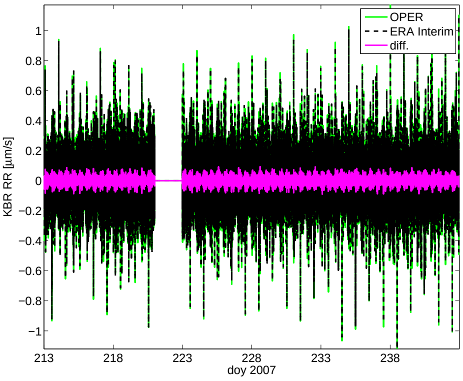

Fig. 10.7: KBRR-residuals for August 2007 after removing the ECMWF OPER (green) and the ERA-Interim (black) data and their differences (magenta). Unit: $\mu m/s$.

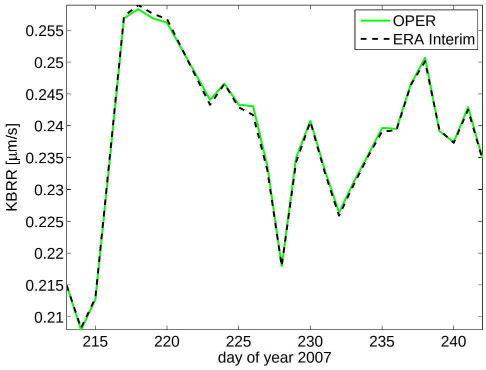

Fig. 10.8: Daily rms of KBRR-residuals after removing the ECMWF OPER (green) and the ERA-Interim (black) data. August 2007, Unit: $\mu m/s$.

Differences are here in the sub-$\mu m/s$-range. Especially in South-America, Greenland and Antarctica, the rms of the KBRR-residuals could have been reduced/improved by using the ERA-Interim data (red-colored regions in Fig. 10.9). Also in the power spectral density of the KBRR-residuals in Fig. 10.10 hardly any differences can be seen between the two data sets. But, concerning the psd of the differences, one can state, that although the differences are small, they are still significant at certain periods.

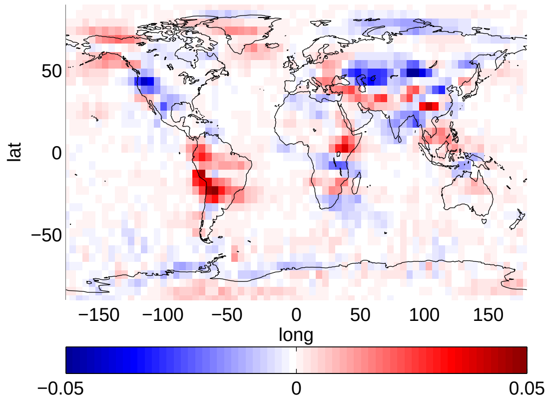

Fig. 10.9: Rms differences between using the ECMWF OPER and ERA-Interim data over 1 month of KBRR-residuals in bins of 5° × 5° in longitude and latitude. August 2007, Unit: $\mu m/s$.

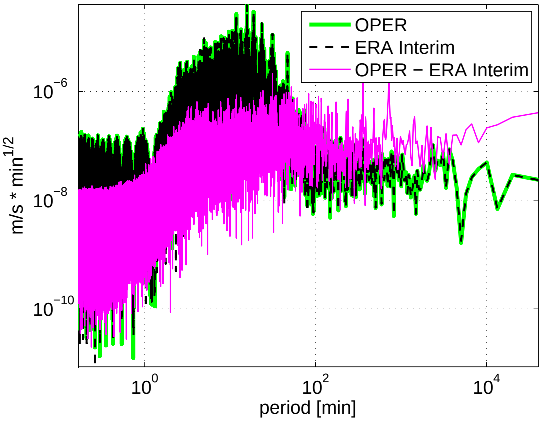

Fig. 10.10: PSD of 1 month (August 2007) KBRR-residuals after removing the ECMWF OPER (green), the ERA-Interim (black) data and the PSD of the differences (magenta).

Summary - ECMWF ERA-Interim vs. ECMWF Operational data

- while the operational ECMWF data (OPER) has a vertical resolution of 91 model levels, the atmospheric parameters from the ECMWF's ERA-Interim data pool have a lower resolution of 60 vertical model levels
- differences between the AOD products determined with OPER and ERA-Interim data are in the mm-range and thus in the sensitivity range of the GRACE and future gravity field missions (min: -1.16 mm, max: 2.94 mm, mean: 0.59 mm, rms: 0.26 mm)
- whether using OPER or ERA-Interim data affects a monthly gravity field solution in the mm-range (min: -1.16 mm, max: 1.16 mm, mean: 0.00 mm, rms: 0.20 mm)
- the global weighted rms of the analyzed monthly gravity field solution (August 2007) slightly increases by 0.3 % when applying ERA-Interim data
- the daily rms of the KBRR-residuals over August 2007 is slightly reduced ($\sim$ 0.04 %) when using ERA-Interim data
- concerning the rms of KBRR-residuals as a function of longitude and latitude, one can state, that especially in the Antarctic regions, South-America and Greenland, the ERA-Interim data slightly performs better than OPER. The rms of the KBRR-residuals is affected in the sub-$\mu m/s$-range. (min: -0.05 $\mu m/s$, max: 0.05 $\mu m/s$ /mean: 0.00 $\mu m/s$, rms: 0.01 $\mu m/s$)

Using ERA-Interim instead of operational ECMWF data will have a significant effect on GRACE and future gravity field mission data analysis. One should be aware, that the operational ECMWF data, currently used for the computation of the de-aliasing product, is not consistent with time and contains jumps of several hPa due to model changes (cf. Fig. 10.1), which will have also consequences on any mass estimates derived from GRACE data (cf. e.g. *Duan et al.* (2012)). Using the ERA-Interim data would avoid these inconsistencies. However, one should be aware, that ERA-Interim data provides a lower resolution than the currently used operational data. This might also affect the AOD product and further gravity field data analysis. In addition, using the ERA-Interim data would mean for the GRACE community to accept longer waiting times for the release of the monthly gravity fields and associated products, as the ERA-data are normally updated only once per month.

10.2. Enhanced spatial resolution of the ocean model

The RL04 and RL05 AOD products, which are provided by GFZ, are analyzed, and the effect of the enhanced spatial resolution of the ocean model on GRACE gravity field processing will be investigated. In the following two scenarios are compared to each other:

- OMCT@1.875° = ocean bottom pressure fields from OMCT in 1.875° x 1.875° grid resolution (as it is used in the official de-aliasing RL04 process)
- OMCT@1° = ocean bottom pressure fields from OMCT in 1° x 1° grid resolution (more details about the changes of OMCT@1° see Sect. 6) (as it is used in the official de-aliasing RL05 process)

The two cases only vary in the ocean bottom pressure input fields. The atmospheric part for the calculation of the de-aliasing product has been unchanged. In consequence, all effects shown in this chapter are due to the enhanced spatial resolution of the ocean model. Figure 10.11 shows the OMCT@1.875° and OMCT@1° mean fields and their differences. Clearly, the higher resolution is visible. Maximum differences in the magnitude of the ocean bottom pressure signal appear (cf. Tab. 10.3). The global rms of the mean field differences is about 0.44 hPa. Especially, in the coastal regions as well as on tectonic plate boundaries large differences between the two spatial resolutions can be observed.

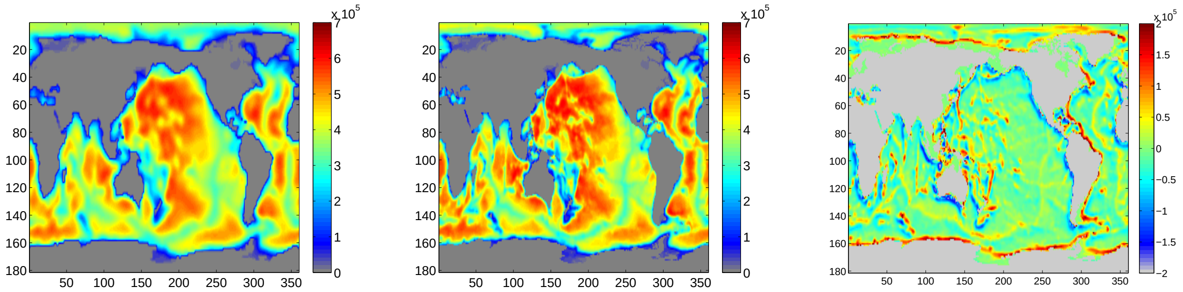

(a) (b) (c)

Fig. 10.11: Mean ocean bottom pressure field over two years (2001+2002). (a) OMCT@1.875°, (b) OMCT@1°, (c) differences (a)-(b). Unit: hPa.

	min	max	mean	wrms
OMCT@1.875°	0.00	5.96	2.67	2.04
OMCT@1°	0.00	6.12	2.67	2.13
diff.	−3.11	4.62	0.00	0.44

Tab. 10.3: Statistics on the mean OMCT@1.875° and OMCT@1° ocean bottom pressure fields. Unit: 10^5 hPa

As the mean ocean bottom pressure field is subtracted from the ocean bottom pressure in order to get instantaneous ocean bottom pressure mass changes, we have a look at the residual ocean bottom pressure fields for the two scenarios. Fig. 10.12c reflects the differences between OMCT@1.875° and OMCT@1° ocean bottom pressure variations. Again, significant differences of up to 62 hPa can be observed, especially in the Antarctic Circumpolar Current (ACC).

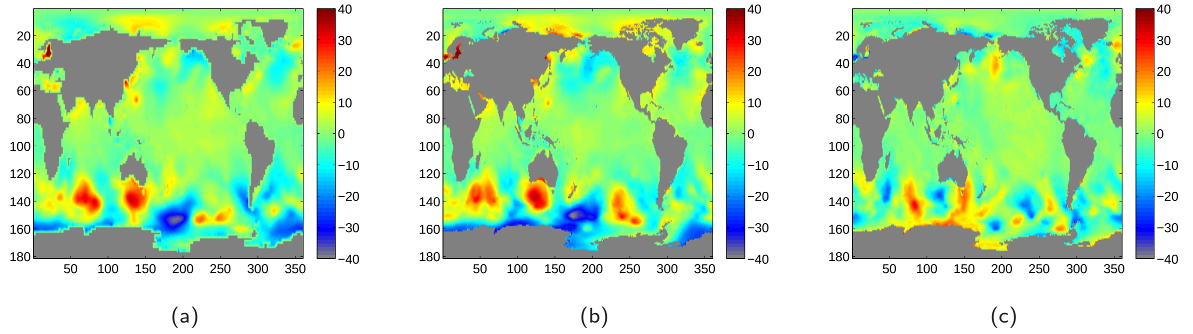

Fig. 10.12: Residual ocean bottom pressure (after subtraction of the 2001+2002 mean field). (a) OMCT@1.875°, (b) OMCT@1°, (c) differences (a) - (b), 01.08.2007, 00h. Unit: hPa.

	min	max	mean	wrms
OMCT@1.875°	−38.58	58.08	0.00	6.25
OMCT@1°	−44.28	69.13	0.00	6.53
diff.	−61.95	41.66	0.00	4.83

Tab. 10.4: Statistics on the residual OMCT@1.875° and OMCT@1° ocean bottom pressure fields. 01.08.2007, 00h. Unit: hPa.

Impact of the enhanced spatial resolution of the ocean model on the AOD product

Table 10.5 and Figure 10.14 visualizes the effect of the enhanced spatial ocean bottom pressure resolution on the AOD product. Three monthly means (January, April, July) of the two AOD products are shown here. The differences between the OMCT@1.875° and OMCT@1° scenarios reach up to 5 mm in terms of geoid heights (cf. January, Fig. 10.14g). The maximum differences appear in regions with high ACC-variability, but also in the Indian ocean as well as in almost the whole Pacific region. Comparing the differences in the combined atmospheric and oceanic de-aliasing product between OMCT@1.875° and OMCT@1° (Fig. 10.14) with the differences between the mean ocean bottom pressure input fields (Fig. 6.2 in Sect. 6.1), clear correlation patterns are visible, which shows us that the ocean model differences are - as expected - propagated to the AOD product. Having a look at the red and magenta lines in Fig. 10.13, we can retain, that the enhanced spatial resolution of the de-aliasing ocean model is expected to have an effect on current GRACE solutions in the very long wavelengths ($n \leq 15$).

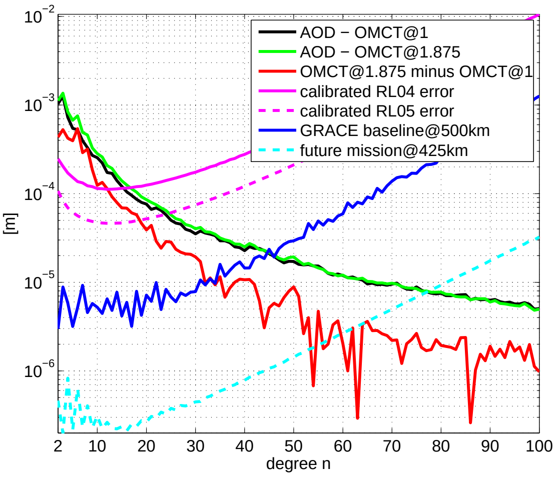

Fig. 10.13: Differences between the OMCT@1.875° AOD and OMCT@1° AOD in terms of degree standard deviations for geoid heights. January 2007. Unit: m.

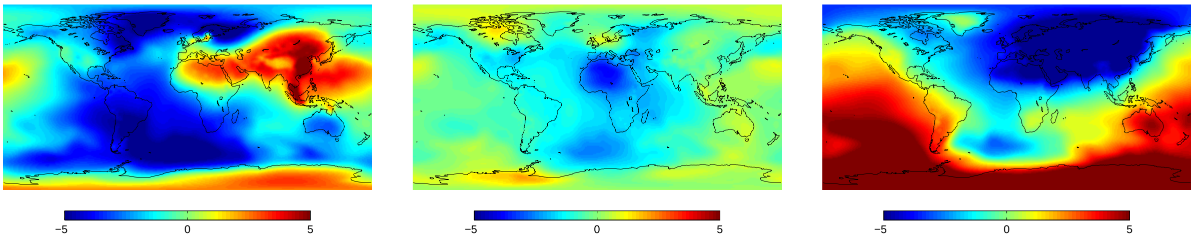

(a) OMCT@1.875° - Jan (b) OMCT@1.875° - Apr (c) OMCT@1.875° - Jul

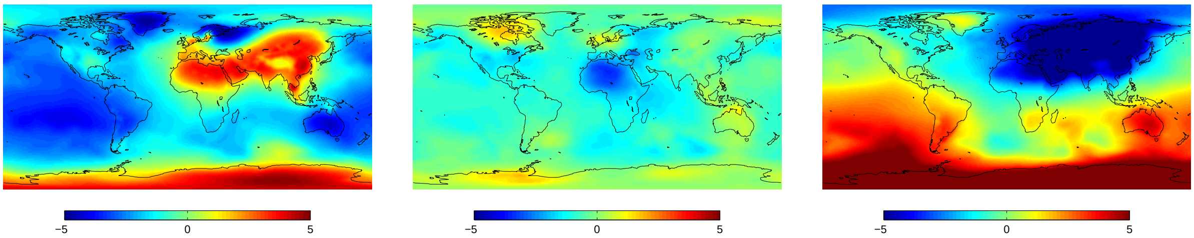

(d) OMCT@1° - Jan (e) OMCT@1° - Apr (f) OMCT@1° - Jul

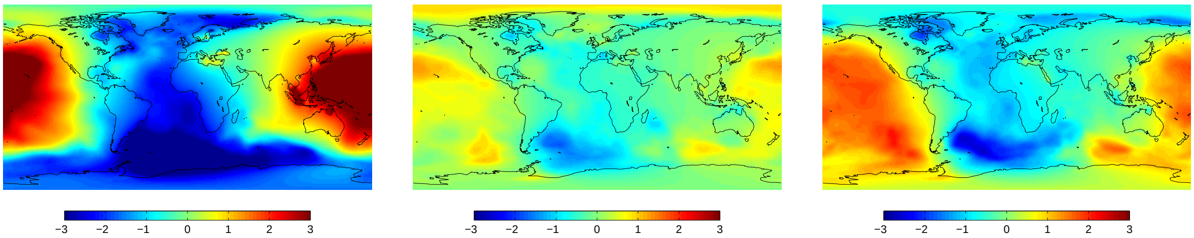

(g) Diff - Jan (h) Diff - Apr (i) Diff - Jul

Fig. 10.14: Monthly mean of the OMCT@1.875° AOD and OMCT@1° AOD products and their differences in terms of geoid heights for January (fist column), April (mid column) and July (third column) 2007. Unit: mm.

	OMCT@1.875°	OMCT@1°	diff
Jan	-6.55/7.52/ - 1.35/2.47	-5.15/4.85/ - 1.27/1.98	-5.05/4.80/ - 0.08/2.08
Feb	-4.57/2.39/ - 1.19/0.95	-3.62/2.21/ - 1.15/1.02	-1.80/2.14/ - 0.04/0.80
Mar	-4.64/2.58/ - 1.09/0.97	-3.56/3.03/ - 0.99/1.13	-2.03/1.22/ - 0.01/0.53
Apr	-3.92/2.12/ - 0.78/0.91	-3.49/1.93/ - 0.75/0.69	-1.80/1.32/ - 0.03/0.52
May	-6.94/3.61/ - 0.60/2.35	-6.64/2.94/ - 0.62/1.79	-2.14/1.65/+0.03/0.82
Jun	-8.23/5.19/ - 0.15/2.54	-7.79/5.25/ - 0.16/2.37	-2.27/2.09/+0.01/1.00
Jul	-9.05/8.43/+0.33/3.61	-8.61/7.74/+0.26/3.02	-2.63/2.15/+0.07/1.03
Aug	-5.80/5.68/+0.24/2.54	-5.25/4.45/+0.28/1.85	-2.46/1.77/ - 0.04/1.04
Sep	-7.50/3.40/ - 0.48/2.18	-5.18/2.18/ - 0.44/1.38	-3.16/1.98/ - 0.04/1.06
Oct	-4.42/6.43/ - 1.19/1.79	-4.50/6.72/ - 1.14/1.94	-1.80/1.76/ - 0.05/0.82
Nov	-4.25/3.20/ - 1.49/1.35	-4.77/3.52/ - 1.45/1.32	-2.68/1.89/ - 0.04/1.01
Dec	-4.71/4.92/ - 1.66/1.85	-4.99/5.42/ - 1.53/2.19	-2.53/1.81/ - 0.12/0.96

Tab. 10.5: Statistics on the monthly mean OMCT@1.875° and OMCT@1° AOD coefficients and their differences in terms of geoid heights for 2007. min/max/mean/wrms. Unit: mm

.

Impact of the enhanced spatial resolution of the ocean model on a monthly gravity field solution

Whether applying the OMCT@1.875° or OMCT@1° product during de-aliasing has a significant effect on the monthly gravity field solutions. The differences between the two scenarios have a maximum amplitude of 1-2 *mm* in terms of geoid heights (cf. Tab. 10.6). Comparing Figs. 10.15g-i with Figs. 10.14, we can see clearly some correlation patterns, which again show, that the AOD differences are somehow propagated to the monthly gravity field solutions, although there is a whole parametrization process in between.

The global weighted rms (wrms) is often taken as a key parameter to assess the quality of a monthly gravity field solution. After subtraction of a best known mean static gravity field, the assumption is made, that the wrms of a monthly gravity field solution becomes smaller and thus better, the more high-frequent mass variations are 'removed' during the de-aliasing process. Analyzing the monthly gravity field solutions w.r.t. the global wrms, we can retain that for eight of the twelve months of year 2007, the wrms could have been reduced by about 0.6 % for May 2007 and about 9.6 % for July 2007 by applying the OMCT@1° instead of the OMCT@1.875° AOD (cf. Tab. 10.6).

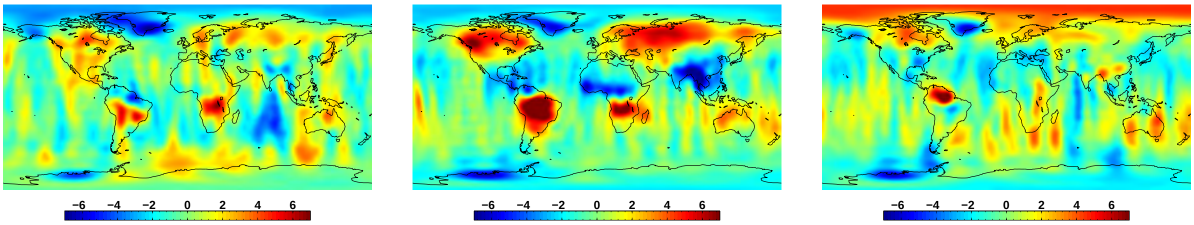

(a) OMCT@1.875° - Jan (b) OMCT@1.875° - Apr (c) OMCT@1.875° - Jul

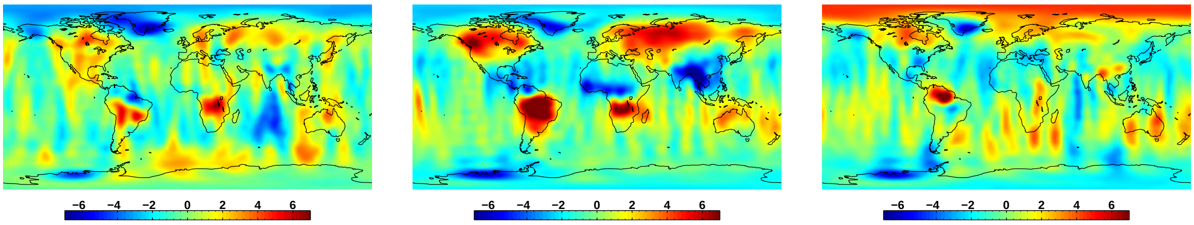

(d) OMCT@1° - Jan (e) OMCT@1° - Apr (f) OMCT@1° - Jul

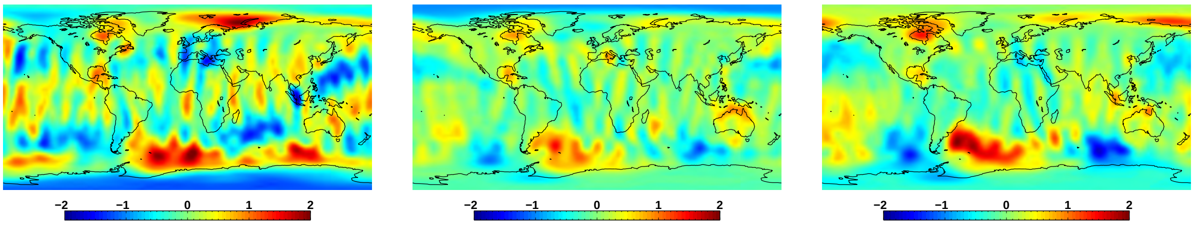

(g) Diff - Jan (h) Diff - Apr (i) Diff - Jul

Fig. 10.15: Monthly gravity field solutions for OMCT@1.875° AOD and OMCT@1° AOD products and their differences in terms of geoid heights for January (fist column), April (mid column) and July (third column) 2007. Unit: mm.

	OMCT@1.875°	OMCT@1°	diff	Δ in %
Jan	-6.89/6.89/+0.01/1.63	-7.06/6.86/+0.03/1.56	-1.92/2.10/ - 0.02/0.60	+4.3
Feb	-12.97/12.49/+0.02/1.97	-12.78/12.78/+0.01/1.99	-0.94/1.19/+0.01/0.34	-1.0
Mar	-7.25/11.42/+0.02/1.90	-7.36/11.33/+0.02/1.91	-1.07/1.09/+0.00/0.29	-0.5
Apr	-8.10/11.94/+0.01/2.09	-7.97/12.18/+0.01/2.04	-1.28/1.49/+0.00/0.36	+2.4
May	-7.07/12.49/ - 0.01/1.70	-7.21/12.68/ - 0.01/1.69	-1.23/1.57/+0.00/0.39	+0.6
Jun	-6.43/13.22/ - 0.03/1.40	-6.35/13.39/ - 0.03/1.39	-1.91/1.47/+0.00/0.42	+0.7
Jul	-6.31/9.14/ - 0.02/1.67	-6.34/9.31/ - 0.02/1.51	-1.76/1.96/+0.00/0.49	+9.6
Aug	-10.09/8.13/+0.01/1.51	-10.36/7.80/+0.02/1.55	-1.83/1.64/+0.00/0.43	-2.6
Sep	-11.89/9.41/+0.02/1.85	-11.31/9.18/+0.02/1.76	-1.86/2.05/+0.00/0.53	+4.9
Oct	-13.06/6.83/+0.00/1.90	-13.04/6.99/+0.01/1.86	-1.44/1.41/+0.01/0.40	+2.1
Nov	-11.86/5.99/ - 0.02/1.78	-11.65/5.90/ - 0.02/1.74	-2.16/2.00/ - 0.01/0.47	+2.2
Dec	-9.82/5.85/ - 0.01/2.00	-10.21/5.62/ - 0.00/2.09	-2.21/1.56/+0.00/0.44	-4.5

Tab. 10.6: Statistics on the monhtly gravity field solutions for the OMCT@1.875° and OMCT@1° AOD product. min/max/mean/wrms. Unit: mm. A positive change Δ in percent means that OMCT@1° improves (reduces) the monthly gravity field solution (global weighted rms) w.r.t. the OMCT@1.875° AOD.

Impact of the enhanced spatial resolution of the ocean model on KBRR-residuals

KBRR-residuals are another parameter to assess the quality of the modelled observations w.r.t. the observed/measured ones. If they can be reduced by using the OMCT@1° AOD product, it would imply that the enhanced spatial resolution of the ocean model is more realistic and catches more high-frequent variations than the standard OMCT@1.875° AOD product.

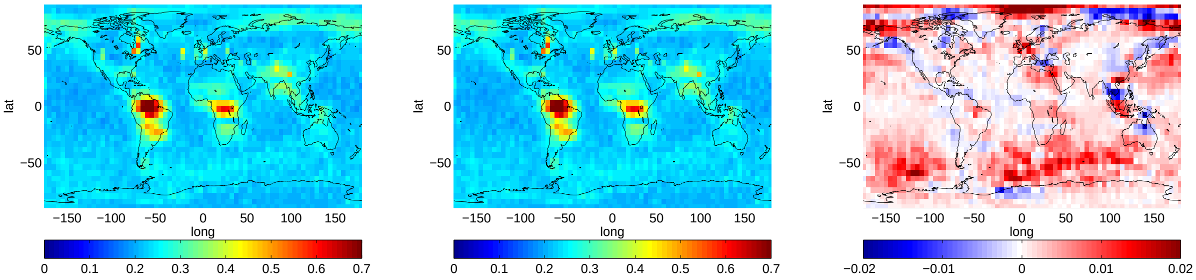

(a) (b) (c)

Fig. 10.16: Rms over 1 year (2007) of KBRR-residuals in bins of 5°x5° in longitude and latitude. (a) OMCT@1.875°, (b) OMCT@1°, (c) and the differences (a) minus (b), Unit: μm/s.

First, we have a look at Fig. 10.16 and the rms over 1 year of KBRR-residuals as a function of latitude and longitude. Like in the residual ocean bottom pressure differences (Fig. 10.12), we can observe the highest deviations between OMCT@1.875° and OMCT@1° in regions with high ACC-variability, but also in the Indian ocean. OMCT@1.875° has a higher rms in these regions (as the difference between OMCT@1.875° and OMCT@1° is positive), which in turn means, that the currently used OMCT@1.875° AOD product seems to over-estimate the variations in these Southern ocean regions. In general, one could summarize, that the rms differences are smaller in the temperate zones than in the higher latitudes. In addition, the OMCT@1° shows slightly higher rms values in near-coastal regions and in the Arctic Ocean between longitudes of +75° and +175°.

The same conclusions apply for the KBRR-residuals themselves. The KBRR-residual differences between the OMCT@1.875° and OMCT@1° cases are illustrated in Fig. 10.17. The blue color indicates regions where the standard OMCT@1.875° product reveals smaller (better) residuals than the OMCT@1° product. We can observe for January to March 2007 smaller and thus reduced KBRR-residuals in the Southern polar regions when applying OMCT@1°. However, the enhanced spatial resolution of the ocean model seems to perform worse than the OMCT@1.875° model for April to September, as the KBRR-residuals are getting larger, especially in the ACC region and the northern polar regions. In addition, we can also observe here for almost all months a better performance of the OMCT@1.875° model in near- continental regions. This is due to a known problem of the OMCT@1° which is over-estimating the trends (*Dobslaw et al.*, 2012).

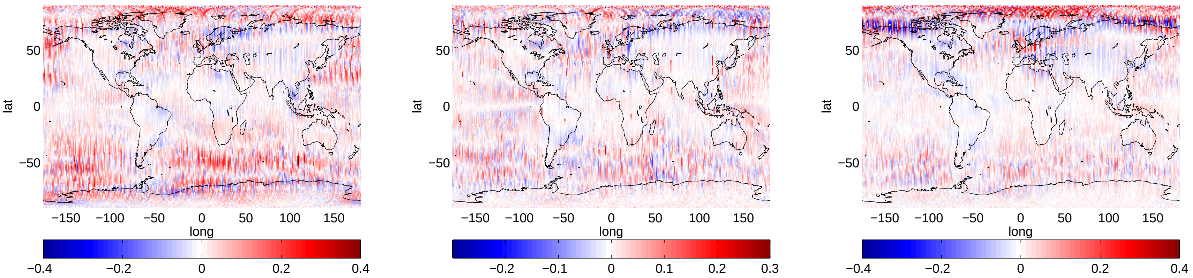

(a) Jan (b) Feb (c) Mar

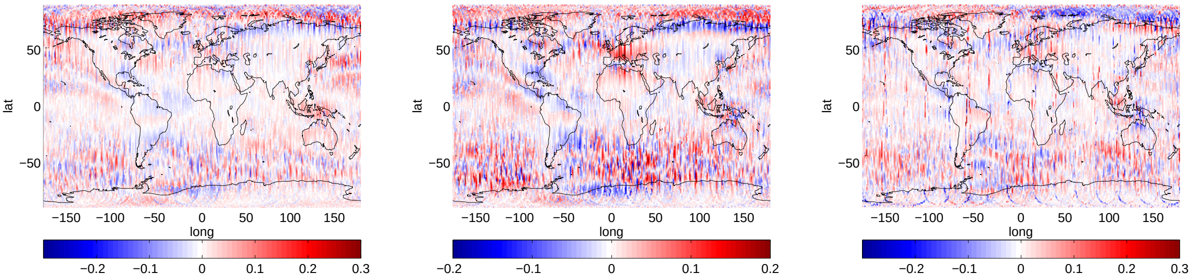

(d) Apr (e) May (f) Jun

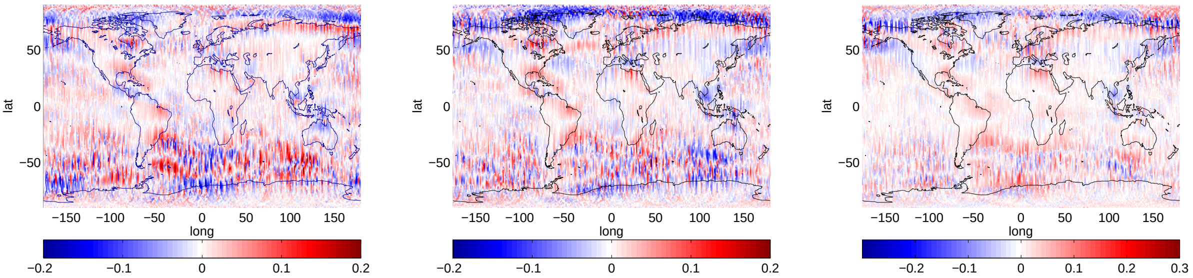

(g) Jul (h) Aug (i) Sep

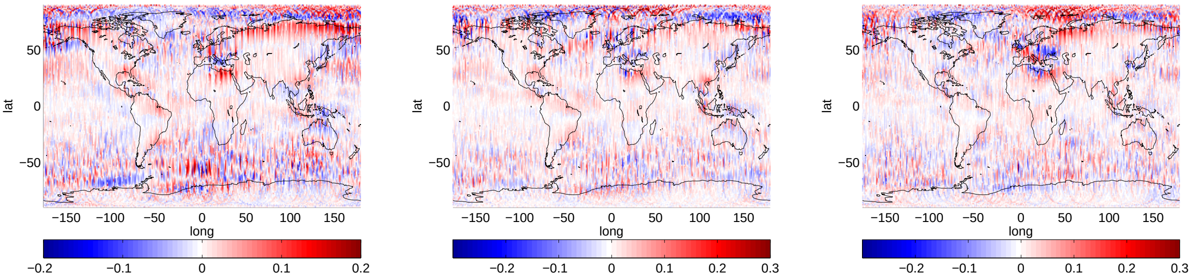

(j) Oct (k) Nov (l) Dec

Fig. 10.17: Monthly KBRR-residual differences in bins of 1° × 1° in longitude and latitude between the OMCT@1.875° and OMCT@1° case. Red indicates that the KBRR-residuals are reduced/improved by using OMCT@1° w.r.t. OMCT@1.875°. Blue indicates regions where the standard OMCT@1.875° product shows smaller (better) residuals. Unit: μm/s.

The daily rms of the KBRR-residuals over one year reflect again, that OMCT@1° leads to slightly better (reduced) results (Fig. 10.20) than OMCT@1.875°. Especially, in the first 120 days of year 2007 (January to April) an improvement of about 2.2 % by using OMCT@1° can be observed. Analyzing the daily rms over the whole year 2007, one has to retain, that the mean rms of the KBRR-residuals could only be reduced by about 0.8 %. The 5-second KBRR-residuals against time, illustrated in Fig. 10.18, show hardly any difference between the two AOD cases. But having a look at Fig. 10.19 and the spectral amplitudes of the two time series, one can see some significant reductions of the amplitudes when applying OMCT@1° instead of OMCT@1.875°, especially at the harmonics of the orbital frequency between 10 minutes and 25 minutes. When analyzing the KBRR-residuals against latitude (Fig. 10.21) and longitude (Fig. 10.22), one can observe, that the regions of the main improvements are between 20° to 90° latitude and 150° to 220° as well as 320° to 360° longitude.

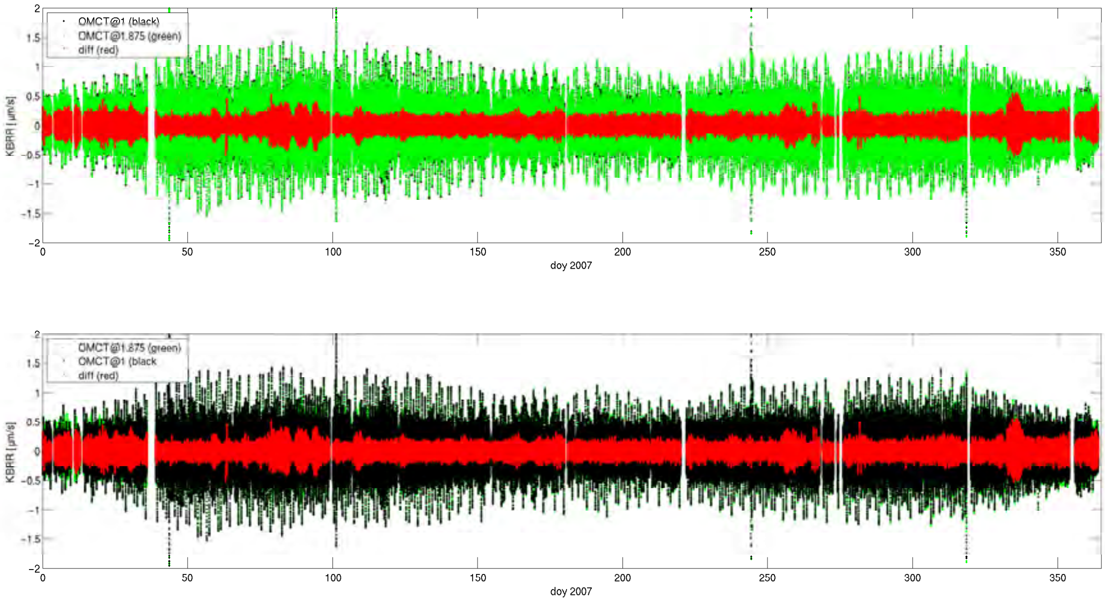

Fig. 10.18: KBRR-residuals for 2007 after removing the OMCT@1.875° AOD (green) and the OMCT@1° AOD (black) and their differences (red). Unit: μm/s.

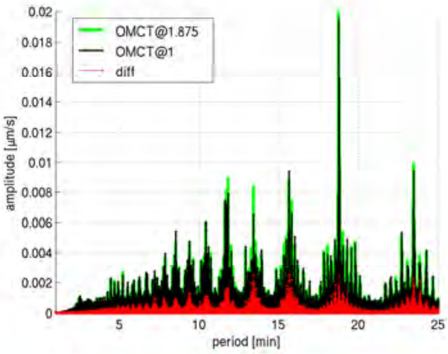

Fig. 10.19: Spectra of 1 year (2007) KBRR-residuals after removing OMCT@1.875° AOD (green) and OMCT@1° AOD (black) and the spectra of the differences (red). Unit: μm/s.

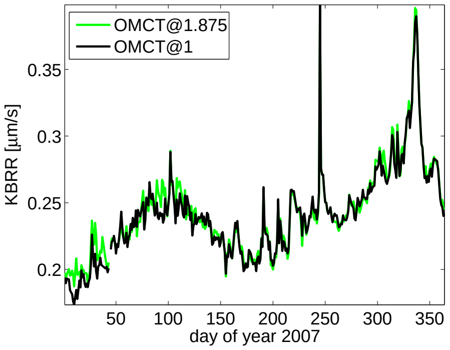

Fig. 10.20: Daily rms of KBRR-residuals for 2007 after removing OMCT@1.875° AOD (green) and OMCT@1° AOD (black). Unit: μm/s.

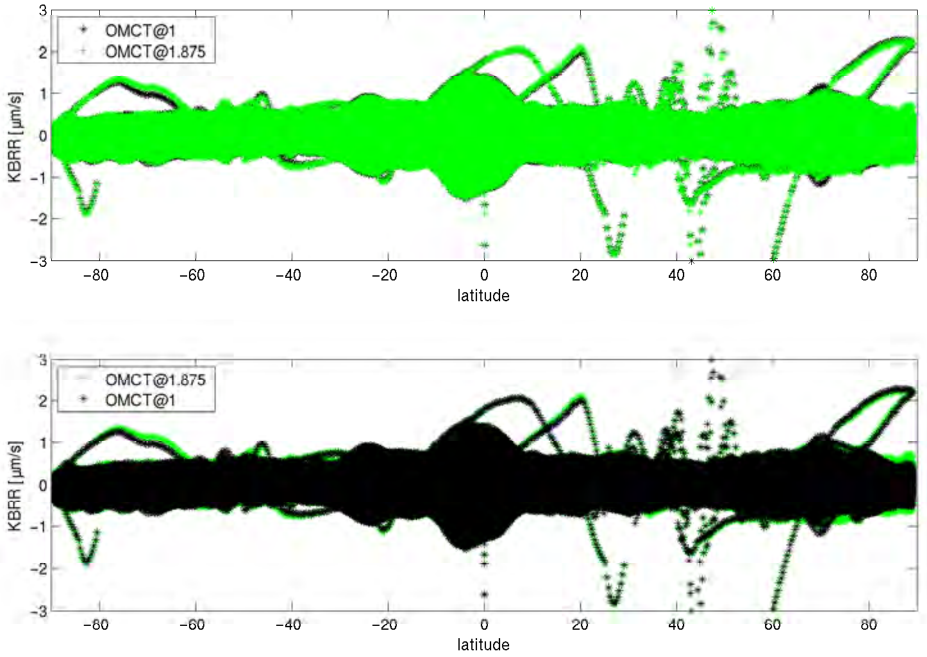

Fig. 10.21: KBRR-residuals for 2007 against latitude after removing OMCT@1.875° AOD (green) and OMCT@1° AOD (black). Unit: µm/s.

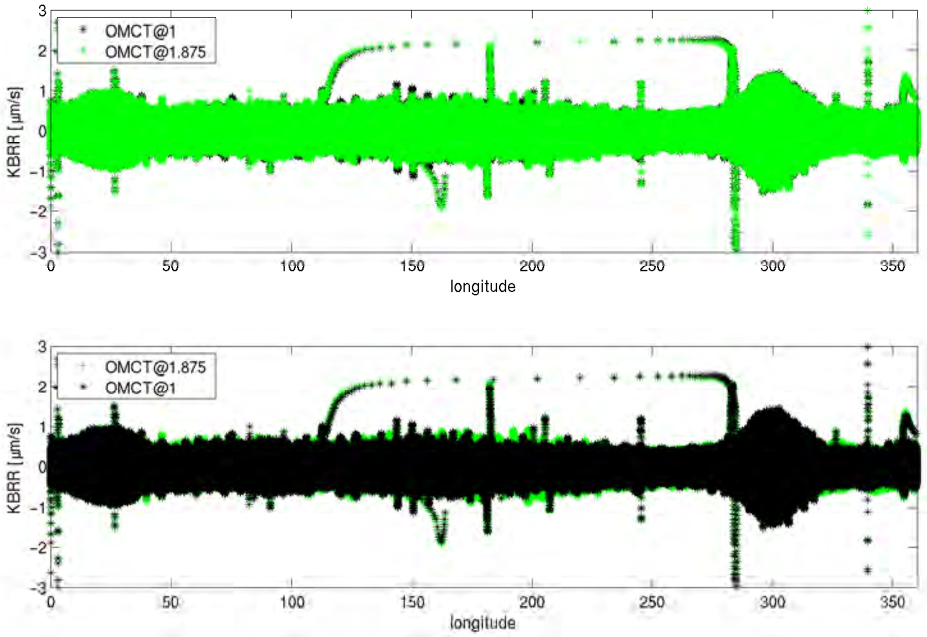

Fig. 10.22: KBRR-residuals for 2007 against longitude after removing OMCT@1.875° AOD (green) and OMCT@1° AOD (black). Unit: µm/s.

Summary - The impact of an enhanced spatial resolution of the ocean model

- in contrast to the RL04 AOD product, where a spatial resolution of the ocean model of $1.875° \times 1.875°$ was given, the new RL05 AOD product is determined by using an enhanced $1° \times 1°$ spatial resolution
- differences between the RL04 and RL05 AOD products are in the mm range and can reach up to 0.5 *cm*. The differences appear mainly in regions with high ACC (Antarctic Circumpolar Current) variability
- whether using RL04 or RL05 affects a monthly gravity field solution in the *mm*-range
- the global weighted rms of the monthly gravity field solutions improves/reduces for 8 out of 12 months in year 2007 when applying RL05 instead of RL04. The rms could have been improved by 0.7 % to 4.3 % depending on the analyzed month.
- the daily rms of the KBRR-residuals over 2007 is slightly reduced (~ 0.8 %) when using RL05
- the improvement of the rms of KBRR-residuals by either using RL04 or RL05 seems not to be globally present. In regions with high ACC-variability and in the Indian ocean RL05 improves the residuals, whereas RL04 leads to better/improved residuals in near-continental and polar regions.

In summary, we can state, that the enhanced spatial resolution of the ocean model is able to slightly improve the KBRR-residuals on a global scale and more significantly regionally. OMCT@1° leads to reduced KBRR-residuals in the Southern oceans, as well as to a reduction of the daily rms of the KBRR-residuals of 2.2 %, at least for the first 4 months of year 2007. Though, OMCT@1° is also showing some weaknesses w.r.t. OMCT@1.875°. Due to the over-estimated trends, OMCT@1° leads to worse results in the near-coastal regions. Solving these remaining problems within the OMCT data will probably lead to further improved AOD products and thus improved GRACE and future gravity field time series.

10.3. An alternative time span for the mean fields

In this chapter the effect of changing the subtracted mean field is investigated. As described in chapter 3, a mean surface pressure field and a mean ocean pressure field is usually subtracted from the instantaneous atmospheric pressure as well as from the ocean bottom pressure in order to analyze gravitational variations. By definition the mean mass distribution of the atmosphere and ocean belongs to the static part of the gravity field. Only deviations from the mean value are taken into account during atmospheric and oceanic de-aliasing. In the current GFZ processing, mean fields (GFZmeans) covering a two year period (2001+2002) are subtracted. By substituting these mean fields by alternative ones, we get insight into the importance of these mean values for the de-aliasing process as well as for the GRACE processing.

Three different mean fields are considered:

- GFZmean = mean ocean bottom pressure and atmospheric pressure covering the period 2001 and 2002 (as it is used in the standard (GFZ) de-aliasing process)
- GOCEmean = mean ocean bottom pressure and atmospheric pressure covering the period 2004 to 2007 (the same mean fields are used in the GOCE processing (*Bouman et al.*, 2009), thus this scenario is called GOCEmean)
- MONTHLYmean = mean ocean bottom pressure and atmospheric pressure covering the period of the corresponding month

In the following, the GOCEmean and MONTHLYmean scenarios are compared to the GFZmean. Figures 10.23 and 10.24 show the applied mean fields and their differences. Figure 10.23d shows, that the differences of the GFZmean and GOCEmean in the vertically integrated atmospheric pressure are highly correlated with the topography (e.g. Himalaya - Hindu Kush - region, Andes, Rocky Mountains, etc.). The correlation with the topography is probably due to the fact, that ECMWF's atmospheric model was subject to a model change in February 2006 (cf. e.g. Sect. 10.1). And due to the fact, that the GOCEmean is computed covering the period 2004 to 2007, this model change, where also the orography has been changed, is reflected in the differences. But also in Antarctica the GOCEmean shows signifcant deviations from the GFZmean. Over the ocean (cf. Fig. 10.23e) larger differences appear in regions with high atmospheric variability. In addition, significant differences can also be observed around Greenland. The differences over land (especially in mountainous) areas are by a factor 3 to 4 higher than over the ocean, as mentioned before mainly due to the model change in ECMWF data. From Tab. 10.8 it can be concluded, that either subtracting the GFZmean or GOCEmean mean field cause differences in the vertically integrated atmospheric pressure of up to 80 hPa with a rms of 4.66 hPa for $n = 30$.

Having a look at Figs. 10.23f and g, one can see, that the differences in the vertically integrated atmospheric pressure between the GFZmean and MONTHLYmean case are slightly higher than between the GFZmean and GOCEmean scenario. Again, the differences are highly correlated with the topography and show especially over the ocean some similar patterns as the foregoing comparison. This might be again due to a model change of ECMWF data in 2006. Over land, deviations between the GFZmean and MONTHLYmean scenario of up to 81 hPa and a rms of 5.75 hPa for $n = 5$ appear.

	min	max	mean	wrms
GFZmean	541.21	1034.85	996.69	65.91
GOCEmean	541.50	1033.95	996.35	66.29
MONTHLYmean	546.20	1042.12	996.69	66.30
GFZmean - GOCEmean	−73.84	74.32	0.34	4.14
GFZmean - MONTHLYmean	−71.98	81.32	0.00	5.75

Tab. 10.7: Statistics on the mean vertical integrated atmospheric pressure fields GFZmean, GOCEmean, and MONTHLYmean (Aug 2007) and their differences for n=5. Unit: hPa.

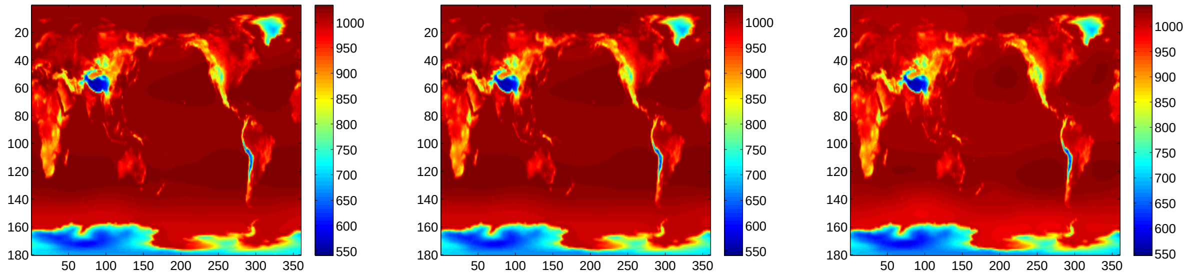

(a) GFZmean (b) GOCEmean (c) MONTHLYmean

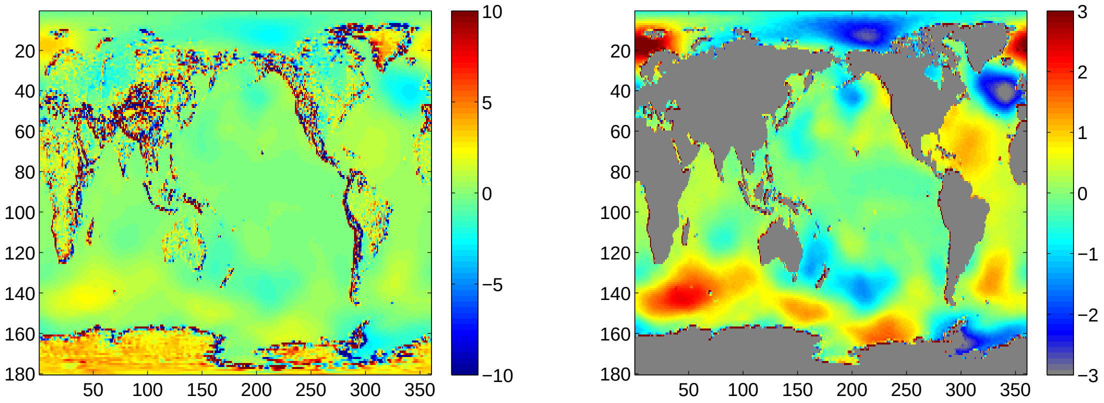

(d) GFZmean - GOCEmean (e) GFZmean - GOCEmean over ocean

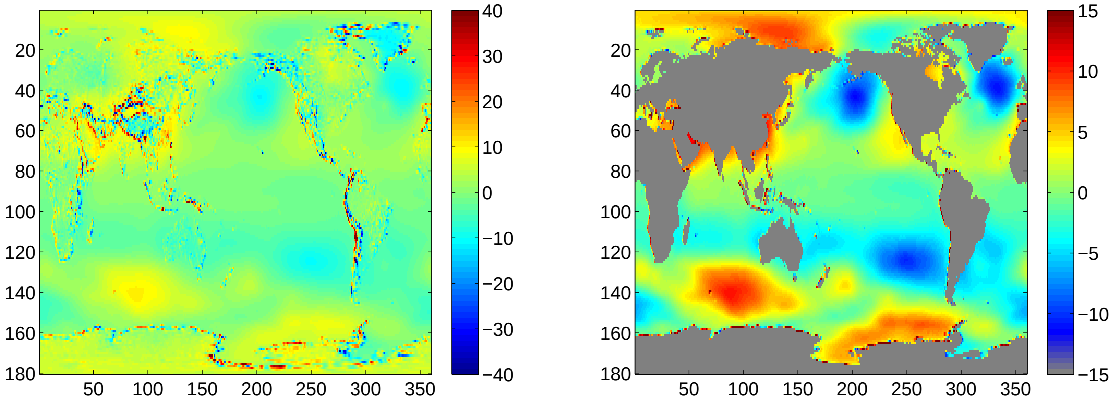

(f) GFZmean - MONTHLYmean (g) GFZmean - MONTHLYmean over ocean

Fig. 10.23: Mean vertical integrated atmospheric pressure fields for n=5. (a) GFZmean, (b) GOCEmean, (c) MONTHLY-mean (Aug 2007), (d) GFZmean minus GOCEmean, (e) GFZmean minus GOCEmean: over ocean, (f) GFZmean minus MONTHLYmean, (g) GFZmean minus MONTHLYmean: over ocean. Unit: hPa.

Analyzing the mean ocean bottom pressure differences (cf. Fig. 10.24d,e), one can say that in both comparisons especially south-west of Africa and south of Greenland higher differences appear between the three mean fields. Compared to the atmospheric pressure, in general the differences in the ocean bottom pressure mean fields are smaller. The differences between the GFZmean and GOCEmean are in the range of -10.27 hPa to +5.52 hPa with a mean of 0.2 Pa and a global rms of 0.73 hPa, while the differences between the GFZmean and MONTHLYmean scenario are with maximum -21.36 hPa and a global rms of 2.96 hPa slightly larger (cf. Tab. 10.9).

	GFZmean - GOCEmean				GFZmean - MONTHLYmean			
degree n	min	max	mean	wrms	min	max	mean	wrms
1	-74.66	73.50	0.17	4.12	-72.31	81.53	-0.07	5.76
5	-73.84	74.32	0.34	4.14	-71.98	81.32	0.00	5.75
10	-72.80	75.35	0.56	4.18	-71.56	81.06	0.09	5.75
20	-70.67	77.47	1.00	4.36	-70.70	80.52	0.27	5.74
30	-68.47	79.65	1.46	4.66	-69.80	79.95	0.47	5.75
50	-68.83	84.21	2.44	5.59	-67.90	78.72	0.88	5.79
70	-58.88	89.05	3.49	6.87	-65.84	77.38	1.33	5.88
91	-53.29	94.62	4.67	8.50	-63.50	75.84	1.86	6.05

Tab. 10.8: Statistics on the differences between the mean vertically integrated atmospheric pressure fields GFZmean, GOCEmean, and MONTHLYmean (Aug 2007) for various degrees n. Unit: hPa.

We can summarize, that there are significant differences in the GFZmean, GOCEmean, and MONTHLYmean concerning the ocean as well as the atmospheric pressure. Differences are up to almost 80 hPa in the vertically integrated atmospheric pressure (depending on the analyzed degree n) and approximately 11 hPa in the ocean bottom pressure between the GFZmean and GOCEmean case. Slightly larger differences of up to 81 hPa in the vertically integrated pressure and approximately 21 hPa in the ocean bottom pressure occur between the GFZmean and MONTHLYmean scenario.

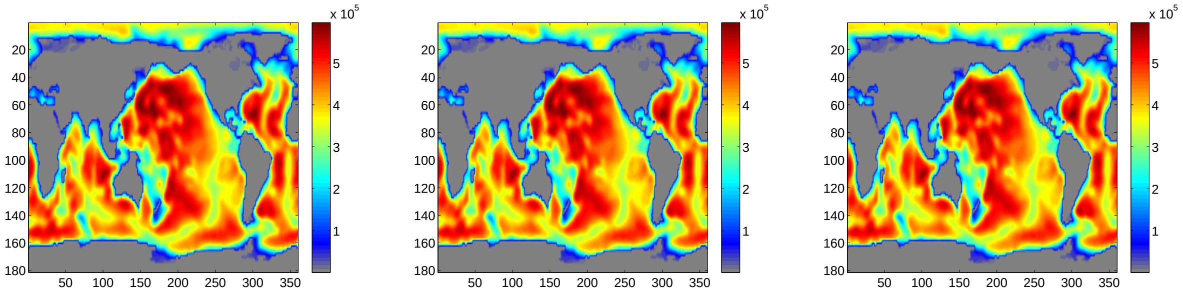

(a) GFZmean (b) GOCEmean (c) MONTHLYmean

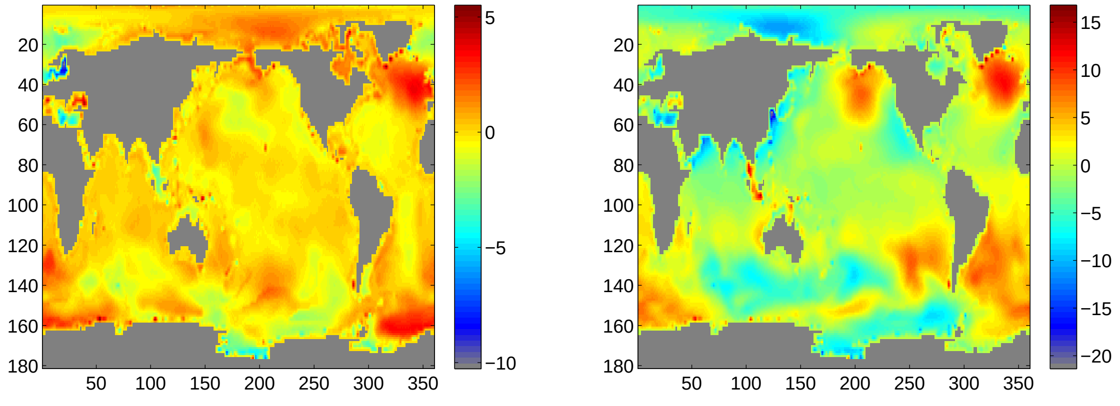

(d) GFZmean - GOCEmean (e) GFZmean - MONTHLYmean

Fig. 10.24: Mean ocean bottom pressure fields. (a) GFZmean, (b) GOCEmean (c) MONTHLYmean (d) GFZmean minus GOCEmean, (e) GFZmean minus MONTHLYmean (Aug 2007). Unit: hPa.

	min	max	mean	wrms
GFZmean [10^5 hPa]	0.00	5.96	2.67	2.04
GOCEmean [10^5 hPa]	0.00	5.96	2.67	2.04
MONTHLYmean [10^5 hPa]	0.00	5.96	2.67	2.04
GFZmean - GOCEmean [hPa]	-10.27	5.52	0.00	0.73
GFZmean - MONTHLYmean [hPa]	-21.36	16.79	0.00	2.96

Tab. 10.9: Statistics on the mean ocean bottom pressure fields GFZmean, GOCEmean, MONTHLYmean (Aug 2007) and their differences.

Impact of the alternative mean fields on the AOD product

The effect of the various mean fields on the AOD are shown in Fig. 10.25. Here, we see the mean AOD product for August 2007, after subtracting the GFZmean (Fig. 10.25a), GOCEmean (Fig. 10.25b), and MONTHLYmean (Fig. 10.25c), and the resulting differences (Fig. 10.25d,e). Subtracting the GOCEmean instead of the GFZmean has an effect of maximum 2.85 mm in terms of geoid heights. As the differences between the GFZmean and GOCEmean are constant over time, the effect on the mean monthly AOD product is also constant. Comparing Figs. 10.23d,e and 10.24d with Fig. 10.25d some correlation patterns can be recognized. Especially, the large differences of the vertically integrated atmospheric pressure (Fig. 10.23d,e) in the Himalaya and Andes are reflected in the AOD differences (Fig. 10.25d). Larger discrepancies also appear in the whole pacific region, the Antarctic as well as in the oceanic areas South of Africa, which are probably due to the ocean bottom pressure differences of the mean fields (cf. Fig. 10.24d).

The differences between the AOD coefficients after subtraction of the GFZmean or the MONTHLYmean show similar patterns, but are by approximately a factor 3 larger than the differences between GFZmean and GOCEmean. Depending on the analyzed month, deviations of up to 8 mm can occur in the de-aliasing product.

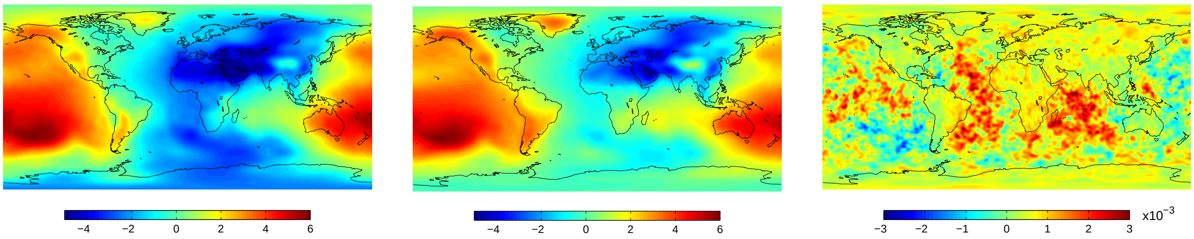

(a) GFZmean (b) GOCEmean (c) MONTHLYmean

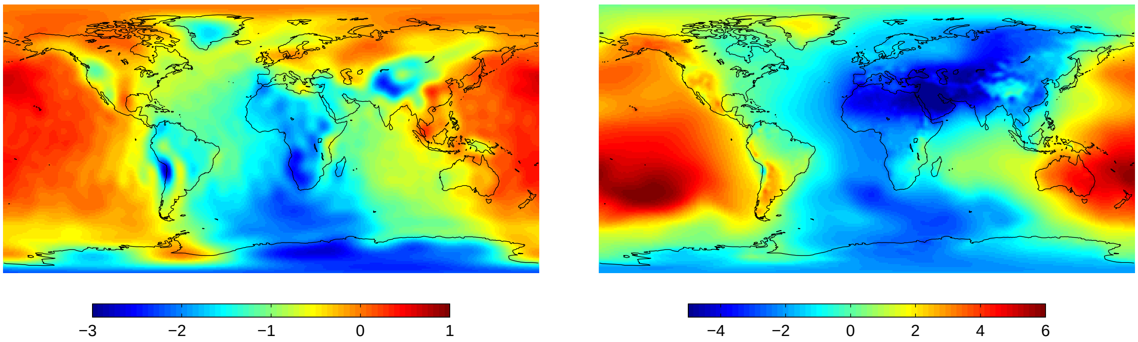

(d) GFZmean - GOCEmean (e) GFZmean - MONTHLYmean

Fig. 10.25: Monthly mean of the GFZmean, GOCEmean, and MONTHLYmean AOD products and their differences in terms of geoid heights for August 2007. Unit: mm.

	min	max	mean	wrms
GFZmean	-6.03	5.90	0.37	2.61
GOCEmean	-4.86	5.91	1.06	2.12
MONTHLYmean	-0.00	-0.00	-0.00	0.00
GFZmean - GOCEmean	-2.85	0.66	-0.69	0.74
GFZmean - MONTHLYmean	-6.36	6.04	0.48	2.62

Tab. 10.10: Statistics on the differences between the GFZmean, GOCEmean, and MONTHLYmean (Aug 2007) AOD products in terms of geoid heights. Unit: mm.

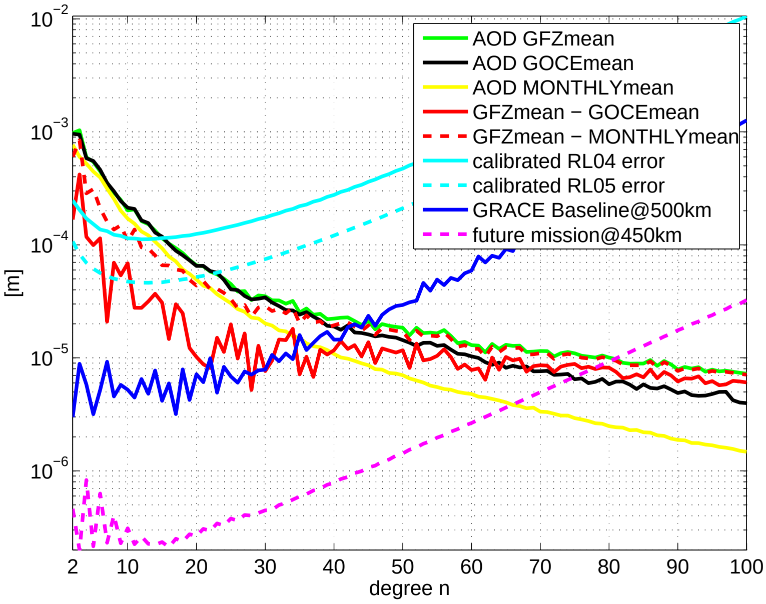

Fig. 10.26: Differences between the GFZmean, GOCEmean, and MONTHLYmean AOD products in terms of degree standard deviations for geoid heights. August 2007. Unit: m.

The effect of either applying the GFZmean, GOCEmean or MONTHLYmean can also be analyzed in terms of degree standard deviations of geoid heights. The continuous and dotted red lines in Fig. 10.26 represent the differences between the GFZmean and GOCEmean, or respectively, GFZmean and MONTHLYmean AOD products. Subtracting the four year mean field (GOCEmean) instead of the two year mean field (GFZmean) is hardly in the sensitivity range of current GRACE results (cf. cyan lines in Fig. 10.26 with continuous red line), but for d/o smaller than 30 and approx. 80 clearly in the sensitivity range of the GRACE baseline and error prediction of future gravity field missions (blue and magenta dotted line in Fig. 10.26). Applying the MONTHLYmean AOD product instead of the GFZmean has a more significant effect and is up to d/o 20 clearly above the current GRACE error, up to d/o 40 still above the GRACE baseline, and up to d/o 80 also in the sensitivity range of the simulated future gravity field mission.

Impact of the alternative mean fields on a monthly gravity field solution

Applying the GOCEmean instead of the GFZmean AOD product has an effect of maximum 1.88 *mm* on a monthly gravity field solution.

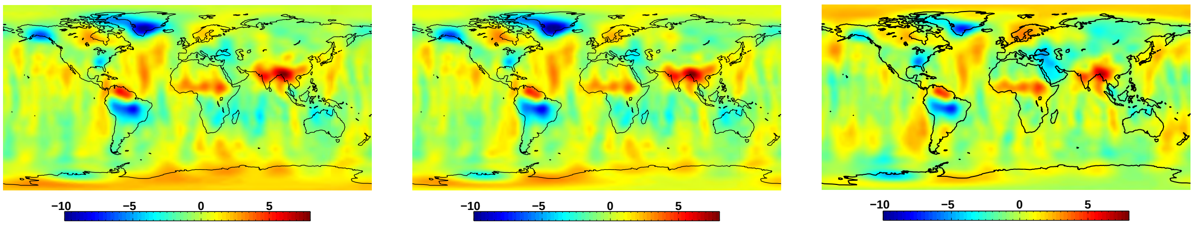

(a) GFZmean (b) GOCEmean (c) MONTHLYmean

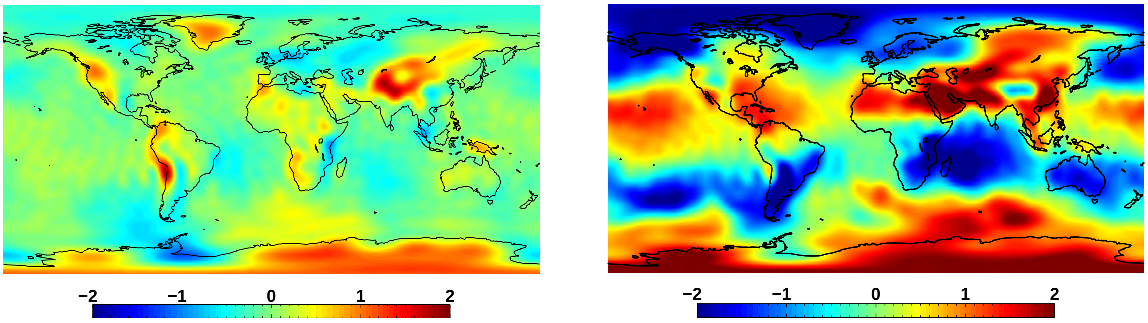

(d) GFZmean - GOCEmean (e) GFZmean - MONTHLYmean

Fig. 10.27: Differences between the monthly gravity field solutions after subtracting the GFZmean, GOCEmean, and MONTHLYmean AOD products. August 2007. Unit: mm.

	min	max	mean	wrms
GFZmean	-10.09	8.06	0.01	1.52
GOCEmean	-11.02	8.13	0.01	1.52
MONTHLYmean	-7.67	7.13	0.01	1.44
GFZmean - GOCEmean	-1.21	1.88	-0.58e-3	0.36
GFZmean - MONTHLYmean	-3.53	3.16	1.70e-3	1.11

Tab. 10.11: Statistics on the differences between the monthly gravity field solutions after applying the GFZmean, GOCEmean, and MONTHLYmean AOD products. Unit: mm. The numbers for GFZmean-GOCEmean are valid for each month, as the offset between the GFZmean, GOCEmean scenario is constant. The numbers for GFZmean-MONTHLYmean show the differences for August 2007.

Comparing Fig. 10.27d with Fig. 10.25d, some 'inverse correlation patterns' can be clearly recognized. These correlations demonstrate that the differences in the AOD coefficients are propagated further on to the monthly gravity field solutions. As there is a whole parametrization process in between the AOD product and the determination of monthly gravity field solutions, the maximum, minimum, and mean amplitudes of the differences are damped (cf. Tabs. 10.10 and 10.11). While the effect of GFZmean vs. GOCEmean on AOD level has a mean global effect of -0.69 *mm*, it has almost none on the monthly gravity field solution level (0.6 μm), although the maximum and minimum differences in a monthly gravity field solution can reach several millimeters.

Analyzing the differences in the monthly gravity field solutions, obtained after applying the GFZmean or MONTHLYmean AOD product, leads to similar conclusions: the AOD differences are further propagated to the monthly gravity field solutions (cf. inverse correlation patterns in Figs. 10.27e and Fig. 10.25e), and the effect on the level of the monthly gravity field solutions is damped compared to the one on AOD level. Maximum differences in the monthly gravity field solution of more than 3 *mm* appear. Regarding the weighted global rms of the monthly gravity field solutions in Tab. 10.11 reveals, that applying the MONTHLYmean instead of the GFZmean AOD reduces/improves the rms by about 5.3 %.

Impact of the alternative mean fields on the KBRR-residuals

Analyzing the rms over 1 year of KBRR-residuals as a function of latitude and longitude in an Earth-fixed system, one can state that compared to the GFZmean the GOCEmean AOD leads to a higher rms in Northern and Southern Greenland, in the Himalaya region as well as in large areas of Antarctica (cf. blue regions in Fig. 10.28d). The intention of the de-aliasing process is to reduce high-frequent signal from the satellite observations. High frequent signals are more or less equal to a higher rms in the KBRR-residuals. Thus, in the above named regions the GFZmean fits better to the modelled world than the GOCEmean as the rms of the KBRR-residuals is smaller. In the ocean areas, in contrast, around latitudes of $-60°$ to $+60°$ there seems to be a slight trend to a reduced and thus improved rms of the KBRR-residuals by using the GOCEmean. This can be confirmed when having a look at the 5-seconds KBRR-residual differences (first row in Fig. 10.29). The red color indicates that the KBRR-residuals are reduced/improved by using the GOCEmean AOD product w.r.t. the GFZmean AOD product. Blue indicates regions where the standard GFZmean product reveals smaller/better residuals. Especially, in the whole Southern ocean region, the KBRR-residuals could have been slightly reduced by using the GOCEmean AOD. For the Arctic region the GFZmean seems to lead to better (smaller KBRR-residuals) results.

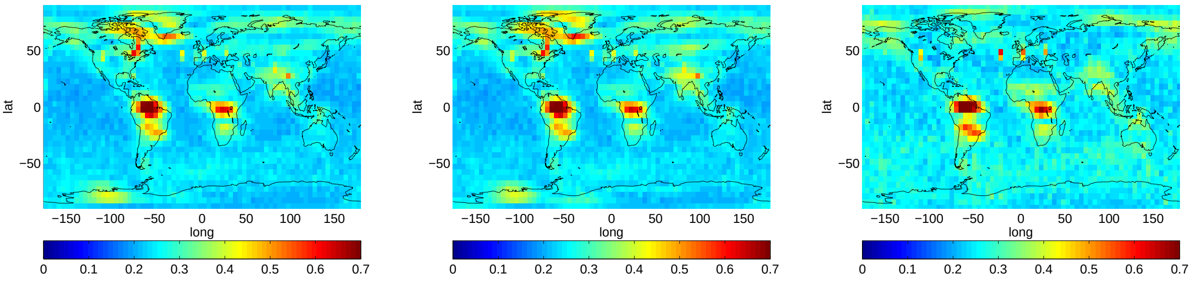

(a) GFZmean (b) GOCEmean (c) MONTHLYmean

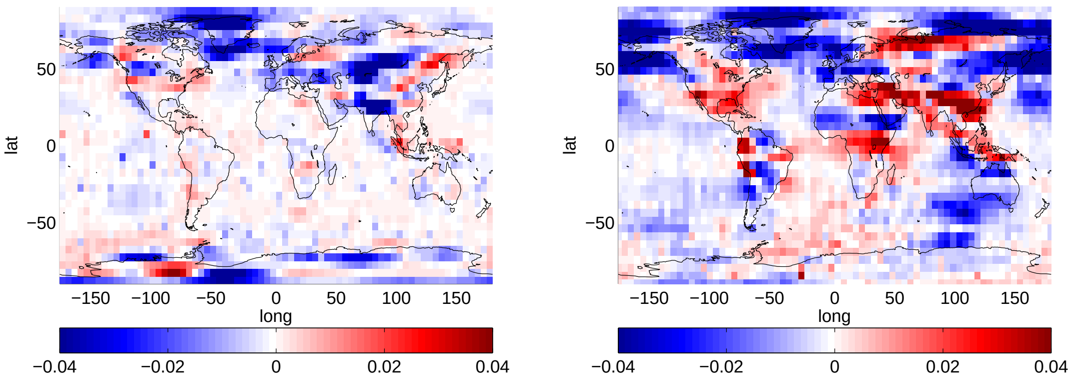

(d) GFZmean - GOCEmean (e) GFZmean - MONTHLYmean

Fig. 10.28: Rms over 1 year (2007) or, respectively, 5 months (Aug to Dec 2007) of KBRR-residuals in bins of $5° \times 5°$ in longitude and latitude. (a) GFZmean, (b) GOCEmean, (c) MONTHLYmean and their differences (d) GFZmean - GOCEmean, (e) GFZmean - MONTHLYmean. Unit: μm/s.

However, plotting the KBRR-residuals over time (Fig. 10.32a), latitude (Fig. 10.35a) and longitude (Fig. 10.35b) no significant differences can be observed between applying the GFZmean or the GOCEmean. The same conclusion can be drawn after analyzing the spectral content (Fig. 10.30) as well as the daily rms of the KBRR-residuals over 1 year (Fig. 10.33). The statement, that there is no significant effect on the KBRR-residuals using either the GFZmean or the GOCEmean AOD product for de-aliasing, has already been indicated when analyzing the degree standard deviation differences between the two AOD products (cf. Fig. 10.26). There, we have already stated, that the AOD differences between the two mean field scenarios is barely in the sensitivity range of current GRACE solutions. Compared to the effect of an enhanced spatial resolution of the ocean model (cf. Sect. 10.2) the effect of applying an alternative mean field for the de-aliasing process is much smaller, approximately by a factor of 3.

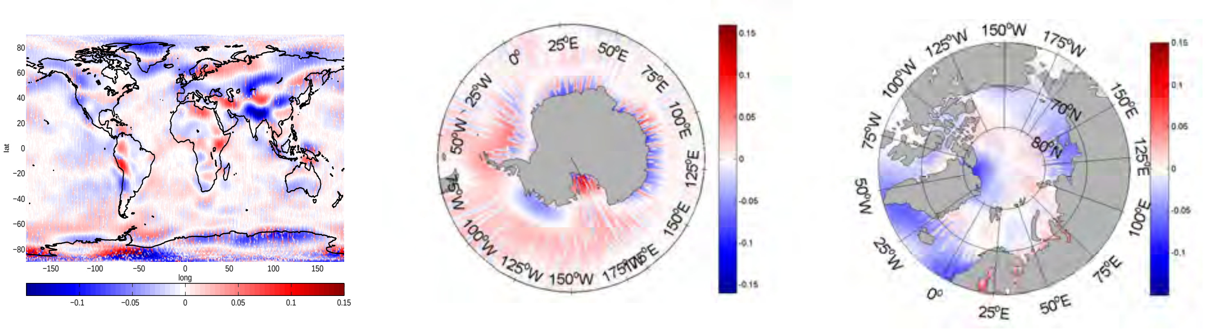

GFZmean - GOCEmean GFZmean - GOCEmean GFZmean - GOCEmean

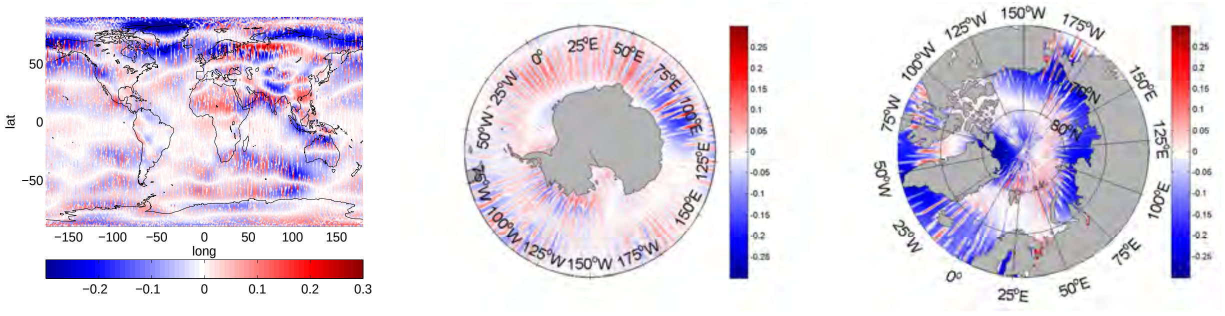

GFZmean - MONTHLYmean GFZmean - MONTHLYmean GFZmean - MONTHLYmean

Fig. 10.29: KBRR-residual differences for 2007 or respectively 5 months (Aug to Dec 2007) in bins of 1° × 1° in longitude and latitude between the GFZmean, GOCEmean and MONTHLYmean scenario. Red indicates that the KBRR-residuals are reduced/improved by using the GOCEmean or MONTHLYmean AOD product w.r.t. the GFZmean AOD product. Blue indicates regions where the standard GFZmean product reveals smaller (better) residuals. Unit: µm/s.

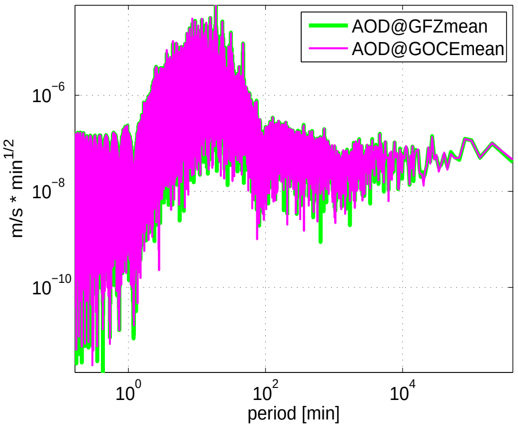

Fig. 10.30: PSD of 1 year (2007) of KBRR-residuals after removing the GFZmean AOD (green) and GOCEmean AOD (magenta).

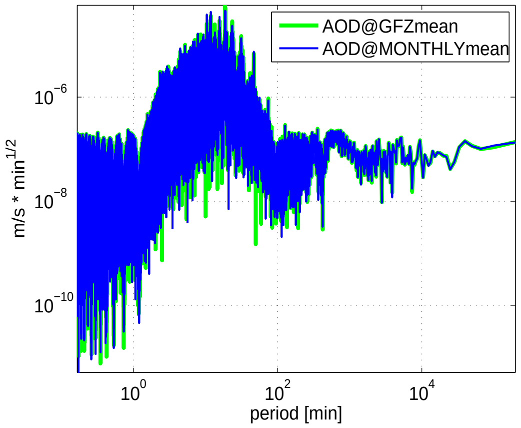

Fig. 10.31: PSD of 5 months (Aug to Dec 2007) of KBRR-residuals after removing the GFZmean AOD (green) and MONTHLYmean AOD (blue).

The effect of the MONTHLYmean compared to the GFZmean AOD product is examined for a time-span of 5 months. The blue regions in Fig. 10.28e illustrate that the MONTHLYmean AOD product leads to higher rms values especially in oceanic regions north of 50° latitude. In contrast, the MONTHLYmean leads to smaller rms values and thus better results in Northern America, central Africa, and the South-Atlantic.

Having a look at the 5-seconds KBRR-residual differences (second row in Fig. 10.29), one can see, that the effect of either applying the GFZmean or MONTHLYmean AOD is in general smaller in oceanic regions than in continental ones - with the exception of regions north of 50° latitude.

Analyzing the KBRR-residuals over time (cf. Fig. 10.32b and Fig. 10.34) one can clearly see, that the residuals for the GFZmean and MONTHLYmean significantly diverge for November and December 2007. Considering the daily rms of the KBRR-residuals, one can state, that the residuals are increased by about 1.5 % when applying the MONTHLYmean AOD scenario. The psd of the two scenarios in Fig. 10.31 show significant differences for periods between 1 minute and 1.7 hours. The MONTHLYmean AOD 'removes' more high-frequent variations than the GFZmean product. This is reasonable, as in the MONTHLYmean AOD product only the high-frequent deviations (from the monthly mean atmospheric and oceanic variations) are taken into account.

Figure 10.36a shows slight improvements/reductions of the KBRR-residuals for latitudes around -60° and $+20^{\circ} to {+}40^{\circ}$ when using the MONTHLYmean AOD product. The KBRR-residuals as a function of longitude show a slight increase of the residuals when applying the MONTHLYmean instead of the GFZmean AOD over almost all latitudes.

However, we can summarize, that in general the effect of applying either the MONTHLYmean AOD or the GFZmean AOD has a larger and more significant effect on the KBRR-residuals when comparing it to the GOCEmean scenario.

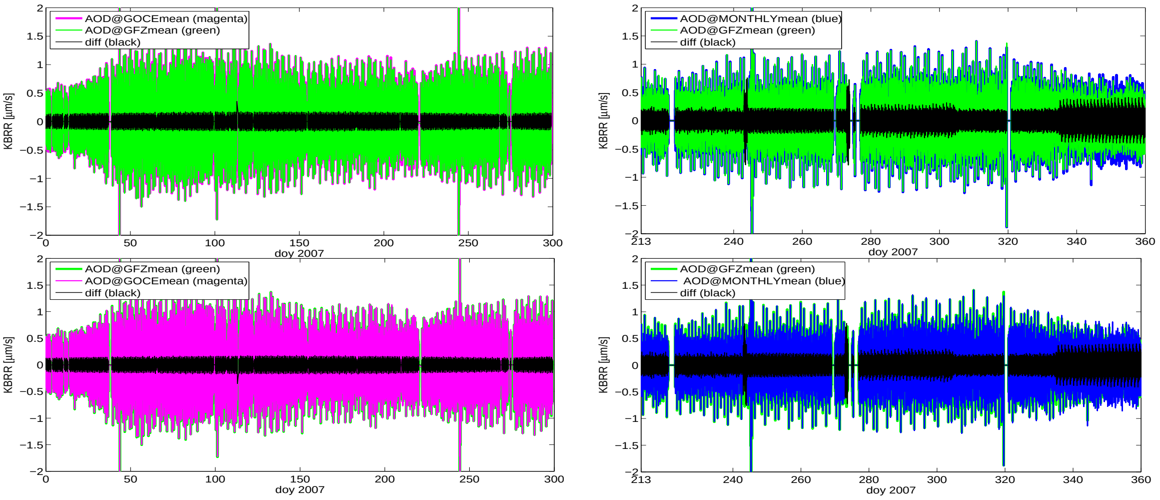

(a) (b)

Fig. 10.32: KBRR-residuals for 2007 or respectively 5 months (Aug to Dec 2007) after removing the GFZmean AOD (green), the GOCEmean AOD (magenta), the MONTHLYmean AOD (blue) and their differences (black). Unit: μm/s.

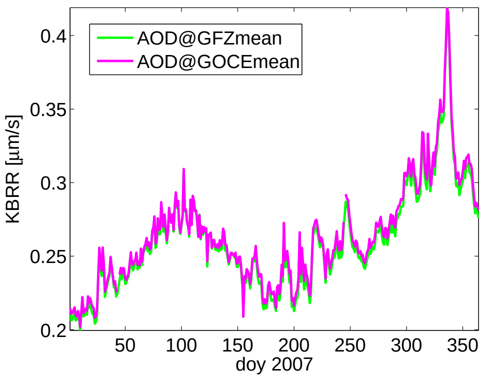

Fig. 10.33: Daily rms of KBRR-residuals for 2007 after removing the GFZmean AOD (green) and GOCEmean AOD (magenta). Unit: μm/s.

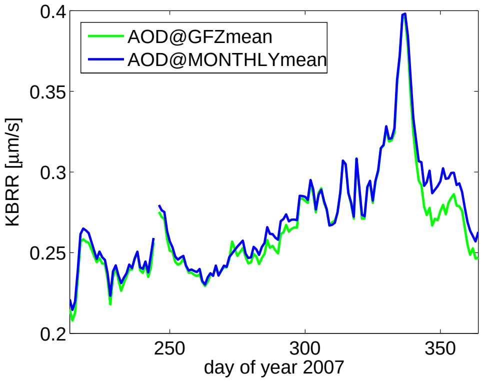

Fig. 10.34: Daily rms of KBRR-residuals for 5 months (Aug to Dec 2007) after removing the GFZmean AOD (green) and MONTHLYmean AOD (blue). Unit: μm/s.

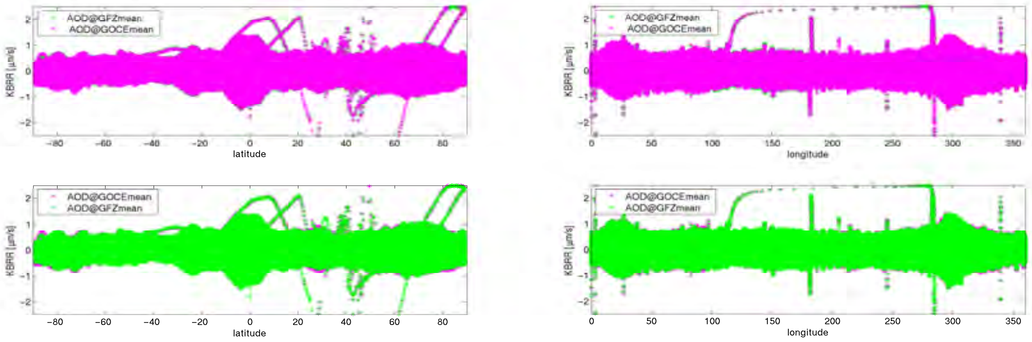

(a) (b)

Fig. 10.35: KBRR-residuals for 2007 against (a) latitude and (b) longitude after removing the GFZmean AOD (green) and GOCEmean AOD (black) product. Unit: μm/s.

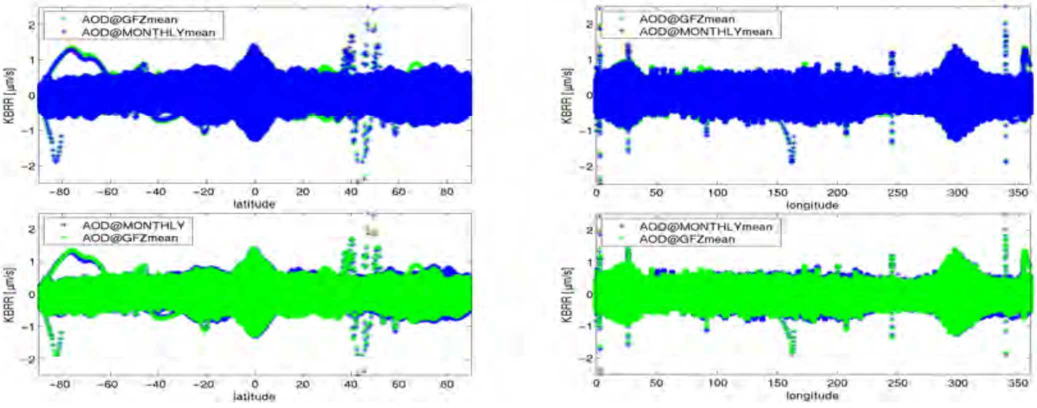

(a) (b)

Fig. 10.36: KBRR-residuals for 5 months (Aug to Dec 2007) against (a) latitude and (b) longitude after removing the GFZmean AOD (green) and MONTHLYmean AOD (blue) product. Unit: μm/s.

Summary - Impact of an alternative time span for the mean-fields

- differences between the vertically integrated atmospheric mean fields GFZmean and GOCEmean/MONTHLYmean can reach up to 80 hPa and are mainly correlated with the topography which is probably due to ECMWF model changes
  (GFZmean - GOCEmean: min: -68.47 hPa, max: 79.65 hPa, mean: 1.46 hPa, rms: 4.66 hPa for degree n=30)
  (GFZmean - MONTHLYmean: min: -69.80 hPa, max: 79.95 hPa, mean: 0.47 hPa, rms: 5.75 hPa for degree n=30)

- differences between the mean ocean bottom pressure fields reach up to maximum 11 hPa for the GOCEmean and 21 hPa for the MONTHLYmean
  (GFZmean - GOCEmean: min: -10.27 hPa, max: 5.52 hPa, mean: 0.00 hPa, rms: 0.73 hPa)
  (GFZmean - MONTHLYmean: min: -21.36 hPa, max: 16.79 hPa, mean: 0.00 hPa, rms: 2.96 hPa)

- differences between the GFZmean and GOCEmean AOD products are constant for all months, are in the mm-range, and thus barely in the sensitivity range of current GRACE gravity field solutions, but still significant concerning the GRACE baseline and error predictions of future gravity field missions
  (min: -2.85 mm, max: 0.66 mm, mean: -0.69 mm, rms: 0.74 mm)

- differences between the GFZmean and MONTHLYmean AOD products vary for each month and reach up almost the cm-level and are thus clearly in the sensitivity range of current GRACE gravity field solutions
  (min: -7.65 mm, max: 3.66 mm, mean: -0.43 mm, rms: 2.28 mm for September 2007)

- whether subtracting the GFZmean or GOCEmean affects a monthly gravity field solution in the mm-range. Again the differences are constant for each month
  (min: -1.21 mm, max: 1.88 mm, mean: 0.00 mm, rms: 0.36 mm)

- whether subtracting the GFZmean or MONTHLYmean can affect a monthly gravity field solution with up to 5 mm
  (min: -3.14 mm, max: 5.09 mm, mean: -0.03 mm, rms: 1.08 mm for December 2007)

- the global weighted rms of the monthly gravity field solutions is only affected by 0.3 % when applying the GFZmean or the GOCEmean
  (1.519 mm for GFZmean vs. 1.524 mm for GOCEmean)

- depending on the analyzed month, the global weighted rms of the monthly gravity field solutions is decreased by up to 5.3 % and increased by up to 30 % when applying the GFZmean instead of the MONTHLYmean AOD product
  (1.52 mm for GFZmean vs. 1.44 mm for MONTHLYmean in August 2007)
  (1.97 mm for GFZmean vs. 2.64 mm for MONTHLYmean in December 2007)

- the daily rms of the KBRR-residuals over 2007 is slightly reduced ($\sim$ 1.6 %) when subtracting the GFZmean

- the daily rms of the KBRR-residuals over August to December 2007 is slightly increased ($\sim$ 1.5 %) when subtracting the MONTHLYmean

- the improvement by either subtracting the GFZmean or GOCEmean on the rms of KBRR-residuals is ambiguous. There are regions where the GFZmean performs slightly better than the GOCEmean, and vice versa. The rms of the KBRR-residuals is affected in the nm/s-range
  (min: -72.33 nm/s, max: 45.26 nm/s, mean: -4.37 nm/s, rms: 11.42 nm/s)

- the improvement by either subtracting the GFZmean or MONTHLYmean on the rms of KBRR-residuals is ambiguous. There are regions where the GFZmean performs better than the MONTHLYmean, and vice versa. The rms of the KBRR-residuals is affected in the nm/s-range
  (min: -92.52 nm/s, max: 104.90 nm/s, mean: -7.83 nm/s, rms: 21.15 nm/s)

10.4. Using daily GRACE solutions for an additional 'hydrological' de-aliasing

In this chapter a so-called AOHD de-aliasing product is determined and applied during GRACE gravity field processing. This means, that besides atmospheric (A) and oceanic (O) mass variations also hydrologic (H) mass variations are removed during the de-aliasing process. For the high-frequent, hydrological mass variations daily ITG-GRACE (see Sect. 7.1) solutions are used.
With the following investigation we want to assess the quality and the 'hydrological' content of the daily ITG-GRACE solutions. Do they really only contain hydrological signal? Are there any other effects contained? Is it reasonable to apply an additional hydrological de-aliasing?

Based on the assumption that all background models (tides, AOD,...) are error-free and reflect the 'true world', the daily ITG-GRACE solutions should mainly contain hydrological signal (apart from instrument errors and unmodelled processes, like ice melting and post-glacial rebound (PGR)). An additional hydrological de-aliasing, therefore, is expected to reduce the KBRR-residuals significantly, especially the strong annual variation should no longer be visible in the KBRR-residuals. Secondly, we expect the reduction mainly on the continents and mainly in regions with high hydrological signals, e.g., in the Amazon, Ganges or Zambezi region. If there are significant improvements of the KBRR-residuals in regions with less hydrological variations, e.g. in oceanic regions, one could assume that the daily ITG-GRACE solutions not only contain hydrological signal, but can also be used to improve the existing atmospheric and oceanic models. This last issue has also been investigated by *Bonin and Chambers* (2011). They compared the daily ITG-GRACE solutions over the ocean with the high-frequency component of sea level variability measured by satellite altimetry and concluded that the true sub-monthly variability in non-tidal ocean mass variability is not adequately represented by the current AOD model, but by the daily ITG-GRACE solutions. At the end, they suggested to use GRACE data itself to improve the de-aliasing model for future GRACE data releases. We will investigate in the following, if we can draw the same conclusions.

Impact of the daily GRACE-solutions on the AOD product

First of all, the daily GRACE solutions are linearly interpolated on a 6-hourly resolution and added to the atmospheric and oceanic potential coefficients. The hereby gained AOHD product is now used for de-aliasing and the results are compared to the standard case, where only the atmospheric and oceanic potential coefficients (AOD) are applied during GRACE gravity field processing. Figure 10.37 shows the AOD (first row) and AOHD (second row) products, as well as their differences (third row) for three months in terms of geoid heights. The first thing we can observe, is that the daily ITG-GRACE solutions clearly contain the expected hydrological signal, which is reflected in the rather strong signal in the main basins of the Earth (Amazon, Ganges, Zambezi). The second issue we can observe, is that also a significant signal due to ice-melting (cf. Greenland) is visible in the daily ITG solutions. This could have been expected, as 'ice' is not contained in the background models, which are 'reduced' from the GRACE solutions in the de-aliasing process. Furthermore, which is more surprising, rather strong signal in oceanic regions can be observed within the daily ITG solutions. The maximum amplitude of the geoid variations induced by AOHD are by a factor 2-3 higher than the variations caused by only AOD (cf. Tab. 10.12). Regarding the degree standard deviations for AOD and AOHD (Fig. 10.38), we can retain, that using AOHD instead of AOD will have for sure a significant impact on current GRACE results (cf. magenta and black dotted line in Fig. 10.38).

	Jan 2007				Aug 2007				Dec 2007			
	min	max	mean	wrms	min	max	mean	wrms	min	max	mean	wrms
AOD	-6.41	7.37	-1.10	2.60	-6.03	5.90	0.37	2.61	-5.07	5.22	-1.41	1.97
AOHD	-12.65	7.30	-1.10	2.88	-12.60	7.03	0.37	0.37	-15.82	5.09	-1.41	2.45
diff.	-4.59	6.97	1.25	1.25	-7.55	13.43	-5.06	2.03	-5.25	11.59	0.00	1.38

Tab. 10.12: Statistics on the AOD and AOHD coefficients and their differences in terms of geoid heights for January, August, and December 2007. Unit: mm.

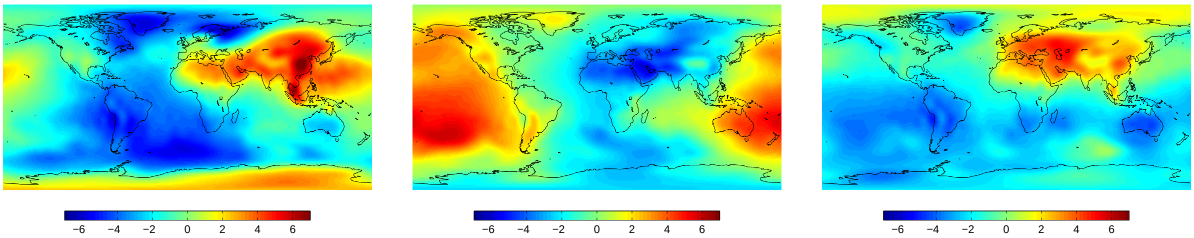

(a) AOD - Jan (b) AOD -Aug (c) AOD - Dec

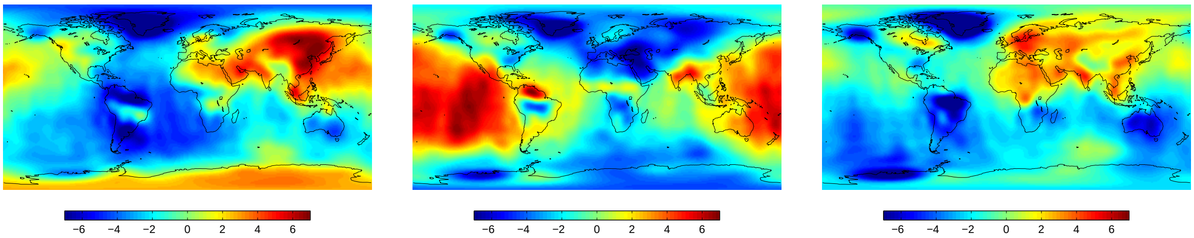

(d) AOHD - Jan (e) AOHD - Aug (f) AOHD - Dec

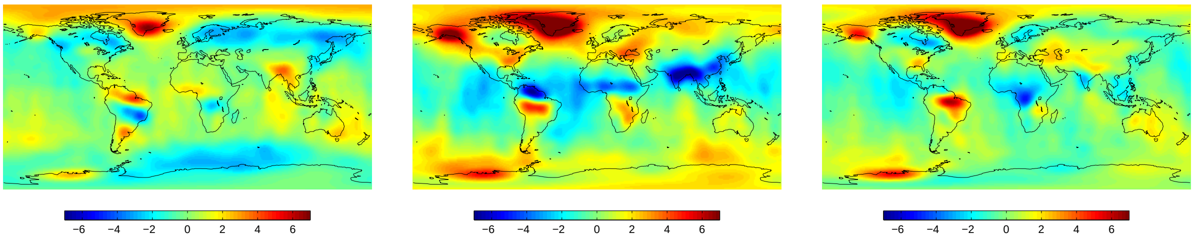

(g) Diff - Jan (h) Diff - Aug (i) Diff - Dec

Fig. 10.37: Monthly mean of the AOD and AOHD products and their differences in terms of geoid heights for January (first column), August (mid column) and December (third column) 2007 . Unit: mm.

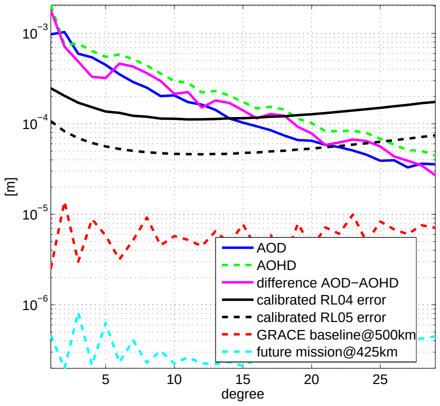

Fig. 10.38: Differences between AOD and AOHD in terms of degree standard deviations for geoid heights. August 2007, Unit: m.

Impact of the additional hydrological de-aliasing on a monthly gravity field solution

Monthly GRACE gravity field solutions mainly contain hydrological signal. By applying AOHD most of this signal should have been 'removed', as the daily ITG-GRACE solutions are supposed to contain exactly this hydrological signal. Figure 10.39 shows, that this is the case. The main hydrological signal in the Amazon, Zambezi or Ganges basin disappears (cf. second row in Fig. 10.39) and the remaining signal content of the monthly gravity field solutions is significantly minimized. The maximum, minimum and mean amplitudes of the monthly gravity field solution differences can reach up to almost 7 *mm*, -11 *mm* and 0.01 *mm* for August 2007 (cf. Tab. 10.13). Again, we can observe, that the differences in the AOD/AOHD coefficients are almost propagated one-to-one to monthly gravity field differences, as there is a high correlation between the spatial patterns in Fig. 10.37g & Fig. 10.39g, Fig. 10.37h & Fig. 10.39h, and Fig. 10.37i & Fig. 10.39i.

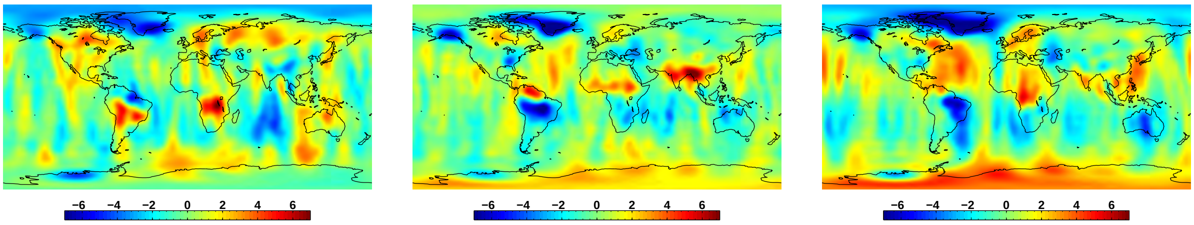

(a) AOD - Jan (b) AOD -Aug (c) AOD - Dec

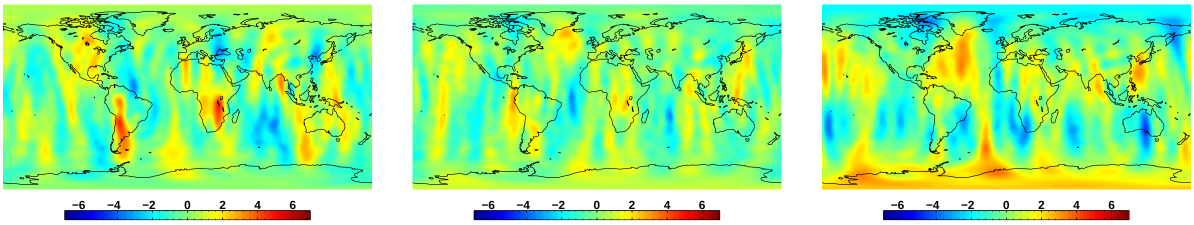

(d) AOHD - Jan (e) AOHD - Aug (f) AOHD - Dec

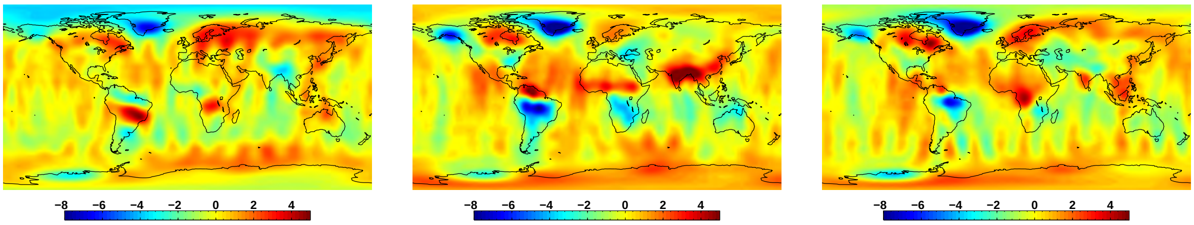

(g) Diff - Jan (h) Diff - Aug (i) Diff - Dec

Fig. 10.39: Monthly gravity field solutions after applying the AOD and the AOHD product and their differences in terms of geoid heights for January, August and December 2007. Unit: mm.

	Jan 2007				Aug 2007				Dec 2007			
	min	max	mean	wrms	min	max	mean	wrms	min	max	mean	wrms
AOD	-6.64	7.33	0.01	1.61	-10.09	8.06	0.01	1.52	-9.30	5.65	-0.02	1.97
AOHD	-3.63	4.80	-0.01	1.15	-3.62	3.12	0.00	0.87	-4.67	3.59	-0.01	1.40
diff.	-7.04	4.92	0.02	1.32	-10.56	6.66	0.01	1.46	-10.59	4.99	0.00	1.37

Tab. 10.13: Statistics on the monthly gravity field solutions after applying the AOD and the AOHD product and their differences. January, August, and December 2007. Unit: mm

Impact of the additional hydrological de-aliasing on the KBRR-residuals

Analyzing the differences in the global rms over 1 month of KBRR-residuals (cf. Fig. 10.40c), we can state, that the introduced AOHD product (Fig. 10.37d,h) is clearly reflected in the rms differences. Also here, the main hydrological signal disappears when using AOHD instead of AOD. Regarding the rms-differences one can retain, that the rms of the KBRR-residuals could have been reduced/improved almost globally (red color in Fig. 10.40c) by using AOHD instead of AOD. Not only in the main hydrological regions of the Earth, but also in the oceanic regions the rms of the KBRR-residuals is reduced when using AOHD. Only some few regions (e.g., Antarctic) remain, where the rms is increased/degraded by using AOHD.

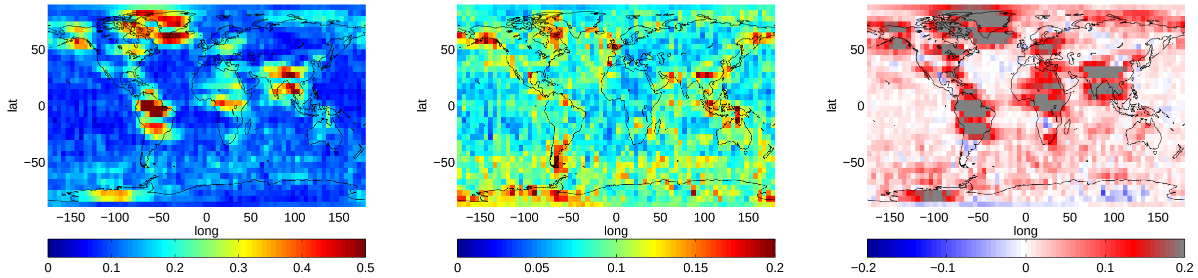

(a) (b) (c)

Fig. 10.40: Rms over one month (Aug 2007) of KBRR-residuals in bins of 5° × 5° in longitude and latitude. (a) AOD, (b) AOHD, (c) and the differences (a) minus (b), Unit: µm/s.

The same conclusions can be drawn for the KBRR-residual differences between the AOD and AOHD scenario, which are illustrated in Fig. 10.42 for January, August and December 2007. Again, the red color indicates regions where the additional hydrological de-aliasing reveals better (smaller) residuals than the standard AOD product. Besides the main hydrological basins, clear improvements are visible in the oceanic regions, e.g., South of Greenland (cf. Fig. 10.42e) or in the Southern oceanic regions.

Also the 5-second KBRR-residuals, plotted against time (cf. Fig. 10.41), show the significant signal reduction of the KBRR-residuals when applying the AOHD product. Having a look at Fig. 10.43, the removal of the main hydrological signal can be clearly seen in the reduction of the daily rms of the KBRR-residuals. The annual (hydrological) variation could have been clearly removed from the KBRR-residuals.

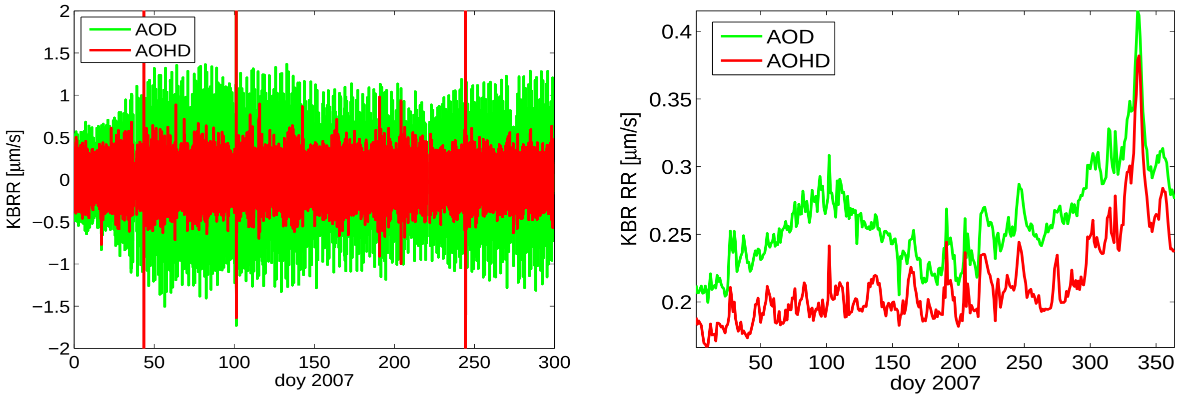

(a) (b)

Fig. 10.41: KBRR-residuals (a) and daily rms (b) of the KBRR-residuals for 2007 after removing the AOD (green) and AOHD (red). Unit: µm/s.

Analyzing the two time series in the frequency domain, one can observe a significant reduction of the amplitudes of the spectral lines when applying AOHD (cf. red and green spectral lines in Fig. 10.43). The reductions are clearly visible down to periods of 3 minutes.

As expected, also the KBRR-residuals, plotted against latitude (Fig. 10.44a) and longitude (Fig. 10.44b), show, that the residuals can be improved globally - and not only in regions with high hydrological variations - when using AOHD.

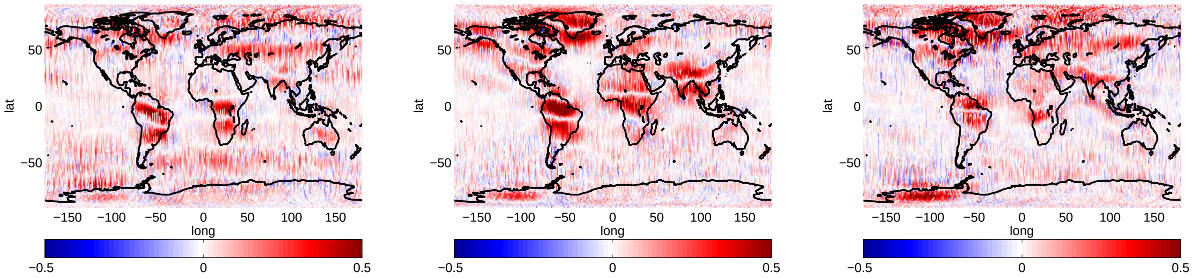

(a) Jan (b) Aug (c) Dec

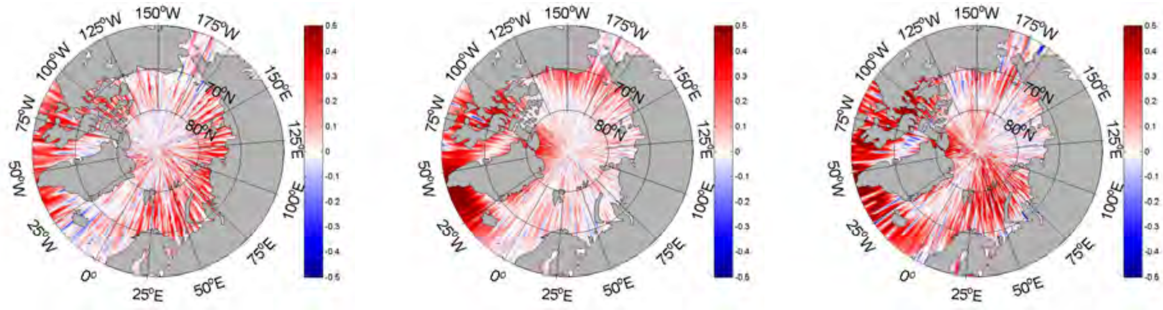

(d) Jan (e) Aug (f) Dec

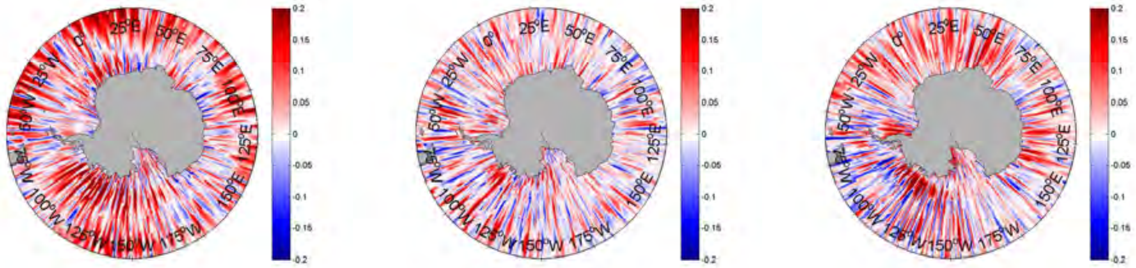

(g) Jan (h) Aug (i) Dec

Fig. 10.42: KBRR-residual differences in bins of $1^\circ \times 1^\circ$ *in longitude and latitude between the AOD and AOHD case. Red indicates that the KBRR-residuals are reduced/improved by using AOHD w.r.t. AOD. Blue indicates regions where the standard AOD product shows smaller (better) residuals. Unit:* $\mu m/s$.

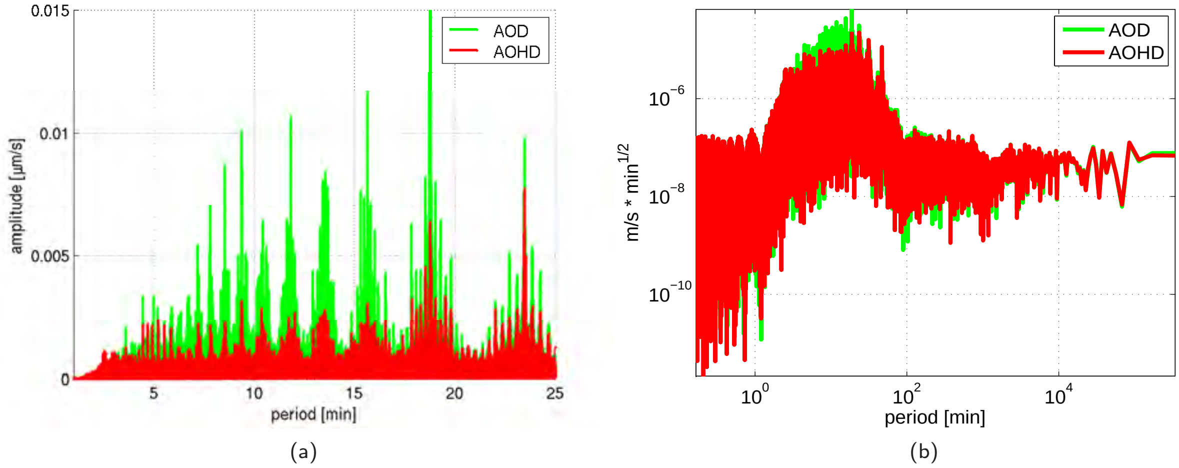

(a) (b)

Fig. 10.43: Spectra (a) and PSD (b) of 1 year (2007) KBRR-residuals after removing AOD (green) and AOHD (red). Unit: μm/s.

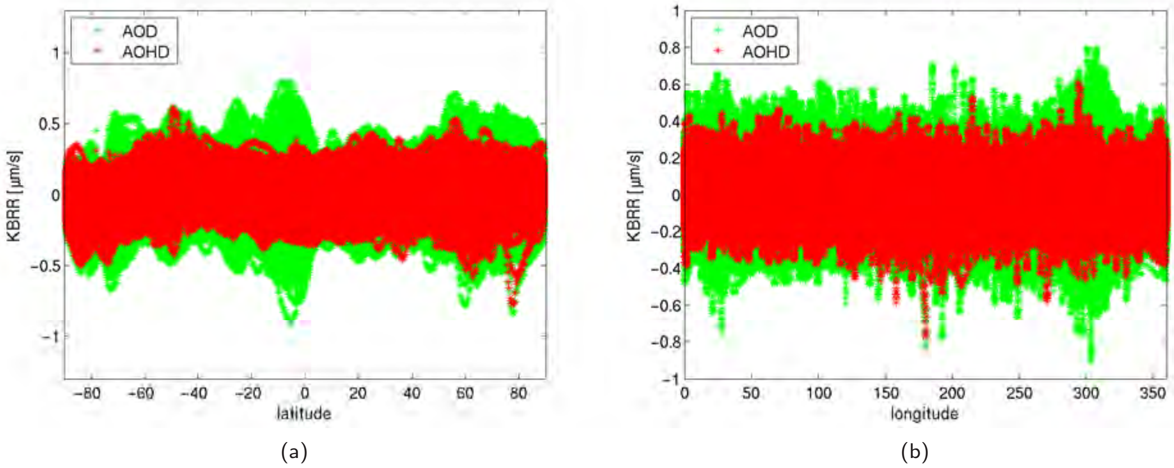

(a) (b)

Fig. 10.44: KBRR-residuals for 2007 against (a) latitude and (b) longitude after removing AOD (green) and AOHD (red). Unit: μm/s.

Summary - Using daily GRACE solutions for an additional 'hydrological' de-aliasing

- the daily ITG-GRACE solutions are interpolated on a 6-hourly resolution and added to the atmospheric & oceanic de-aliasing product (AOD) in order to apply an additional 'hydrological' de-aliasing (AOHD)
- the daily ITG-GRACE solutions should mainly contain hydrological signal (apart from instrument errors and unmodelled processes, like ice melting and post-glacial rebound (PGR))
- differences between the standard AOD and AOHD products can reach up to several cm (min: -7.55 mm, max: 13.43 mm, mean: -5.06 mm, rms: 2.03 mm for August 2007)
- whether subtracting the AOD or AOHD product affects a monthly gravity field solution in the mm to cm-range (min: -10.59 mm, max: 4.99 mm, mean: 0.00 mm, rms: 1.37 mm for December 2007)
- the global weighted rms of the monthly gravity field solutions is reduced by about 28 % to 43 % when applying the AOHD instead of the AOD product (1.52 mm for AOD vs. 0.87 mm for AOHD, August 2007)
- the daily rms of the KBRR-residuals over 2007 is significantly reduced ($\sim$ 19 %) when subtracting AOHD (0.26μm/s for AOD vs. 0.21 μm/s for AOHD)
- effect of an additional hydrological de-aliasing on the rms of KBRR-residuals over 1 year is in the sub-$\mu m/s$-range. Improvements do not only occur in regions with high hydrological variability, but also over the oceans (min: -0.10 $\mu m/s$, max: 0.81 $\mu m/s$, mean: 0.06 $\mu m/s$, rms: 0.09 $\mu m/s$)

In summary, we can state, that the KBRR-residuals can be improved globally - and not only in regions with high hydrological variations - when using AOHD. This brings us back to the discussion at the beginning of this chapter. We can retain, that the daily ITG-GRACE solutions not only contain hydrological signal, but also high-frequent variations probably mainly caused by oceanic mass distributions. As we have seen, the KBRR-residuals, which are a quality measure of gravity field solutions, could have been significantly reduced in regions with high oceanic mass variability, e.g. in the Southern Ocean areas, we dare to corroborate the findings and conclusions of *Bonin and Chambers* (2011). It will be worth starting to use the (daily) GRACE data itself to improve the de-aliasing model, especially the oceanic model, and thus further improve GRACE results.

Part IV.

Summary, Discussion & Outlook

The goal of this thesis was to make a contribution to an improved modelling of non-tidal atmospheric and oceanic mass variations in order to optimize the de-aliasing process, which plays a major role for gravity field processing. For the current gravity field mission GRACE, the de-aliasing process is regarded to be one of the remaining problem areas, leading to the fact, that the accuracy predicted prior to launch could not yet be achieved. To improve the de-aliasing process, various changes in the computation of the de-aliasing product have been made, and their impact on GRACE data analysis has been analyzed (Part III).

The impact is shown on various processing levels: AOD coefficients, monthly gravity field solutions, and KBRR-residuals (before gravity field determination, only based on orbit determination). While the impact on the level of the AOD coefficients themselves does not have any informative value whether the changes made will improve or deteriorate a gravity field solution, monthly gravity field solutions (or the corresponding weighted rms) and KBRR-residuals do have this value. However, it is debatable if the latter or the former are more qualified for demonstrating the quality of a gravity field solution. Some of the analyses made within Part III show a positive effect on the level of the KBRR-residuals, but none on the rms of a monthly gravity field solution. One possible explanation for this could be the following: In the course of gravity field modelling one tries to minimize the observational residuals according to the Gaussian least-squares principle (more details on the BERNESE gravity field processing can be found, i.e. in *Beutler et al.* (2010b) and *Jäggi et al.* (2009a)). By only adjusting orbit parameters, one tries to minimize the differences between the computed observations based on a priori models (all background models: AOD, Tides, ...) and the real observations made by GRACE. For the optimum results, one tries to find the adequate parameterization, e.g., empirical parameters, also called stochastic pulses are introduced in order to minimize the residuals (cf. Sect. 2). These stochastic pulses may absorb signals as well as model errors and unmodelled effects and could be one reason why there is sometimes an effect on the level of KBRR-residuals, but not in the monthly gravity field solutions visible. As there are many screws that can be changed during gravity field determination (e.g., stochastical pulses), we tend to regard the KBRR-residuals as the more suitable quantities to investigate the impact of changes in the de-aliasing product on the quality of gravity field solutions.

The various test scenarios of the de-aliasing coefficients and the main stastical numbers of the effect of the various experiments are summarized in Fig. 10.46. Those de-aliasing scenarios which have a positive effect on GRACE KBRR-residuals and/or monthly GRACE gravity field solutions are shown in green color. In addition, Fig. 10.45 illustrates the various AOD scenarios and their impact on GRACE in terms of degree standard deviations.

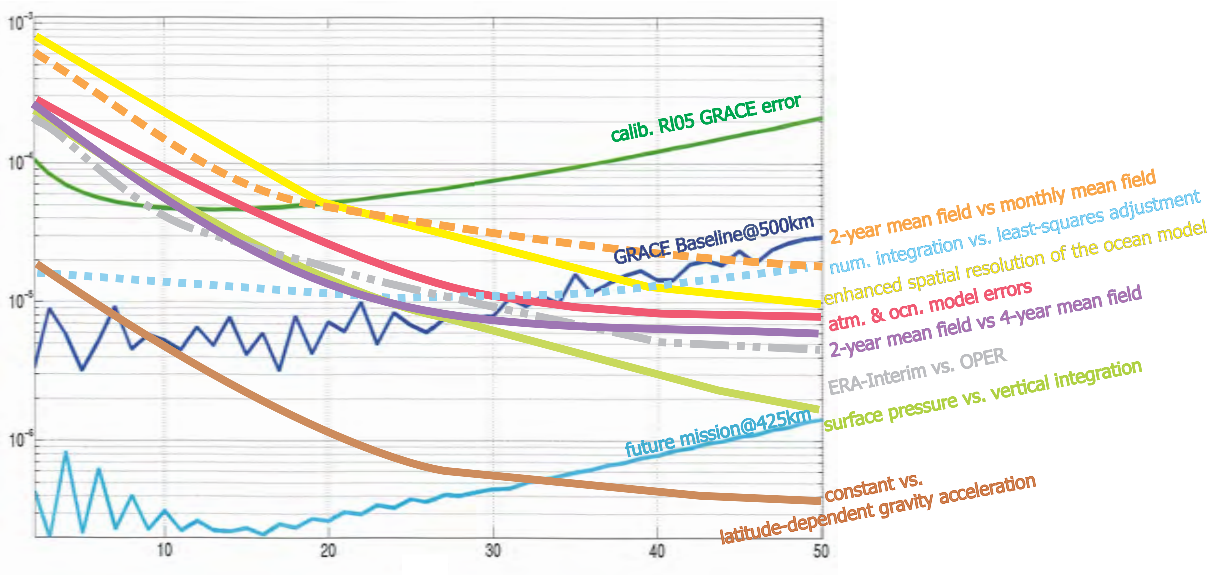

Fig. 10.45: Impact of various de-aliasing scenarios on GRACE and possible future gravity field missions. Unit: m

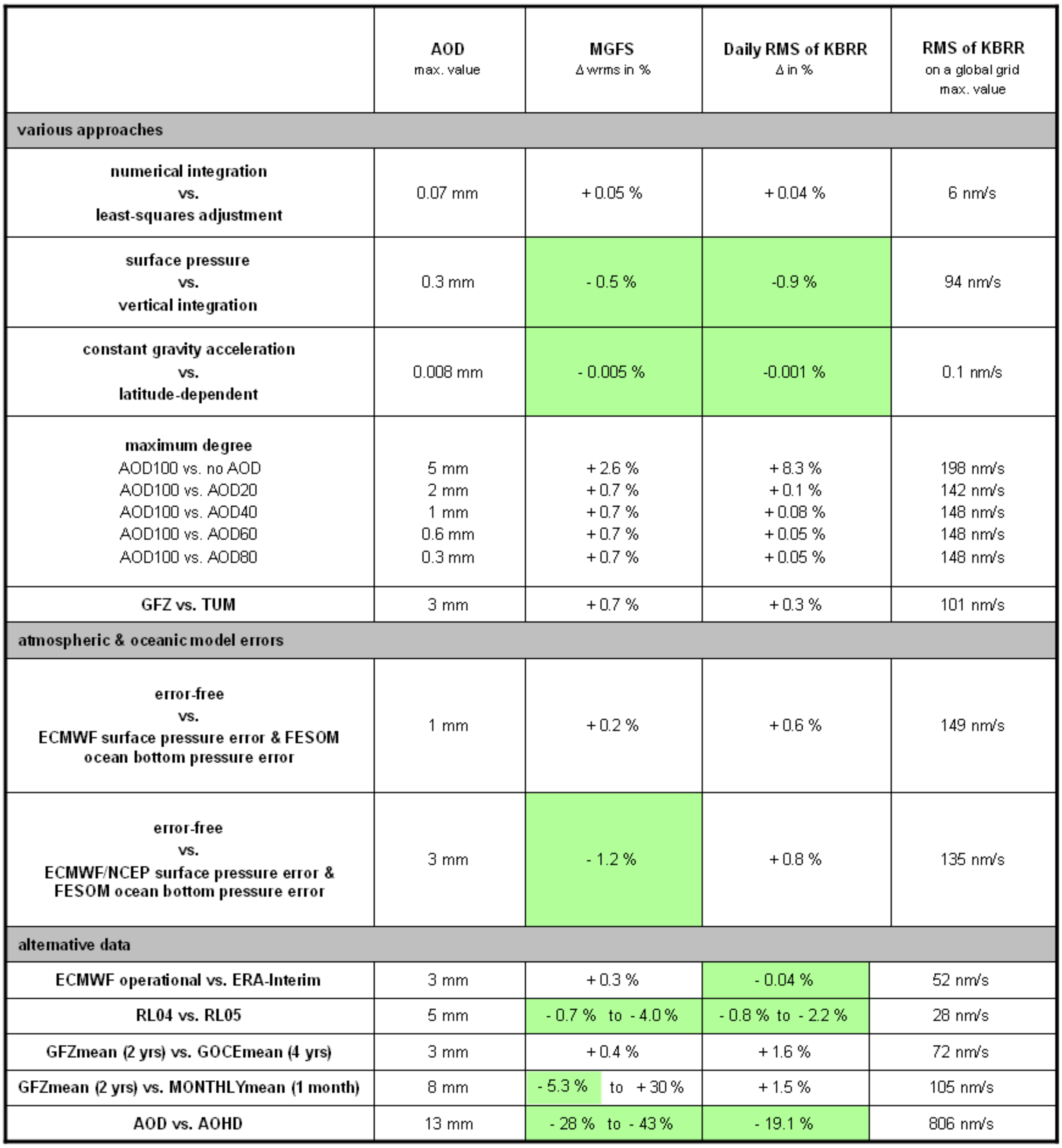

	AOD max. value	**MGFS** Δ wrms in %	**Daily RMS of KBRR** Δ in %	**RMS of KBRR** on a global grid max. value
various approaches				
numerical integration **vs.** **least-squares adjustment**	0.07 mm	+ 0.05 %	+ 0.04 %	6 nm/s
surface pressure **vs.** **vertical integration**	0.3 mm	- 0.5 %	-0.9 %	94 nm/s
constant gravity acceleration **vs.** **latitude-dependent**	0.008 mm	- 0.005 %	-0.001 %	0.1 nm/s
maximum degree				
AOD100 vs. no AOD	5 mm	+ 2.6 %	+ 8.3 %	198 nm/s
AOD100 vs. AOD20	2 mm	+ 0.7 %	+ 0.1 %	142 nm/s
AOD100 vs. AOD40	1 mm	+ 0.7 %	+ 0.08 %	148 nm/s
AOD100 vs. AOD60	0.6 mm	+ 0.7 %	+ 0.05 %	148 nm/s
AOD100 vs. AOD80	0.3 mm	+ 0.7 %	+ 0.05 %	148 nm/s
GFZ vs. TUM	3 mm	+ 0.7 %	+ 0.3 %	101 nm/s
atmospheric & oceanic model errors				
error-free **vs.** **ECMWF surface pressure error & FESOM ocean bottom pressure error**	1 mm	+ 0.2 %	+ 0.6 %	149 nm/s
error-free **vs.** **ECMWF/NCEP surface pressure error & FESOM ocean bottom pressure error**	3 mm	- 1.2 %	+ 0.8 %	135 nm/s
alternative data				
ECMWF operational vs. ERA-Interim	3 mm	+ 0.3 %	- 0.04 %	52 nm/s
RL04 vs. RL05	5 mm	- 0.7 % to - 4.0 %	- 0.8 % to - 2.2 %	28 nm/s
GFZmean (2 yrs) vs. GOCEmean (4 yrs)	3 mm	+ 0.4 %	+ 1.6 %	72 nm/s
GFZmean (2 yrs) vs. MONTHLYmean (1 month)	8 mm	- 5.3 % to + 30 %	+ 1.5 %	105 nm/s
AOD vs. AOHD	13 mm	- 28 % to - 43 %	- 19.1 %	806 nm/s

Fig. 10.46: Overview of the impact of various AOD scenarios. The first column describes the analyzed experiment, and the second column the maximum absolute effect on the AOD product in terms of mm geoid heights. The third column reflects the change in the weighted global rms of the analyzed monthly gravity field solution(s) by alternating the AOD product (which is described in the first column). The fourth column contains the change of the daily rms of the KBRR-residuals in percent. Positive percentages in columns three and four indicate, that the monthly gravity field solution and the daily rms of the KBRR-residuals degrade w.r.t. the 'standard' AOD (named first in column one). A negative sign means an improvement of the alternative AOD product (named at second place in column one) w.r.t. to the 'standard' AOD, i.e., that the green colored boxes show the cases where the GRACE results could have been improved by using an alternative de-aliasing product. The last column describes the absolute maximum effect between the analyzed scenarios on the KBRR-residuals on a global latitude and longitude grid. Deeper analysis on the results summarized above can be found in Sects. 8, 9, and 10.

In the first part (Sect. 8), various de-aliasing approaches have been compared to each other. We have shown, that the differences between the determination of the AOD product by numerical integration and least-squares adjustment are by far the smallest and do currently not affect GRACE. Nevertheless, one should be aware, that the coefficients obtained by least-squares adjustment slightly differ from those determined by numerical integration, and will have an affect on future gravity field missions with an higher accuracy than GRACE. Although the least-squares adjustment requires much more computational effort, one has to switch from the numerical integration to the least-squares adjustment, if one wants to take atmospheric and oceanic model errors into account, and propagate them further on to errors of the de-aliasing coefficients.

Also shown in chapter 8 is the fact, that the vertical integration approach leads to slightly better GRACE results than the surface pressure approach and is thus implemented in the official de-aliasing process.

The investigations on the cut-off frequency (maximum degree) of the de-aliasing product has led us to the conclusions, that - concerning the actual accuracy of gravity field determination with GRACE - it seems to be sufficient to apply the AOD coefficients only up to degree and order 40 (or even only 20). However, there is no doubt about applying or not applying AOD, as the de-aliasing process significantly improves the GRACE gravity field time series.

At the end of Sect. 8, we compared the official RL04 AOD product provided by GFZ with the de-aliasing product determined by our TUM software. The comparison have shown, that there are still significant differences between the two solutions - probably due to the transformation from Gaussian grid to equidistant latitude-longitude grid - and that the GFZ solution as well as the TUM solution do have their pros and cons. Efforts should be made to identify the differences and to combine the pros of the two solutions, in order to derive an optimal de-aliasing product.

In the second part (Sect. 9), the impact of atmospheric and oceanic model errors on AOD and GRACE has been investigated. Therefore, the newly developed de-aliasing approach allowing to take geophysical model errors into account and to propagate them on the de-aliasing coefficients was used. The mathematical model this new approach is based on can be found in Sect. 4 as well as in *Zenner et al.* (2010), *Zenner et al.* (2012a) and *Zenner et al.* (2012b). In our investigations we found, that depending on the chosen surface pressure errors, significant positive effects are visible in monthly GRACE gravity field solutions. Propagating the surface pressure error derived from model inter-comparisons between NCEP and ECMWF further to the de-aliasing coefficients will for example improve the monthly gravity field solution of August 2007 by about 1.2 %, although no positive or significant effect on the level of the KBRR-residuals is visible. It has to be mentioned, that strongly depending on the introduced error maps, different results are obtained and various conclusions can be drawn here. Any variation of the introduced error maps will affect the results. The determination of reasonable error values for surface pressure and ocean bottom pressure is a challenging task, and therefore, further investigations will be needed here. Nevertheless, independently of the reliability of the error maps used within this thesis, our investigations have given for the first time insight into the sensitivity of AOD and GRACE on various geophysical model errors. It was shown, that taking into account atmospheric and oceanic model errors can affect a monthly gravity field solution in the mm-range. One should be aware, that these model errors will also affect, e.g., GRACE derived ice mass balances estimates. A first estimation for the surface pressure error derived from model inter-comparisons between NCEP and ECMWF shows, that the assumed model errors will affect mass estimates, e.g., in the Filchner-Ronne ice shelf in Antarctica by approximately 30 gigatons.

Last but not least, in Sect. 10, the impact of alternative and additional data on AOD and GRACE gravity field processing has been investigated. Starting with an investigation on the impact of using ERA-Interim data instead of the operational ECMWF data for the computation of the de-aliasing product (Sect. 10.1), the users of the GRACE gravity field solutions and the associated de-aliasing products should be aware, that the current (atmospheric) de-aliasing coefficients are not consistent for the GRACE observation time covering the period 2002 to now. This is due to the fact, that for the computation of the de-aliasing product operational data provided by ECMWF is used. These operational data sets are subject to model changes from time to time, like an increase of the horizontal and/or vertical resolution. These model changes in the operational data lead to inconsistencies in the atmospheric model, which in turn are directly reflected in the AOD product (cf. *Gruber et al.* (2008), *Duan et al.* (2012)). These inconsistencies, again, might lead to errors in mass transfer estimates (e.g., mass of the atmosphere, mountain glacier mass balances) deduced from GRACE gravity field solutions. Therefore, the consistency of the horizontal and vertical resolution of the atmospheric (and oceanic) model over longer time periods is essential for any reliable mass transfer estimates. By using ECMWF's ERA-Interim data one would avoid at least such inconsistencies, as the ERA-data are reprocessed with the same (software) settings. Results have shown, that although the effect of using ERA-Interim instead of operational data on level of KBRR-residuals and monthly gravity field solutions is rather small, ERA-Interim will lead to significantly different results (*mm*-range) in the AOD product and have - concerning the GRACE baseline and future gravity field missions - a significant impact for gravity field determination. However, the consistency of the time series by using ERA-Interim can only be achieved at the expense of the vertical spatial resolution, as the ERA-Interim data has a lower spatial resolution than the operational data (60 model levels vs. 91 model levels). In addition it has to be stated here, that the ERA-Interim data sets are only updated once per month, which would mean for the computation of the de-aliasing product and associated gravity field solutions a delay of several weeks. Mainly the latter is the reason why currently for the determination of the AOD product operational ECMWF data is used.

In a next step (Sect. 10.2), the official GFZ RL04 AOD product was compared to the GFZ RL05 solution, where one major change includes the integration of an ocean model with enhanced spatial resolution. Results have shown, that applying RL05 AOD instead of RL04 AOD will improve the monthly gravity fields by about 0.7 % to 4 % depending on the analyzed month. Also the daily rms of the KBRR-residuals could have been improved/reduced by about 0.8 % to 2.2 %, again depending on the analyzed time-span. However, RL05 is still facing some problems, especially in near-continental regions, which is probably due to a strong trend in the RL05 ocean data.

In Sect. 10.3 alternative mean fields for the atmospheric and oceanic mass variations have been tested. On the one hand, the new atmospheric and oceanic mean fields are covering the period 2004-2007 instead of 2001-2002. Results have shown, that no significant improvements concerning the monthly gravity field solutions or the daily rms of the KBRR-residuals could have been achieved when using the alternative mean fields. Though, some regions exist, where the 2004-2007 mean performs slightly better than the one of 2001-2002. On the other hand, the subtraction of a mean field covering the analyzed month has been investigated and compared to the subtraction of the 2001-2002 mean fields. Here, the effect on AOD, monthly gravity field solution, and KBRR-residual level is much more significant. The weighted rms of the monthly gravity field solution is both improved/decreased by up to 5.3 % and degraded/increased by up to 30 %, depending on the analyzed month.

At this point the 'mean field issue' shall be briefly discussed, as it is and will be a topic to be discussed within the framework of future gravity field missions: The intention of the de-aliasing process is to model and 'remove' those high-frequent atmospheric and oceanic mass variations which cannot be observed adequately by GRACE due to the orbit configuration and the associated time and space sampling. Subtracting from the AOD product for a particular month the mean of this month, means that only 'real' (sub-monthly) high-frequent atmospheric and oceanic variations, i.e. the deviations from this monthly mean are taken into account during the de-aliasing process, which in the sense of de-aliasing is actually the goal of this process. In contrast, when a long-term mean of the AOD product (e.g. the 2001+2002 mean field) is subtracted from the AOD product of every month, the resulting AOD fields contain not only the sub-monthly variations, but also sub-annual, and semi-annual variations, which may be observable by GRACE. Also, trends between the analyzed interval and the interval covering the mean field are reflected in the AOD-coefficients. Answering the question about the 'better' or 'worse' approach is not that easy. Various opinions on this topic exist amongst experts. Though, one could answer the question of the 'cleanest' approach, leading to the 'best' solution in the sense of smallest KBRR-residuals. If one wants to minimize the deviations between the modelled and observed world (which are reflected in the KBRR-residuals), one has to subtract from the atmospheric and oceanic mass variations, mean fields covering the identical time period as the static (a-priori) gravity field C^{st}_{nm}/S^{st}_{nm} (cf. Sect. 2), which is introduced for gravity field determination. As this static gravity field contains the mean atmospheric and oceanic mass variations, one should regard the deviations from this mean field in the atmospheric and oceanic de-aliasing process in order to be consistent.

The last investigation within this Section 10 is dealing with the impact of an additional 'hydrological' de-aliasing (Sect. 10.4). An additional 'hydrological' de-aliasing by using the daily ITG-GRACE solutions leads, as expected, to smaller KBRR-residuals. We have shown, that the KBRR-residuals, which are a quality measure of gravity field solutions, could have been significantly reduced not only in regions with high hydrological dynamics, but also in regions with high oceanic mass variability, e.g. in the Southern Ocean areas. Thus, we could confirm the findings and conclusions by *Bonin and Chambers* (2011).

Using the (daily) GRACE data itself will improve the de-aliasing model, especially the oceanic model, and thus further improve GRACE results.

The question of modelling and 'removing' high-frequent hydrological mass variations in addition to the atmospheric and oceanic ones, is subject of permanent discussion amongst the community. Some people pursue the approach of modelling and 'removing' all three mass variations (atmospheric, oceanic, hydrological), which will result in monthly gravity field solutions containing less or hardly any geophysical signal if the 'removed' mass variations are not added back. Only unmodelled mass variations like ice and post-glacial rebound, as well as measuring errors and instrumental errors, should then be contained in the monthly gravity field solutions. This approach could be helpful e.g. for the detection and identification of model insufficiencies. Others are strictly against this approach and argue, that the intention of the GRACE mission is to observe the (hydrological) mass variations and not to model the mass variation in order to get the observations to zero. Furthermore, the monthly GRACE gravity field solutions would become more or less 'unfeasible' for direct geophysical (hydrological) applications and interpretations, unless one does not re-add the 'removed' signals (de-aliasing product). But regardless of which approach one supports, by re-addition of the 'removed' signal during the de-aliasing process, i.e. either of the atmospheric and oceanic de-aliasing coefficients (AOD) or the atmospheric, oceanic, and hydrological (AOHD) ones, the results should be the same.

At length this means the following: As described in Sect. 2 and Fig. 2.1, the monthly gravity field solutions $C_{nm}^{GSM}/S_{nm}^{GSM}$ do not contain any high-frequency atmospheric or oceanic mass variations, if the AOD product is used for de-aliasing, nor do they contain any high-frequent atmospheric, oceanic, and hydrological mass variations, if the AOHD product is applied during the de-aliasing process. Both, re-adding the monthly mean of the AOD or the monthly mean of the AOHD product ($\Delta C_{nm}^{AOM}/\Delta S_{nm}^{AOM}$ or $\Delta C_{nm}^{AOHM}/\Delta S_{nm}^{AOHM}$) to the corresponding monthly gravity field solution ($C_{nm}^{GSM}/S_{nm}^{GSM}$), should lead to the same results. Figure 10.47 illustrates exactly this experiment for three chosen months (January, August, December) of the year 2007. In the first row, the monthly mean of the AOD product is re-added to the corresponding monthly gravity field solution ($C_{nm}^{GSM}/S_{nm}^{GSM} + \Delta C_{nm}^{AOM}/\Delta S_{nm}^{AOM}$). The second row shows the same results for re-adding the monthly mean of the AOHD product to the corresponding monthly gravity field solution ($C_{nm}^{GSM}/S_{nm}^{GSM} + \Delta C_{nm}^{AOHM}/\Delta S_{nm}^{AOHM}$). The third and fourth row illustrate the unfiltered and 800 *km* Gaussian-smoothed differences between rows one and two. As we can see (cf. Figs. 10.47g-l) the unfiltered differences are at the *mm* level. Maximum values of 1.52 *mm* occur. Also a 'striping pattern' shows up, which could lead us to assume, that the remaining 'stripes' in the current GRACE gravity field solutions are - at least partly - due to insufficiently modelled high-frequent signal. Applying the Gaußfilter on the differences leads to damped but still significant amplitudes of maximum 0.7 *mm* in terms of geoid heights. Especially in August 2007 (Fig. 10.47k), significant differences appear in regions with known geophysical processes, e.g. Amazon, Ganges, Brahmaputra, and also oceanic regions with known high variability.

One should be aware, that this will have consequences for several geophysical applications (i.e. mass estimates) using the monthly GRACE gravity field solutions (and the monthly mean de-aliasing products). Depending on the product (AOD or AOHD) which is applied/'removed' in the de-aliasing process, different results are obtained.

In conclusion, within this thesis the impact of various de-aliasing scenarios on AOD and GRACE data analysis has been investigated on several processing levels. Some of the analyses made within this work have a rather small or hardly any impact on current GRACE gravity field processing. Nevertheless, it should be kept in mind, that most of the effects shown will become more and more important if the actual accuracy of GRACE can be further improved towards the expected baseline by other means. In particular, the stochastic modelling of the geophysical input data and the herewith associated determination of reliable uncertainty estimates of the atmospheric and oceanic models will play a major role for de-aliasing. Especially, for future gravity field missions, with significantly improved observation accuracy, an optimal modelling of these high-frequent atmospheric and oceanic mass variations remains a key issue to be solved. The performed investigations within this thesis might help to further optimize the de-aliasing process and thus current and future gravity field time series.

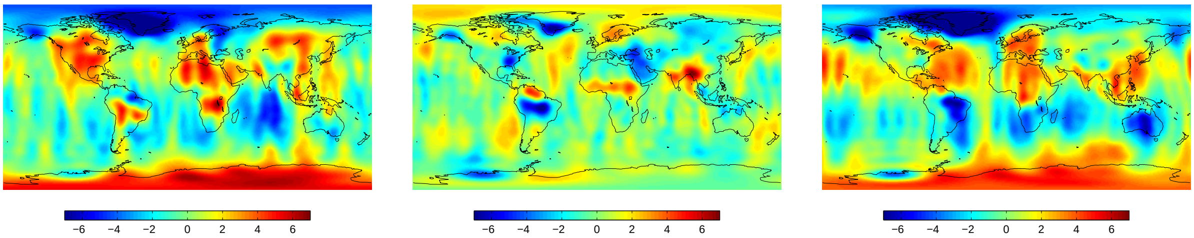

(a) MGFS + AOD (Jan) (b) MGFS + AOD (Aug) (c) MGFS + AOD (Dec)

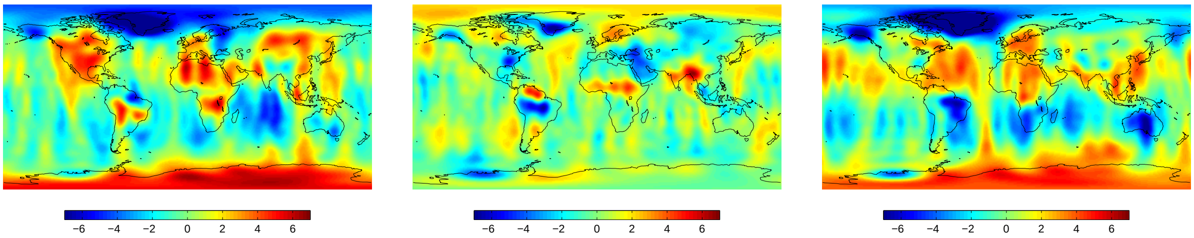

(d) MGFS + AOHD (Jan) (e) MGFS + AOHD (Aug) (f) MGFS + AOHD (Dec)

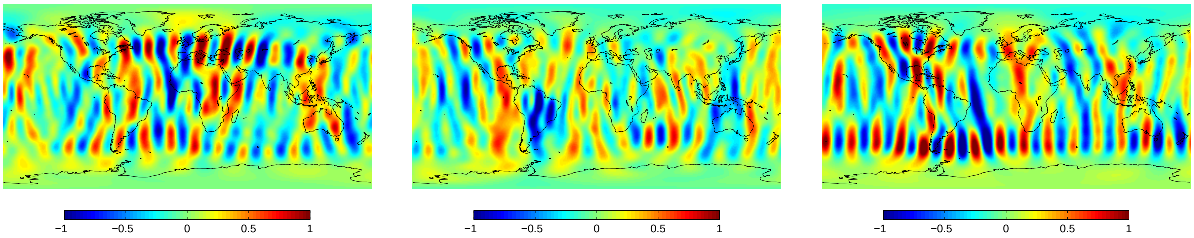

(g) unsmoothed diff. (a) - (d) (h) unsmoothed diff. (b) - (e) (i) unsmoothed diff. (c) - (f)

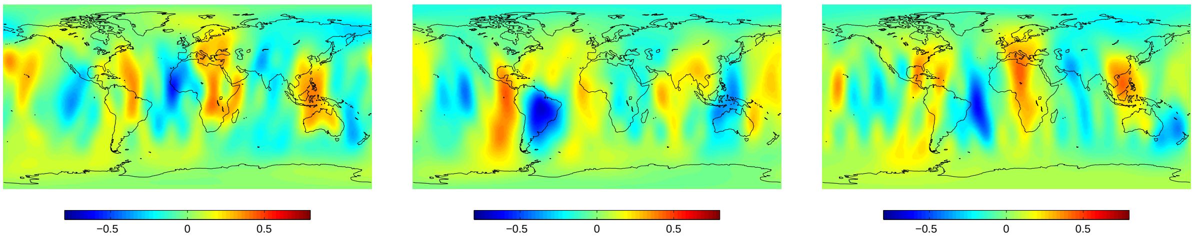

(j) smoothed diff. (a) - (d) (k) smoothed diff. (b) - (e) (l) smoothed diff. (c) - (f)

Fig. 10.47: Monthly gravity field solutions for January (first column), August (second column) and December (third column) 2007 after re-addition of (a-c) the monthly mean AOD product and (d-f) the monthly mean AOHD product, as well as their (g-i) unfiltered and (j-l) filtered (800km Gaufilter) differences in terms of geoid heights. Unit: mm.

Part V.

APPENDICES

11. The gravitational potential of the atmosphere – observations from the Earth's surface and from satellite altitude

It may be anticipated that all the results within this work remain unchanged from the following discussion. However, this chapter exists, because in this work the atmospheric and oceanic potential as well as the effect of various de-aliasing products are often expressed in terms of geoid heights. This is done in order to represent the spectral content of the atmospheric and oceanic potential also in the spatial domain. Geoid heights are chosen as they are - at least for geodesists - a familiar quantity.

In the determination of the atmospheric potential at a certain point P one has to distinguish between two main cases: is the computation point P situated inside or outside the attracting atmospheric masses. From potential theory it is well known, that the gravitational attraction of the atmosphere on a point on the Earth's surface is zero in the case of a radial-symmetric distribution of the atmospheric masses and the potential of the atmosphere above this point is constant. This is not the case for a point above the atmospheric masses in satellite altitude. For a point in satellite altitude the following formulas hold (cf. Sect. 3):

$$V(P) = \frac{GM}{R} \sum_{n=0}^{\infty} \left(\frac{R}{r}\right)^{(n+1)} \sum_{m=0}^{n} \bar{P}_{nm}(\cos\theta) \left[\bar{C}_{nm}\cos m\lambda + \bar{S}_{nm}\sin m\lambda\right] \tag{11.1}$$

$$\left.\begin{array}{c} \bar{C}_{nm} \\ \bar{S}_{nm} \end{array}\right\} = \frac{1}{(2n+1)} \cdot \frac{3}{4\pi R\bar{\rho}} \int\!\!\int_{\sigma} I_n(\theta,\lambda) \cdot \bar{P}_{nm}(\cos\theta) \left\{ \begin{array}{c} \cos m\lambda \\ \sin m\lambda \end{array} \right\} d\sigma \tag{11.2}$$

$$I_n = \int_{R}^{\infty} \left(\frac{r}{R}\right)^{n+2} \rho(r,\theta,\lambda) dr \tag{11.3}$$

with

r,θ,λ = spherical, geocentric coordinates
G = gravitational constant
M = Earth mass
R = radius of the Earth's sphere
ρ = volume density
$d\sigma$ = surface element
$\overline{P}_{nm}$ = associated normalized Legendre polynomials of degree n and order m
$\overline{C}_{nm}$,$\overline{S}_{nm}$ = normalized potential coefficients of degree n and order m

Performing the vertical integration of the atmospheric masses (cf. Sect. 3.2), the integration term turns into:

$$I_n = -\frac{1}{g} \int_{P_S}^{0} \left(\frac{R}{R-H} + \frac{N'}{R}\right)^{n+4} dp \tag{11.4}$$

for observations in satellite altitude. For points on the Earth's surface the following formulas hold:

$$V(P) = \frac{GM}{R}\sum_{n=0}^{\infty}\left(\frac{r}{R}\right)^{n}\sum_{m=0}^{n}\bar{P}_{nm}(\cos\theta)\left[\bar{C}_{nm}\cos m\lambda + \bar{S}_{nm}\sin m\lambda\right] \tag{11.5}$$

$$\left.\begin{array}{c}\bar{C}_{nm}\\ \bar{S}_{nm}\end{array}\right\} = \frac{1}{(2n+1)}\cdot\frac{3}{4\pi R\bar{\rho}}\int\!\!\int_{\sigma} I_n(\theta,\lambda)\cdot\bar{P}_{nm}(\cos\theta)\left\{\begin{array}{c}\cos m\lambda\\ \sin m\lambda\end{array}\right\}d\sigma \tag{11.6}$$

$$I_n = \int_{R}^{\infty}\left(\frac{R}{r}\right)^{n-1}\rho(r,\theta,\lambda)dr \tag{11.7}$$

Again, applying the assumptions made for the vertical integration (cf. Sect. 3.2), turns I_n into

$$I_n = -\frac{1}{g}\int_{P_S}^{0}\left(\frac{R}{R-H}+\frac{N'}{R}\right)^{-n+3}dp. \tag{11.8}$$

Comparing Eq. (11.5) to Eqs. (11.1) we see, that the radius r is now in the numerator of (r/R) and the degree dependent exponent is no longer $(n+1)$, but n. In Eq. (11.7) the ratio also changes. r is now in the denominator, which secures convergence as long as $r > R$.

In principle, it is not allowed to use the LAPLACE equation to propagate the potential from the satellite altitude to the surface and represent them as geoid heights via Eq. (11.1), as the atmospheric layer is not harmonic. Like mentioned before, Eq. (11.1) only holds at satellite altitude. Applying Eq. (11.1), or in other words, transforming the atmospheric and oceanic potential acting on a satellite into geoid heights on the Earth's surface has strictly speaking no physical meaning. Nevertheless, geoid heights were often used within this work in order to illustrate the de-aliasing coefficients, globally. But this issue has no effect on the shown results as we evaluate our investigations basically in terms of differences w.r.t. a standard case.

It would be more correct to derive two sets of coefficients when transforming the atmospheric and oceanic potential to geoid heights (on the Earth's surface). One set of potential coefficients holding for satellite altitude (via Eqs. (11.2) & (11.4)) and a second one derived from Eqs. (11.6) & (11.8) which are holding for the surface.

Figure 11.1 shows the vertically integrated atmospheric pressure I_n valid for points in satellite altitude (Fig. 11.1a) and for points on the Earth's surface (Fig. 11.1b), as well as their differences (Fig. 11.1c). The differences (cf. Tab. 11.1) reach up to 10 hPa for degree $n = 100$.

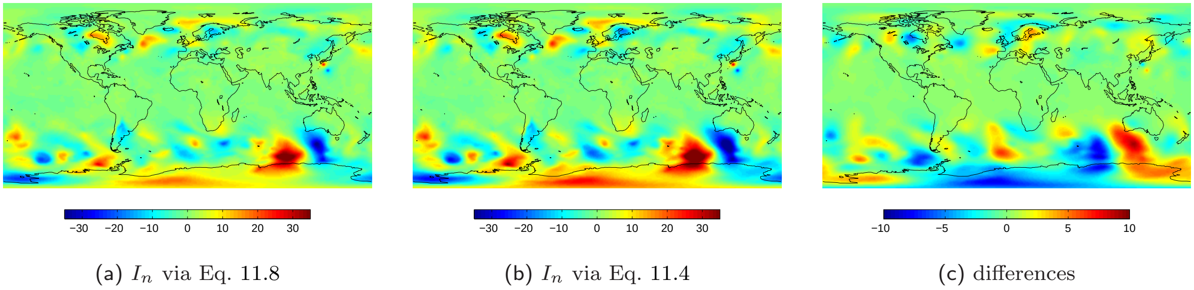

(a) I_n via Eq. 11.8

(b) I_n via Eq. 11.4

(c) differences

Fig. 11.1: Vertically integrated atmospheric pressure I_n for (a) satellite observations and (b) observations on the Earth's surface and (c) their differences. 01.08.2007, 00h. $n = 100$. Unit: hPa.

	$n = 100$				$n = 10$				$n = 1$			
	min	max	mean	wrms	min	max	mean	wrms	min	max	mean	wrms
I_n Eq. 11.4	-44.87	49.89	-0.00	6.17	-39.80	45.46	-0.01	5.45	-39.36	45.06	-0.01	5.39
I_n Eq. 11.8	-35.06	40.80	-0.02	4.79	-38.78	44.52	-0.01	5.31	-39.21	44.92	-0.01	5.37
diff.	-9.54	10.04	-0.02	1.75	-0.99	1.03	-0.00	0.18	-0.14	0.15	0.00	0.03

Tab. 11.1: Statistics on the vertically integrated atmospheric pressure I_n for points in satellite altitude (Eq. 11.4) and points on the Earth's surface (Eq. 11.8). 01.08.2007. 00h. Unit: hPa.

The differences between the atmospheric potential coefficients holding for satellite altitude and the ones holding for the Earth's surface are in the sub-mm range (min/max/mean/rms: -0.24/0.25/0.00/0.04 mm), when regarding geoid heights (cf. Fig. 11.2).

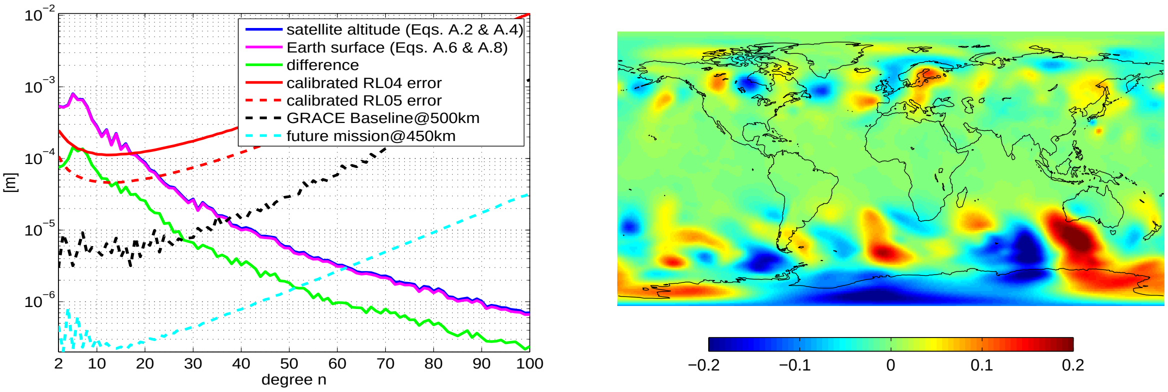

(a) (b)

Fig. 11.2: Comparison of the atmospheric potential for points in satellite altitude and points on the Earth's surface. (a) Degree standard deviations in terms of geoid heights. Unit: m. (b) Differences in terms of geoid heights. 01.08.2007 00h. Unit: mm.

12. ECMWF atmospheric model levels

Figure 12.1 shows the ECMWF model level definitions[1]. Each of the 91 model levels N is given with level dependent coefficients a, b provided with the meteorological data. The half-level ph and full-level pf pressure values are given in column four and five and are determined by the level dependent coefficients a, b given in column two and three and the pressure at the Earth's surface (P_s=1013.2500 hPa) (cf. Eq. 3.24 in Sect. 3.3). Level 91 corresponds to the Earth's surface, level 1 with a pressure of 0.01 hPa to the top of the atmosphere ($\sim$ 80 km).

N	**a**	**b**	**ph [hPa]**	**pf [hPa]**
0	0.000000	0.000000	0.0000	----
1	2.000040	0.000000	0.0200	0.0100
2	3.980832	0.000000	0.0398	0.0299
3	7.387186	0.000000	0.0739	0.0568
4	12.908319	0.000000	0.1291	0.1015
5	21.413612	0.000000	0.2141	0.1716
6	33.952858	0.000000	0.3395	0.2768
7	51.746601	0.000000	0.5175	0.4285
8	6.167656	0.000000	0.7617	0.6396
9	108.715561	0.000000	1.0872	0.9244
10	150.986023	0.000000	1.5099	1.2985
11	204.637451	0.000000	2.0464	1.7781
12	271.356506	0.000000	2.7136	2.3800
13	352.824493	0.000000	3.5282	3.1209
14	450.685791	0.000000	4.5069	4.0176
15	566.519226	0.000000	5.6652	5.0860
16	701.813354	0.000000	7.0181	6.3417
17	857.945801	0.000000	8.5795	7.7988
18	1036.166504	0.000000	10.3617	9.4706
19	1237.585449	0.000000	12.3759	11.3688
20	1463.163940	0.000000	14.6316	13.5037
21	1713.709595	0.000000	17.1371	15.8844
22	1989.874390	0.000000	19.8987	18.5179
23	2292.155518	0.000000	22.9216	21.4101
24	2620.898438	0.000000	26.2090	24.5653
25	2976.302246	0.000000	29.7630	27.9860
26	3358.425781	0.000000	33.5843	31.6736
27	3767.196045	0.000000	37.6720	35.6281
28	4202.416504	0.000000	42.0242	39.8481
29	4663.776367	0.000000	46.6378	44.3310
30	5150.859863	0.000000	51.5086	49.0732
31	5663.156250	0.000000	56.6316	54.0701
32	6199.839355	0.000000	61.9984	59.3150
33	6759.727051	0.000000	67.5973	64.7978
34	7341.469727	0.000000	73.4150	70.5061
35	7942.926270	0.000014	79.4434	76.4292
36	8564.624023	0.000055	85.7016	82.5725
37	9208.305664	0.000131	92.2162	88.9589
38	9873.560547	0.000279	99.0182	95.6172
39	10558.881836	0.000548	106.1445	102.5813
40	11262.484375	0.001000	113.6382	109.8913
41	11982.662109	0.001701	121.5502	117.5942
42	12713.897461	0.002765	129.9403	125.7453
43	13453.225586	0.004267	138.8558	134.3981
44	14192.009766	0.006322	148.3260	143.5909
45	14922.685547	0.009035	158.3816	153.3538
46	15638.053711	0.012508	169.0545	163.7180
47	16329.560547	0.016860	180.3786	174.7166
48	16990.623047	0.022189	192.3889	186.3837
49	17613.281250	0.028610	205.1223	198.7556
50	18191.029297	0.036227	218.6172	211.8697
51	18716.968750	0.045146	232.9140	225.7656
52	19184.544922	0.055474	248.0547	240.4844
53	19587.513672	0.067316	264.0833	256.0690
54	19919.796875	0.080777	281.0456	272.5644
55	20175.394531	0.095964	298.9895	290.0175
56	20348.916016	0.112979	317.9651	308.4774
57	20434.158203	0.131935	338.0245	327.9948
58	20426.218750	0.152934	359.2221	348.6233
59	20319.011719	0.176091	381.6144	370.4182
60	20107.031250	0.201520	405.2606	393.4375
61	19785.357422	0.229315	430.2069	417.7338
62	19348.775391	0.259554	456.4813	443.3441
63	18798.822266	0.291993	483.8506	470.1659
64	18141.296875	0.326329	512.0662	497.9584
65	17385.595703	0.362203	540.8577	526.4620
66	16544.585938	0.399205	569.9401	555.3989
67	15633.566406	0.436906	599.0310	584.4855
68	14665.645508	0.475016	627.9669	613.4989
69	13653.219727	0.513280	656.6129	642.2899
70	12608.383789	0.551458	684.8491	670.7310
71	11543.166992	0.589317	712.5573	698.7032
72	10471.310547	0.626559	739.5739	726.0656
73	9405.222656	0.662934	765.7697	752.6718
74	8356.252930	0.698224	791.0376	778.4036
75	7335.164551	0.732224	815.2774	803.1575
76	6353.920898	0.764679	838.3507	826.8141
77	5422.802734	0.795385	860.1516	849.2512
78	4550.215820	0.824185	880.6080	870.3798
79	3743.464355	0.850950	899.6602	890.1340
80	3010.146973	0.875518	917.2205	908.4403
81	2356.202637	0.897767	933.2247	925.2226
82	1784.854614	0.917651	947.6584	940.4416
83	1297.656128	0.935157	960.5245	954.0914
84	895.193542	0.950274	971.8169	966.1707
85	576.314148	0.963007	981.5301	976.6735
86	336.772369	0.973466	989.7322	985.6311
87	162.043427	0.982238	996.8732	993.3027
88	54.208336	0.989153	1002.8013	999.8373
89	6.575628	0.994204	1007.4431	1005.1222
90	0.003160	0.997630	1010.8488	1009.1459
91	0.000000	1.000000	1013.2500	1012.0494

Fig. 12.1: ECMWF model level definitions. a, b are level dependent coefficients provided by ECMWF. Half-level ph, and full-level pf corresponding values of pressure for a surface pressure of $P_s = 1013.250$ hPa (level $N = 91$) are given in the last two columns.

---

[1] `http://www.ecmwf.int/products/data/technical/model_levels/model_def_91.html`

Bibliography

Apel, J. (1987), *Principles of Ocean Physics*, International Geophysics Series, Academic Press.

Bettadpur, S. (2007), Level-2 Gravity field product user handbook, *GRACE Project Documentation Rev 2.3*, Austin, Texas.

Bettadpur, S., F. Flechtner, and R. Schmidt (2006), Usage guidelines for GFZ RL03 and JPL RL02 GRACE gravity fields & atmosphere/ocean background models, *Tech. rep.*

Beutler, G., A. Jäggi, L. Mervart, and U. Meyer (2010a), The celestial mechanics approach: application to data of the GRACE mission, *Journal of Geodesy*, *84*, 661–681, doi:10.1007/s00190-010-0402-6.

Beutler, G., A. Jäggi, L. Mervart, and U. Meyer (2010b), The celestial mechanics approach: theoretical foundations, *Journal of Geodesy*, *84*, 605–624, doi:10.1007/s00190-010-0401-7.

Bonin, J. A., and D. Chambers (2011), Evaluation of high-frequency oceanographic signal in GRACE data: Implications for de-aliasing, *Geophysical Res. Lett.*, *38*, L17,608, doi:10.1029/2011GL048881.

Bouman, J., S. Rispens, T. Gruber, R. Koop, E. Schrama, P. Visser, C. Tscherning, and M. Veicherts (2009), Preprocessing of gravity gradients at the GOCE high-level processing facility, *Journal of Geodesy*, *83*, 659–678, doi: 10.1007/s00190-008-0279-9.

Chen, J., C. Wilson, B. Tapley, and S. Grand (2007), GRACE detects coseismic and postseismic deformation from the Sumatra-Andaman earthquake, *Geophys. Res. Lett*, *34*, L13,302, doi:10.1029/2007GL030356.

Dach, R., U. Hugentobler, P. Fridez, and M. Meidl (Eds.) (2007), *Bernese GPS Software*, Astromical Insitute, University Bern, Bern, Switzerland.

Dee, D. P., S. M. Uppala, A. J. Simmons, P. Berrisford, P. Poli, S. Kobayashi, U. Andrae, M. A. Balmaseda, G. Balsamo, P. Bauer, P. Bechtold, A. C. M. Beljaars, L. van de Berg, J. Bidlot, N. Bormann, C. Delsol, R. Dragani, M. Fuentes, A. J. Geer, L. Haimberger, S. B. Healy, H. Hersbach, E. V. Holm, L. Isaksen, P. Kallberg, M. Köhler, M. Matricardi, A. P. McNally, B. M. Monge-Sanz, J.-J. Morcrette, B.-K. Park, C. Peubey, P. de Rosnay, C. Tavolato, J.-N. Thépaut, and F. Vitart (2001), The ERA-interim reanalysis: configuration and performance of the data assimilation system, *Quarterly Journal of the Royal Meteorological Society*, *137*(656), 553–597, doi:10.1002/qj.828.

Dehne, M., F. Guzmán Cervantes, B. Sheard, G. Heinzel, and K. Danzmann (2009), Laser interferometer for spaceborne mapping of the Earth's gravity field, *Journal of Physics Conference Series*, *154*(1), doi:10.1088/1742-6596/154/1/012023.

Dobslaw, H. (2007), *Modellierung der allgemeinen ozeanischen Dynamik zur Korrektur und Interpretation von Satellitendaten*, Scientific technical report, GFZ.

Dobslaw, H., F. Flechtner, I. Bergmann-Wolf, C. Dahle, R. Dill, S. Esselborn, I. Sasgen, and M. Thomas (2012), Simulated High-Frequency Atmosphere-Ocean Mass Variability for De-Aliasing of Satellite Gravity Observations: AOD1B RL05, *submitted to Geophys. Res. Lett.*

Döll, P., F. Kaspar, and B. Lehner (2003), A global hydrological model for deriving water availability indicators: model tuning and validation, *Journal of Hydrology*, *270*(1), 105–134.

Drijfhout, S., C. Heinze, M. Latif, and E. Maier-Reimer (1996), Mean circulation and internal variability in an ocean primitive equation model, *Journal of Physical Oceanography*, *26*(4), 559–580, früher: S. Drijfhout, C. Heinze, M. Latif, and E. Maier-Reimer (1995): Mean circulation and internal variability in an ocean primitive equation model. Max-Planck-Institut für Meteorologie, Report No. 177.

Duan, J., C. K. Shum, J. Guo, and Z. Huang (2012), Uncovered spurious jumps in the GRACE atmospheric de-aliasing data: potential contamination of GRACE observed mass change, *Geophysical Journal International*, doi:10.1111/j.1365-246X.2012.05640.x.

ECMWF (2008a), *IFS Documentation -Cy33r1. Part III: Dynamics and numerical procedures.*

ECMWF (2008b), *IFS Documentation -Cy33r1. Part IV: Physical processes.*

ECMWF (2009), *MARS User Guide. Technical Notes.*

Flechtner, F. (2007a), AOD1B product description document, *GRACE Project Documentation Rev. 3.1*, GFZ, Potsdam, Germany.

Flechtner, F. (2007b), GFZ level-2 processing standards document, *GRACE Project Documentation Rev. 1.0*, GFZ, Potsdam, Germany.

Flechtner, F., and T. Gruber (2007), Vereinfachte Darstellung der GRACE Datenalayse, DFG priority programm 1257: Mass transport and mass distribution in the system Earth.

Flechtner, F., C. Dahle, K. Neumayer, R. König, and C. Förste (2010), The release 04 CHAMP and GRACE EIGEN gravity models, in *System Earth via Geodetic-Geophysical Space Techniques, Adv. Technologies in Earth Sciences*, edited by F. Flechtner, M. Mandea, T. Gruber, M. Rothacher, J. Wickert, and A. Güntner, Springer, Berlin Heidelberg, doi: 10.1007/978-3-642-10228-8_4.

Floberghagen, R., M. Fehringer, D. Lamarre, D. Muzi, and B. Frommknecht (2011), Mission design, operation and exploitation of the Gravity field and steady-state ocean Circulation Explorer, *Journal of Geodesy*, *85(11)*, 749–758, doi: 10.1007/s00190-011-0498-3.

Greatbatch, R. J. (1994), A note on the representation of steric sea level in models that conserve volume rather than mass, *Journal of Geophysical Research*, *99*, 12,767–12,771, doi:10.1029/94JC00847.

Gruber, T., T. Peters, and L. Zenner (2008), The role of the atmosphere for satellite gravity field missions, in *Observing our Changing Earth*, *International Association of Geodesy Symposia*, vol. 133, edited by M. G. Sideris, pp. 105–112, Springer Berlin Heidelberg, doi:10.1007/978-3-540-85426-5_13, 10.1007/978-3-540-85426-5_13.

Han, S., C. Jekeli, and C. Shum (2004), Time-variable aliasing effects of ocean tides, atmosphere, and continental water mass on monthly mean GRACE gravity field, *J Geophys Res*, *109*, B04403, doi:10.1029/2003JB002501.

Heiskanen, W., and H. Moritz (1967), *Physical Geodesy*, W.H. Freeman, San Francisco.

Hibler, W. (1979), A dynamic thermodynamic sea ice model, *J. Phys. Oceanogr.*, *9*, 815–846, doi:http://dx.doi.org/10.1175/1520-0485(1979)009⟨0815:ADTSIM⟩2.0.CO;2.

Jacobson, M. Z. (2005), *Fundamentals of Atmospheric Modeling*, 2 ed., Cambridge University Press.

Jäggi, A. (2006), Pseudo-stochastic orbit modeling of low earth satellites using the global positioning system, Ph.D. thesis, Astronomical Institute, University of Bern, Switzerland.

Jäggi, A., U. Hugentobler, and G. Beutler (2006), Pseudo-Stochastic Orbit Modeling Techniques for Low-Earth Orbiters, *Journal of Geodesy*, *80*, 47–60, 10.1007/s00190-006-0029-9.

Jäggi, A., G. Beutler, U. Meyer, L. Prange, R. Dach, and L. Mervart (2009a), AIUB-GRACE02S - Status of GRACE gravity field recovery using the celestial mechanics approach, in *Geodesy for Planet Earth*, edited by Springer.

Jäggi, A., G. Beutler, L. Prange, U. Meyer, L. Mervart, R. Dach, R. Rummel, and T. Gruber (2009b), Gravity field determination at AIUB: current activities., EGU General Assembly 2009, EGU2009-8714.

Jäggi, A., G. Beutler, and L. Mervart (2010), GRACE Gravity Field Determination Using the Celestial Mechanics Approach – First Results, in *Gravity, Geoid and Earth Observatio*, *International Association of Geodesy Symposia*, vol. 135, edited by S. P. Mertikas, pp. 177–184, Springer Berlin Heidelberg, doi:10.1007/978-3-642-10634-7_24.

Kalman, R. E. (1960), A New Approach to Linear Filtering and Prediction Problems, *Transactions of the ASME - Journal of Basic Engineering*, (82, Series D), 35–45.

Kim, J. (2000), Simulation study of a low-low satellite-to-satellite tracking mission, Ph.D. thesis, University of Texas, Austin, US.

Koch, K. (1999), *Parameter Estimation and Hypothesis Testing in Linear Models*, 2nd edn. Springer, Berlin Heidelberg New York.

Kurtenbach, E. (2011), Entwicklung eines Kalman-Filters zur Bestimmung kurzzeitiger Variationen des Erdschwerefeldes aus Daten der Satellitenmission GRACE, Ph.D. thesis, Intitut für Geodäsie und Geoinformation, Universität Bonn.

Kurtenbach, E., T. Mayer-Gürr, and A. Eicker (2009), Deriving daily snapshots of the Earth's gravity field from GRACE L1B data using kalman filtering, *Geophysical Res. Lett.*, *36*, L17102, doi:10.1029/2009GL039564.

Lemoine, F., D. Smith, L. Kunz, R. Smith, N. Pavlis, K. S.M., D. Chinn, M. Torrence, R. Willamson, C. Cox, K. Rachlin, Y. Wang, K. S.C., R. Salman, R. Trimmer, R. Rapp, and R. Nerem (1997), The development of the NASA GSFC and NIMA Joint Geopotential Model., in *IAG Symposia: Gravity, Geoid and Marine Geodesy*, edited by J. Segawa, H. Fujimoto, and S. E. Okubo, pp. 461–469, Springer.

Lemoine, J.-M., S. Bruinsma, S. Loyer, R. Biancale, J.-C. Marty, F. Perosanz, and G. Balmino (2007), Temporal gravity field models inferred from GRACE data, *Advances in Space Research*, *39*(10), 1620 – 1629, doi:10.1016/j.asr.2007.03.062.

Loomis, B. D., R. Nerem, and S. Luthcke (2012), Simulation study of a follow-on gravity mission to GRACE, *Journal of Geodesy*, *86*, 319–335, doi:10.1007/s00190-011-0521-8.

Mayer-Gürr, T. (2007), ITG-Grace03s: The latest GRACE gravity field solution computed in Bonn, presentation at GSTM+SPP, Potsdam.

Mayer-Gürr, T., E. Kurtenbach, and A. Eicker (2010a), ITG-Grace2010 gravity field model.

Mayer-Gürr, T., E. Kurtenbach, and A. Eicker (2010b), Different representations of the time variable gravity field to reduce the aliasing problem in GRACE data analysis, in *Proceedings VII Hotine-Marussi Symposium on Theoretical and Computational Geodesy*, Springer Berlin Heidelberg.

Munk, W., and G. McDonald (1960), *The rotation of the Earth*, Cambridge University Press, Cambridge.

NCEP (2010), *NCEP Daily Global Analyses data provided by the NOAA/OAR/ESRL PSD*, Boulder, Colorado, USA.

Neumeyer, J., J. Hagedoorn, J. Leitloff, and T. Schmidt (2004), Gravity reduction with three-dimensional atmospheric pressure data for precise ground gravity measurements, *Journal of Geodynamics*, *38*, 437 – 450, doi:10.1016/j.jog.2004.07.006.

Peters, T. (2007), Modellierung zeitlicher schwerevariationen und ihre erfassung mit methoden der satellitengravimetrie, Ph.D. thesis, Fakultät fr Bauingenieur- und Vermessungswesen, TU München.

Pichler, H. (1997), *Dynamik der Atmosphäre*, Spektrum-Hochschultaschenbuch, Spektrum Akademischer Verlag.

Pierce, R., J. Leitch, M. Stephens, P. Bender, and R. Nerem (2008), Intersatellite range monitoring using optical interferometry, *Appl. Opt.*, *47*(27), 5007–5019, doi:10.1364/AO.47.005007.

Ponte, R., and J. Dorandeau (2003), Uncertainties in ECMWF surface pressure fields over the ocean in relation to sea level analysis and modeling, *Journal of Atmospheric and Oceanic Technology*, *20*, 301, doi:10.1175/1520-0426(2003)020⟨0301:UIESPF⟩2.0.COand2.

Salstein, D., R. Ponte, and K. Cady-Pereira (2008), Uncertainties in atmospheric surface pressure fields from global analyses, *Journal of Geophysical Research*, *113*, doi:10.1029/2007JD009531.

Sheard, B., G. Heinzel, K. Danzmann, D. A. Shaddock, W. M. Klipstein, and W. M. Folkner (2012), Intersatellite laser ranging instrument for the GRACE follow-on mission, *Journal of Geodesy*, *online*, doi:10.1007/s00190-012-0566-3.

Swenson, S., and J. Wahr (2002), Estimated effects of the vertical structure of atmospheric mass on the time-variable geoid, *J. Geophys. Res.*, *107(B9)*, 2194, doi:10.1029/2000JB000024.

Thomas, M. (2002), Ocean induced variations of Earth's rotation - results from a simultaneous model of global circulation and tides, Ph.D. thesis, University of Hamburg, Germany.

Thomas, M., J. Sündermann, and E. Maier-Reimer (2001), Consideration of ocean tides in an OGCM and impacts on subseasonal to decadal polar motion excitation, *Geophysical Res. Lett.*, *28*(12), 2457, doi:10.1029/2000GL012234.

Thompson, P., S. Bettadpur, and B. Tapley (2004), Impact of short period, non-tidal, temporal mass variability on GRACE gravity estimates, *Geophys. Res. Lett.*, *31*, L006619, doi:10.1029/2003GL019285.

Timmermann, R., S. Danilov, J. Schröter, C. Böning, D. Sidorenko, and K. Rollenhagen (2009), Ocean circulation and sea ice distribution in a finite element global sea ice - ocean model, *Ocean modelling*, *27*(3-4), 114–129, doi:10.1016/j.ocemod.2008.10.009.

Uppala, S. M., P. W. Kallberg, A. J. Simmons, U. Andrae, V. D. C. Bechtold, M. Fiorino, J. K. Gibson, J. Haseler, A. Hernandez, G. A. Kelly, X. Li, K. Onogi, S. Saarinen, N. Sokka, R. P. Allan, E. Andersson, K. Arpe, M. A. Balmaseda, A. C. M. Beljaars, L. V. D. Berg, J. Bidlot, N. Bormann, S. Caires, F. Chevallier, A. Dethof, M. Dragosavac, M. Fisher, M. Fuentes, S. Hagemann, E. Hlm, B. J. Hoskins, L. Isaksen, P. A. E. M. Janssen, R. Jenne, A. P. McNally, J.-F. Mahfouf, J.-J. Morcrette, N. A. Rayner, R. W. Saunders, P. Simon, A. Sterl, K. E. Trenberth, A. Untch, D. Vasiljevic, P. Viterbo, and J. Woollen (2001), The ERA-40 re-analysis, *Quarterly Journal of the Royal Meteorological Society*, *131*(656612), 2961–3012, doi:10.1256/qj.04.176.

U.S. Standard Atmosphere (1976), U.S. Standard Atmosphere 1976, *Tech. rep.*, U.S. Government Printing Office, Washington, D.C.

Visconti, G. (2001), *Fundamentals of Physics and Chemistry of the Atmosphere*, Springer.

Wei, M., Z. Toth, and Y. Zhu (2010), Analysis differences and error variance estimates from multi-centre analysis data, *Australian Meteorological and Oceanographic Journal*, *59/SP*, 25–34.

Werth, S., A. Güntner, S. Petrovic, and R. Schmidt (2009), Integration of GRACE mass variations into a global hydrological model, *Earth and Planetary Science Letters*, *277*(1-2), 166–173, doi:10.1016/j.epsl.2008.10.021.

Wilhelm, H., W. Zürn, and H. Wenzel (1997), *Tidal phenomena*, Lecture notes in Earth sciences, Springer.

Wolff, J., E. Maier-Reimer, and S. Legutke (1996), The Hamburg Ocean primitive equation model HOPE, *Tech. Rep. 13*, DKRZ, Hamburg.

Zenner, L., T. Gruber, A. Jäggi, and G. Beutler (2010), Propagation of atmospheric model errors to gravity potential harmonics - impact on GRACE de-aliasing, *Geophys. J. Int.*, (182), 797–807, doi:10.1111/j.1365-246X.2010.04669.x.

Zenner, L., E. Fagiolini, I. Daras, F. Flechtner, T. Gruber, T. Schmidt, and G. Schwarz (2012a), Non-tidal atmospheric and oceanic mass variations and their impact on GRACE data analysis, *Journal of Geodynamics*, *59-60*, 9 – 15, doi:10.1016/j.jog.2012.01.010.

Zenner, L., T. Gruber, G. Beutler, A. Jäggi, F. Flechtner, T. Schmidt, J. Wickert, E. Fagiolini, G. Schwarz, and T. Trautmann (2012b), Using atmospheric uncertainties for GRACE de-aliasing: first results, in *Geodesy for Planet Earth, IAG Symposia*, vol. 136, edited by S. Kenyon, M. Pacino, and U. Marti, pp. 147–152, Springer, doi:10.1007/978-3-642-20338-1_18.

Acknowledgments - Dank

First, I'd like to thank my supervisors Thomas Gruber, Roland Pail and Reiner Rummel for giving me the opportunity to do this work, for supporting me, and especially for pushing me to finish it. Many thanks also to Maik Thomas from GFZ for accepting the assessor job. Furthermore, I want to express my gratitude to Gerhard Beutler and Adrian Jäggi from the Astronomical Institute Bern, Switzerland. Not only for providing the BERNESE gravity field software and additional analysis software, but also for the fruitful and instructive discussions and the patient answering to many question concerning the BERNESE software.

Moreover, I'd like to thank the DeutscheForschungsGemeinschaft (DFG) for funding the SPP1257 projects IMPLY and IDEAL-GRACE as well as the International Graduate School for Science and Engineering (IGSSE) of the TU München for supporting this work.

Many thanks to all my colleagues at IAPG for an always pleasant and good working atmosphere. Even though I might running the risk annoying some colleagues by not mentioning them explicitly by name, I dare to express my special thanks to Christian Ackermann, Markus Heinze and Peter Steigenberger for supporting me with their technical knowledge and helpfulness concerning data acquisition, Linux-Cluster, Perl, LaTeX and any other Hard- or Software related problems. Thanks belongs also to Martin Horwath for detailed and fruitful discussions on the de-aliasing issue as well as to Claudia Stummer for supporting me, especially in times of 'minor motivation'.

Last but not least and most of all, I want to thank my family for always supporting me!